

City Research Online

City St George's, University of London

Citation: Nicholas, S (2022). High fidelity simulation of turbulent flows over filamentous surfaces. (Unpublished Doctoral thesis, City, University of London)

This is the accepted version of the paper.

This version of the publication may differ from the final published version. To cite this item please consult the publisher's version.

Permanent repository link: https://openaccess.city.ac.uk/id/eprint/29198/

Copyright and Reuse: Copyright and Moral Rights remain with the author(s) and/or copyright holders. Copies of full items can be used for personal research or study, educational, or not-for-profit purposes without prior permission or charge, unless otherwise indicated, provided that the authors, title and full bibliographic details are credited, a hyperlink and/or URL is given for the original metadata page and the content is not changed in any way. For full details of reuse please refer to City Research Online policy.

City Research Online: http://openaccess.city.ac.uk/ publications@citystgeorges.ac.uk

High Fidelity Simulation of Turbulent Flows Over Filamentous Surfaces



Shane Nicholas

School of Mathematics, Computer Science & Engineering

City, University of London

Submitted in part fulfilment of the degree of

Doctor of Philosophy

31st August 2022

Contents

List of Figures **vii**

List of Tables **xix**

Acknowledgements **xxi**

Declaration **xxiii**

Summary **xxv**

Nomenclature **xxix**

Acronyms **xxxix**

1 Introduction **1**

1.1 Introduction 1
1.2 Thesis structure 8
1.3 Author's Contribution 10

2 Literature Review **13**

2.1 Introduction 13
2.2 Classification of canopy flows 14
2.3 Coherent structures in canopy flows 18
2.4 Reconfiguration of canopies 21
2.5 Numerical investigations of canopy flows 24

3 Numerical Techniques **27**

3.1 Introduction 27
3.2 Finite Volume Method 28
3.3 Time discretisation 33
3.4 Poisson Solution Technique 35
3.5 Numerical Implementation 36
3.5.1 Turbulent channel flow 39

3.6 Immersed Boundary Method . . . 42
3.6.1 Interpolation and convolution . . . 44
3.6.2 Flow over a cylinder . . . 49
3.7 Flow over a rigid canopy . . . 53
3.7.1 Large eddy simulation . . . 53
3.7.2 Numerical setup . . . 56
3.7.3 Validation case . . . 59

4 Numerical investigation of regime transition in canopy flows 63

4.1 Introduction . . . 63
4.2 Numerical Setup . . . 64
4.3 Results and Discussion . . . 67
4.4 Concluding Remarks . . . 81

5 On the effects of in-plane solidity on the different regimes of canopy flows 85

5.1 Introduction . . . 85
5.2 Numerical Setup . . . 87
5.3 Results and Discussion . . . 90
5.3.1 Mean flow characteristics . . . 90
5.3.2 Canopy layer: scaling laws . . . 96
5.3.3 Heuristic model . . . 99
5.3.4 Statistical characterisation of the flow . . . 104
5.3.5 Structure of canopy flows . . . 114
5.4 Concluding Remarks . . . 140

6 On the effects of filaments inclination on canopy flows 143

6.1 Introduction . . . 143
6.2 Numerical Setup . . . 145
6.3 Results and Discussion . . . 147
6.3.1 A new phenomenological model . . . 151
6.3.2 Statistical characterisation of canopy flows . . . 154
6.3.3 Virtual origin framework in the roughness regime . . . 160
6.3.4 Prediction of drag change via the virtual origins . . . 169
6.3.5 Structure of the canopy flow regimes . . . 173
6.4 Concluding Remarks . . . 187

7 Relevance and Outlook 191

8 Conclusions **197**

8.1 Regime transition in canopy flows 198
8.2 Effect of filament spacing in canopy flows 200
8.3 Effect of filament inclination in canopy flows 204
8.4 Future Work 207

Bibliography **211**

List of Figures

1.1 Typical examples of textured biological surfaces (a) Silky shark skin (b) Sea leopard skin. (c) Skua wing in landing approach. (d) Lotus leaves. Extracted from Bechert *et al.* (2000*b*). 2

2.1 Geometrical parameters that govern canopy flows according to Nepf (2012), where H, h, d and ΔS represents the flow depth, canopy height, diameter of stem and stem spacing, respectively. 14

2.2 Sketch of the typical mean velocity profiles shape of canopy flows in sparse (left image), transitional (middle image) and dense (right image) regimes. The typical dominant turbulence scales are also sketched. Inspired from Nepf (2012). 16

2.3 Sketch of the typical zonal classification of the canopy according to Poggi *et al.* (2004*b*). Each zone is characterised by its characteristic length scale. The mixing layer is characterised by a superposition of three length scales. 18

3.1 (a): a typical CV with the compass notation used for the neighbour cell centres and the CV faces. (b) a typical CV with a skewed grid. 29

3.2 Scalability of the finite volume code with the two dimensional (a) and one dimensional (b) poisson solver. The dashed line represents the reference linear value, while the solid lines are the speed-up of our code ($\bigcirc$ $njm = 194$; $\triangle$ $njm = 388$; $\square$ $njm = 776$). (c) Spatial accuracy of the finite volume code. The dashed lines represents the first and second order accuracy, while the solid line is the accuracy of our finite volume code. 38

3.3 Sketch of the channel geometry. 39

3.4 (a): Mean velocity profile in wall units. (b) Reynolds stresses as function of wall normal distance scaled with outer flow units. The solid, dashed, dotted and dot-dash lines represents the streamwise, wall normal spanwise, and anisotropic terms, respectively. The circles in both the plots are used for the results by Moser *et al.* (1999) 40

3.5 The total shear stress (solid line), decomposed in the viscous stress (dash-dotted line) and Reynolds shear stress (dashed line) obtained from from simulation. The circles in both the plots are used for the results by Kim *et al.* (1987). 42
3.6 (a): Kernel function proposed by Roma *et al.* (1999). (b) Taken from Pinelli *et al.* (2010). The black rectangle is the cage around one of the Lagrangian points, shown as dots. The squares represents grid points, and the black ones are the grid points falling within the cage. 45
3.7 Sketch of the computational domain around a cylinder. 50
3.8 (a) Grid in the proximity of the cylinder (computational nodes are plotted with a skip index of 5). (b) The values of ϵ (Equation 3.65) for every Lagrangian point. 51
3.9 (a) Contours of the spanwise vorticity, ω_z. (b) Evolution of the lift C_L (solid line) and drag coefficients C_D (dashed line) over time. 51
3.10 (a) Contours of the streamwise velocity u/U_∞. (b) u/U_∞ (solid line) and v/U_∞ (dashed line) velocity profiles at $x = 10D$. The red dashed line represents the zero velocity line, while the blue dashed lines mark the boundaries of the cylinder. 52
3.11 Sketch of the computational domain. 56
3.12 (a) Geometrical parameters that characterises an idealised canopy composed of cylindrical filaments according to Nepf (2012). The velocity profile (given in blue) corresponds to a typical dense canopy regime (Monti *et al.*, 2020) (b) The mesh employed in the current investigation with emphasis in the wall-normal direction. 57
3.13 Filament cross section representation with RKPM method using four Lagrangian nodes. 58
3.14 (a) Computational domain with the filaments distribution: wall-parallel view. (b) random allocation of each filament into its own tile of size $\Delta S \times \Delta S$ is highlighted. 59
3.15 (a) Mean velocity profile normalised by the outer flow units (i.e., open channel height H and bulk velocity U_b). (b) r.m.s of the velocity fluctuations re-scaled by the local friction velocity, as a function of the wall normal distance. The square symbol represents the profiles extracted from Monti *et al.* (2020) for the configuration $\lambda = 0.14$, while the x symbols represents the profiles obtained in the current thesis for the same nominal solidity. 60

4.1 (a) Ratio of the sub-grid scale energy to the total fluctuating energy as a function of the wall normal direction (b) Ratio between eddy viscosity and the physical viscosity along the wall normal direction. The parameters have been averaged both in space (i.e., homogenous directions) and time. 66

4.2 Mean velocity profiles (a) in terms of the outer flow units (i.e., H and U_b). The circle symbols presents the mean locations of the internal inflection point and dashed lines represents the virtual origin. The black horizontal line represents the canopy height (h), while the dashed lines represents the position of the virtual origin (see text for definition) (b) in terms of the wall units. The $\tilde{y}^+$ represents the wall normal coordinates made non-dimensional with the inner and outer wall units, based on their origin. See text for colour-band and description on the virtual origin . 68
4.3 Mean locations of the mean velocity features, revealing the extent of the localised layers embedded within the canopy. The dashed and solid horizontal line. 70
4.4 Velocity fluctuations distributions made non-dimensional with the outer friction velocity ($u_{\tau,o}$). The solid, dashed and dotted lines represents the streamwise, wall normal and spanwise components. See text for colour-band. 71
4.5 (a) Mean momentum balance, with solid, dashed, and dotted lines representing the viscous, Reynolds stress, and the cumulative drag contributions. The solid black line represents the norm of the average pressure gradient. (b) Viscous and Reynolds stresses re-scaled with the local friction velocity $u_{\tau,l}$. 72
4.6 (a) Velocity and (b) vorticity fluctuations distributions rescaled with the local friction velocity scale ($u_{\tau,l}$) and the open channel height (H). The solid, dashed and dotted lines represents the streamwise, wall normal and spanwise components. See text for colour-band. 73
4.7 Distributions of the velocity fluctuations (a,c) and the stresses as a function of the non-stretched (top row) and stretched (bottom row) viscous units. The solid, dashed and dotted lines in the first columb represents the streamwise, wall normal and spanwise components. The solid and dashed lines in the second column represents the viscous and Reynolds stresses. See text for colour-band. 74
4.8 Form induced dispersive stresses as a function of wall normal distance normalised with the canopy height. The solid, dashed and dotted lines represents the streamwise, wall normal and spanwise components, while the symbols represents the anisotropic term ($u'_d v'_d$). See text for colour-band. 76
4.9 Wall parallel instantaneous snapshots located at $y/H = 0.02$ (a), (b), (e), (f) and at $y/H = 0.15$ (c), (d), (g), (h). The first and third columns represents the streamwise fluctuations, while the The second and fourth columns represents the spanwise fluctuations ($u'^+, w'^+ \in [-4, 4]$). The top and bottom row represents the TS and TD configurations, respectively. 77

4.10 Pre-multiplied spectra of the velocity fluctuations, as a function of the wall normal distance and the streamwise (top row) and spanwise wavelength (bottom row) scaled with the outer units. The first, second and third columns represents the streamwise, wall normal and spanwise components, respectively. The short vertical lines presents the wavelength of the mean filament spacing corresponding to the two canopy configurations, while the black line represents the wavelength equivalent of filament diameter. 78

4.11 Pre-multiplied spectra of the velocity fluctuations, as a function of the streamwise and spanwise wavelength scaled with the outer units. The three rows (top to bottom) corresponds to three wall normal locations $y = 0.02H, h, 0.15H$. Panels (a, d and f), (b, e and h) and (c, f and i), represents the streamwise, wall normal and spanwise components, respectively. See Figure 4.10 for the definitions of the colour lines. . . . 80

4.12 Magnitude of the pre-multiplied co-spectra of the $u'v'$ as a function of the wall normal direction scaled in outer units. The left and right panels represents the dependence on the streamwise (λ_x/H) and spanwise (λ_z/H) wavelength, respectively. See Figure 4.10 for the definitions of the colour lines. 82

4.13 Instantaneous iso-surfaces of the streamwise velocity fluctuations for the TS (a) and TD (b) configurations. The longitudinal plane presents contours of positive (solid) and negative (dashed) (w') that have been averaged along the streamwise direction. The streamlines drawn at the end lateral plane have been obtained by averaging the u' and v' along the spanwise direction 82

5.1 Left panel (a): Mean velocity profiles made non dimensional with the half channel height H and the bulk velocity U_b. See Table 5.1 for symbols. The red and blue symbols represents the internal inflection point and the virtual origin, respectively. Right panel (b): Direct comparison with the mean profiles inside the canopy obtained by Monti *et al.* (2020) (dashed lines) for the same solidity values: blue is the present DR case and red is the RD case, respectively. 90

5.2 Mean locations of the features observed in the mean velocity profiles: inner inflection point (red horizontal line); virtual origin (black horizontal line) and the outer inflection point (blue horizontal line) as a function of the solidity λ. Note that the canopy becomes sparser (smaller λ) when increasing the mean filament spacing ΔS. 93

5.3 Left: (a) mean locations of the inner inflection point as a function of solidity λ. Right: (b) mean locations of the virtual origin measured from the canopy tip as a function of λ. Both parameters are made non dimensional using the half channel height H. The solid lines are best fits for the current data, while the dashed lines fit the results from Monti *et al.* (2020). For symbols meaning please refer to Table 5.1 for symbols. 96

5.4 Mean location of the inner inflection point as a function of the aspect ratio λ. The mean locations are scaled by the mean filament spacing ΔS and the canopy height h (symbols as in table 5.1). The solid line represents a polynomial best fit through the internal inflection points for all canopy data. 97

5.5 Mean location of the virtual origin measured from the canopy tip, as a function of solidity (λ). Panel (a) shows the scaling with ΔS, while panel (b) presents the scaling with the canopy height h (Symbos as in table 5.1. The solid line represents a polynomial fit passing through the virtual origin positions of the full canopy database. 98

5.6 Sketch of the largest possible vortex size that can penetrate the canopy from the outer layer and its corresponding location of the virtual origin from the bottom wall. The idealised vortex is presented as a characteristic eddy with diameter $\Delta S - d$. 100

5.7 Mean location of the virtual origin scaled with the mean filament spacing (ΔS), as a function of the aspect ratio ($\Delta S/h$). See Table 5.1 for symbols. 100

5.8 Contours of the instantaneous vorticity fluctuations extracted from a $y-z$ cross plane: on the left column ω_x' (i.e. streamwise component) and on the right ω_y' (i.e. wall-normal component). Each row, from top to bottom represents an increasing solidity value (see table 5.1). The colour code, from red to blue represents positive to negative values. The vorticity fluctuations have been made non dimensional with the outer flow variables (i.e., H and U_b), and the corresponding dimensionless vorticity fluctuations $\omega_x' H/U_b$ and $\omega_y' H/U_b$ are both within the range $[-8, 8]$ 102

5.9 Extent of the overlap region, re-scaled with the mean thickness of the transitional layer as a function of λ . The solid line represents the polynomial fit. See Table 5.1 for symbols. 103

5.10 Left (a): Mean velocity profiles normalised with the two friction velocities (see text). The abscissa $\tilde{y}^+$ represents the wall normal coordinates in wall units determined using either the inner or the outer friction velocity and considering either the wall or the virtual origin as the zero of the wall-normal axis: $\tilde{y}^+ = yu_{\tau,in}/\nu$ and $\tilde{y}^+ = (y - y_{vo})u_{\tau,out}/\nu$. The solid line without symbols refers to the profile of a canonical smooth wall channel flow at $Re_\tau = 950$ (Hoyas & Jiménez, 2008). The sub-plot positioned at the left, top corner is a magnification the profiles in the logarithmic region. On the right panel (b), the roughness function (Hama, 1954) is plotted as a function of λ for all considered canopies. The solid line represents a polynomial fit for cases obtained varying ΔS (current investigation), while the dashed line represents a polynomial fit for the cases considered in Monti *et al.* (2020). See Table 5.1 for the symbols meaning. 104

5.11 Mean filament spacing (a) and effective canopy height (b) expressed in outer wall units ($u_{\tau,out}$), as a function of λ for all considered canopies. See Table 5.1 for symbols. 106

5.12 Non dimensional form of equivalent sand roughness (k_s/k) as a function of the effective solidity (λ_{eff}) (a) and solidity (λ) (b). The value of k_s/k have been rescaled with a filament drag coefficient C_d (Jiménez, 2004) computed at the mid-location of the filaments, where the localised flow is unaffected by the fixed and free ends. The dashed lines are from Jiménez (2004). See Table 5.1 for symbols. Other symbols represents non-circular roughness elements: $*$ - spanwise fences (Schlichting, 1937); 'x' - spanwise fences (Webb *et al.*, 1971); 108

5.13 Diagonal Reynolds stresses plotted as a function of the wall normal coordinate in external units (H). The stresses are scaled with the *outer* friction velocity (top row) computed at the virtual origin ((5.2)). Left to right the panels represent the streamwise (a), the wall normal (b) and the spanwise (c) components, respectively. See table 5.1 for symbols. . 110

5.14 Diagonal Reynolds stresses, scaled with the local friction velocity, plotted as a function of the wall normal direction of the external units (H). The subplots on the top right corner of each panel show the distributions within by the canopy layer. The a, b and c panels represent the streamwise, the wall normal and spanwise component, respectively. Panel d shows the magnitude of the internal peak as a function of $\Delta S/h$. See Table 5.1 for symbols. 112

5.15 Top: Wall normal distributions of the diagonal Reynolds stresses represented as a function of the two stretching factors: h (a) and ΔS (b). The profiles have been normalised by the local friction velocity as in equation 6.3. The solid, dashed and dotted lines represents the streamwise, wall normal and spanwise components, respectively. See Table 5.1 for symbols. 113

5.16 Time and tile-ensemble averaged flow fields (see text for description of the averaging procedure) in the intra-canopy region corresponding to the five canopy configurations. The panels a, b, c, d and e correspond to the SR, TR, MD, RD and DR cases respectively. The iso-contours represented in the cross-planes and wall parallel planes, corresponds to the wall normal velocity, with blue and red regions representing negative and positive values within the range $[-0.3, 0.8]/U_b$. The wall parallel planes correspond to the wall normal locations of 5%, 45%, and 95% of the canopy height. The streamlines have been computed using the tile-ensemble averaged flow field. 115

5.17 Velocity distributions for the DR case seen as a cavity flow (a). Dashed and solid black lines represents streamwise and wall normal distributions. (b) The filament Reynolds number distribution based on the bulk velocity in the canopy layer and the filament diameter for both the actual simulations (solid line) and for the ones conducted in Monti *et al.* (2020) (dashed line). See Table 5.1 for symbols. 117

5.18 Components of the dispersive (form-induced) stresses as a function of the wall normal direction. Panels (a), (b), (c) and (d) represent the streamwise, the wall normal, the spanwise and the anisotropic terms, respectively. The dispersive fluctuations are made non-dimensional with the local friction velocity defined in Equation 6.3, while the wall normal coordinate is scaled with the canopy height. Dashed lines are denoted by the respective velocity fluctuations normalised by the local friction velocity. See Table 5.1 for symbols. 118

5.19 Instantaneous realisations of the non dimensional velocity fluctuations in the wall parallel plane located at the inner inflection point. The panels in the rows from left to right represent the three velocity components u', v' and w'. The panels in the columns, top to bottom, display the cases ordered by increasing solidity. The iso-contours have been scaled with the local friction velocity. The colour codes, ranging from red to blue, represent positive to negative values. The velocity ranges are $u'^{+} \in [-3, 3]$, $v'^{+} \in [-2, 2]$ and $w'^{+} \in [-3, 3]$. 121

5.20 Iso-surface of the two-dimensional two-point velocity auto-correlation function shown as a function of the wall-normal distance in the intra-canopy region. The panels in the rows from left to right correspond to the three velocity components, streamwise, wall normal and spanwise, respectively. The panels in the columns, top to bottom, display the cases ordered by increasing solidity. The red and blue iso-surfaces represent the regions of positive and negative correlations. The green translucent slice shows the mean location of the inner inflection point while the yellow one indicates the position of the virtual origin. 123

5.21 Premultiplied spectra of the fluctuating velocity components represented as a function of the streamwise wavelength (λ_x/H) and wall normal distance (y/H). The rows, left to right refer to the three velocity components, with the first column (*a*,*d*,*g*,*j* and *m*), second column (*b*,*e*,*h*,*k* and *n*) and third column (*c*,*f*,*i*,*l* and *o*) representing the pre-multiplied spectra $\kappa_x\Phi_{u'u'}/u^2_{\tau,l}$, $\kappa_x\Phi_{v'v'}/u^2_{\tau,l}$ and $\kappa_x\Phi_{w'w'}/u^2_{\tau,l}$, respectively. Solidity decreases moving from top to bottom. 126

5.22 Premultiplied spectra of the fluctuating velocity components $\kappa_z\Phi_{u'u'}/u^2_{\tau,l}$, $\kappa_z\Phi_{v'v'}/u^2_{\tau,l}$ and $\kappa_z\Phi_{w'w'}/u^2_{\tau,l}$ represented as a function of the spanwise wavelength (λ_z/H) and wall normal distance (y/H). Panels ordered as in figure 5.21. 127

5.23 Iso-surfaces of two-dimensional pre-multiplied spectra of the fluctuating velocity components represented as a function of the wall paralell wavelengths (λ_x/H and λ_z/H) and wall normal distance (y/H). The first column (*a*,*d*,*g*,*j* and *m*), the second column (*b*,*e*,*h*,*k* and *n*) and third column (*c*,*f*,*i*,*l* and *o*) represent the $\kappa_x\kappa_z\Phi_{u'u'}/u^2_{\tau,l}$, $\kappa_x\kappa_z\Phi_{v'v'}/u^2_{\tau,l}$ and $\kappa_x\kappa_z\Phi_{w'w'}/u^2_{\tau,l}$ premultipled spectra respectively. The rows top to bottom, correspond to decreasing in-plane solidity. See text for the meaning of the lines and colours. Note that the isosurfaces are open-ended in the wall normal direction because the region above the canopy is not considered in the panels. 129

5.24 Magnitude of premultiplied cospectra for the streamwise and the wall normal velocity fluctuations as a function of the streamwise and spanwise wavelengths. Panels a-e represent the streamwise wavelength for increasing values of λ. Panels f-j represent the streamwise wavelength ordered with λ as in the a-e cases. The contours are extracted within the range $[0, 0.4]$ using a 0.02 increment. 133

5.25 Ratio between the number of events occurring in the 2^{nd} and in the 4^{th} quadrant corresponding to the ejection and sweep events, as a function of the wall normal direction. The red and blue dashed lines indicate the location of the canopy tip and the virtual origin, respectively. The figures a-e are arranged according to the ascending order of λ 134

5.26 Two-dimensional pre-multiplied spectra of the wall normal fluctuating velocity component extracted at $y^+_{out} = 60$, as a function of the streamwise (λ_x/H) and spanwise (λ_z/H) wavelength, scaled with the open channel height H. The panels ($a - e$) highlights the spectral content for the configurations with increasing in-plane solidity (i.e., SR to DR cases). 137
5.27 (a) Streamwise wavelength of the large scale spanwise coherent motions (made dimensionless with the canopy height h) above the canopy tip as a function of the shear length scale. The solid lines correspond to the current simulations, while the dashed line correspond to the estimate proposed by Raupach *et al.* (1996).(b) Velocity difference within the canopy outer layer scaled by the bulk velocity, shown as a function of the solidity. Solid lines obtained in the current investigation, and dashed lines obtained in the study by Monti *et al.* (2020). See Table 5.1 for symbols. 138
5.28 Instantaneous iso-surfaces of the q-criterion of the second invariant of the velocity tensor. The panels from a to e correspond to decreasing canopy sparsity values (i.e., SR to DR cases). The panel on the far lateral side shows the streamlines that have been determined by considering the spanwise averaged velocity fluctuations (i.e., $\langle u \rangle_z$ and $\langle v \rangle_z$). The panel located at the downstream end of the domain shows contours of positive (solid lines) and negative (dashed lines) spanwise fluctuations that have been obtained after a streamwise average operation. The iso-surfaces have been coloured by the fluctuating streamwise velocity values. The pink line in the $x - z$ plane indicates the canopy height. 140

6.1 Sketch of the inclined canopy configurations considered in the current investigation. The overall shape of the filament is defined by the angle of inclination (θ°), sheath region (h_s), length of the inclined region (l_i) and the frontal projected height (h) 145
6.2 (a) Mean velocity profile scaled with the open channel height (H) and bulk velocity (U_b), (b) Mean locaitons of the outer inflection point (red), virtual origin (blue) and internal inflection point (green), for the various configurations considered in the current study. See Table 6.1 for symbols. 148
6.3 (a) Extent of the outer layer within the canopy normalised by the frontal projected height of the canopy, (b) Thickness of the internal layer scaled with the mean filament spacing. See Table 6.1 for symbols. Red and blue symbols represents the data extracted from Monti *et al.* (2020) and chapter 5, respectively. 150
6.4 Phenomenological model that proposes a new geometrical length scale to the characterise the penetration of the external flow. 151

6.5 (a) Geometrical penetration depth scaled with the filament length (l) as a function of the angle of inclination in radians. (b) The extent of the outer layer within the canopy normalised by the newly proposed geometrical penetration depth. See Table 6.1 for symbols. 152
6.6 (a) Mean velocity profile normalised with two friction velocity (i.e., inner and outer). The $\tilde{y}^+$ represents wall normal coordinate non-dimensionalised by the respective friction velocities. The solid red line represents the canonical smooth wall open turbulent channel flow. (b) Resistance function plotted against the solidity of the canopy configurations, . See Table 6.1 for symbols. 154
6.7 (a) Non dimensional effective canopy height vs non-dimensional spacing. (b) Resistance function ΔU^+ related to the effective canopy aspect ratio Λ_{eff}. See Table 6.1 for symbols. 157
6.8 Diagonal terms of the Reynolds stresses normalised by the outer friction velocity (top row) and the local friction velocity scale (bottom row), as given in Equation 6.3. The columns from left to right represents the streamwise, wall normal and spanwise components, respectively. See Table 6.1 for symbols. 158
6.9 (a) Frontal projection of the canopy, which is characterised by geometrical parameters used to compute the groove cross sectional area, as defined by Garcia-Mayoral & Jimenez (2011). (b) Drag change (resistance function) represented against the non-dimensional square root of the groove cross sectional area. The symbols of the extremely inclined cases are filled for clarity. The green, blue and red coloured triangular symbols represents triangular, v-shaped and bladed riblets, respectively. The data were extracted from Endrikat *et al.* (2021). 161
6.10 Conventional way of presenting turbulence statistics, (a) Mean velocity profile, (b) r.m.s velocity fluctuations, (c) Reynolds shear stress with the origin located at canopy edge. The black, blue and red colours represents the smooth wall open channel at $Re_\tau = 326$, $\theta^\circ = 77.5$ and $\theta^\circ = 90$, configurations, respectively. The solid, dashed and dotted lines of (b) and (d), represents the streamwise, wall normal and spanwise components, respectively. 163
6.11 Turbulence statistics that have been shifted by the origin for turbulence (ℓ_T^+). Mean velocity profile shifted by drag change (a) and the modified drag change (b), r.m.s velocity fluctuations (c), Reynolds shear stress (d). The black, blue and red colours represents the smooth wall open channel at $Re_\tau = 326$, $\theta^\circ = 77.5$ and $\theta^\circ = 90$, configurations, respectively. The solid, dashed and dotted lines of (b) and (d), represents the streamwise, wall normal and spanwise components, respectively. 165

6.12 Sketch of idealised concept that leads to the introduction of the transpiration term in Equation 6.5. Left - side view of the variation in the mean velocity along the streamwise direction, inducing a transpiration into the filamentous layer. Right - top view of the canopy that redistributes the influx momentum in the wall parallel directions. 166

6.13 Instantaneous realisations of the streamwise (first column) and wall normal (second column) components located at a wall parallel plane of $y^+_{h_\perp} + \ell^+_T = 20$. The rows from top to bottom corresponds to the smooth wall open channel, $\theta^\circ = 77.5$ and $\theta^\circ = 90$, configurations, respectively. The colour band from red to blue represents positive to negative. The velocity fluctuations were made non-dimensional with the $u_{\tau,out}$ and ν, with a depicted range of $u'^+ \in [-5, 5]$ and $v'^+ \in [-1, 1]$. 168

6.14 (a) Mean velocity profile according to the drag change proposed in Equation 6.5, (b) transpirational virtual origin as a function of the origin for the turbulence, (c) drag change as a function of the abstract origin for the turbulence and (d) drag change as a function of the transpirational velocity at the tip of the canopy. The colours of the solid line can be associated with the symbols as given in Table 6.1. The black horizontal line represents $\Delta U^+ = 0$. The dashed line represents a linear relationship $\Delta U^+ = 13.42 v^+_h$ according to Orlandi & Leonardi (2008). The coloured *o* symbols represents data extracted from Abderrahaman-Elena *et al.* (2019), O - colocated posts, O - colocated posts with varying heights, O - staggered posts (streamwise) and O - staggered posts (spanwise). 171

6.15 One dimensional pre-multiplied spectra as a function of the wall normal (y/H) direction and the streamwise wavelength (λ_x/H). The rows from top to bottom represents the ascending order of increasing θ. The columns from left to right represents $k_x\phi_{u'u'}/u^2_{\tau,l}$ with a range of [0, 0.8] and incremental of 0.1, $k_x\phi_{v'v'}/u^2_{\tau,l}$ with a range of [0, 0.3] and incremental of 0.02, and $k_x\phi_{w'w'}/u^2_{\tau,l}$ with a range of [0, 0.4] and incremental of 0.04. The yellow, green and red vertical lines represents the wavelength at $\lambda_x/H = d$, $\lambda_x/H = \Delta S$ and $\lambda_x/H = h$, respectively. The red, yellow and cyan horizontal dashed lines represents $y/H = h$, $y/H = y_{ip}$ and $y/H = y_{vo}$, respectively. 176

6.16 One dimensional pre-multiplied spectra as a function of the wall normal (y/H) direction and the streamwise wavelength (λ_z/H). The rows from top to bottom represents the ascending order of increasing θ°. The columns from left to right represents $k_z\phi_{u'u'}/u^2_{\tau,l}$ with a range of [0, 1] and incremental of 0.1, $k_z\phi_{v'v'}/u^2_{\tau,l}$ with a range of [0, 0.4] and incremental of 0.04, and $k_z\phi_{w'w'}/u^2_{\tau,l}$ with a range of [0, 0.5] and incremental of 0.05. Coloured lines have the same meaning as in Figure 6.15. 177

6.17 Two dimensional pre-multiplied spectra of $k_x k_z \phi_{v'v'}/u^2_{\tau,l}$ as a function of the streamwise and spanwise wavelengths, extracted at a wall parallel plane located at $y^+_{out} = 20$. The black lines with filled contour represents the $\theta = 77$, while the red lines represents $\theta = 60$ configuration. 178
6.18 Contour maps representing the two-point autocorrelation functions of the velocity fluctuations in the streamwise direction. The columns left to the right showcases the autocorrelation for u', v'. The contours levels are denoted by [-0.4,1], associated with the blue to red region with an increment of 0.1.The negative values are plotted with a dashed line. The green horizontal line denotes the height of the canopy. 180
6.19 IContour maps representing the two-point autocorrelation functions of the velocity fluctuations in the spanwise direction. The columns left to the right showcases the autocorrelation for u', v'. The contours levels are denoted by [-0.4,1], associated with the blue to red region with an increment of 0.1.The negative values are plotted with a dashed line. The green horizontal line denotes the height of the canopy. 181
6.20 Magnitude of one dimensional pre-multiplied cospectra ($k_x|\phi_{u'v'}|/u^2_{\tau,l}$ and $k_z|\phi_{u'v'}|/u^2_{\tau,l}$) as a function of the wall normal (y/H) direction, the streamwise (λ_x/H) and spanwise (λ_z/H) wavelength. The top two rows concerns the λ_x/H and the last two rows represents λ_z/H. The panels from left to right has been ordered in the increasing values of θ°. The $k_x|\phi_{u'v'}|/u^2_{\tau,l}$ with a range of [0, 0.2] and incremental of 0.02, and $k_z|\phi_{u'v'}|/u^2_{\tau,l}$ with a range of [0, 0.5] and incremental of 0.05, Coloured lines have the same meaning as in Figure 6.15. 182
6.21 Instantaneous realisations of the streamwise (first column) and wall normal (second column) and spanwise (third column) components located at a wall parallel plane of $y/H = y_{ip}$. The rows from top to bottom corresponds to the $\theta^\circ = 0$, $\theta^\circ = 33.5$, $\theta^\circ = 48.25$, $\theta^\circ = 60$, configurations, respectively. The colour band from red to blue represents positive to negative. The velocity fluctuations were made non-dimensional with the local friction velocity formulation (see Equation 6.3), with a depicted range of $u'^+ \in [-3, 3]$, $v'^+ \in [-2, 2]$ and $w'^+ \in [-3, 3]$. 185

List of Tables

2.1 Canopy configurations previously investigated by Monti *et al.* (2020) . 25

3.1 Aerodynamic coefficients for the cylinder simulations campaign. The data of the reference case shown in the first row are taken from Guilmineau & Queutey (2002) 52

4.1 Simulation parameters considered in the current investigation 65

5.1 Simulation parameters considered in the current investigation: (λ) is the solidity; $\Delta S/h$ is the canopy *aspect ratio*; $n_i \times n_k$ is the filaments count ratio, where n_i and n_k are the number of filament rows in the streamwise and spanwise directions, respectively; $Re_{\tau,o}$ is the friction Reynolds number based on the friction velocity ($u_{\tau,o}$) computed at the virtual origin (to be introduced later). Δy_w^+ and Δy_c^+ are the grid spacings, in viscous units, within the region next to the impermeable wall 88

5.2 Parameters of the canopy configurations investigated by Monti *et al.* (2020). All the canopies shared the same mean filament spacing of $\Delta S/H = \pi/24$. 89

6.1 Simulation parameters considered in the current investigation. The filament distribution is maintained at $n_i \times n_k = 96 \times 72$, where n_i and n_k are the number of filament rows in the streamwise and spanwise directions, respectively; $Re_{\tau,o}$ is the friction Reynolds number based on the friction velocity ($u_{\tau,o}$) computed at the virtual origin. The grid resolution in the streamwise and spanwise directions are denoted by Δx^+ and Δz^+, respectively. The wall normal resolution of the numerical grid in the region near the impermeable wall and canopy top are denoted in Δy_w^+ and Δy_h^+ 146

6.2 Parameters used in the virtual origin framework (Ibrahim *et al.*, 2021). The slip velocity at the tip of the canopy is defined by U_s^+, while ℓ_T^+ represents the virtual origin for the turbulence. The virtual origin for the velocity fluctuations are given by ℓ_u^+, ℓ_v^+ and ℓ_w^+, respectively. The drag is computed via the formulation presented in Equation 6.5. 169

Acknowledgements

First and foremost I would like to thank my supervisors Dr. Mohammed Omidyeganeh and Prof. Alfredo Pinelli for their unwavering support, guidance and friendship throughout my entire PhD. I am very grateful for their time, patience and care invested in both my personal and professional life, continuously inspiring me to push boundaries. I am also grateful to the School of Mathematics, Computer Science and Engineering, at City, University of London for funding my Ph.D studies. I am also grateful to Dr. Alessandro Monti and Dr. Marco E. Rosti of Okinawa Institute of Science and for their support and guidance during my Ph.D programme. The acknowledgement is extended to the colleagues in the High Performances Computing (HPC) infrastructures where the most of present numerical simulations have been carried out. I am grateful to Sylvain Laizet (Imperial College) on behalf of the U.K. Turbulent Consortium (grant EPSRC EP/L000261/1) and the EPSRC (Engineering and Physical Sciences Research Council) for granting the access to the ARCHER and ARCHER2 U.K. National Supercomputing Service, and CSD3 - Cambridge Service for Data-Driven Discovery; Chris Marshall (City, University of London) for the access to the City, University of London HPC SOLON and HYPERION. I also thank Nathalie Chatelain of the Post-Graduate-Research office at City, University of London for the administrative support provided throughout my PhD program.

I could not have completed this without the support of my fellow colleagues and friends. A thank-you goes to Ale, Carlo, Erika, Isabella, Mohamed, Muthu, Narges, Omar, Qianhui, Raphael and Tariq. Also thanks to all the staff, past and present at City who have helped me throughout my entire time at university; especially Jamshid Nouri, Roger Valsler, Chak Cheung, Chetan Jagadeesh and Youyou Yan.

I would also like to thank my parents, Dada and Mama and, sisters, Michelle and Shanelle, and my brother, Prajeeth for their support throughout my time at university and support when I needed it. Also to my extended family, uncles Brian and Victor, aunts Devika and Jean, and especially my cousins Mike, Claudia, Kevin, Shobita, Shehan and Shohan, who have always helped and supported me - keeping me sane, especially during the COVID lockdown. I would also like to give a special mention to my biggest fans Liam and Jayke. Finally, I would like to thank my loving girlfriend Shenella for always being there for me over the years, words cannot even begin to convey my gratitude.

Declaration

I, Shane Nicholass, declare that this thesis entitled *On the numerical investigation of the turbulent flow developed over filamentous surfaces.* and the work presented in the thesis are both my own, and have been generated by me as the result of my own original research. I grant powers of discretion to the University Librarian to allow the thesis to be copied in whole or in part without further reference to the author. This permission covers only single copies made for study purposes, subject to normal conditions of acknowledgements. I confirm that:

- this work was done wholly or mainly while in candidature for a research degree at this University;
- where I have consulted the published work of others, this is always clearly attributed;
- where I have quoted from the work of others, the source is always given. With the exception of such quotations, this thesis is entirely my own work;
- I have acknowledged all main sources of help;
- parts of this work have been published as

    1. Nicholas, S., Omidyeganeh, M. and Pinelli A. 'Numerical investigation of regime transition in canopy flows'. *Flow Turbulence and Combustion* accepted for publication.
    2. Monti, A., Nicholas S., Omidyeganeh M., Pinelli A., Rosti M.E., 'On the solidity parameter in canopy flows', *Journal of Fluid Mechanics*, 945, 2022.

Signed:.....

Date:.....

Summary

Detailed analysis of turbulent shear flows that develop over filamentous surfaces has been carried out, in the context of an open channel flow at moderate bulk Reynolds number (i.e., $Re_b = U_b H/\nu$, H being the open channel height and U_b the bulk velocity). The various filamentous surfaces found in nature present large variations in the geometrical configurations and the mechanical properties since they fulfil many biological tasks simultaneously. Thus, the number of free parameters that characterise a specific type of filamentous layer, or a specific type of canopy, is quite large (e.g. density ratios, flexibility, sizes, levels of submersion, arrangement, active or passive motions, . . .). To unravel the physical mechanisms of these flows by incorporating all these geometrical parameters into a comprehensive parametric investigation is an almost impossible task. This motivated Nepf (2012) to classify the overall behaviour of the flow by solely considering the geometrical features of the canopy. By reviewing a number of previous research work on canopy flows, she suggested using the solidity (λ) to classify the various flow behaviours observed in the case of submerged canopies. The magnitude of λ, enabled the identification of two asymptotic regimes: sparse and dense. The turbulent flow that develops above sparse canopy regimes is treated as a boundary layer that develops over a rough wall. On the other hand, the profound drag imposed by the filaments in the context of a dense regime yields a couple of inflection points in the mean velocity profile. These points allow the establishment of two separate shear layers within the canopy: an inner region (very close to the canopy bed), an outer region (which extends above the canopy edge), and an overlap region that exists in between these layers, which has been often described as a "mixing layer" (Finnigan, 2000). While the physical characterisation of the two asymptotic regimes is fairly understood, the transitional conditions remain an open question since the physical characteristics unique to the sparse and dense scenarios coexist in the transitional regime.

Although various publications have appeared in previous literature, they are either based on experimental work or oversimplified simulations. In this context, the current thesis provides an accurate and detailed characterisation of canopy flows via a fully resolved, numerical approach that is capable of tackling rigid, filamentous canopies made of cylindrical stems mounted normally to an impermeable wall. In particular, the simulation directly tackles the region occupied by the canopy, imposing the zero-velocity condition on every single stem by means of an immersed boundary method (Pinelli *et al.*,

2010), thus mitigating the problems associated with canopy modelling. The outer flow is dealt with a large-eddy formulation that adopts a state-of-the-art grid independent closure for the unresolved scales of motion (Piomelli *et al.*, 2015).

In the first part of the thesis, the regime transition of canopy flows is investigated. We have selected two-layer configurations characterised by filament spacing ratios such that the geometrical features of the two layers allow us to classify them as canopies in the transitional regime. In particular, the solidity was modified solely by decreasing the average distance between the adjacent filaments. This results in configurations that reside below and above the transitional threshold of $\lambda \simeq 0.15$. This enabled us to untangle the physical character of the flow in a transitional regime by analysing the relative positions of the inflection points and virtual origin (abstract origin seen from the external flow), which conditions the transition between the two asymptotic regimes. The coherent structures that emerge at the onset of the regime transition are also explored. Finally, the scaling argument for the mean flow quantities presented in the context of sparse and dense canopies is extended to the transitional regime. Following these observations, we embarked on a parametric study to investigate the influence of the average distance between adjacent filaments (or equally, the stem number density) on the different hydrodynamic regimes. A total of five canopy configurations have been selected for the study. All of them share the same frontal projected height, while the in-plane solid fraction of the canopy has been systematically varied to match the sparse, dense, and transitional canopy flow regimes. In particular, the configurations with the smallest and largest ΔS are representative of the sparse and dense regimes, respectively, while the intermediate cases nominally belong to the transitional regime. The mean filament spacing is generally considered the most important length scale of the canopy as it discriminates the scales of the outer flow that can penetrate into the canopy and controls the overall interactions between the inner and outer flows. The positional variation of the features of the mean velocity profile enabled us to propose a conceptual model, that describes the transition occurring between a sparse and a dense regime. Lastly, the coherent structures that emerge at the onset of different regimes are also compared, highlighting the role played by ΔS in controlling the interaction between the inner and outer flows.

In the second part of the thesis, a series of numerical investigations were conducted to study the effect of the filament's inclination on turbulent shear flows developing above a canopy. Inspired by the ability of a naturally occurring canopy to modulate the local permeability, we consider a filamentous layer that is inclined along the streamwise direction. The resulting canopy is composed of rigid, cylindrical filaments, flush mounted onto the impermeable bottom wall of an open channel. The filaments, are characterised by a complex topology that mimics the mean streamlined posture of a typically reconfiguring aquatic vegetation (Nepf, 2012). The inclination angle θ°

of the canopy has been varied, whilst maintaining a constant in-plane solid fraction $\Delta S/H = \pi/48$ and filament length $h/H = 0.1$. In all the resulting configurations, it is indeed the angle of inclination that dictates the solidity λ of the canopy, leading to the establishment of different flow regimes (i.e., sparse or dense). We have considered a total of six configurations such that θ systematically spans $\theta \in [0, 90]$, with the lowest corresponding to the fully dense regime. It is found that a simple inclination yields a substantially different flow behaviour when compared with perpendicular, which is amplified at the onset of extreme angles, promoting new hydrodynamic regimes.

Keywords: canopy flow, scaling, large coherent structures, large-eddy simulation, immersed boundary method.

Nomenclature

Mathematical Symbols

$\mathcal{C}$	Convolution operator.
$\mathcal{D}$	Divergence operator.
$\mathcal{G}$	Gradient operator.
$\mathcal{I}$	Interpolation operator.
$\mathcal{L}$	Laplacian operator.
$\mathcal{N}$	Nonlinear operator.
$\mathbb{R}$	Real numbers set.
$\mathbb{Z}$	Integer numbers set.

Greek Characters

Γ	Surface of the immersed body.
Δl	Grid spacing in a generic direction.
ΔS	Average linear spacing between two consecutive filaments
Δt	Time step.
ΔU	Velocity difference between the low- and the high-speed free-stream regions in a mixing-layer.
ΔU^+	Roughness function/drag change.
ΔV	Volume of a single CV.
Δx	Grid spacing in the streamwise direction.
Δy	Grid spacing in the wall normal direction.
Δz	Grid spacing in the spanwise direction.
Λ_x	Streamwise wavelength of the initial Kelvin-Helmholtz instability in a mixing-layer.
$\Phi_{u'u'}$	Spectrum of the streamwise velocity fluctuations component.
$\Phi_{v'v'}$	Spectrum of the wall normal velocity fluctuations component.

$\Phi_{w'w'}$ . . . . . Spectrum of the spanwise velocity fluctuations component.

$\Phi_{u'v'}$ . . . . . Cospectrum of the streamwise and wall-normal velocity fluctuations components.

Ω . . . . . Domain size.

Ω_f . . . . . Support size.

α . . . . . Stretching factor.

δ . . . . . Dilation parameter.

δ_e . . . . . Penetration length.

$\delta_{i,j}$ . . . . . Kronecker's delta.

δ_ν . . . . . Viscous length

δ_ω . . . . . Vorticity thickness.

ϵ . . . . . Characteristic volume related to the local dilation coefficients of the window function

. . . . . Turbulence dissipation.

$\vec{\epsilon}$ . . . . . Characteristic volume vector related to the local dilation coefficients of the window function.

η . . . . . Dilation parameter.

κ . . . . . Von Karman constant

. . . . . Modified wavenumber.

κ_x . . . . . Streamwise wavenumber.

κ_z . . . . . Spanwise wavenumber.

λ . . . . . Solidity.

$\lambda_\perp$ . . . . . Solidity based on frontal projected height.

. . . . . Interpolation factor.

λ_{eff} . . . . . Effective solidity.

λ_x . . . . . Streamwise wavelength.

λ_z . . . . . Spanwise wavelength.

μ . . . . . Dynamic viscosity.

ν . . . . . Kinematic viscosity.

ν_τ . . . . . Subgrid viscosity.

ν_{SFS} . . . . . Subfilter viscosity.

ρ . . . . . Density.

σ . . . . . Dilation parameter.

τ . . . . . Total stress.

$\tau_{i,j}$ . . . . . Generic component of the viscous stress tensor.

θ° . . . . . Angle of inclination.

. . . . . Generic component of the sub-grid stress tensor.

. . . . . ϕ Projection variable.

. . . . . ϕ_{eddy} Eddy diameter.

ω_x . . . . . Streamwise vorticity component.

ω_y . . . . . Wall-normal vorticity component.

ω_z . . . . . Spanwise vorticity component.

Roman Characters

A . . . . . Matrix of the discrete integral of the product between two window functions centred in two different Lagrangian nodes.

B . . . . . Vogel number

Bu . . . . . Buoyancy number.

. . . . . Log-law parameter.

Ca . . . . . Cauchy number.

C_D . . . . . Drag coefficient.

C_L . . . . . Lift coefficient.

CV . . . . . Control Volume.

D . . . . . Drag.

. . . . . Cylinder diameter.

D_0 . . . . . Integral value of the mean drag.

D_r . . . . . Drag per unit length.

DR . . . . . Dense regime.

DRM . . . . . Dense regime of Monti *et al.* (2020).

E . . . . . Computational node to the east of P.

F . . . . . Generic flux on the surface of a CV.

F_i . . . . . Vectorial field: ith component.

$\mathbf{F}$ . . . . . Force field on the Lagrangian grid.

F^c . . . . . Convective flux.

F^d . . . . . Diffusive flux.

F_D . . . . . Drag force of the canopy.

H . . . . . Open channel height.

. . . . . Half channel height.

. . . . . Rescaling matrix.

L . . . . . Lift per unit length.

L^* . . . . . Reference length.

L_s . . . . . Shear scale.

L_x . . . . . Streamwise length of the domain.

L_y . . . . . Wall-normal length of the domain.

L_x . . . . . Spanwise length of the domain.

$L_{P,E}$ . . . . . Length between nodes P and E.

M . . . . . Matrix of the moments obtained from the reproducing conditions.

MD . . . . . Mildly dense.

MD . . . . . Mildly dense of Monti *et al.* (2020).

MI . . . . . Mild inclination.

N . . . . . Computational node to the north of P.

. . . . . Number of nodes on the Lagrangian grid.

NI . . . . . Negligible inclination.

P . . . . . Pressure.

. . . . . Computational node considered.

. . . . . Turbulence production.

Q . . . . . Generic function integrated over the volume of a CV.

RD . . . . . Relative dense regime.

Re . . . . . Reynolds number.

Re_b . . . . . Bulk Reynolds number.

Re_τ . . . . . Friction Reynolds number.

$Re_{\tau,l}$ . . . . . Local friction Reynolds number.

Re_D . . . . . Reynolds number based on the free-stream velocity and the cylinder diameter.

Re_d . . . . . Reynolds number based on the mean velocity in the canopy layer and the stems diameter.

RSI . . . . . Relatively strong inclination.

$R_{u'u'}$ . . . . . Autocorrelation function of the pre-averaged streamwise velocity fluctuations.

$R_{v'v'}$ . . . . . Autocorrelation function of the pre-averaged streamwise velocity fluctuations.

$R_{w'w'}$ . . . . . Autocorrelation function of the pre-averaged streamwise velocity fluctuations.

S . . . . . Surface.

. . . . . Computational node to the south of P.

$S_{i,j}$ . . . . . Generic component of the strain rate tensor.

SI . . . . . Strong inclination.

SOC . . . . . Smooth open channel.

SR . . . . . Sparse regime.

SRM . . . . . Sparse regime of Monti *et al.* (2020).

. . . . . T_n Characteristic time-scale of filament.

T_f . . . . . Time scale of the cyclic turbulent events.

T^+ . . . . . Time scale number.

TD . . . . . Transitionally dense.

TR . . . . . Transition regime.

TRM . . . . . Transition regime of Monti *et al.* (2020).

TS . . . . . Transitionally sparse.

U^* . . . . . Reference velocity.

U_b . . . . . Bulk velocity.

U_∞ . . . . . Free-stream velocity.

$\mathbf{U}$ . . . . . Velocity field on the Lagrangian grid.

V . . . . . Volume.

VSI . . . . . Very strong inclination.

W . . . . . Computational node to the west of P.

WI . . . . . Weak inclination.

$\mathbf{X}$ . . . . . Lagrangian grid nodes.

a . . . . . Ratio between the canopy solid frontal area and the volume of interest occupied by the canopy.

. . . . . Adjustable parameter.

b . . . . . Bottom face of a CV.

b_i . . . . . One-dimensional modified window function coefficients.

$b_{i,j}$ . . . . . Two-dimensional modified window function coefficients.

$b_{i,j,k}$ . . . . . Three-dimensional modified window function coefficients.

$\vec{b}$ . . . . . Modified window function coefficients.

d . . . . . Filaments diameter.

e . . . . . East face of a CV.

$\mathbf{e}_\eta$ . . . . . Versor parallel to the CV surface

$\mathbf{e}_\xi$ . . . . . Versor directed alongside the line connecting the nodes P and E.

$\mathbf{e_i}$ . . . . . Versor in the ith direction.

$\vec{e_l}$ . . . . . Zeros vector with first term equal to one.

f . . . . . Generic integrand function.

. . . . . Generic function.

f_i . . . . . Body force: ith component.

$\mathbf{f}$ . . . . . Body force vector.

f_a . . . . . Approximated function.

h . . . . . Canopy height.

$h_\perp$ . . . . . Frontal projected height of canopy.

h_s . . . . . Height of sheath region.

i . . . . . Integer counter.

j . . . . . Integer counter.

k . . . . . Integer counter.

. . . . . Roughness length.

k_{eff} . . . . . Effective canopy height.

k_s . . . . . Equivalent sand roughness length.

l . . . . . Integer counter.

. . . . . Length of filament.

ℓ_N . . . . . Transpirational virtual origin.

ℓ_T . . . . . Virtual origin for turbulence.

ℓ_u . . . . . Virtual origin for streamwise velocity fluctuations.

ℓ_{uv} . . . . . Virtual origin for streamwise Reynolds shear stress.

ℓ_v . . . . . Virtual origin for streamwise wall-normal fluctuations.

ℓ_w . . . . . Virtual origin for spanwise velocity fluctuations.

m . . . . . Integer counter.

m_i . . . . . Moments obtained from the reproducing conditions.

$\dot{m}$ . . . . . Mass flux.

n . . . . . North face of a CV

. . . . . Interpolating polynomial degree.

n_i . . . . . Normal versor: ith component.

$\mathbf{n}$ . . . . . Normal versor.

n_i . . . . . Number of nodes in the streamwise direction.

n_j . . . . . Number of nodes in the wall-normal direction.

n_k . . . . . Number of nodes in the spanwise direction.

p . . . . . Pressure.

q . . . . . Generic integrand function.

r . . . . . Normalised curvilinear coordinate.

$\mathbf{r}$ . . . . . Position vector.

s . . . . . South face of a CV.

. . . . . Curvilinear coordinate.

t . . . . . Time.

. . . . . Top face of a CV.

. . . . . Curvilinear coordinate.

u . . . . . Streamwise velocity component.

u_i . . . . . Velocity: ith component.

$\mathbf{u}$ . . . . . Velocity vector.

u_τ . . . . . Friction velocity.

$u_{\tau,l}$ . . . . . Local friction velocity.

v . . . . . Wall-normal velocity component.

. . . . . Curvilinear coordinate.

w . . . . . Spanwise velocity component.

. . . . . West face of a CV.

w_δ . . . . . Mono-dimensional kernel function.

$w_{\delta,\eta}$ . . . . . Two-dimensional kernel function.

$w_{\delta,\eta,\sigma}$ . . . . . Three-dimensional kernel function.

w_η . . . . . Mono-dimensional kernel function.

w_σ . . . . . Mono-dimensional kernel function.

x . . . . . Streamwise coordinate.

. . . . . Generic variable.

x_i . . . . . Coordinates: ith component.

$\mathbf{x}$ . . . . . Grid (or Eulerian grid) nodes.

y . . . . . Wall-normal coordinate.

$\tilde{y}$ . . . . . Wall-normal coordinate with a shifted origin.

y_{inf} . . . . . Wall-normal location of the internal inflection point.

y_{vo} . . . . . Wall-normal location of the virtual origin.

y^+_α . . . . . Scaled local wall units.

$y^+_{\Delta S}$ . . . . . Local wall units scaled with ΔS.

z . . . . . Spanwise coordinate.

Operators . .

$\langle \cdot \rangle$ . . . . . Average in time and in the two homogeneous spatial directions.

$\langle \cdot \rangle_x$ . . . . . Average in the streamwise (homogeneous) spatial direction.

$\langle \cdot \rangle_z$ . . . . . Average in the spanwise (homogeneous) spatial direction.

$\cdot'$ . . . . . Fluctuations value.

$\bar{\cdot}$ . . . . . Quantity related to the resolved field.

$\hat{\cdot}$ . . . . . Fourier coefficient.

$\tilde{\cdot}$ . . . . . Quantity related to the modified window function.

Subscripts

$\cdot_P$	Quantity related to the node P.
$\cdot_E$	Quantity related to the node E.
$\cdot_e$	Quantity related to the east face of a CV.
$\cdot_w$	Quantity computed at the wall..
$\cdot_h$	Quantity computed at the canopy tip.
$\cdot_{in}$	Quantity related to the inner flow, in particular computed at the wall.
$\cdot_{old}$	Quantity related to the previous time-step.
$\cdot_{out}$	Quantity related to the outer flow, in particular computed at the canopy tip or at the virtual origin.
$\cdot_{rms}$	RMS value.

Superscripts

$\cdot^+$	Wall (or local wall) units.
$\cdot^*$	Predicted quantity.
$\cdot^\Gamma$	Boundary value of a quantity on the immersed body.
$\cdot^n$	Time n.

Acronyms

2D . . . . . Two-dimensional.

3D . . . . . Three-dimensional.

BiCGStab . . . Bi-conjugate Gradient Stabilised.

DF . . . . . Direct Forcing.

DNS . . . . . Direct numerical simulation.

FFT . . . . . Fast Fourier Transform.

IBM . . . . . Immersed Boundary Method.

ILSA . . . . . Integral Length Scale Approximation.

LES . . . . . Large Eddy Simulation.

MPI . . . . . Message Passing Interface.

RANS . . . . . Reynolds Averaged Navier Stokes.

RKPM . . . . . Reproducing Kernel Particule Method.

RMS . . . . . Root mean square.

RHS . . . . . Right Hand Side.

SFS . . . . . Sub-Filter Scale.

SGS . . . . . Sub-Grid Scale.

TBL . . . . . Turbulent boundary layer.

1 Introduction

Contents

1.1 **Introduction** 1
1.2 **Thesis structure** 8
1.3 **Author's Contribution** 10

1.1 Introduction

Surfaces covered by arrayed, textured layers anchored to a substrate and exposed to viscous flows are common in nature. The complex interaction between the individual elements embedded in the textured layer and the surrounding flow has paved the way for bio-inspired technological advances in aeronautics, hydraulics, chemical engineering, environmental, medical and biological sciences. Investigating the manipulation of the surrounding flow imposed by the textures is a challenging task due to the existence of a wide range of free parameters that characterise the respective geometry of the textures. For example height, shape, spacing, density, flexibility, alignment etc. Over the years, many researchers believe that the small-scale features present on the outer surface of biological species, play an important fluid dynamic role. Thus, the main challenge experienced by fluid dynamicists stems from the intricate details of the complex interplay between the surrounding flow and the individual textures Such details include the

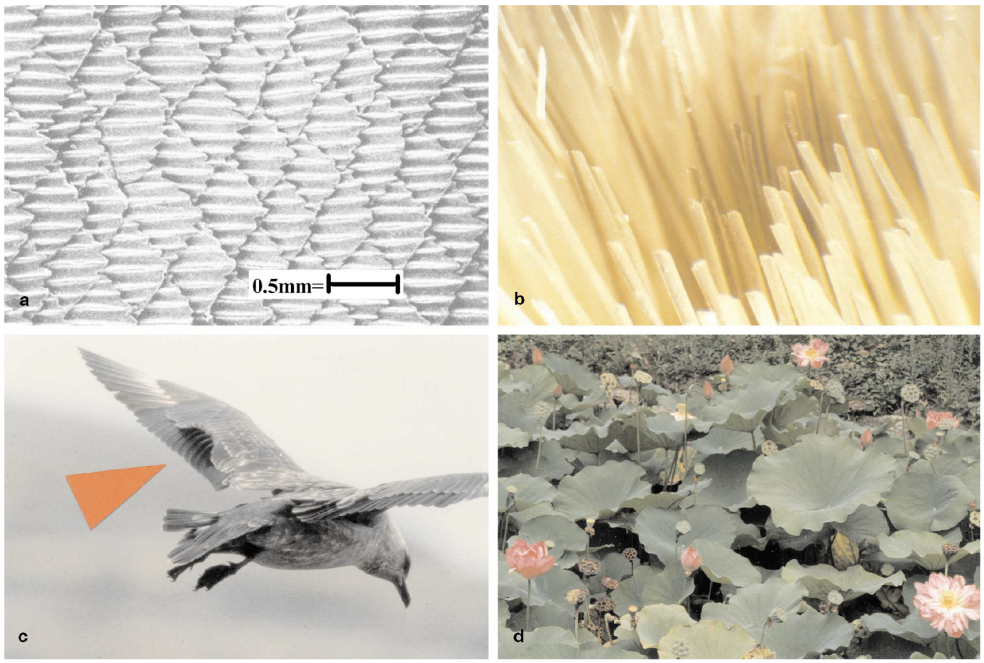


Figure 1.1: Typical examples of textured biological surfaces (a) Silky shark skin (b) Sea leopard skin. (c) Skua wing in landing approach. (d) Lotus leaves. Extracted from Bechert *et al.* (2000*b*).

permeability, dynamic and/or adaptive reconfiguration, the modulation of the near wall turbulent structures, triggering the transition to turbulence and the interaction with the discrete fluid trapped in the micro-cavity (i.e. superhydrophobicity).

Living organisms use surfaces with complex textures and their interaction with surrounding fluid flows to achieve a number of tasks. Let us consider a few examples that highlight the fluid dynamic role played by the various textured layers. Under the microscope, the wings of many species of insects are covered with setae (bristles). In particular, the dense hairy coating populating the wings of a ladybug is believed to repel water (Bottaro, 2019). Moreover, the scales observed on the wings of butterflies and moths present themselves as a porous layer, in which air can flow within the small pores and reach the impermeable surface. The scales of the permeable substrate define a complex microstructure (protrusions in three-dimensional space), which aids in self-cleaning under the rain by decreasing the wet area of the wing and enhancing light absorption and refraction (Zheng *et al.*, 2007; Perez Goodwyn *et al.*, 2009). These scales, together with the overall morphology of a butterfly wing, may also contribute to an increase in the lift generation (Kovalev, 2008; Park *et al.*, 2010). The microstructures on

the butterflies and moths were not very dissimilar to the dermal tooth-like structures observed on the dermis of sharks. These denticles are characterised by a stem, crown and a series of ridges that are present on the outer surface of the crown (Dillon *et al.*, 2017). Interestingly, the dermal elements vary in size, shape, spacing, crown angle and presence/absence of ridges depending on their location on the body.(Ankhelyi *et al.*, 2018). The great white shark's capability of swimming at a remarkable speed (almost $60km/h$) has motivated a number of experimental and numerical investigations focused on the eventual hydrodynamic advantages offered by the particular morphology of the skin. In particular, the outer serrations/corrugations interact with the surrounding flow to decrease the skin frictional drag (Bechert *et al.*, 2000*a*), which has given birth to the well known riblets that are capable of modulating the near-wall turbulent cycle (Luchini *et al.*, 1991). The underlying dermis exhibits elastic behaviour that yields large-scale undulations that can have a direct impact on the propulsion power required by the shark. The coupled interaction of the dermal structures and the flexible dermis with the surrounding viscous flow results in an enhanced propulsive performance (Oeffner & Lauder, 2012). Beyond the obvious fluid dynamics role, the dermal structures achieve a wide range of functions, including abrasion strength, defence, and luminance (Dillon *et al.*, 2017). Similar to sharks, certain families of fish have scales (comb-like structures) and mucus-secreting glands located on the outer skin, respectively. The latter, in particular, is associated with an excellent skin frictional drag reduction in the form of a slip velocity experienced by the outer flow (Rosen & Cornford, 1971). Apart from the hydrodynamic function, mucus also contributes towards a number of tasks, including reproduction, ion and water regulation, respiration, and disease resistance (Shephard, 1994). The examples mentioned above clearly illustrate the various scales present on the outer dermis of fish. However, many mammals have hair (fur or feathers) that interacts with the surrounding viscous flow. One such area of research that has received recent attention focuses on pinnipeds. In particular, the outer skin of a fur seal is covered with a dense flexible hairy layer that is oriented along the streamwise direction (flow direction), which can be envisaged as a porous substrate with dynamically altering permeability. The ability of the hairy layer to adapt and re-orient to the surrounding turbulent flow

enables the substrate to achieve a skin frictional drag reduction performance greater than the static riblets (Itoh *et al.*, 2006). The observed drag reduction can be associated with anisotropic permeability of the hairy layer that yields a decrease in the streamwise turbulence intensity. Moreover, seals are also known for their accurate tracking of the hydrodynamic trails created by their prey (Triantafyllou *et al.*, 2016). These highly sensitive undulatory whiskers are believed to play a vital role in enabling the seals to detect their prey effectively under poor visual conditions by sensing the vorticity field (Dehnhardt *et al.*, 2001), This has resulted in many fluid dynamists pursuing research in the field of bio-inspired flow sensors. On the other hand, birds have been at the forefront of biological inspiration for many years. In particular, there is a diverse range of feathers, which vary in size and density, and many researchers have speculated that each type of feather is associated with a certain aerodynamic function. The most important feathers in terms of aerodynamics are located at the wings and tail, as they play an important role in aerodynamic flight control (Brücker & Weidner, 2014). The best example of a nature-inspired engineering device that has been applied to a real-world aircraft is the winglet, a device located at the wingtip that palliates the lift-induced drag. Another important function of the feathers is their contribution towards aerodynamic noise reduction or silent flight. In particular, the owl is known for its quiet, low-speed flight, which allows them to apprehend their prey without being perceived by them. It is believed that the individual features of the feathers combine to achieve silent flight. In particular, the leading edge serrations located at the primary feather act as vortex generators that stabilise the air as it flows over the wing. The porous velvet-like structure decreases the friction noise, and the trailing edge flexible fringes limit the broadband of the scattered noise (Bachmann, 2010). Further interesting examples can be derived from the plant kingdom. The lotus leaf is well-known for its remarkable superhydrophobicity (Koch & Barthlott, 2009). In an ideal scenario, when a water drop is placed on the surface of a lotus leaf, it slides away easily whilst maintaining a quasi-spherical shape without wetting the underlying surface. Conversely, when considering the entire plant, we move into a familiar area of research formally known as canopy flows, which is characterised by the flow that develops through and above a group of plants or trees. The

hydrodynamic interaction between the canopy and the surrounding air or water flow plays a vital role in biological, geomorphological, and hydrological processes (Nepf, 2012). Vegetative plants are often characterised by flexible elements that deform and adapt to the localised flow. The adaptive reconfigurations are believed to yield a decrease in resistive force and avoid uprooting under strong currents (Vogel, 1984). Similarly, at a cellular level, fluid transport and locomotion due to motile cilia are ubiquitous phenomena in biological organisms. Ciliated walls are also commonly found in many living organs and participate in a number of physiological processes like locomotion, digestion, circulation, respiration, and reproduction (Fliegauf *et al.*, 2007). The ability of individual textures to dynamically reconfigure their morphology to the localised structure of the surrounding fluid flow, leading to manipulation of the overall arrangement of the flow in the vicinity of the wall, is a fundamental feature shared by a wide range of biological species. The examples highlighted above present an active or passive flow control technique, where the properties of the textured structure observed on the outer skin of many living organisms adapt to an outer flow modulation to deliver benefits or alleviate hostile conditions: decrease drag; limit the extent of separated regions; reduce aerodynamic noise; improve mixing; reduce wall/bed shear stress; efficient pumping, etc. Therefore, it is imperative to achieve a deep understanding of the dominant physical mechanisms that emerge as a result of the adaptive reconfiguration of the particular texture induced by the surrounding flow. Unravelling the physical mechanisms that are associated with the dynamical fluid-structure interaction will pave the way toward a large number of technological advances in the fields of aeronautics, hydraulics, chemical engineering, environmental, medical, and biological sciences, leading to the inception of the design and application of compliant surfaces that can be characterised as multi-functionary surfaces.

The investigation of flow over such textured surfaces must proceed with care since biological evolution, which has been taking place for over a million years, is governed by its own laws and constraints. Thus, the biological textures currently observed by humans may have undergone many design iterations before reaching their current state and may continue to evolve with time. The customary laws exploited by nature

that govern evolution are not limited by human knowledge and perspective, but these physical laws are complex and highly dependent on fulfilling multiple functions required by the respective biological species. Many primary functions in nature, such as hunting for prey, escaping a predator or finding a mate for reproduction, do not translate into technical objectives in a real-world scenario. As a result, simply mimicking these biological features would not result in an optimal solution for a single specific function; rather, evolution has progressively focused on providing the optimal solution for a wide range of functions. For instance, the mucus skin on aquatic animals provides protection from the high salinity of seawater and predators while also providing a means of drag reduction by way of a slip velocity (Bechert *et al.*, 2000*b*). Furthermore, it is naive to think that the direct imitation of such natural textured surfaces would lead to immediate technological advances since the geometrical and flow conditions associated with the respective biological species are subjected to a larger parametric space (i.e., a wide range of geometrical length and velocity scales). As an example, we consider the flow sensing technique of a seal. These whiskers have led to an impressive bio-inspired flow sensing technique (Beem *et al.*, 2012; Elshalakani *et al.*, 2020). However, the complexities associated with the overall structure of the sensory organs of the respective animal and the way it processes and translates the information via the central nervous system are still not well understood (Triantafyllou *et al.*, 2016). This leads to the issue of wishful thinking in conjunction with biological observations. As a matter of fact, drag reduction research is usually motivated by high expectations. The actual effects, however, are generally modest (i.e. 10% skin friction drag reduction in corrugated surfaces). Nevertheless, there is no harm in achieving small improvements, particularly if several of them are simultaneously used once. In human technology, engineers or computer technologists have improved and optimised their creations in many small iterations to arrive at something that finally appears as a breakthrough. Natural evolution proceeds very successfully in the same way.

In the current thesis, we are interested in the example presented by vegetation, which concerns the study of the interaction between vegetative canopies and the surrounding flow. In general, plants are characterised by leaves, stems, and branches, which form

a complex structure. Based on the length scales of the vegetation (i.e., plant height) and the boundary layer that develops above a canopy (i.e., planetary boundary layer thickness or river depth), we can classify the vegetation into terrestrial and aquatic canopies. Thus, a vegetative habitat, formed by a community of plants and trees, covers a large area of terrestrial and aquatic regions, providing a sustainable environment for biological species. This essentially falls into the category of flows that develop above filamentous surfaces. At this condition, the canopy layer can be envisaged as a permeable substrate with high porosity, which modulates the flow in many ways across various scales, ranging from individual plants to group plants. Generally speaking, a terrestrial canopy controls the transfer of momentum (generating turbulent eddies), exchanging radiation energy, heat, and other scaler quantities (including water vapour and carbon dioxide exchange) with the surrounding atmosphere. Vegetative canopies also serve as a good source and sink of several traffic-related air pollutants (Lee *et al.*, 2018). Similarly, aquatic vegetation observed in freshwater and saltwater regions provides many ecological services. Macrophytes present a compelling case for aquatic canopies since they significantly affect the stream, controlling the sediment transport, creating habitats for micro-organisms, influencing the nutrient transport, and improving water quality (Mars *et al.*, 1999). The canopy, by slowing down the fluid motion in the intra-canopy region, decreases the sediment resuspension and controls the nutrient and oxygen exchange (Hurd, 2000). The economic impact of the nutrient uptake cycle has been estimated to be over 10 trillion dollars globally (Costanza *et al.*, 1997). The societal, ecological, technological, and economic impact has driven a special interest in understanding the physical mechanisms associated with the interaction between the vegetation and the surrounding flow. In this flow regime, the canopy-fluid interaction triggers the development of large coherent turbulent structures that condition the scalar parameters that govern the nutrient exchange, sediment deposition, and the chemical reaction within the vegetative layers.

1.2 Thesis structure

The outline of the thesis is as follows: In Chapter 2, we present the literature review relevant to the topics tackled in the present work. The chapter incorporates both experimental and numerical investigations that have been reported thus far. The methodology employed in the current thesis is presented in Chapter 3. The chapter includes the baseline problem, physical and mathematical definitions of the flow, together with the adopted numerical discretisation and its validation. Chapter 4 covers the analysis and discussion of the results obtained when considering the turbulent flow over a wall-normal rigid canopy in a transitional regime. The content of this chapter has been accepted for publication in the journal of Flow, Turbulence and Combustion. In Chapter 5 we discuss the influence of the mean filament spacing of the canopy layer on the transition of the sparse-dense asymptotic regime classification (Nepf, 2012). In particular, we will investigate the interaction between the "localised flow layers" embedded within the canopy using a detailed spectral decomposition of the energy content of the velocity fluctuations and the autocorrelation function. Chapter 6 focuses on how the filament inclination along the mean flow direction influences the surrounding turbulent flow and ultimately, its contribution towards the transition of the asymptotic regimes. Currently, the contents of Chapter 5 and Chapter 6 are being collated into a couple of articles, which will be submitted to the Journal of Fluid Mechanics. Finally, some concluding remarks will be made at the end of the thesis and presented in Chapter 8. An outlook on the continuation of this research work will be put forward.

The structure of each results and discussion chapter is: (i) An introduction – where introductory remarks on the work is given and this section also includes a brief literature review of relevant previous work. (ii) Numerical set-up – an overview of the numerical techniques is given. (iii) Results-discussion – the results are given and the discussion on the findings in is given.

The results and analysis produced in this thesis have been submitted to the aforementioned archival journals and have been presented at national and international conferences.

List of publications

- Nicholas, S., Omidyeganeh, M. and Pinelli A. 'Numerical investigation of regime transition in canopy flows'. *Flow Turbulence and Combustion* 1-21, 2022.

- Monti, A., Nicholas S., Omidyeganeh M., Pinelli A., Rosti M.E., 'On the solidity parameter in canopy flows', *Journal of Fluid Mechanics*, 945, 2022.

List of conference proceedings

- Nicholas S., Omidyeganeh M., Pinelli A.,'Effects of In-Plane Solidity on the Different Regimes of Canopy Flows'. In: *5*th session of the UK Turbulence Consortium (UKTC) Talk Series, London, UK, 2021.

- Nicholas S., Omidyeganeh M., Pinelli A., 'Manipulations of Wall Bounded Flows Inspired by Shark Skin Denticles', In *25*th International Congress of Theoretical and Applied Mechanics (ICTAM), Milan, Italy, 2021.

- Nicholas S., Omidyeganeh M., Pinelli A., 'Effects of In-Plane Solidity on the Different Regimes of Canopy Flows'. UK Fluid Conference (UKFN), Southampton, UK, 2021.

- Nicholas S., Omidyeganeh M., Pinelli A., 'Large Eddy Simulations of Different Regimes in Canopy Flows', In *13*th International ERCOFTAC Symposium on Engineering, Turbulence, Modelling and Measurements (ETMM13), Island of Rhodes, Greece, 2021.

- Nicholas S., Monti A., Rost M.E., Omidyeganeh M., Pinelli A. 'Effects of Canopy Inclination on the Different Regimes of Canopy Flows', UK Turbulence Consortium (UKTC) Annual Meeting, London, UK, 2022.

- Nicholas S., Omidyeganeh M., Pinelli A., 'Effects of In-Plane Solidity on the Different Regimes of Canopy Flows', In *1*st Spanish Fluid Mechanics Conference, Cádiz, Spain, 2022.

- Nicholas S., Monti A., Rost M.E., Omidyeganeh M., Pinelli A. 'On the Effects of Filament Inclination on Canopy Flows', European Drag Reduction and Flow Control Meeting (EDRFCM) Paris, France, 2022.

- Nicholas S., Omidyeganeh M., Pinelli A., 'High Fidelity Simulations of Different Regimes in Canopy Flows ', In *14*th European Fluid Mechanics Conference (EFMC), Athens, Greece, 2022.

- Nicholas S., Omidyeganeh M., Pinelli A., 'On the Effects of In-Plane Solidity on the Different Regimes of Canopy Flows'. In *4*th International Conference on Numerical Methods in Multiphase Flow (ICNNMF4), Venice, Italy, 2022.

1.3 Author's Contribution

In this section we recognise the individual author's contributions towards the results and discussion chapters present in the current thesis. The main author of all the results and discussion chapter is Shane Nicholas (SN) and the other contributing authors are Alessandro Monti (AM), Marco Edoardo Rosti (MER), Mohammed Omidyeganeh (MO) and Alfredo Pinelli (AP).

The first results and discussion chapter on the regime transition of the canopy flows (i.e., Chapter 4) was published in the Journal of Flow Turbulence and Combustion. SN, MO and AP devised the plan of the study. SN planned and carried out the numerical simulations to accumulate the data and conducted the data analysis, while SN, MO and AP contributed to the interpretation of the results. SN took the lead in writing and preparing the draft manuscript. All authors reviewed the results and approved the final version of the manuscript. All authors provided critical feedback to shape the research direction, analysis and manuscript.

The second results and discussion chapter based on the effect of the in-plane solidity of canopy flows (i.e., Chapter 5) produced with the aim of publishing its content in high impact archival journals. SN, MO and AP devised the plan of the study. SN planned and carried out the numerical simulations to accumulate the data. In the later stages SN conducted the data analysis, while SN, AM, MO and AP contributed to the interpretation

of the results. SN took the lead in writing and preparing the draft manuscript with the help of AP. All authors reviewed the results and approved the final version of the manuscript. Over the course of the chapter all authors provided critical feedback and helped shape the research, analysis and manuscript.

The final results and discussion chapter is based on the effects of the canopy inclination (i.e., Chapter 6). SN, AM, MO and AP devised the plan of the study. SN planned and carried out the numerical simulations to accumulate the data. SN also conducted the data analysis, while SN, AM, MER, MO and AP contributed towards the interpretation of the results. Similar to the previous chapters, SN took the lead in writing and preparing the draft manuscript. All authors reviewed the results and approved the final version of the manuscript. Critical feedback was provided by all authors, which helped shape the direction of the research, analysis and the manuscript. Finally, We aim to get this chapter published in the high impact archival journals.

Although not included in the current thesis, the authors SN, MO and AP have contributed towards a journal article that was published in the Journal of Fluid Mechanics recently (Monti *et al.*, 2022). The authors (SN, MO and AP) contributed towards the interpretation of the results and approved the final version of the manuscript. This work was done in collaboration with AM and MER.

2
Literature Review

Contents

2.1 Introduction **13**
2.2 Classification of canopy flows **14**
2.3 Coherent structures in canopy flows **18**
2.4 Reconfiguration of canopies **21**
2.5 Numerical investigations of canopy flows **24**

2.1 Introduction

In the early 1940s, the investigation of turbulent flows that develops over fully submerged vegetative canopies was pioneered by Ree & Palmer (1949). The study put-forward the first methodology to estimate the overall drag induced by the vegetative canopy in the setting of an open channel flow. This enabled the authors to predict actual discharge capacity of a vegetative channel. The inception of the pioneering publication by Ree & Palmer (1949) have been the catalyst in sparking the interest of many researches in the field of fluid mechanics, hydrology and meteorology. This has led to the emergence of numerous investigations that have led to the better understanding of canopy flows, in the form of three annual reviews by Raupach & Thom (1981), Finnigan (2000) and Nepf (2012), and other reviews (Belcher *et al.*, 2012; Brunet, 2020). This can be attributed to

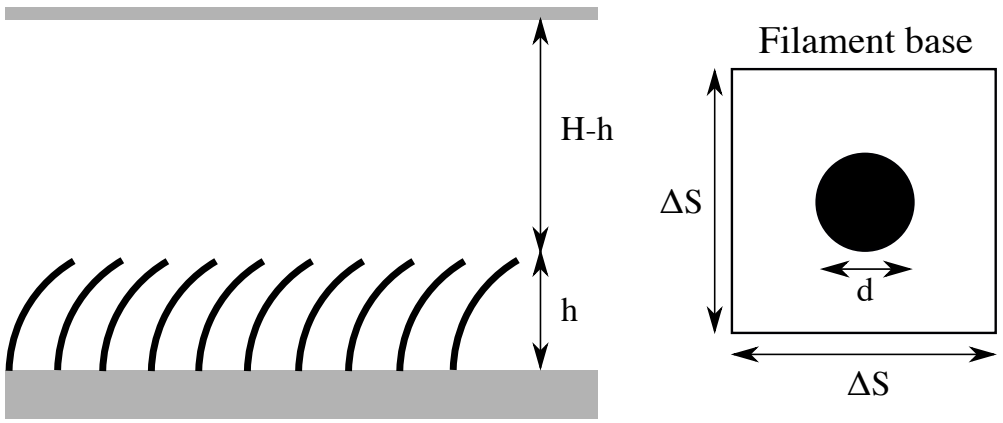


Figure 2.1: Geometrical parameters that govern canopy flows according to Nepf (2012), where H, h, d and ΔS represents the flow depth, canopy height, diameter of stem and stem spacing, respectively.

the variations present in the vegetation (i.e., terrestrial or aquatic), which translates to the large number of free parameters that needs to be accounted for, when dealing with canopy flows. The canopy height, density, spacing, stiffness, level of submergence and Reynolds number are just a few parameters that are contained within the parameter-space that characterises various regimes of canopy flows. Although many state of the art research practices have emerged recently, understanding the physical behaviour and the interplay of all the parameters with the surrounding turbulent flow seems to be an impossible task.

2.2 Classification of canopy flows

The recent review by Nepf (2012) and her collaborators, proposed a couple of classification based purely on the geometrical parameters of an aquatic canopies observed in fresh- and saltwater vegetation. The first classification, termed as the *level of submergence*, is defined as the ratio between the canopy height h and the flow depth H. This classification enables us to identify three types of canopies. The type of canopy termed as *emergent* (Nepf, 1999), satisfies the condition $H/h \approx 1$, where the canopy occupies the full extent of the submergence depth and typically penetrates the upper surface of the river channel. In these conditions, the integral length scale of turbulence is governed either by the filament diameter d or by the average spacing between adjacent filaments (ΔS),

depending on their relative size (Nepf, 2012). Thus, the turbulence in this type of canopy is mainly generated by the localised influence canopy filaments, predominantly in the wall parallel directions (i.e., longitudinal) (Nepf & Vivoni, 2000). In these conditions, the momentum equation reduces to a balance between the hydrodynamic force that drives the flow (i.e., pressure gradient or bed slope) and the canopy drag, which results in a self similar velocity profile (Lightbody & Nepf, 2006), that depends solely on the ratio between the frontal projected area and the volume of the canopy, i.e., $a(y) = d(y)/\Delta S^2$. Conversely, when $H/h > 10$, we can identify deeply submerged canopies. Apart from the elements-based flow deep inside the canopy, the canopy also communicates with the overlying flow along the wall normal direction (Ghisalberti & Nepf, 2009). Alternatively, deeply submerged asymptotically behaves as a terrestrial canopy when the depth of the flow is large (i.e., $H \longrightarrow \delta_P$, where δ_P is the planetary boundary thickness). In the community of terrestrial vegetation, these canopies are also referred to as *unconfined* canopies. In between these conditions there exists an intermediate condition, known as shallow submerged canopies ($1 < H/h < 10$), where the evolution and organisation of the large scale coherent structures above the canopy are limited by the flow depth (Nepf & Vivoni, 2000). The separation of the various types canopies based on the level of submergence allows us to comprehend the relative importance between the turbulent stresses, pressure gradient and drag forces.

The second classification proposed by (Nepf, 2012), focuses on submerged canopies, which presents a behaviour that is substantially different from the emergent ones. This geometrical classification known as the canopy solidity (i.e., λ), is defined as,

$$\lambda = \int_0^h a(y)dy \tag{2.1}$$

i.e., the ratio between the frontal projected area to the base area. In the special case of uniform filament diameter, the solidity is reduced as,

$$\lambda = \frac{dh}{\Delta S^2} \tag{2.2}$$

where d and ΔS are the filament diameter and spacing, respectively. Figure 2.1 offers a sketch summarising these geometrical parameters. Using the magnitude of the

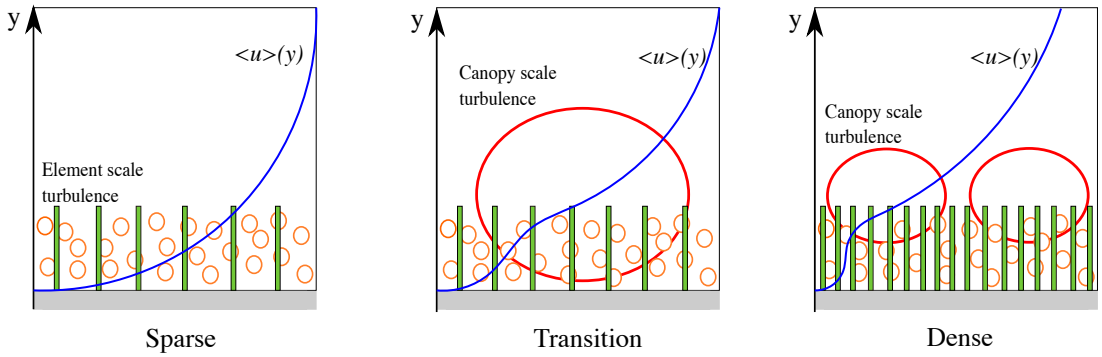


Figure 2.2: Sketch of the typical mean velocity profiles shape of canopy flows in sparse (left image), transitional (middle image) and dense (right image) regimes. The typical dominant turbulence scales are also sketched. Inspired from Nepf (2012).

solidity (λ) as an indicator, (Nepf, 2012), suggested that two canopy flow regimes can be anticipated. In particular, for values of $\lambda << 0.1$ the canopy flow develops into a sparse regime characterised by a mean velocity profile analogous to the one of a rough wall boundary layer (Jiménez, 2004). in which, the drag offered by the canopy is very small as compared to the one of the bed. On the other hand, for larger values of λ (i.e., $\lambda >> 0.1$), the drag imposed by the canopy becomes dominant. In this condition, termed as the dense regime, the mean velocity distribution exhibits a couple of inflection points: located at the top of the canopy and another one closer to the canopy bed, that arises due to the no slip condition at the canopy bed. The former may induce a Kelvin-Helmholtz (KH) type instability leading to the generation of large scale spanwise coherent motions (Raupach *et al.*, 1996; Finnigan, 2000; Ghisalberti & Nepf, 2002) The inflection point, located at the tip of the canopy, is a direct consequence of the abrupt discontinuity in the drag profile. Poggi *et al.* (2004*b*), by conducting a series of experiments on canopies with different stems number densities (i.e., modifying the mean filament spacing by increasing/decreasing the number of stems that populates the bed), observed a pronounced inflection point in the mean velocity profile for the canopies characterised by $\lambda > 0.1$. Conversely, in the sparse regime ($\lambda << 0.1$), the authors did not observe (or very mild) a clear inflection point in the mean velocity distribution and suggested as an upper bound for the solidity value leading to a sparse regime (i.e., $\lambda < 0.04$). The couple of inflection points allows us to establish of two separate shear layers.

Flows over canopies are often analysed using a zonal approach, as originally proposed by Belcher *et al.* (2003), A clear-cut classification of the zones has been proposed by several authors (Poggi *et al.*, 2004*b*; Nezu & Sanjou, 2008; Monti *et al.*, 2020). Inspired by the experimental observations of Poggi *et al.* (2004*b*), the authors proposed two phenomological models. In the sparse regime, the flow is considered to behave like a boundary layer that develops over a rough surface, with the canopy acting as the canonical rough-wall, while in the dense regime the overall flow structure can be envisaged as a weighted superimposition of three different dominant flow behaviours. In particular, the flow behaviours and their phenomenological classifications are based on the size of the largest eddy that can be locally hosted in the canopy layer (see Figure 2.3). A typical zonal classification splits the canopy layer into three layers. The first layer called as the inner region lies deep inside the canopy (i.e., $y/h << 1$, emergent zone). The flow is characterised by a von Kármán vortex street for sufficiently high Reynolds number, which size and intensity highly depend on the filament diameter and the local intra-canopy velocity. Next is an outer region (i.e., $y/h >> 1$, i.e. the logarithmic zone), where the flow resembles a boundary layer developing above a rough wall that can be characterised by a classical shifted boundary layer formulation (Finnigan, 2000), when the canopy is characterised by a large H/h ratio (Raupach *et al.*, 1996). In this condition the outer logarithmic perceives the displaced wall as the origin, instead of the canopy bed (Jiménez, 2004). However, for shallowly/partially submerged canopies, the development of the external flow is constrained by the space available between the canopy edge and the free surface (Nepf, 2012). The final (third) region sandwiched between the innermost and outermost region (i.e, the mixing zone), would behave as a turbulent mixing layer. This zone is characterised by three characteristic length scales (i.e., stem diameter, boundary layer thickness and shear length scale) associated with the inner, outer and mixing layer, respectively. An alternative classification, proposed by Monti *et al.* (2020), identifies the zones according to the positions of three characteristic locations of the mean velocity profile: two inflection points (the inner, by the bed and the outer at the canopy tip) and the virtual origin (location of the virtual wall seen by the outer flow). The inner and outer zones span the region extending from the bed to

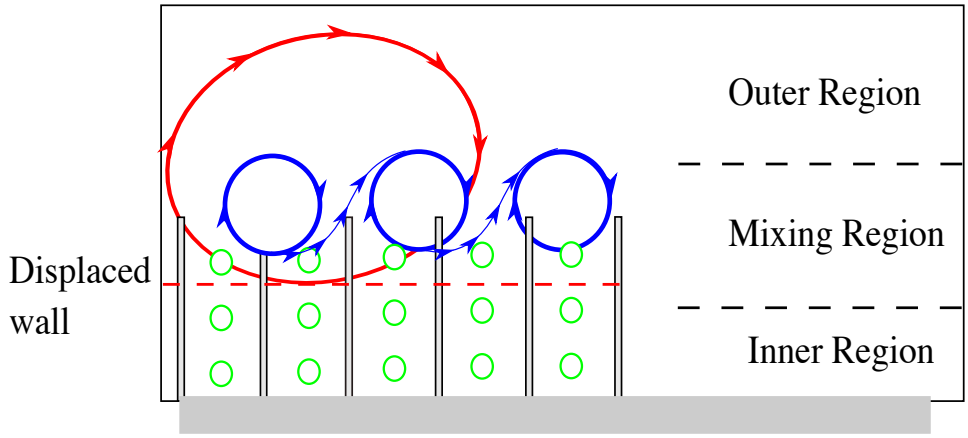


Figure 2.3: Sketch of the typical zonal classification of the canopy according to Poggi *et al.* (2004*b*). Each zone is characterised by its characteristic length scale. The mixing layer is characterised by a superposition of three length scales.

the inner inflection point and virtual origin up to the outer inflection point. Between the two, an overlapping region is identified which existence highly depends on the actual canopy flow regime. In particular, values of $\lambda > 0.15$ correspond to the presence of an overlap region which existence can also be utilised as a criterion to identify the the inception of the dense regime when varying λ. Higher values of λ induce an enlargement of the overlap and therefore a decoupling between the inner and the outermost layer.

2.3 Coherent structures in canopy flows

The similarities between the coherent structures appearing on the top of dense canopies (as a result of the inflected mean velocity profile) and the canonical mixing layer, have induced several authors (Raupach *et al.*, 1996; Finnigan, 2000) to put forward a conceptual model to explain the emergence of the typical structure found above dense canopies. In particular, the formation of the observed spanwise coherent turbulent structures with a size of the order of the canopy height h, were attributed to the roll up of the initial KH waves that were induced by the inflected mean velocity profile. The overall sizes of these KH waves are comparable to the height of the canopy (i.e., $O(h)$). In the aquatic vegetation community, the resulting coherent structures are referred to as the canopy-scale turbulence (Nepf, 2012). These vortices are expected to control the bulk momentum transport between the outer and inner regions of the canopy that nominally

falls in the dense regime. By comparing with results from a Direct Numerical Simulation (DNS) (Rogers & Moser, 1994) of a fully developed three dimensional plane mixing layer, Raupach *et al.* (1996), observed that the streamwise wavelength (Λ_x) corresponding to the most amplified, initial KH mode is preserved downstream the canopy in fully developed conditions. In general, mixing layers are often described by the wavelength of the initial KH instability Λ_x and the vorticity thickness (δ_ω), which is defined as,

$$\delta_\omega = \frac{\Delta U}{(\partial \langle u \rangle / \partial y)_{max}} \tag{2.3}$$

where ΔU is the velocity difference between the low- and high-speed free-stream regions and $\partial \langle u \rangle / \partial y$ is the maximum shear. In particular, the ratio between wavelength of the initial KH instability and the vorticity thickness falls into a specific range $3.5 < \Lambda_x/\delta_\omega < 5$ (Finnigan, 2000). These authors also suggest that in canopy flows, a direct comparison with the coherent structures appearing in canonical mixing-layer flows can be inferred in the region close to the canopy edge. To complete the mixing layer analogy, another transversal length scale based on the local shear stress at the top of the canopy was introduced. This new length scale, known as the *shear length scale*, can be defined whenever that the mean velocity underneath the tip is much smaller that the value of the mean velocity at the tip itself (i.e. the mean velocity at the inflection point). If this condition is met (which is usually the case for dense canopies), this length scale is assumed to be proportional to the thickness of the vorticity layer (δ_ω) that develops above the canopy, and is defined as,

$$L_s = \frac{\langle u \rangle (h)}{(\partial \langle u \rangle / \partial y)_{y=h}} \approx \frac{1}{2}\delta_\omega \tag{2.4}$$

where $\langle u \rangle (h)$ and $(\partial \langle u \rangle / \partial y)_{y=h}$ is the mean velocity and the shear at the edge of the canopy. In the dense regime, the aforementioned authors conjectured that the ratio between Λ_x and shear length scale is within the range is within the range $7 < \Lambda_x/L_s < 10$. The compilation of several experimental campaigns provided evidence for the this range and put forward the sharper estimate $\Lambda_x \simeq 8.1 L_s$. A further experimental confirmation of the validity of the fully developed mixing layer analogy was also provided by Ghisalberti & Nepf (2004), that reported a constant thickness of the vorticity

layer along the streamwise direction above the canopy. It should be noted that the typical structures forming above the canopy (typically in the shape of rollers) do not present a well defined vorticity structure, making the detection of these rollers an uneasy task (Finnigan *et al.*, 2009). Other authors, by conducting a linear stability analysis, were able to explain some aspects of the temporal evolution of the instability mechanism leading to the generation of the structures located at the top of the canopy (White & Nepf, 2007; Luminari *et al.*, 2016; Zampogna *et al.*, 2016). In another linear stability study (Sharma & García-Mayoral, 2020*b*), the authors assumed a linear correlation between shear length scale (L_s) and the mean filament spacing (ΔS), and report an intensification of the KH instability signature when ΔS is increased . A few authors have attempted to investigate the emergence of the spanwise vorticity rollers using a Large Eddy Simulations (LES) with the canopy modelled as a system of volume forces (Finnigan *et al.*, 2009; Bailey & Stoll, 2016). By employing a composite averaging procedure based on a pressure trigger, similar to a conditional averaging procedure proposed by Antonia (1981), these authors were able to study the generation and the evolution of the rollers into alternating *head-up head-down* hairpin vortices. The presence of those hairpin structures that can actually penetrate the canopy is believed to play a central role in the momentum flux between the canopy and the outer layer (Nepf, 2012). Monti *et al.* (2019) have recently observed how the outer, quasi-streamwise vortices cause the loss of the spanwise coherent nature of the vorticity rollers. The occurrence of the spanwise coherent vorticity structures were also reported by several other authors in the context of turbulent flows that develops over permeable substrates (Jimenez *et al.*, 2001; Rosti *et al.*, 2018*a*; Gómez-de Segura & García-Mayoral, 2019) or ribletted surfaces (Garcia-Mayoral & Jimenez, 2011; Endrikat *et al.*, 2021), where their appearance corresponds to the breakdown of the linear drag decrease with riblets protrusion. Recently, another type of coherent motions occuring in the inner portion of dense canopies has been identified by Monti *et al.* (2020). The authors, by carrying out stem resolved simulations using an efficient Immersed Boundary (IBM) formulation (Pinelli *et al.*, 2010) were the first in observing this inner inflection point of the mean velocity profile. The latter is produced as a result of the merging of the linear velocity profile characterising the region in the

vicinity of the bed with the convex shape of the mean velocity distribution at the canopy tip (see Figure 3.12a). The same authors have also highlighted the importance of the sweep events, mainly due to the wall normal penetration of the outer structure, that behaving like jets impinging on the bed generate a spanwise and diagonal modulation of the streamwise and spanwise velocity components, respectively.

2.4 Reconfiguration of canopies

All the classifications reported thus far were based on investigations that dealt with canopies, which are composed of rigid elements that do not conform to the local turbulent structure. However, the flexibility of the canopy leads to higher complexity in describing the flow features due to the added spatio-temporal scales that arise as a result of the adaptive reconfiguration of the canopy. Indeed, elastic hairy/filament elements embedded on textured surfaces can drastically modulate the overall near-wall turbulent structure. At the limit of the dense regime, the resulting substrate can be perceived as a porous layer that is characterised by a locally dynamic permeability tensor, and the entrainment of the flow within the layer depends on the natural frequency of the filamentous surface (Sundin & Bagheri, 2019; Tschisgale *et al.*, 2021). The recent numerical investigation by Sundin & Bagheri (2019) sheds some important insight into the temporal scale of the fluid-structure interaction. By conducting a surface time scale analysis, the authors observed three regimes that was dependent on the time-scale number (T^*). which is defined as the ratio between the characteristic surface time scale based on the natural frequency of the filaments (T_n) and the time scale of the cyclic turbulent events involving the near wall quasi-streamwise vortices (T_f) (i..e., $T^* = T_n/T_f$). In particular, in the first regime ($T^* >> 1$), termed as *negligible* reconfiguration, the hairy surface does not respond to the overlying turbulent flow. In this condition, the surface can be perceived as a rigid, rough surface. Indeed, if $T \gtrapprox 1$, few filaments maybe able to capture the slow moving turbulent structures. On the other hand, if $T^* << 1$ (*strong* reconfiguration), the hairy surface reaches equilibrium with the surrounding turbulent fluctuations, which is characterised by a two way coupling, between the surrounding turbulent flow and the elements embedded in the substrate.

In this regime, the surrounding flow loses part of its coherence, leading to increased turbulence isotropy (i.e., increased drag). However, a combination of specific properties (bending rigidity) and arrangements of the flexible hairs has the potential to decrease the drag in the form of decreased spanwise meandering and the stabilisation of the quasi-streamwise velocity streaks (Brücker, 2011). The last regime corresponds to a resonance condition where the surface characteristic time scale resonates with the turbulent forcing $T^* \simeq 1$. This condition leads to a significant increase in the velocity and displacement amplitudes of the flexible elements.

The difference between an elastic canopy and that of a rigid case mainly affects the drag exerted by the canopy on the mean velocity. In particular, the filaments embedded in a flexible canopy assumes a new shape after the flow-induced deformation. Indeed, the filaments respond to the surrounding fluid motion and bend along the dominant flow direction (Vogel, 1984). Thus, the elements assume a more streamlined shape, decreasing their frontal projected area perpendicular to the flow when compared with the rigid upright filaments. Nature uses adaptive reconfiguration as a mode of mitigating uprooting or breaking under strong currents by both terrestrial and aquatic plants (De Langre, 2008). The variation of the drag due to the reconfiguration and its effect on the velocity can be characterised by the departure of the canonical quadratic drag law (Vogel, 1984). In particular, the impact of reconfiguration is incorporated using the Vogel exponent (B), which modifies the drag law as, $D \propto \langle u \rangle^{2+B}$, where $\langle u \rangle$ is the mean velocity, with the Vogel exponent falling in the range $-2 < B < 0$. Alternatively, the overall stiffness of the flexible elements can be used to characterise the adaptive reconfiguration. In particular, the posture of the filaments embedded in the canopy is governed by two parameters: Cauchy (Ca) and Buoyancy (Bu) number, which reads as,

$$Ca = \frac{1}{2}\frac{\rho C_D b \langle u \rangle^2 l^3}{EI} \tag{2.5}$$

$$Bu = \frac{\Delta \rho g b t l^3}{EI} \tag{2.6}$$

where ρ is the density of the fluid, $\Delta\rho$ is the density difference between the fluid and the filament, g is the gravitational accretion, E is the elastic modulus, l is the length of filament and $I = bt^3/12$ is the second moment of area of filament, assumed as a blade with finite thickness t and width b. The main effect of the buoyancy is limited to delaying the onset of the blade reconfiguration (Luhar & Nepf, 2011). Based on the non-dimensional parameters described above, two asymptotic regimes can be identified. In particular, when the elements are nearly rigid, the reconfiguration of the canopy is negligible ($Ca < 1$) and the quadratic drag law is recovered, i.e., $B \approx 0$. Conversely, the filaments exhibits localised flow-induced deformation in a strong reconfiguration regime ($Ca > 100$), and the Vogel exponent depends on the initial shape of the element. In particular, if one characteristic length scale is lost, the Vogel exponent takes on the value of $B \approx -2/3$. This condition is typically associated with scenarios, such as bending of a beam or rectangle along a single axis. In certain conditions, the reconfigurations leads to a loss in two characteristic length, for example crumpling of a paper or the rolling of a disk into a cone. The resulting Vogel exponent is $B \approx -4/3$ (De Langre *et al.*, 2012). In between these regimes, there exists a transition of weak reconfiguration ($1 < Ca < 100$), which acts a proxy, for the separation of the negligible and strong reconfiguration regimes. In particular, Pan *et al.* (2014), by conducting an exhaustive investigational campaign, including both experimental and numerical (LES) approaches, observed a peak absolute magnitude of the Vogel exponent (i.e., $B \approx 1.1$) at $Ca \approx 21$, which can be defined as a sharp transition. On the onset of the weak reconfiguration regime, the sweeps associated with the external turbulent flow and KH coherent structures developed at the edge of the canopy, preferentially penetrates the canopy layer. A recent study by Tschisgale *et al.* (2021) observed a novel strong structure (KH/HP), which emerges when the KH vortices located at the canopy edge and hairpins associated with the velocity streaks in the outer region, merge together. When these strong events impinges the canopy layer with sufficient momentum able to generate enough drag to overcome buoyancy and rigidity, the filaments start to move in a synchronous (*honami* for terrestrial vegetation, *monani* for aquatic plants) or asynchronous (gently swaying) manner (Okamoto & Nezu, 2009). Concerning the synchronous motion of

the canopy, Ghisalberti & Nepf (2002) observed that the frequency associated with the coherent deformation of the filaments was in good agreement with the predicted frequency for KH instability in free mixing-layers. This suggests that both physical phenomenon are correlated with each other. The presence of honami or equivalently monami, also affects the turbulent momentum flux and mixing between the canopy and the overlying turbulent flow. Although homami allows turbulent fluxes to penetrate closer to the canopy bed, the overall momentum transfer is less efficient (i.e., low turbulent shear stress magnitude), when compared with the rigid canopy conditions (Nepf, 2012). This is attributed to the fact that the strong events are dampened by the coherent motions of the canopy.

2.5 Numerical investigations of canopy flows

Despite the numerous publications that has appeared in archival research, aimed of unravelling the physics of canopy flows, most of the knowledge accumulated thus far were mainly based on the limited information obtained from laboratory experiments based on two-dimensional or point-wise measurements (Raupach *et al.*, 1996; Finnigan, 2000; Ghisalberti & Nepf, 2002; Poggi *et al.*, 2004*b*; Ghisalberti & Nepf, 2004; Liu *et al.*, 2008; Nezu & Sanjou, 2008; Nepf, 2012) and few numerical predictions based on oversimplified flow-vegetation interaction models (López & García, 2001; Defina & Bixio, 2005; Harman & Finnigan, 2007; Finnigan *et al.*, 2009). Indeed, in theory, high-fidelity simulations have the potential to become a useful tool in the study of canopy flows or in general terms for the investigation of turbulent that develops above a textured surface, which would provide the researchers with the full three-dimensional information about the flow. The renewed interest in canopy flows has being driven by the recent developments in numerical techniques (Moin & Mahesh, 1998; Moser *et al.*, 2021) and the emergence of novel mathematical formulations (Mittal & Iaccarino, 2005*a*; Bottaro, 2019; Griffith & Patankar, 2020) that enable researchers to tackle fluid problems involving interfaces with surfaces and materials with complex topologies. To enable high fidelity simulations also translates into the possibility of achieving more detailed insight of the flow behaviour as compared to experimental techniques which

Nominal Regime	*Solidity(λ)*	*Height (h/H)*	*Mean spacing ($\Delta S/H$)*
Mildly Sparse	*0.07*	*0.05*	$\pi/24$
Transitional	*0.14*	*0.10*	$\pi/24$
Mildly Dense	*0.35*	*0.25*	$\pi/24$
Dense	*0.56*	*0.40*	$\pi/24$

Table 2.1: Canopy configurations previously investigated by Monti *et al.* (2020)

efficiency is hindered in the vicinity and in the interior of the canopy layer (i.e., $y/h << 2$). However, it is worth mentioning that the use of multi-plane tele-centric 2D particle image velocimetry (PIV) measurements have proven to be able to provide a sparse characterisation of the flow in the intra canopy region (Chagot *et al.*, 2020). Because of the experimental limitations related with the difficulty in probing the void space in between adjacent filament especially in the context of a dense canopy, researchers have relied on numerical modelling and simulations to obtain a full three dimensional description of the flow that develops above and within a canopy. In the case of closely packed canopies (i.e., $\Delta S/h << 1$), some researchers have used a homogenised drag model coupled with a LES closure model to simulate the effects of the canopy on the flow (Watanabe, 2004; Cui & Neary, 2008; Dupont & Brunet, 2008; Finnigan *et al.*, 2009; Bailey & Stoll, 2016). This approach revealed to deliver reasonable results in capturing the flow behaviour in the vicinity of the canopy, however, they fail to provide a detailed characterisation of the flow behaviour in the interior of the canopy layer and at the interface with the outer flow. Moreover, their employability is is strictly limited to the dense canopies, where the dominant length scale of the canopy (i.e., ΔS) is much smaller than the integral length scale of the outer flow (i.e., $\Delta S << L$). More recently, the use of Immersed Boundary formulations have proven to be quite successful in capturing the dynamical mechanisms of the flow developing within the canopy layer, by enforcing the proper (e.g. zero velocity) boundary condition on each filament (Monti *et al.*, 2019; Sharma & García-Mayoral, 2020*a*; Tschisgale *et al.*, 2021). This approach allowed to shed some light on some unanswered questions such as the conditions associated with the insurgence and the characterisation of different flow behaviours in the various layers of the canopy and their modulation by the respective canopy regimes. This is still an

open area with the available investigations covering limited scenarios. Furthermore, the interplay of the various localised layers that exists within the canopy in different flow regimes, particularly in the transition regime is still unclear. In addition, the existence of robust scaling laws that go beyond the solidity value (λ) that could provide an *a-priori* prediction of the flow canopy regime based on the geometrical properties and/or external flow characteristics, has not been clearly proposed yet (Monti *et al.*, 2020).

In particular, the effects of frontal solidity on the inceptions of the different flow regimes was investigated in the framework of a parametric study conducted by Monti *et al.* (2020), where the canopy height was systematically changed. More in details, the shortest and the tallest canopies were chosen to correspond to the two asymptotic regimes and the intermediate ones constitute the transitional regime (see Table 2.1). On the other hand, the importance of the in-plane solidity (e.g. fraction of open area in a wall-parallel cross-section of the canopy) and the influence of filament inclination in the genesis of the different canopy flow regimes has never been explored in details. The present thesis constitutes the main motivation of this study. When keeping the height of the canopy frozen while changing the in-plane solidity, the main geometrical length scale becomes the mean distance between adjacent filaments (i.e., ΔS). This length scale governs the penetration of the turbulent eddies of the outer flow into the canopy. In the limiting behaviour (i.e., $\Delta S/h << 1$), we would expect the canopy to behave as an-isotropic permeable substrate with relaxed wall normal permeability. On the other hand, introducing a simple filament angle of inclination, may modulate the mode of communication between the canopy layer and the external boundary layer, leading to new unexplored regimes. By incorporating the results of the seminal work of Monti *et al.* (2020), we aim at establishing a more complete canopy database allowing to identify dominant flow features characterising different canopy flow regimes and eventually, to draw final conclusions on general canopy flows.

3
Numerical Techniques

Contents

3.1 Introduction 27
3.2 Finite Volume Method 28
3.3 Time discretisation 33
3.4 Poisson Solution Technique 35
3.5 Numerical Implementation 36
3.5.1 Turbulent channel flow 39
3.6 Immersed Boundary Method 42
3.6.1 Interpolation and convolution 44
3.6.2 Flow over a cylinder 49
3.7 Flow over a rigid canopy 53
3.7.1 Large eddy simulation 53
3.7.2 Numerical setup 56
3.7.3 Validation case 59

3.1 Introduction

The current investigation deals with the governing equations of an incompressible, iso-choric, unsteady flow, i.e. the Navier Stokes equations. The mass and the momentum conservation equations in an inertial, cartesian frame of reference can be written as,

$$\frac{\partial u_i}{\partial x_i} = 0 \tag{3.1}$$

$$\frac{\partial u_i}{\partial t} + \frac{\partial u_i u_j}{\partial x_j} = -\frac{\partial P}{\partial x_i} + \frac{1}{Re}\frac{\partial^2 u_i}{\partial x_j x_j} + f_i \tag{3.2}$$

where u_i is the ith velocity component, P is the pressure, f_i is the volume force and lastly Re is the Reynolds number. The above equations were made non dimensional by selecting an appropriate reference length (L^*) and velocity scale (U^*) that is representative of the analysed flow conditions. In the momentum equation, the choice of the length and velocity scales corresponds to a non-dimensional parameter termed as the Reynolds number, that is defined by $Re = \rho U^* L^*/\mu$, where ρ is the density and μ is the dynamic viscosity. The application of appropriate initial and boundary condition yields a well-posed problem that can be solved with the methods described below.

3.2 Finite Volume Method

A numerical solution to the set of governing equations (i.e., Equation 3.1 and Equation 3.2) is obtained by applying the Finite Volume approach. A comprehensive discussion of the current methodology is provided in the well-written book by Ferziger *et al.* (2002) and in the framework of past PhD thesis by Rosti (2016), Monti (2019) and Suardi (2020). Nevertheless, for the sake of completeness, we shall provide a brief introduction to cover every problem encountered in the current thesis. Initially, the incompressible Navier Stokes equations defined in Equation 3.1 and 3.2 are integrated over an arbitrary control volume V, yielding their integral form,

$$\frac{\partial}{\partial t}\int_V u_i dV + \int_S u_i u_j n_j dS = -\int_V \frac{\partial p}{\partial x_i} + \int_S \tau_{i,j} n_j dS + \int_V f_i dV \tag{3.3}$$

$$\int_S u_i n_i dS = 0 \tag{3.4}$$

where S is the surface that bounds the control volume V , n_i is the ith component of the outward vector normal to S and $\tau_{i,j}$ is the viscous stress tensor, which is given below,

$$\tau_{i,j} = \frac{1}{Re}\left(\frac{\partial u_i}{\partial x_j} + \frac{\partial u_j}{\partial x_i}\right) \tag{3.5}$$

In order to compute the surface integrals (i.e. the fluxes), we have employed the well known Gauss' theorem to the terms with the surface integrals to a generic differentiable vector field F_i.

$$\int_V \frac{\partial F_i}{\partial x_i} dV = \int_S F_i n_i dS \tag{3.6}$$

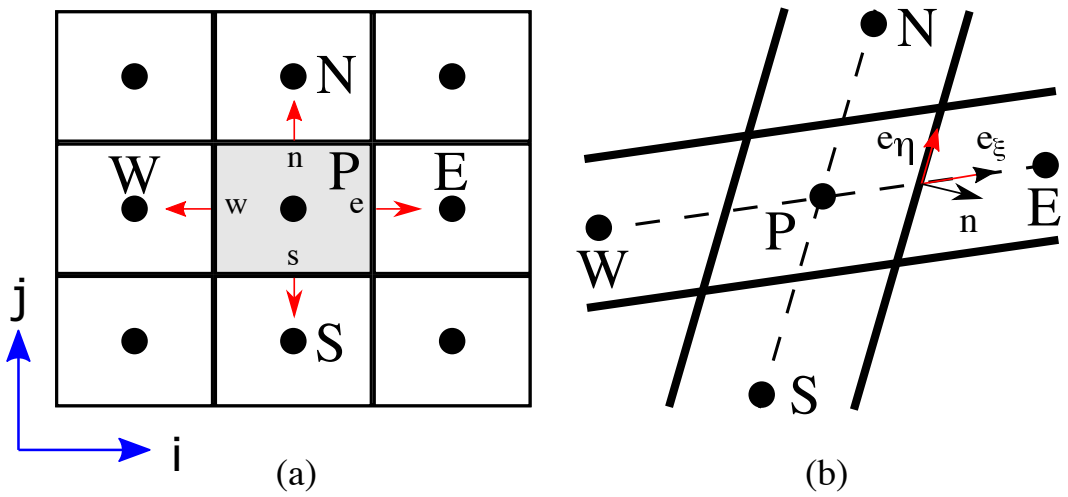


Figure 3.1: (a): a typical CV with the compass notation used for the neighbour cell centres and the CV faces. (b) a typical CV with a skewed grid.

To obtain the numerical approximations to the solution of the governing equations (Equations 3.3 and 3.4), we subdivide the domain into a finite number of contiguous, non overlapping Control Volumes (CVs), and the conservation equations are applied to the individual CVs (see Figure 3.1). By construction, the employed method is conservative, presuming that the surface integrals are the same for the CVs sharing a boundary. For instance, consider a CV and its neighbour, the fluxes entering the CV is the same as the fluxes exiting the neighbouring CV. The computational node is defined at the centre of the CV, in which all the averages of the computational variables (u_i and p) are formally assigned. Therefore, the colocated approach delivers a number of advantages: the number of coefficients data that is computed and stored is minimised, programming is simplified and complicated domains are dealt with ease. However, this approach may lead to difficulties with the pressure-velocity coupling and the occurrence of the spurious oscillations in the pressure field due to the emergence of the non conservation of mass (see Section 3.3).

In order to solve the governing equations (Equations 3.3 and 3.4), we have to introduce a numerical approximation for the volume and surface integrals. This is achieved via a quadrature formulae. In the current thesis, the shape of the CV can be described by a cuboidal shape in three dimensions (quadrangular in the bi-dimensional scenario), which is composed six surfaces that bounds the CV (four in 2D). Figure 3.1,

presents a typical two-dimensional control volume and the corresponding notation used in the current thesis. The extension of this in the three-dimensions is straightforward. Thus, the net flux through the surface of a CV boundary is simply the sum all the contributions over all the faces i.e., six faces for 3D (or equivalently four faces for 2D).

$$\int_S f dS = \sum_k \int_{S_k} f dS \tag{3.7}$$

where f is any component of the flux vector in the direction normal to the face of the CV (i.e., the normal convective ($\int_S u_i u_j n_j dS$) and or viscous ($\int_S \tau_{ij} n_j dS$) flux term in the momentum conservation equation. Note that the viscosity is a constant parameter for an incompressible fluid and the viscous flux reduces to

$$\int_S \tau_{ij} n_j dS = \frac{1}{Re} \int_S \frac{\partial u_i}{\partial x_j} n_j dS \tag{3.8}$$

The surface integral is approximated using the mid-point rule, which yields a second order accurate approximation. In this quadrature, the integral is approximated as the product of the integrand at the cell face centre and the corresponding surface area. As an example, in a two dimensional cell, the flux on the east face of a rectangular cell would read as:

$$F_e = \int_{Se} f dS \approx f_e S_e \tag{3.9}$$

Equation 3.9 requires the values of the variables at the cell face centre. In order to determine these values, we use a linear interpolation between the two neighbouring nodes, f_E and f_P. For example the value of the cell face centre at the location e (i.e., east face) would read,

$$f_e = f_E \lambda_e + f_P (1 - \lambda_e) \tag{3.10}$$

where the linear interpolation factor λ_e is defined as,

$$\lambda_e = \frac{x_e - x_p}{x_E - x_P} \tag{3.11}$$

This method is also second-order accurate and on a Cartesian mesh would correspond to the central-difference approximation of the first derivative in a finite difference

framework. The assumption of a linear variation between points P and E, also provides a simple method to approximate the derivative,

$$\left(\frac{\partial f}{\partial x}\right) \approx \frac{f_E - f_P}{x_E - x_P} \tag{3.12}$$

There are some terms that require the integration over a volume of a CV, therefore we estimate the integral with a second accurate approximation that is obtained by extending the midpoint rule in three dimensions. In this technique, the integral is estimated as a product of the integrand at the cell centre and the corresponding volume,

$$Q_p = \int_V q dV \approx q_P V_P \tag{3.13}$$

where q_P is the value of q at the CV centre and V_P is the volume of the respective cell. Having set the computational node in the centroid of the CV, no interpolation to compute q_P is needed.

Based on the approximations described above, we are now able to write the full spatial approximations of Equation 3.3 and Equation 3.4. The volume integrals, corresponding to the unsteady, pressure and forcing terms, can be easily computed applying Equation 3.13. The convective flux F^c is computed by assuming that the mass flux m is already known using the midpoint rule approximation.

$$F_e^c = \int_{S_e} u\boldsymbol{u}.\boldsymbol{n} \approx \dot{m}_e u_e \tag{3.14}$$

here, again for the sake of simplicity, we have considered only the x component of the velocity field, $\dot{m}_e$ is the mass flux on the face e computed as,

$$\dot{m}_e = \int_{S_e} u_j n_j dS \approx (\boldsymbol{u}.\boldsymbol{n})_e S_e \tag{3.15}$$

In order to compute the diffusive flux F^d

$$F_e^d = \int_{S_e} \frac{1}{Re}\frac{\partial u}{\partial x_j} n_j dS \approx \frac{1}{Re}(\boldsymbol{\nabla} u.\boldsymbol{n})_e S_e \tag{3.16}$$

the gradient of u at the cell face centre is needed. First, we approximate the derivative at the CV centre by the average value over the cell

$$\left(\frac{\partial u}{\partial x_i}\right)_P \approx \frac{\int_V \frac{\partial u}{\partial x_i} dV}{V_P} \tag{3.17}$$

then, we apply the Gauss theorem to the numerator

$$\int_V \frac{\partial u}{\partial x_i} dV = \int_{S_e} u\boldsymbol{e_i}.\boldsymbol{n} dS \approx \sum_c u_c S_c^i \qquad for \quad c = e, n, w, s, b, t \tag{3.18}$$

where $\boldsymbol{e_i}$ is the unit vector in the $i-th$ direction. Finally, the derivative can be computed as,

$$\left(\frac{\partial u}{\partial x_j}\right)_P \approx \frac{\sum_c u_c S_c^i}{V_P} \tag{3.19}$$

Using interpolated cell face values to compute the derivative may generate an oscillatory solution. To solve this problem we use the so-called deferred correction method (Böhmer *et al.*, 1984) as proposed by Muzaferija (1994), where an additional term is added, which is the difference between the correct and approximated flux. The diffusive flux is corrected as follows,

$$F_e^d = F_{e\ impl}^d + [F_{e\ expl}^d - F_{e\ impl}^d]^{old} \tag{3.20}$$

where "old" means a value from the previous iteration or time step, and "expl" or "impl" means that the term is treated explicitly or implicitly, respectively. When the line connecting nodes P and E is orthogonal to the cell face, the derivative with respect to $\boldsymbol{n}$ can be approximated by a derivative with respect to the coordinate $\boldsymbol{e}_\xi$ along that line, and the implicit flux is written with a second order accurate approximation as

$$F_{e\ impl}^d = \frac{1}{Re} S_e \left(\frac{\partial u}{\partial \xi}\right)_e \tag{3.21}$$

When the grid is non-orthogonal, the deferred correction term must contain the difference between the gradient in the $\boldsymbol{n}$ and $\boldsymbol{e}_\xi$ (see Figure 3.1b). So, the diffusive flux can be written as

$$F_e^d = \frac{1}{Re} S_e \left(\frac{\partial u}{\partial \xi}\right)_e + \frac{1}{Re} S_e \left[\left(\frac{\partial u}{\partial n}\right)_e - \left(\frac{\partial u}{\partial n}\right)_e\right]^{old} \tag{3.22}$$

where the first term on the right hand side is the one treated implicitly, while the second one is the deferred correction, which is calculated using interpolated cell centre gradients, resulting in the following expression for the diffusive fluxes,

$$F_e^d = \frac{1}{Re} S_e \frac{u_E - u_P}{L_{P,E}} + \frac{1}{Re} S_e (\nabla \mathbf{u}_e^{old}.(\mathbf{n} - \mathbf{e}_\xi) \tag{3.23}$$

If the line connecting nodes P and E is orthogonal to the cell face, the deferred correction term is null as expected. Note that, this correction does not affect the second-order accuracy of the method.

3.3 Time discretisation

The numerical solution of the incompressible Navier-Stokes equations is complicated by the lack of an independent equation for the pressure. In fact, the continuity equation does not have an explicit time derivative applied to the pressure or to the density variable. Therefore, when dealing with incompressible flows, the thermodynamics becomes meaningless and the absolute pressure is of no significance (only its gradient affects the flow). Thus, the continuity equation is just a kinematic constraint on the velocity field, rather than a dynamic equation. A way out to this problem is to construct a pressure field that guarantees satisfaction of the continuity constraint. One of the canonical ways to solve this problem is to rely on the fractional step method. This technique was firstly developed by Chorin (1968) and later on modified and improved by several other authors. The results obtained in the thesis rely on a modified version of the method originally proposed by Kim & Moin (1985). The algorithm is based on the Helmholtz Hodge's decomposition of the velocity field into a solenoidal and an irrotational part, and consists of two stages: the prediction step, where the momentum equation is solved without satisfying the continuity equation, and the correction step, where the previous solution is corrected by projecting the velocity field onto a divergence-free field.

We can write the numerical discretisation of the incompressible Navier-Stokes equations concisely as follows,

$$\frac{u^* - u^n}{\Delta t} = -\mathcal{N}_l(u^n, u^{n-1}) + \frac{1}{Re}\mathcal{L}(u^*, u^n) - \mathcal{G}(\phi^n) \tag{3.24}$$

$$\frac{u^{n+1} - u^*}{\Delta t} = -\mathcal{G}(\phi^{n+1}) \tag{3.25}$$

with the constraint

$$\mathcal{D}(u^{n+1}) = 0 \tag{3.26}$$

where u^* is the predicted velocity field, u^n is the solenoidal velocity field at the nth time step, Δt is the time step, $\mathcal{N}_l, \mathcal{G}, \mathcal{D}$ and $\mathcal{L}$ are the discrete nonlinear, gradient, divergence and Laplacian operators, respectively, and ϕ is the projection variable. Note that, the operators include coefficients that are specific to the selected time scheme. The variable ϕ^{n+1} to be used in the projection (Equation 3.25) can be found by solving a Poisson equation for ϕ, obtained by applying the divergence operator to Equation 3.25, which gives

$$\mathcal{L}\phi^{n+1} = \frac{1}{\Delta t}\mathcal{D}(u^*) \tag{3.27}$$

with a boundary condition,

$$\frac{\partial \phi^{n+1}}{\partial n} = 0 \tag{3.28}$$

with n being the outward normal vector. So, the sequence to solve the incompressible Navier-Stokes equations by a fractional step method consist of a prediction step (Equation 3.24), a Poisson equation (Equation 3.27), and a final correction step (Equation 3.25). The solution technique of the Poisson equation will be discussed in the subsequent subsection.

When a colocated arrangement of variables on a numerical grid is used, the divergence term of Equation 3.27 requires the values of the velocities at cell faces that can be obtained by linear interpolation. As a consequence, the Poisson equation needs to be discretised on a grid which is coarser than the one used for the predicted variables. The mismatch in the number of discrete values makes the kernel of the pressure operator non trivial giving rise to pressure spurious modes. To eliminate those modes we use a method originally proposed by Rhie & Chow (1983). Initially, we solve the momentum equation as usual, and then (before solving the Poisson equation) the mass fluxes obtained with the interpolated velocity are corrected by subtracting the difference between the pressure gradient and the interpolated gradient at the cell face location obtained at the previous time step.

$$\dot{m}_e = (\boldsymbol{u}.\boldsymbol{n}_e S_e) - \Delta t S_e[(p_E - p_P) - \nabla p.e_\xi]^{old} \tag{3.29}$$

This method automatically detects the oscillations and smooths them out.

3.4 Poisson Solution Technique

As mentioned in the previous section, apart from the pressure gradient, the absolute pressure has no significant contributions towards overall the flow. The fractional step formulation used in the thesis, leverages this property and constructs the pressure field such that it satisfies the continuity constraint. The parameter ϕ, that ensures a divergence-free velocity field, is obtained by, applying the divergence operator to Equation 3.24. The resulting Poisson equation in the context of a three-dimensional flow reads as,

$$\frac{\partial^2\phi}{\partial x^2} + \frac{\partial^2\phi}{\partial y^2} + \frac{\partial^2\phi}{\partial z^2} = r \tag{3.30}$$

where $r = \frac{1}{\Delta t}\mathcal{D}(u^*)$. From a computational effort point of view, the most expensive step is the one related with the solution of the Poisson pressure equation. If the problem at hand is characterised by a one or two homogenous direction, we can simplify the solution of the three-dimensional by employing periodic boundary conditions.

For instance, if the spanwise direction is homogenous (i.e., flows over airfoils or flows around a cylinder), we can assume periodic boundary conditions and a 3D Poisson's equation can be transformed into a series of two-dimensional Helmholtz equations in the wave numbers space via a discrete fast Fourier transform (FFT). In particular, assuming the spanwise direction z to be the periodic direction, ϕ is transformed in the wave number space using the discrete anti-transform,

$$\phi(x, y, z) = \sum_{l=0}^{N-1} \hat{\phi}(x, y) exp(ilz) \tag{3.31}$$

where $\hat{\phi}$ is the lth Fourier coefficient of the variable ϕ and N is the number of modes considered (i.e. $l = 0, 1.....N-1$). We can obtain the set of N decoupled Helmholtz equations with the aid of the orthonormality of the Fourier basis.

$$\frac{\partial^2\hat{\phi}_l}{\partial x^2} + \frac{\partial^2\hat{\phi}_l}{\partial y^2} - \kappa_l\hat{\phi}_l = \hat{r}_l \tag{3.32}$$

Where κ_l is the modified wavenumber and $\hat{r}_l$ is the Fourier transform of the right hand side of Equation 3.27. Further insight can be found in Canuto *et al.* (2012) and details on the solution technique of the Helmholtz equations are described in the next subsection.

On the other, in the current thesis we are interested in a specific configuration (i.e. channels), which belongs to a special class of domains, that is characterised by two homogeneous directions in the streamwise (x) and spanwise (z) directions. Thus, we can enforce periodic boundary conditions and transform the three-dimensional Poisson equation into a series of one-dimensional equations in the wavenumber space via an efficient multidimensional FFT in the wall parallel directions. In particular, assuming the streamwise x and spanwise z directions to be the periodic, ϕ is transformed in the wave number space using the discrete anti-transform,

$$\phi(x,y,z) = \sum_{m=0}^{N_i-1} \sum_{l=0}^{N_k-1} \hat{\phi}(y) exp(i(mx + lz)) \tag{3.33}$$

where $\hat{\phi}$ is the mth and lth Fourier coefficient of the variable ϕ, while N_i and N_k is the number of modes considered (i.e. $m = 0, 1.....N_i - 1$ $l = 0, 1.....N_k - 1$). Using the orthonormality of the Fourier basis, we obtain a set of $N_i \times N_k$ decoupled equations,

$$\frac{\partial^2 \hat{\phi}_l}{\partial y^2} - \kappa_l \hat{\phi}_l - \kappa_m \hat{\phi}_m = \hat{r}_{l,m} \tag{3.34}$$

where κ_m and κ_l is the streamwise and streamwise modified wave-numbers, respectively, and $\hat{r}_l$ is the Fourier transform of the RHS of Equation 3.27. The transformed equation, discretised with a central differencing scheme, yields a tri-diagnal system, that can be solved directly. Further details on the solution technique are provided in the subsequent subsection.

3.5 Numerical Implementation

The discrete counterparts of Equations 3.3 and 3.4, have been implemented in a well-established curvilinear finite volume code (Omidyeganeh & Piomelli, 2011, 2013*a*; Rosti *et al.*, 2016) written in Fortran 77. As previously mentioned, the code approximates the fluxes using a second-order central formulation (Figure 3.2c) and the method proposed by Rhie & Chow (1983) to avoid the pressure spurious oscillations. The equations are advanced in time using a second-order semi-implicit fractional-step procedure. (Kim & Moin, 1985), where the implicit Crank-Nicolson scheme is implemented for

the wall-normal diffusive terms while an explicit Adams-Bashforth scheme is applied to the other terms.

When there is a single homogenous direction (spanwise), the Poisson's pressure equation, which needs to be solved at each time step to enforce the solenoidal condition of the velocity field, is transformed into a series of two-dimensional Helmholtz equations in the wavenumber space via a Fast Fourier Transform (FFT) in the spanwise direction. Each of the resultant elliptic 2D problem is then solved using a preconditioned Krylov method (using the PETSc library implementation, Balay *et al.* (2017)) In particular, we have found the iterative Bi-conjugate Gradient Stabilised (BiCGStab) method (Sleijpen *et al.*, 1994) with an algebraic multi-grid pre-conditioner (boomerAMG, Yang *et al.* (2002)) to behave quite efficiently. The code is parallelised using the domain decomposition technique and the message passing interface (MPI) library. Figure 3.2a shows the strong scaling of the code, defined as the ratio between the time needed to perform a one-time step with one processor T_1 and the time using n processors T_n, carried out on the ARCHER2 platform. This test has been produced with a series of channel flow simulations at friction Reynolds number, based on the mean wall-shear velocity and the channel half height, $Re_\tau = 1000$. The test was performed on a Cartesian grid with $10080 \times nj \times 16$ points in x, y and z directions, respectively. Different series have been produced varying the number of points in the wall-normal direction, nj. For every series (solid lines with symbols), the problem size has then been kept fixed while increasing the computing nodes up to 20 (each node has 128 CPUs). The dashed line shows the ideal strong scaling. The solid lines overcome the ideal scaling for the lower number of nodes. This effect is caused by the nonlinearity of the memory (and cache) available increasing the number of nodes.

Conversely, when both the wall-parallel directions (i.e., streamwise and spanwise) are periodic, the Poisson equation that needs to be solved at each time step is transformed into a series of one-dimensional equations in the wavenumber space via an efficient multidimensional FFT (Dalcin *et al.*, 2019). In particular, we segregate the domain into slabs in the streamwise direction to exploit parallel performance. Initially, the equations are transformed along the spanwise direction. Then, we perform an efficient

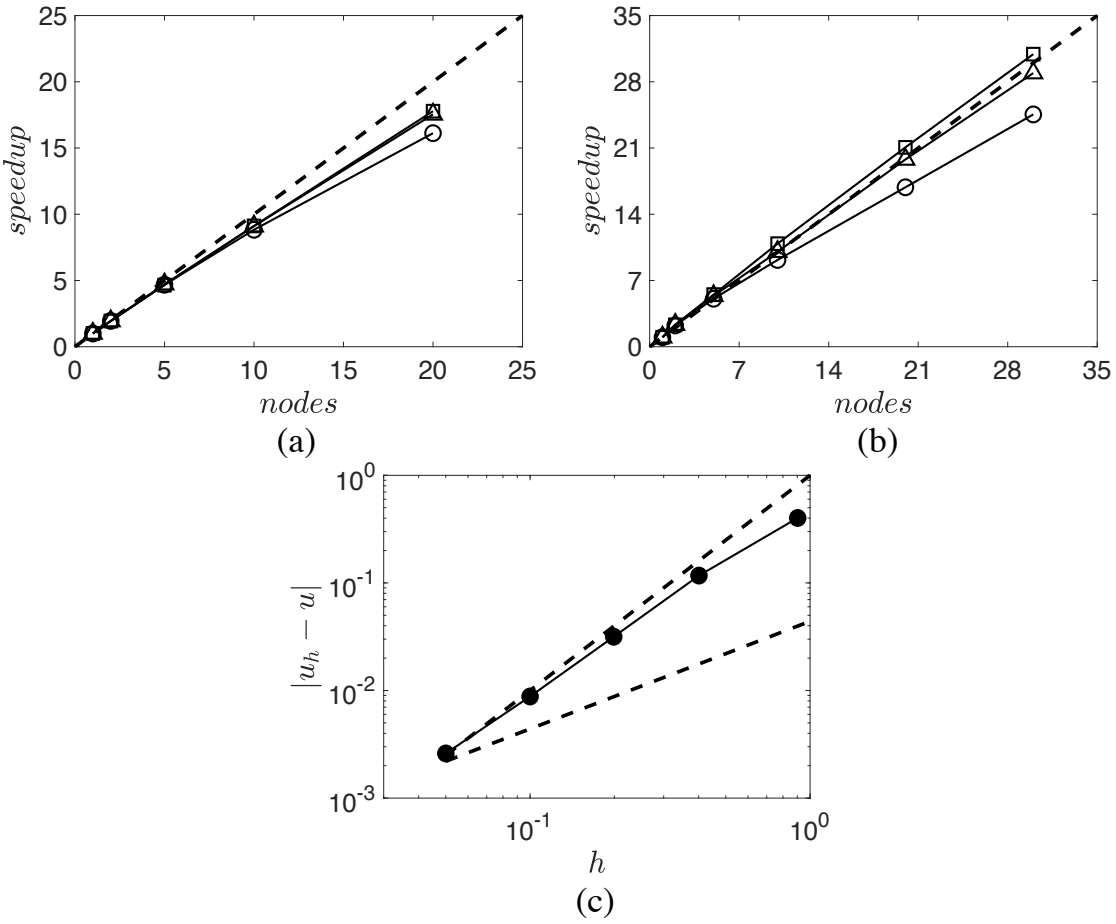


Figure 3.2: Scalability of the finite volume code with the two dimensional (a) and one dimensional (b) poisson solver. The dashed line represents the reference linear value, while the solid lines are the speed-up of our code (○ $njm = 194$; △ $njm = 388$; □ $njm = 776$). (c) Spatial accuracy of the finite volume code. The dashed lines represents the first and second order accuracy, while the solid line is the accuracy of our finite volume code.

data redistribution as described in Dalcin *et al.* (2019) moving towards a spanwise slab decomposition. At the end of this step, we transform the equations along the streamwise direction, yielding a series of one-dimensional equations in the wavenumber space. The resulting equations are solved directly, using Cholesky's factorisation technique (Higham, 2009). Figure 3.2b reveals the strong scaling of the code, similarly observed for the two-dimensional Poisson solver. The simulations carried out were carried out on the Cambridge Service for Data-driven Discovery (CSD3) platform. This test has been produced with a series of channel flow simulations at the same nominal friction Reynolds number (i.e., $Re_\tau = 1000$) considered in the previous test. However, the current test was performed on a Cartesian grid with $7680 \times nj \times 3840$ points in the

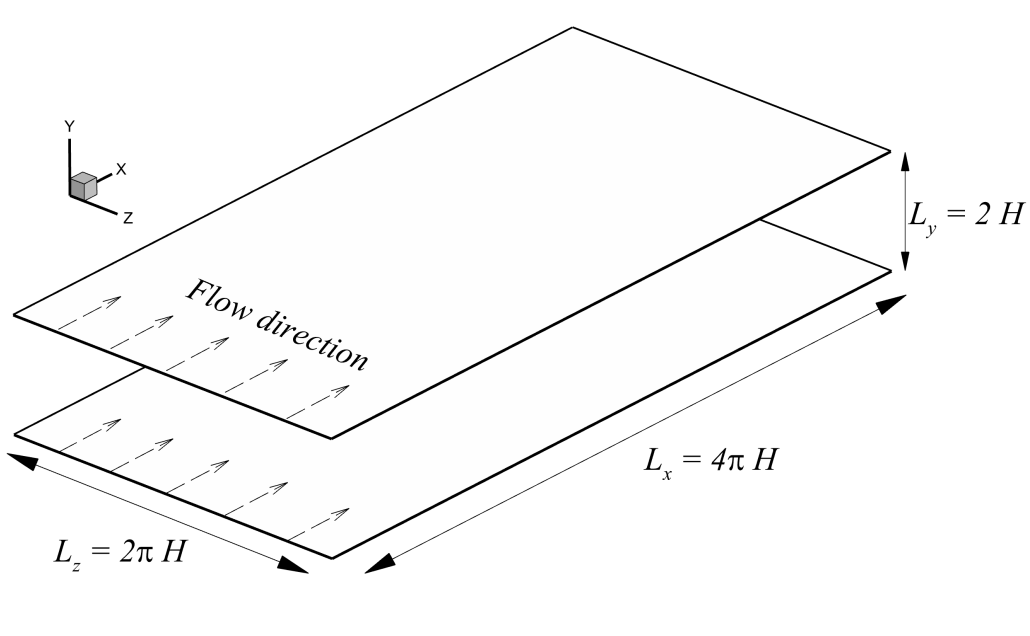


Figure 3.3: Sketch of the channel geometry.

x, y and z directions respectively. Similar to the previous series, the plots have been produced by varying the number of points in the wall-normal direction. For every series, the problem size has then been kept fixed while increasing the number of computing nodes by up to 30 (each node has 32 CPUs). The solid lines reveal a strong scaling with the increasing number of points in the wall-normal direction.

3.5.1 Turbulent channel flow

We consider the flow of an incompressible viscous fluid through a channel with smooth, impermeable walls, as sketched in Figure 3.3. We introduce the Cartesian coordinate system shown in Figure 3.3, where x, y and z denote the streamwise, wall normal and spanwise coordinates, while u, v and w denote the respective components of the velocity vector field. The lower and upper walls are placed at a distance $L_y = 2H$, and are located at $y = 0$ and $y = 2H$, respectively. At the walls, a no-slip condition is imposed. It is assumed that the fully developed turbulent channel flow is homogeneous in the streamwise and spanwise directions, so that periodic boundary conditions can be used in these directions. The use of the periodic boundary condition can be justified

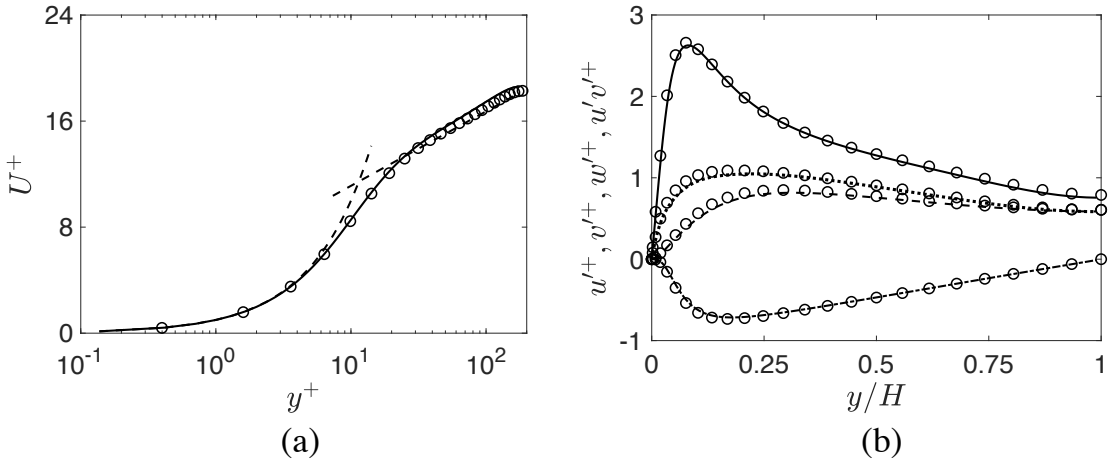


Figure 3.4: (a): Mean velocity profile in wall units. (b) Reynolds stresses as function of wall normal distance scaled with outer flow units. The solid, dashed, dotted and dot-dash lines represents the streamwise, wall normal spanwise, and anisotropic terms, respectively. The circles in both the plots are used for the results by Moser *et al.* (1999)

if the computational box is long and large enough to include the largest eddies in the flow (Kim & Moin, 1985).

In order to write the problem in a dimensionless form, we select the channel semi-height as characteristic length,

$$L^* = H \tag{3.35}$$

and the bulk velocity as the characteristic velocity,

$$U^* = U_b = \frac{1}{2H}\int_0^{2H} \langle u \rangle (y) dy \tag{3.36}$$

where $\langle u \rangle$, $\langle v \rangle$ is the mean velocity in the streamwise direction and the operator $\langle . \rangle$ indicates the average over both time and homogeneous directions i.e., x and z. With this choice, the bulk Reynolds number is defined as,

$$Re_b = \frac{U_b H}{\nu} \tag{3.37}$$

where ν is the kinematic viscosity defined as $\nu = \mu/\rho$.

To validate the value of the code used, we select a typical channel flow simulation at $Re_b = 2800$ and we compare our results with the ones in the well-known, seminal paper by Moser *et al.* (1999). The simulation is carried out on a computational grid of

$256 \times 192 \times 192$ in the x, y and z directions respectively. The computational domain size is set to $4\pi H$, $2H$ and 2π, in the x, y and z directions respectively. The mesh in the non-homogeneous direction y has been generated with the stretching function,

$$y = \frac{\tanh(\alpha \bar{y})}{\alpha} \tag{3.38}$$

where α is an adjustable stretching factor used to modify the mesh distribution, especially near the wall and $\bar{y}$ is an uniform mesh grid with constant spacing coming from the lower to the upper wall. With the mentioned grid, the resolution turns out to be $\Delta x^+ = 8.6$, in wall units in the stream-wise direction, $\Delta z^+ = 5.8$, in the spanwise direction, and with a minimum $\Delta y^+ = 0.13$ in the wall-normal direction which is less than 1. The wall units, indicated by the superscript $.^+$ are measured in terms of the viscous length δ_ν which is defined as follows,

$$\delta_\nu = \frac{\nu}{u_\tau} \tag{3.39}$$

where u_τ is the friction velocity that, in a turbulent channel flow with solid impermeable walls is defined as follows,

$$u_\tau = \sqrt{\nu \frac{d\langle u \rangle}{dy}\bigg|_{y=0}} \tag{3.40}$$

where $y/H = 0$ is the location of the wall. Note that the viscous length and the friction velocity as reference length and velocity scale respectively, are used in the near the wall region. The Reynolds number based on the friction velocity u_τ and the channel semi-height is called friction Reynolds number Re_τ and is defined as $Re_\tau = u_\tau H \nu$. In our case, with the choice of $Re_b = 2800$, the friction Reynolds number turns out to be $Re_\tau = 180$.

Figure 3.4a hows the mean velocity profiles $U^+ = U/u_\tau$ versus the logarithm of the distance from the wall expressed in wall units. The solid line is used for the results of our simulation, while the circles for the reference values of Moser *et al.* (1999). The agreement is very good, even if our friction velocity is slightly underestimated. This can also be seen in the collapse of the non-dimensional r.m.s of the velocity fluctuations, as given in Figure 3.4b.

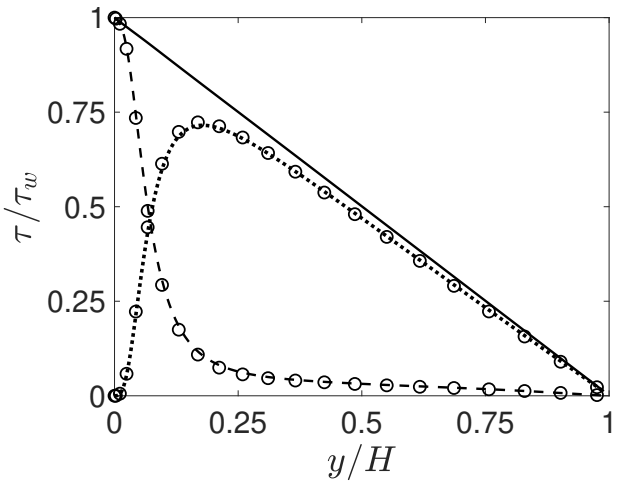


Figure 3.5: The total shear stress (solid line), decomposed in the viscous stress (dash-dotted line) and Reynolds shear stress (dashed line) obtained from from simulation. The circles in both the plots are used for the results by Kim *et al.* (1987).

The total shear stress, τ defined as the sum of the Reynolds shear stress with the viscous stress, given as,

$$\tau = \mu \frac{d\langle u \rangle}{dy} - \rho \langle u'v' \rangle \tag{3.41}$$

is given in the Figure 3.5 and once again compared with the results by Moser *et al.* (1999). The good agreement between the results is evident yet again. The next section will introduce the immersed boundary method which is the technique that has been chosen to deal with the presence of complex and/or moving portions of the boundary.

3.6 Immersed Boundary Method

The Immersed Boundary Method (IBM) is a numerical technique used to simulate flow fields past moving/rigid bodies that do not necessarily conform with the computational grid. The pioneer of this numerical technique has been Charles Peskin, who, back in the seventies, was able to simulate the blood flow around the natural mitral valve in a human heart (Peskin, 1972). As mentioned, the main feature of this method is that the numerical grid does not need to conform to the geometry of the object, which is replaced by a body force distribution $\boldsymbol{f}$ that mimic the effect of the body on the fluid by restoring the desired velocity boundary values on its immersed surface.

This technique has drawbacks and advantages that need to be considered. Concerning the former, surely the imposition of the right boundary conditions is not straightforward and the impact of the method on the accuracy and conservation properties of the numerical scheme is not obvious. Moreover, a body-fitted grid would allow a better control on the grid resolution close to the boundary of the body. Despite this, the advantages of the IBM become huge when dealing with complex surfaces or moving bodies. In fact, with complex surfaces, the primary advantage brought by the IBM is the simplification of the grid generation process that could be burdensome. When it comes to moving bodies, the computational cost of regenerating the grid at every time step would significantly impact the overall computational cost. Moreover, the IBM allows keeping a Cartesian grid that has a significant lower computational cost per grid-point compared with a curvilinear, body-shaped grid (Mittal & Iaccarino, 2005*b*). Many IBMs were proposed in the past (a detailed overview can be found in Mittal & Iaccarino (2005*b*)). The main difference between the methods is related with the way in which the aforementioned body force distribution is computed. IBMs can be grouped in two main categories, the continuous and discrete forcing ones. In the first approach the forcing is incorporated into the continuous equations before discretisation, whereas in the second approach the forcing is introduced after the equations are discretised. The method that we will use belongs to the first group (Liu *et al.*, 1995, 1996), and is termed as Reproducing Kernel Particle Method (RKPM) and was developed by Pinelli *et al.* (2010).

Next, we explain how the equations are modified to take into account the presence of an immersed body when using the RKPM approach. Firstly, the surface Γ of the immersed surface delimiting the body is discretised using N markers, called Lagrangian points X. These points, in general, do not correspond with the grid nodes x. The discrete equations are then modified in order to accomplish the presence of the immersed body by introducing the body force distribution, as mentioned above. The surface that delimits the immersed body is discretised with a *Lagrangian grid* using N number markers that, in general, do not conform with the underlying domain grid (*Eulerian grid*). To advance in time the Navier-Stokes equations, firstly, a simple prediction step (Equation 3.24) is performed, without taking into account the presence of the immersed object. To

compute the velocity onto the embedded geometry, $\boldsymbol{U}^*$ an interpolation operator, $\mathcal{I}$, is applied to the surrounding Eulerian grid points with corresponding velocity $\boldsymbol{u}^*$,

$$\boldsymbol{U}^* = \mathcal{I}(\boldsymbol{u}^*) \tag{3.42}$$

The values of $\boldsymbol{U}^*$ are then used to determine a distribution of singular forces along Γ that restore the prescribed boundary values $\boldsymbol{U}^\Gamma$ as,

$$\boldsymbol{F}^* = \frac{\boldsymbol{U}^\Gamma - \boldsymbol{U}^*}{\Delta t} \tag{3.43}$$

The force field defined over Γ is transformed into a body force distribution applied to fluid grid using a convolution operator, C,

$$\boldsymbol{f}^* = C(\boldsymbol{F}^*) \tag{3.44}$$

Then, the prediction step of the momentum equation is repeated adding the computed volume force field as a source term,

$$\frac{\boldsymbol{u}^* - \boldsymbol{u}^n}{\Delta t} = -\mathcal{N}_l\left(\boldsymbol{u}^n, \boldsymbol{u}^{n-1}\right) + \frac{1}{Re}\mathcal{L}\left(\boldsymbol{u}^*, \boldsymbol{u}^n\right) - \mathcal{G}(\phi^n) + \boldsymbol{f}^* \tag{3.45}$$

and a new predicted, non-solenoidal velocity field $\boldsymbol{u}^*$ is computed. Finally, the time advancement step can be completed with the usual solution of the pressure Poisson's equation and the predicted velocity field is projected onto a divergence free space. The given procedure is common to a number of IB methods. The peculiarity of the present method concerns the way in which the operators $\mathcal{I}$ and C are built.

3.6.1 Interpolation and convolution

We use the Reproducing Kernel Particle Method (RKPM) (Liu *et al.*, 1995, 1996; Zhang *et al.*, 2004; Pinelli *et al.*, 2010) to define the interpolation and spreading operators. In this method, the approximation $f_a(x)$ of the value of a given smooth function at point $x \in \Omega$ can be expressed as a *kernel* approximation,

$$f_a(x) = \int_\Omega w_\delta(x - s) f(s) ds \tag{3.46}$$

where w_δ is a non negative kernel function with compact support, and the subscript indicates the dependence of the kernel function on a parameter δ, called dilation

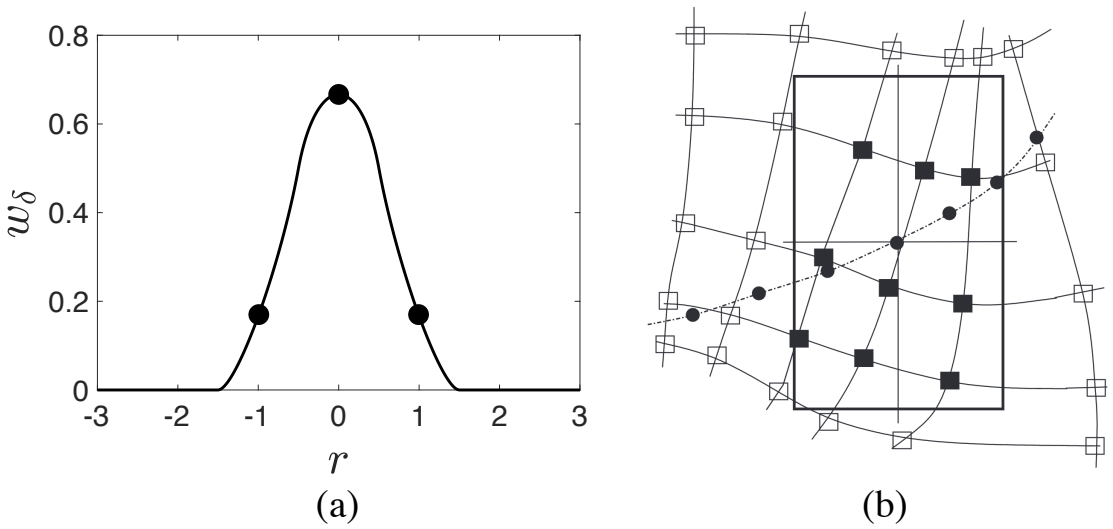


Figure 3.6: (a): Kernel function proposed by Roma *et al.* (1999). (b) Taken from Pinelli *et al.* (2010). The black rectangle is the cage around one of the Lagrangian points, shown as dots. The squares represents grid points, and the black ones are the grid points falling within the cage.

parameter. The latter determines the dimension of the support, Ω_I. Hence, w_δ is non zero only in a sub-domain Ω_I of Ω and zero elsewhere, i.e. in $\Omega_I \backslash \Omega$. It is worth noticing from Equation 3.46 that, if the kernel is the Dirac delta function, then $f_a(x) = f(x)$ and the considered function f is exactly reproduced. Roma *et al.* (1999) proposed a discrete approximation of the kernel function.

$$w_\delta(r) = \begin{cases} \frac{1}{6}\left(5 - 3|r| - \sqrt{-3(1-|r|)^2 + 1}\right) & \text{if } 0.5 \leq |r| \leq 1.5, \\ \frac{1}{3}\left(\frac{1}{3}(1 + \sqrt{-3r^2 + 1}\right), & \text{if } |r|, \\ 0, & \text{otherwise,} \end{cases} \tag{3.47}$$

with $r = (x - s)/\delta$ (see Figure 3.6), that satisfies the following properties.

1. $w_\delta(r)$ is continuous;

2. $w_\delta(r)$=0 if $|r| > 1.5$;

3. $\sum_l w_\delta(r - l) = 1$;

4. $\sum_l (r - l) w_\delta(r - l) = 0$;

5. $\sum_l [w_\delta(r - l)]^2 = 1/2$;

The latter is valid $\forall_r \in \text{Re}$ and $\forall_l \in \mathbb{Z}$. Figure 3.6a shows the function w_δ and its discrete counterpart (represented with dots in the figure), considering $r = 0.0$. The discrete kernel function is not null only for $l = -1, 0, 1$. Since the previous properties involve the natural number l, they can be satisfied by a function interpolated using Equation 3.46 and Equation 3.47 only if the nodes are equi-spaced. To extend this approach to a non-uniform nodes distribution, following Liu *et al.* (1995) and Pinelli *et al.* (2010), we use a modified window function $\tilde{w}_\delta$ defined as,

$$\tilde{w}_\delta(x-s) = \sum_{i=0}^{n} b_i (x-s)^i w_\delta(x-s) \tag{3.48}$$

where b_i, are $n+1$ coefficients determined by imposing the continuous equivalent of properties 3 and 4,

$$\tilde{m}_i(x) = \int_\Omega (x-s)^i \tilde{w}_\delta(x-s) ds = \delta_{i,0} \quad \text{for } i = 0, 1, ...n \tag{3.49}$$

where $\delta_{i,j}$ is the Kronecker's delta. Note that these conditions imply the exact representation of the elements of the canonical polynomial base.$1, x, x^2, ...$ The number n is the higher order of the polynomial that we want to represent exactly. For example, $n = 2$ would lead to an exact representation of all polynomials of degree up to 2. Substituting Equation 3.48 and Equation 3.49, we obtain,

$$\tilde{m}_i(x) = \int_\Omega (x-s)^i \tilde{w}_\delta(x-s) ds = \sum_{j=0}^{n} b_j m_{i+j}(x) = \delta_{i,0} \tag{3.50}$$

for $i = 0, 1, ..., n$, where we have defined,

$$m_i(x) = \int_\Omega (x-s)^i w_\delta(x-s) ds \tag{3.51}$$

The above formulation (i.e., Equation 3.50) form a symmetric linear system $M\vec{b} = \vec{e}_1$, where the right hand side $\vec{e}_1$ is a vector, whose elements are all zeros, except the first one which is equal to 1. From the solution of this linear system (Equation 3.50), we can obtain the coefficients b_i and, finally, we can write the corrected window function (here given for $n = 2$) as,

$$\tilde{w}_\delta(x-s) = [b_o + (x-s)b_1 + (x-s)^2 b_2]\tilde{w}_\delta(x-s) \tag{3.52}$$

The procedure can be extended to higher dimensions, defining the window function as a Cartesian product of the $1D$ kernels. In $2D$, it becomes,

$$w_{\delta,\eta}(x-s, y-t) = w_\delta(x-s)w_\eta(y-t) \tag{3.53}$$

and in 3D,

$$w_{\delta,\eta,\sigma}(x-s, y-t) = w_\delta(x-s)w_\eta(y-t)w_\sigma(z-v) \tag{3.54}$$

where δ, η and σ are the dilation parameters in the coordinate directions. The linear systems to find the coefficients $b_{i,j}$ and $b_{i,j,k}$ are obtained from the following conditions.

$$\tilde{m}_{i,j} = \int_\Omega (x-s)^i (y-t)^j \tilde{w}_{\delta,\eta} ds = \delta_{l,0} \quad \text{for } i, j = 0, 1, ..., n \tag{3.55}$$

in $2D$, where $l = i + j$ and $i + j \leq$, and

$$\tilde{m}_{i,j,k} = \int_\Omega (x-s)^i (z-v)^k \tilde{w}_{\delta,\eta,\sigma} ds = \delta_{l,0} \quad \text{for } i, j, k = 0, 1, ...n \tag{3.56}$$

in $3D$, where $l = i + j + k$ and $i, j, k \leq n$. So, the corrected window functions in $2D$ and $3D$ are,

$$\begin{aligned} \tilde{w}_{\delta,\eta}(x-s, y-t) = [b_{0,0} + (x-s)b_{1,0} + (y-t)b_{0,1} + \\ (x-s)(y-t)b_{1,1} + (x-s)^2 b_{2,0} + (y-t)^2 b_{0,2}] w_{\delta,\eta}(x-s, y-t) \end{aligned} \tag{3.57}$$

and

$$\begin{aligned} \tilde{w}_{\delta,\eta,\sigma}(x-s, y-t, z-v) = [b_{0,0,0} + (x-s)b_{1,0,0} + (y-t)b_{0,1} + \\ (z-v)b_{0,0,1} + (x-s)(y-t)b_{1,1,0} + (y-t)(z-v)b_{0,1,1} + \\ (x-s)(z-v)b_{1,0,1} + (x-s)^2 b_{2,0,0} + (y-t)^2 b_{0,2,0} + \\ (z-v)^2 b_{0,0,2}] w_{\delta,\eta,\sigma}(x-s, y-t, z-v) \end{aligned} \tag{3.58}$$

respectively.

Finally, we briefly describe the implementation of the IBM based on RKPM. Around every node belonging to the Lagrangian lattice, X, we define a cage that contains at least three nodes of the underlying Eulerian mesh in every direction, as shown in Figure 3.6b, whose edges measure 3δ, 3η and 3σ in x, y and z, respectively, as suggested by Equation 3.47. Once the Eulerian nodes that fall within the cage have been identified,

the terms of the moments matrix (the $3D$ version of Equation 3.47) can be numerically evaluated to assemble the local window function, using the mid-point quadrature rule. The coefficients $\vec{b}$ of the correction polynomials are found by solving the symmetric linear system ($M\vec{b} = \vec{e}_1$) for every Lagrangian point. Due to the very low values that the window function may take at the nodes close to the boundary of the cage, the moment matrix may become ill conditioned. This problem is avoided by re-scaling the linear system and solving the equivalent one $HMH^{-1}\vec{b} = \vec{e}_1$, where the diagonal matrix H has the inverse of the dilation factors in the main diagonal. In $3D$, H can be written as,

$$H = \text{diag}\left(1, \frac{1}{\delta}, \frac{1}{\eta}, \frac{1}{\sigma}, \frac{1}{\delta\eta}, \frac{1}{\eta\sigma}, \frac{1}{\delta\sigma}, \frac{1}{\delta^2}, \frac{1}{\eta^2}, \frac{1}{\sigma^2}\right) \tag{3.59}$$

Once the coefficients $\vec{b}$ have been computed, the window function, $\tilde{w}_{\delta\eta\sigma}$, can be used for the interpolation Equation 3.42 and spreading Equation 3.44 operations. In particular, the discrete interpolation, using the midpoint rule, becomes,

$$U_l = \mathcal{I}(u_{i,j,k}) = \sum_{i,j,k \in \Omega_I} \tilde{w}_{\delta,\eta,\sigma}\left(x_{i,j,k} - X_l\right) \Delta V_{i,j,k} \tag{3.60}$$

while the spreading operation reads as,

$$f_{i,j,k} = C(\mathcal{F}_l) = \sum_{l=1}^{N} F_l \tilde{w}_{\delta,\eta,\sigma}\left(x_{i,j,k} - X_l\right) \epsilon_l \tag{3.61}$$

where ϵ_l is a characteristic volume related to the local dilation coefficients of the window function. To determine the correct value of ϵ_l, first, we consider the value of the force on the Lagrangian points, obtained by interpolation,

$$F_l = \sum_{i,j,k \in \Omega_I} f_{i,j,k} f_{i,j,k} \tilde{w_{\delta,\eta,\sigma}}\left(x_{i,j,k} - X_l\right) \Delta V_{i,j,k} \tag{3.62}$$

then, we replace with $f_{i,j,k}$ with Equation 3.61, thus obtaining,

$$F_l = \sum_{i,j,k \in \Omega_I} \left[\sum_{m=1}^{N} F_m \tilde{w}_{\delta,\eta,\sigma}\left(x_{i,j,k} - X_m\right) \epsilon_m\right] \tilde{w}_{\delta,\eta,\sigma}\left(x_{i,j,k} - X_l\right) \Delta V_{i,j,k} \tag{3.63}$$

The linear system of Equations 3.63 can be written, using a matrix notation as,

$$A\text{diag}(\vec{\epsilon})\vec{F} = \vec{F} \tag{3.64}$$

By requiring that $\vec{\epsilon}$ is independent of the actual force distribution, we obtain the constraint det $[A\text{diag}\vec{\epsilon} - I = 0]$, whose solution is found by solving,

$$A\vec{\epsilon} = \vec{I} \tag{3.65}$$

where $\vec{I}$ is a vector of ones. As shown by Pinelli *et al.* (2010), the conditioning of the matrix A depends on the ratios between the distances of the Lagrangian nodes and the local grid size (or slightly higher), the linear system for $\vec{\epsilon}$ is a well conditioned and is easily solved.

3.6.2 Flow over a cylinder

The validation of the RKPM immersed boundary implementation is done by simulating the flow of an incompressible viscous fluid around a circular cylinder, as sketched in Figure 3.8. We introduce the Cartesian coordinate system shown in Figure 3.8. where x and y denote the streamwise and normal coordinates, while u and v denote the respective components of the velocity vector field. On the lower and upper surfaces, we impose the free-slip condition, while the no-penetration and no-slip conditions are imposed on the body surface. On the lower and upper surfaces, we impose the free slip condition, i.e.,

$$\frac{\partial u_i}{\partial y} = 0; \quad v = 0 \tag{3.66}$$

while the no-slip condition is imposed on the body surface. At the inlet, a uniform velocity in the streamwise direction, U_∞ is imposed, while a convective outflow condition, computed using,

$$\frac{\partial \boldsymbol{u}_i}{\partial t} + (\boldsymbol{u}_{old}.\nabla)\boldsymbol{u} = 0 \tag{3.67}$$

where $\boldsymbol{u}_{old}$ is the velocity computed at the previous time-step, is enforced at the outlet. The problem is made dimensionless by using the cylinder diameter as characteristic length,

$$L^* = D \tag{3.68}$$

and the free-stream velocity as characteristic velocity,

$$U^* = U_\infty \tag{3.69}$$

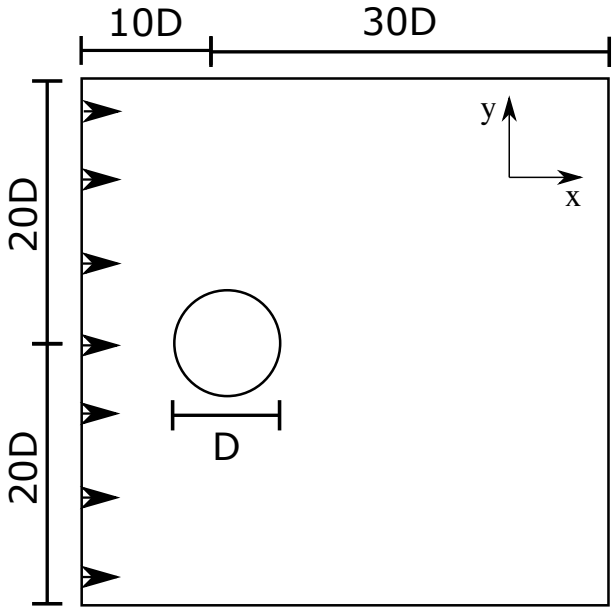


Figure 3.7: Sketch of the computational domain around a cylinder.

Consistently, the Reynolds number is defined as,

$$Re_D = \frac{U_\infty D}{\nu} \tag{3.70}$$

We fixed the Reynolds number based on the diameter to $Re_D = 100$ The simulation is is carried out on a lattice of 700×699 that spans a computational domain of $40D \times 40D$. The centre of the cylinder is at $(x_c, y_c) = (10D, 20D)$ and its surface is discretised with 320 equi-spaced Lagrangian points. In the region inside and surrounding the cylinder, the mesh is uniform with a spacing of $0.0083D$ and stretches towards the boundaries of the domain, as shown in Figure 3.8a. Note that the same figure also illustrates the grid points that are present inside the cylinder. Figure 3.8b reports the values of ϵ (see Equation 3.65) computed for every Lagrangian point. Note that the square root of the average value ϵ is close to the mesh spacing.

Figure 3.9a shows the instantaneous contours of the spanwise vorticity ω_z around the cylinder. At this Reynolds number, the wake of the cylinder is characterised by the von Karman vortex street typical of bluff bodies. Vortices of opposite sign are shed from the cylinder periodically, at a Strouhal number equal to $S_t = f_s D/u_\infty = 0.17$, which is close to the experimental value of $S_t = 0.165$ reported by Williamson (1996). The value was obtained by the spectrum of the instantaneous lift coefficient value,

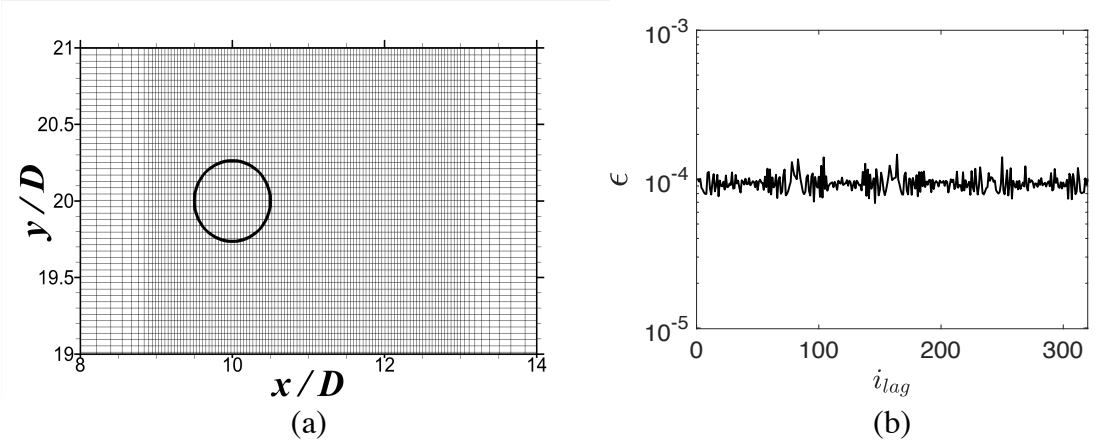


Figure 3.8: (a) Grid in the proximity of the cylinder (computational nodes are plotted with a skip index of 5). (b) The values of ϵ (Equation 3.65) for every Lagrangian point.

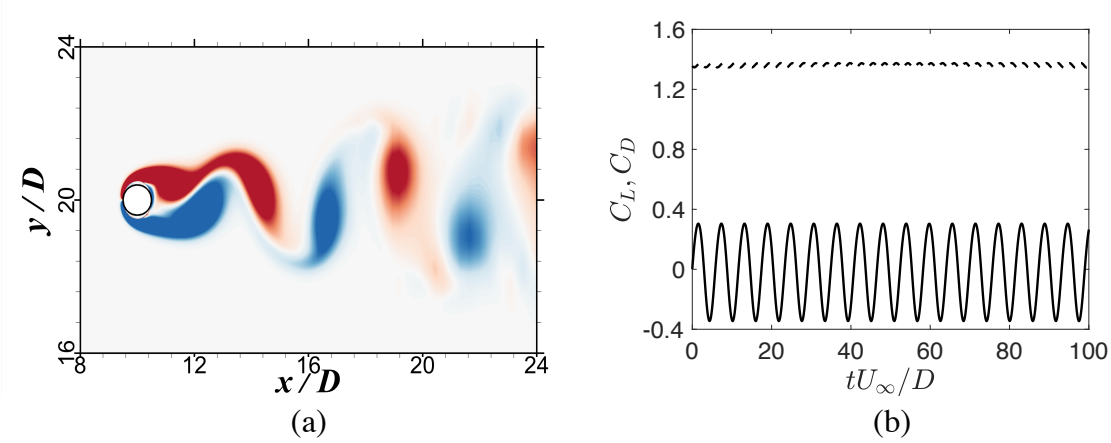


Figure 3.9: (a) Contours of the spanwise vorticity, ω_z. (b) Evolution of the lift C_L (solid line) and drag coefficients C_D (dashed line) over time.

$C_L = 2L/(\rho U_\infty^2 D)$, (where L is the lift per unit length), whose time history is reported in Figure 3.9b with a solid line together with the drag coefficient, $C_D = 2D_r/(\rho U_\infty^2 D)$, (where D_r is the drag per unit length), shown with a dashed line. The mean lift and drag coefficients are $C_L = 0$ and $C_D = 1.35$, respectively. The maximum absolute lift value is $C_L^{max} = 0.35$. These results show good agreement with the ones obtained by Guilmineau & Queutey (2002), who found a mean drag coefficient $C_D = 1.35$ and a maximum lift equal to $C_L^{max} = 0.36$, using an O-type structured grid, with a mesh built using 120 points in the angular direction and 100 points in the radial direction. The first points of the mesh in the fluid are located at $y = 0.001D$ away from the cylinder wall.

Table 3.1 reports the mean drag coefficients C_D and the maximum instantaneous lift

Case	*N*	C_L^{max}	C_D
Ref	-	*0.36*	*1.35*
Cyl-1	*100*	*0.23*	*1.52*
Cyl-2	*144*	*0.28*	*1.48*
Cyl-3	*216*	*0.21*	*1.41*
Cyl-4	*288*	*0.37*	*1.37*
Cyl-5	*320*	*0.36*	*1.35*
Cyl-6	*350*	*0.36*	*1.35*

Table 3.1: Aerodynamic coefficients for the cylinder simulations campaign. The data of the reference case shown in the first row are taken from Guilmineau & Queutey (2002)

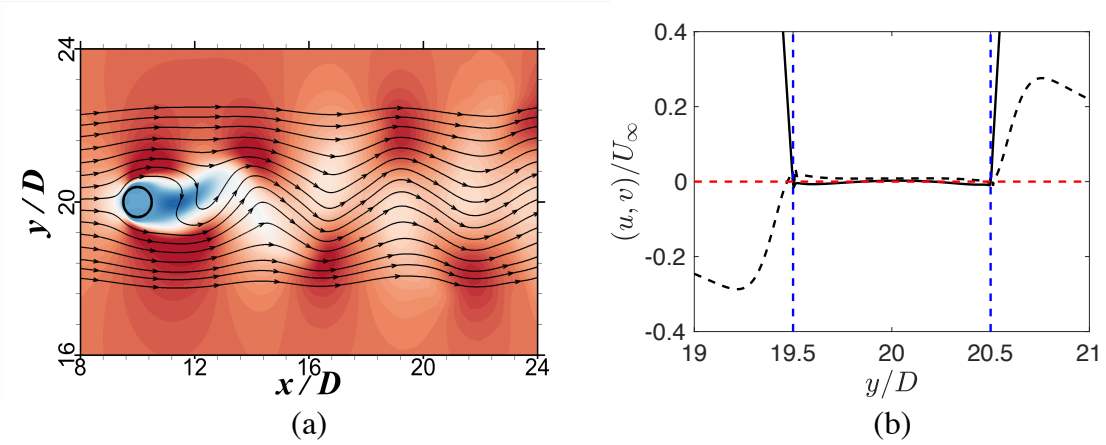


Figure 3.10: (a) Contours of the streamwise velocity u/U_∞. (b) u/U_∞ (solid line) and v/U_∞ (dashed line) velocity profiles at $x = 10D$. The red dashed line represents the zero velocity line, while the blue dashed lines mark the boundaries of the cylinder.

coefficients C_L^{max} obtained from various simulations, changing the number of Lagrangian points used to represent the cylinder surface. We notice that the cases with 320 and 380 points have the same values, meaning that 320 points are enough to correctly represent the solid cylinder at this Reynolds number.

Figure 3.10a shows the contours of the instantaneous streamwise velocity around the cylinder. In Figure 3.10b the u and v velocity profiles on a vertical line passing through the centre of the cylinder at $x = 10D$ are reported using solid and dashed lines, respectively. Both the velocity components have values close to 0, at the cylinder boundary. The symbols represent the points of the mesh, showing the density of the mesh in the cylinder region.

3.7 Flow over a rigid canopy

We now briefly describe the numerical set-up that has been used as a common ground to simulate the flow above an rigid canopy composed of resolved filamentous elements. In order to be able to correctly simulate this flow, avoiding very costly simulations that would have taken very long time, we used a Large Eddy Simulation (LES) approach. The computational cost is lowered by reducing the computational grid that would be necessary to catch the right dissipation induced, for instance, by the wakes behind the canopy elements as the Reynolds number is increased. In order to include this contribution and make sure that the dissipation introduced in the flow field is enough, we need to add an unresolved sub-grid stress tensor to the Navier-Stokes momentum equation. In this section, in particular, we will introduce the closure model used to deal with the sub-grid stress tensor for the LES, the grid and the boundary conditions. Then we turn our attention to the implementation of the numerical techniques described in the preceding sections. Lastly the description of test cases used to verify and to validate the numerical implementation are provided.

3.7.1 Large eddy simulation

Generally speaking, Large Eddy Simulations (LES) are based on the hypothesis that the small-scale turbulent eddies are mainly responsible for dissipating energy when compared to the larger turbulent eddies. In this formulation, the large energy-carrying eddies are fully resolved, while the isotropic small-scale eddies are modelled. This may be an effective strategy since the large eddies are responsible for the majority of the momentum transport and thus the model inaccuracies are less significant when compared with the Reynolds Averaged Navier Stokes (RANS) formulations. Also, the isotropic and homogeneous nature of the small-scale eddies results in a simpler modelling task. The governing equations for the resolved eddies can be derived by applying the filtering operation to the conservation of mass and momentum described in Equation 3.1 and Equation 3.2,

$$\frac{\partial \overline{u}_i}{\partial x_i} = 0 \tag{3.71}$$

$$\frac{\partial \overline{u}_i}{\partial t} + \frac{\partial \overline{u}_i \overline{u}_j}{\partial x_j} = -\frac{\partial P}{\partial x_i} + \frac{1}{Re}\frac{\partial^2 \overline{u}_i}{\partial x_j x_j} - \frac{\partial \tau_{i,j}}{\partial x_j} + f_i \tag{3.72}$$

where x, y and z represent the streamwise, wall-normal, and spanwise directions. The over-bar represents the filtered velocity and $\overline{u}$, $\overline{v}$ and $\overline{w}$ represents the streamwise, wall-normal and spanwise velocity components. Although this approach seems to be advantageous, the non-linear interaction of the turbulent scales prohibits the decoupling of the unresolved and the resolved field. (Leonard, 1975). Thus, the filtered momentum equations have additional stress terms that contain all the contributions from the unresolved eddies. The resulting unresolved stresses, known as the sub-grid scale stresses (SGS) are modelled as,

$$\tau_{i,j} - \frac{\delta_{i,j}}{3}\tau_{k,k} = -2\nu_\tau S_{i,j} \tag{3.73}$$

where $S_{i,j}$ is the resolved strain rate and ν_τ is the eddy viscosity. Generally, the eddy viscosity ν_τ is formulated in terms of the model constant, length scale and velocity scale. In particular, the model length scale is related to the filter width (Δ). The latter is defined as the characteristic length scale of the filtering operations, or equivalently, the turbulence resolution length scale, which characterises the smallest eddy size that is resolved in the formulation (Pope, 2004). The well-known Smargorinsky model is considered the pioneering SGS model for Large Eddy Simulations (Smagorinsky, 1963; Lilly, 1966). In this formulation, the eddy viscosity is defined as $\nu_T = (C_s\Delta)^2|\overline{S}|$ (where C_s is the Smagorinsky model constant, Δ is the filter width that is proportional to the grid size h and $|\overline{S}|$ is the magnitude of the resolved strain rate). Its inception revolutionised the field of LES and has resulted in subsequent SGS models, that employ different strategies (Piomelli *et al.*, 1988, 1991; Piomelli, 1999). For instance, the velocity scale, required by the eddy viscosity formulation is computed by considering a separate transport equation (Yoshizawa, 1982; Ghosal *et al.*, 1995), determining the model constant dynamically (Germano *et al.*, 1991; Germano, 1992)

The filter width (Δ) plays a vital role in modelling the dynamics of the unresolved scales. In most cases, it is a common practice to relate the Δ to the grid size (h), where the filter width is proportional to the grid size (i.e. $\Delta = nh$, where n is the proportionality constant), since the smallest resolved eddy must be larger than the grid size. However,

this choice will have a number of implications. As the grid is refined, Δ decreases and the well-known asymptotic behaviour of the LES approaching DNS is achieved. But this is poor practice since grid refinement also affects the modelling of the unresolved eddies together with the discretisation errors. In most cases, the grid is expected to be refined in regions of high shear, therefore the relationship between the filter width (Δ) and the grid size (h) is not straightforward. In particular, the use of local refinement (sudden variations) leads to aliasing errors associated with the eddy viscosity ν_τ. One way around this problem is to define Δ such it is completely decoupled from the fully resolved grid. In the current thesis, we have adopted the decoupled formulation, known as the Integral Length Scale Approximation (ILSA), that was initially proposed by Piomelli *et al.* (2015). The proposed model defines a new model length scale (L) that is related to the turbulence itself, rather than the grid size, thus Piomelli *et al.* (2015) rephrased the sub-grid scale stresses (SGS) as sub-filter scale (SFS). Thus the closure problem associated with LES is embedded in the SFS stresses, which reads as,

$$\tau^a_{i,j} = \tau_{i,j} - \frac{\delta_{i,j}}{3}\tau_{k,k} = -2\nu_{\mathrm{SFS}}\overline{S}_{i,j} \tag{3.74}$$

where $\overline{S}_{i,j}$ is the resolved strain rate and the ν_{SFS} is the eddy viscosity. In the ILSA model, the eddy viscosity formulation is given as,

$$\nu_{\mathrm{SFS}} = (C_k L)^2 \, |\overline{S}| \tag{3.75}$$

where C_k is the model constant and the L integral length scale. The latter is determined by computing an approximation to the local integral length scale, thus relating the latter to the filter width ($\Delta \propto L$). In particular, the corresponding length scale is determined by $L = \langle \mathcal{K}_{est} \rangle^{3/2} / \varepsilon_{tot}$, (where K_{est} is the turbulent kinetic energy of the resolved scales and the ε_{tot} is the total dissipation). Note that the $\langle . \rangle$ operator represents a spatial averaging operator applied in the homogeneous direction. Both the length scale and the model constant required by the model closure are computed locally and instantaneously, thus eliminating any dependence on the Eulerian grid (Rouhi *et al.*, 2016). This formulation delivers a number of advantages: the LES formulation is now transformed into a physical model for turbulence, it is independent of the errors imposed by the numerical grid,

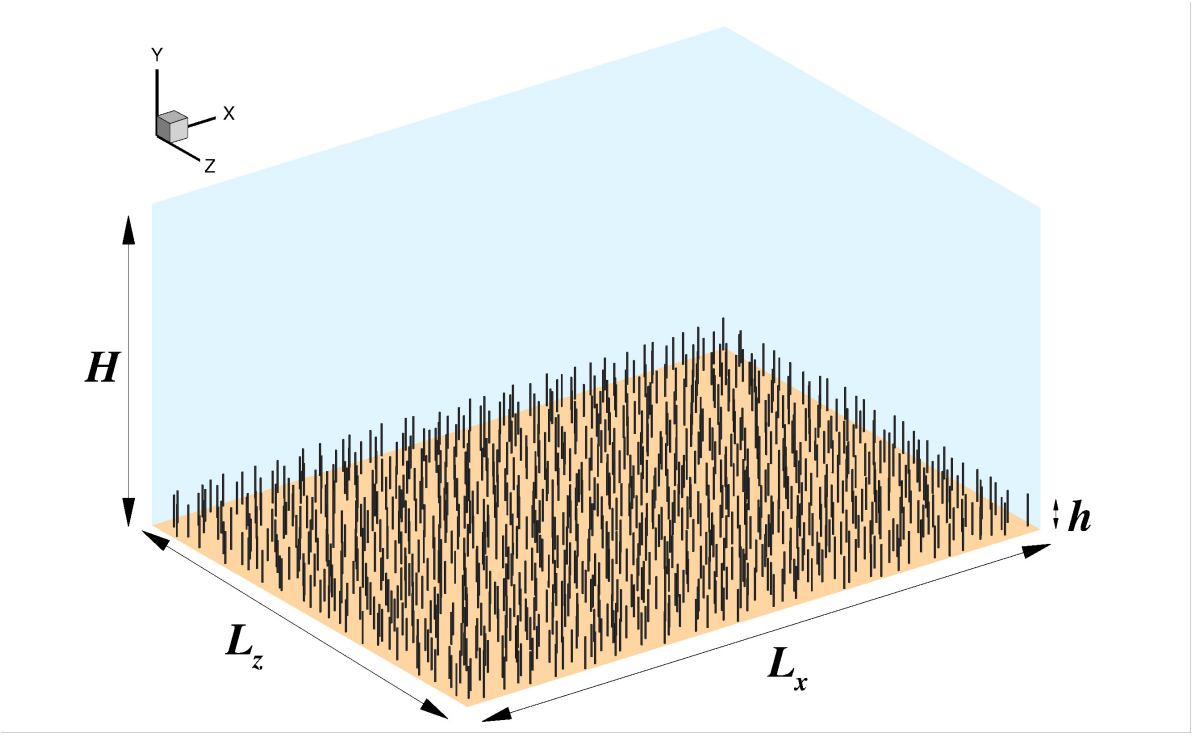


Figure 3.11: Sketch of the computational domain.

and the model constant C_k is computed locally and at each time step. Therefore, the ILSA method is a very robust, adaptable, and inexpensive tool for LES.

3.7.2 Numerical setup

We consider an incompressible three-dimensional unsteady flow field in an open-channel that develops above a rigid canopy composed of slender and cylindrical filaments that are flush mounted perpendicular to an impermeable wall. The domain in a Cartesian frame of reference would corresponds to x_1, x_2 and x_3 (u_1, u_2 and u_3) the streamwise, wall-normal and spanwise directions (velocities), respectively, also referred to x, y and z (u, v and w). The flow in all the studied configurations is driven by a uniform pressure gradient along the streamwise direction, which maintains a bulk velocity, that reads as,

$$U_b = \frac{1}{H}\int_0^H \langle u \rangle dy \tag{3.76}$$

This essentially keeps the desired, Reynolds number based on the open channel height (H) and bulk velocity, at $Re_b = U_b H/\nu = 6000$, where ν is the kinematic viscosity.

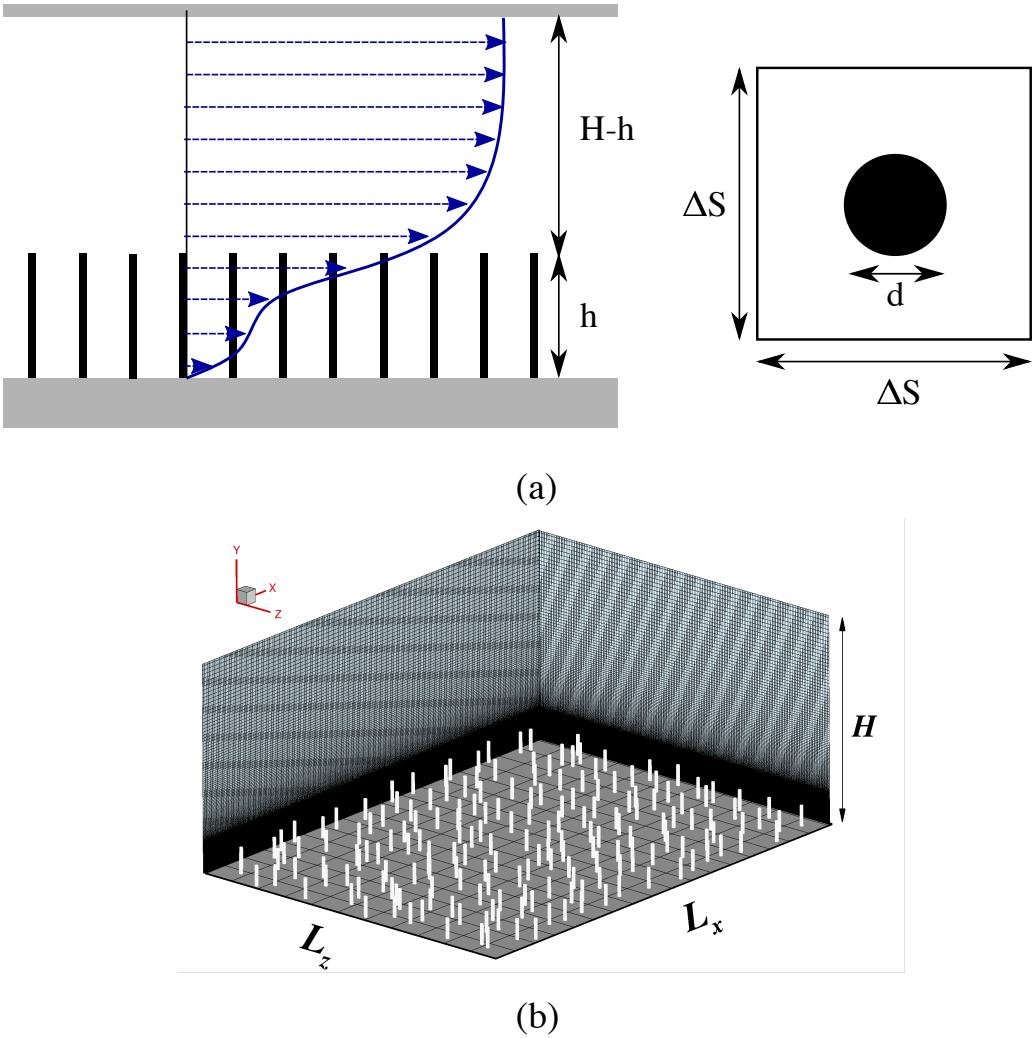


Figure 3.12: (a) Geometrical parameters that characterises an idealised canopy composed of cylindrical filaments according to Nepf (2012). The velocity profile (given in blue) corresponds to a typical dense canopy regime (Monti *et al.*, 2020) (b) The mesh employed in the current investigation with emphasis in the wall-normal direction.

The computational domain is meshed with uniform spacing in the homogeneous directions and with a stretched grid in a wall-normal direction to capture the right shear in the region of a very high-velocity gradient (see Figure 3.12b). The canopy elements are resolved directly by introducing a set of rigid and solid filaments of finite cross-section, related to the local grid size, which is placed perpendicularly to the horizontal wall. To impose the boundary conditions that each rigid filament exerts on the fluid (i.e., zero velocity) we have used the IBM described in §3.6. Each filament has a finite, circular cross-sectional area and is discretised using a set of Lagrangian nodes distributed along the filament in the wall-normal direction. The nodes discretising the

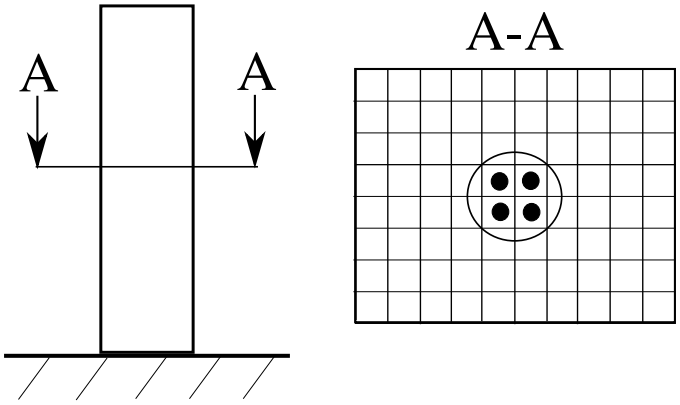


Figure 3.13: Filament cross section representation with RKPM method using four Lagrangian nodes.

filament do not need to conform to the underlying Eulerian grid. More specifically, a compact support defining the cross-sectional size of each rod is centred around each Lagrangian node and the body force required to enforce the Dirichlet type boundary condition is computed and spread on each support as a part of the time-advancing scheme (Pinelli *et al.*, 2010). The dimension of this compact support depends on the local grid size and defines the hydrodynamic thickness (i.e., the diameter) of the filament. In the current numerical set-up, using a uniform grid in the wall parallel directions, the thickness of each filament is estimated to be of about $d \approx 2.2\Delta x_i$ (Δx_i being the grid size in the streamwise and spanwise directions). Further details on the adopted IBM, its properties and implementation are extensively described and discussed for various flow configurations in Pinelli *et al.* (2010) and Favier *et al.* (2014), while the IBM assessment in the context of canopy flows, including its calibration of the support cage required to deliver the desired resolution and its extensive validation campaign with respect to canonical Direct Forcing (DF) methods (Fadlun *et al.*, 2000), is described and discussed in Monti *et al.* (2019).

The domain has been segregated into tiles of area ΔS^2 and a single filament has been placed in each tile, following a random distribution. The tile size (ΔS) and the filament height (h) have been chosen in order to design the required canopy configuration, which is ultimately, based on the solidity $\lambda = dh/\Delta S^2$ (Nepf, 2012) (see Figure 3.12a). The random assignment of the filament on each tile has been selected in order to avoid the

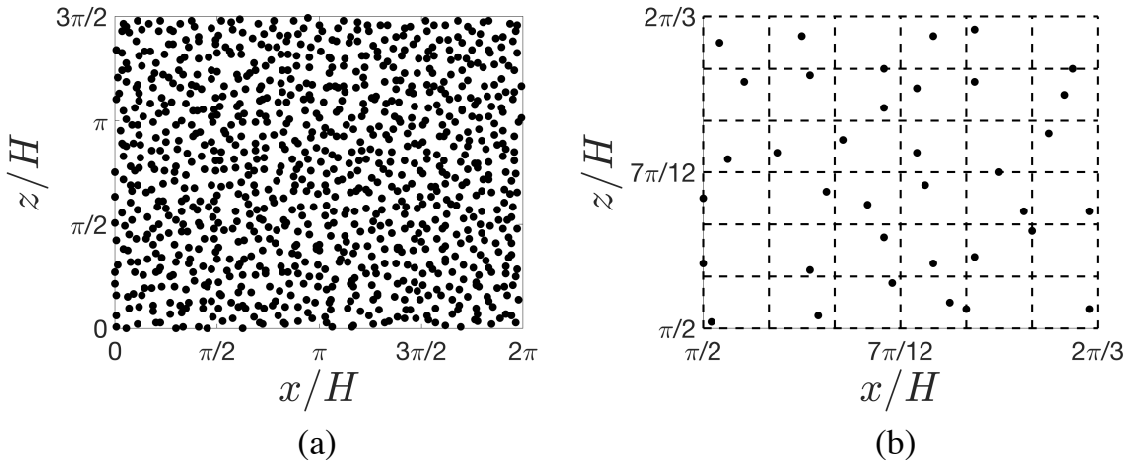


Figure 3.14: (a) Computational domain with the filaments distribution: wall-parallel view. (b) random allocation of each filament into its own tile of size $\Delta S \times \Delta S$ is highlighted.

introduction of any particular momentum increase or decrease into the canopy layer due to the blockage effect introduced by the filaments.

The simulations have been carried out on a periodic box in the streamwise (x) and spanwise (z) directions. The choice of selecting a streamwise periodic condition has been motivated by the experiments of Ghisalberti & Nepf (2004). Although they observed the presence of a mixing layer developing at the canopy edge, they also suggested that its thickness was independent of the streamwise location, meeting the conditions required by periodic boundaries. At the bottom wall, a no-slip boundary condition is imposed while a free-slip condition is set at the top surface (see Equation 3.66).

3.7.3 Validation case

While the baseline Navier-Stokes solver was extensively validated in the past (Omidyeganeh & Piomelli, 2011, 2013*a*,*b*; Rosti *et al.*, 2016), its combination with a filamentous surface requires further attention. The IBM on its own has been validated by Pinelli *et al.* (2010), and its coupling with the baselines code SUSA has been reported in previous studies (Pinelli *et al.*, 2017; Rosti *et al.*, 2018*b*; Monti *et al.*, 2019, 2020). In particular, the implementation of the adopted IBM in the context of canopy flows was validated by Monti *et al.* (2019). The authors compared the numerical predictions of the overall methodology with the experimental measurements of Shimizu *et al.* (1991). The

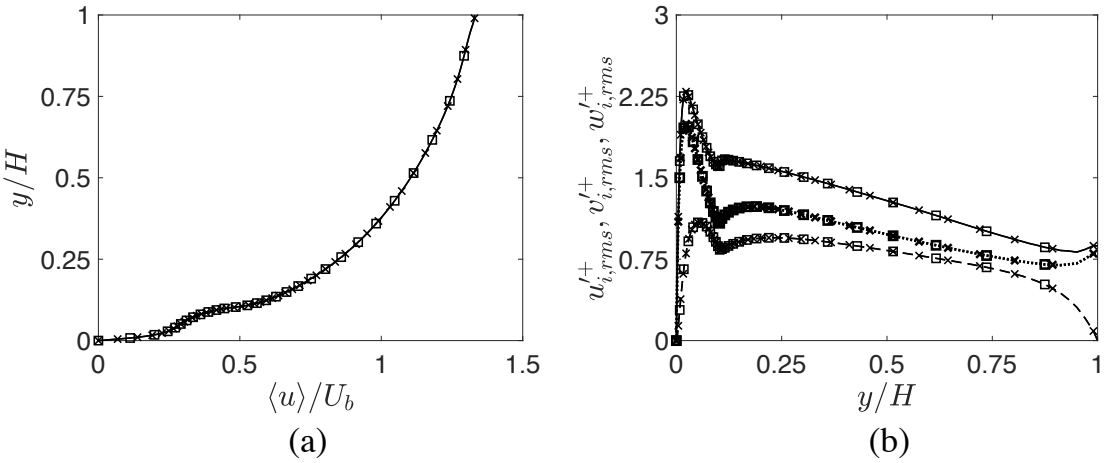


Figure 3.15: (a) Mean velocity profile normalised by the outer flow units (i.e., open channel height H and bulk velocity U_b). (b) r.m.s of the velocity fluctuations re-scaled by the local friction velocity, as a function of the wall normal distance. The square symbol represents the profiles extracted from Monti *et al.* (2020) for the configuration $\lambda = 0.14$, while the x symbols represents the profiles obtained in the current thesis for the same nominal solidity.

comparison between the statistics measured in a rigid canopy and the actual predictions presented a good agreement. In the current thesis, we have implemented a new numerical treatment of IBM. In particular, IBM has been distributed locally, which is now capable of handling a large number of immersed objects. This approach requires further validation.

To verify the validity of the implemented technique, we have considered the transitional configuration ($\lambda = 0.14$) of Monti *et al.* (2020). The considered canopy is composed of cylindrical filaments that are flush mounted perpendicular to the bottom wall. The filaments are characterised by height $h/H = 0.1$ and spacing $\Delta S/H = 0.13$, and are distributed on the impermeable wall following the random assignment defined in the previous subsection. The selected mesh, which is homogenous in the wall parallel directions, allows us to define the same hydrodynamic thickness of the filament (i.e., $d \approx 2.2\Delta x$). The simulations have been carried out, by considering a domain that matches the one considered by Monti *et al.* (2020), with $L_x/H = 2\pi$, $L_y/H = 1$ and $L_z/H = 1.5\pi$ denoting the streamwise, wall-normal and spanwise lengths of the domain. The computational box has been treated with the same boundary conditions highlighted in the previous subsection. Concerning the features of the numerical grid, we have employed a stretched distribution based on a tangent hyperbolic function in the wall-

normal direction. The resolution of the selected mesh based on the outer flow units (i.e., friction velocity computed at the outer flow origin $u_{\tau,o}$) is given as $\Delta x^+ = 8.2$, $\Delta z^+ = 8.2$, $\Delta y_w^+ = 0.38$ and $\Delta y_c^+ = 0.38$, where Δy_w and Δy_c are wall normal spacing at the wall and at the edge of the canopy. These values satisfy the standard DNS thresholds (Kim *et al.*, 1987; Lee & Moser, 2015*a*). A uniform pressure gradient in a streamwise direction is evaluated at each time step and is used to drive the flow. The pressure gradient in turn maintains the bulk Reynolds number at $Re_b = U_b H/\nu = 6000$.

Figure 3.15 presents the numerical predictions of the current methodology and the results obtained from Monti *et al.* (2020). In particular, the mean velocity profiles (see Figure 3.15a) scaled with the outer flows units (i.e., open channel height H and bulk velocity U_b) illustrate an excellent collapse. The r.m.s of the velocity fluctuations have been made non-dimensional by considering a local friction velocity formulation $u_{\tau,l} = \sqrt{\nu \partial_y \langle U \rangle - \langle u'v' \rangle}$. The choice of which, will be discussed in the subsequent sections. The scaled profiles reveal a good agreement.

4

Numerical investigation of regime transition in canopy flows

Contents

4.1 Introduction **63**
4.2 Numerical Setup **64**
4.3 Results and Discussion **67**
4.4 Concluding Remarks **81**

4.1 Introduction

Thus far, the majority of the work accumulated on canopy flows has been limited to experiments (Poggi *et al.*, 2004*b*; Ghisalberti & Nepf, 2009) and few simplified simulations based on a homogenised drag model (Cui & Neary, 2008; Zampogna & Bottaro, 2016). However, the recent increase in computational power and the availability of novel immersed boundary formulations, have provided the framework for the insurgence of high fidelity canopy flow simulations (Monti *et al.*, 2019; Sharma & García-Mayoral, 2020*a*). In the used formulations, the authors by enforcing the boundary condition on every single filament, were able to capture the essential dynamics of the flow that develops within the canopy layer and shed some light on the physics mechanisms that

emerge on the onset of the different flow regimes. Although some promising results were obtained, this still remains an open area of research, with the available literature covering a limited number of configurations. In particular, the so called *transitional regime* that exists in between the two asymptotic regimes (i.e., sparse and dense) (Nepf, 2012) remains an unchartered territory, as the flow field is characterised by a complex transition from a rough-wall like behaviour to canonical mixing layer flows. Furthermore the interplay between the various localised layers that exist within the canopy and their thicknesses in the transitional regime still need complete characterisations.

In this chapter we have conducted a series of highly resolved simulations of open-channel turbulent flows, where the bottom impermeable wall is covered by a canopy of cylindrical rigid filaments. The boundary condition (zero velocity) was enforced on every single filament with the aid of a state of the art immersed boundary formulation. Different to the previous work by Monti *et al.* (2020), the selected configurations shares the same level of submergence (i.e., $H/h = 10$) and have been obtained by modulating the average distance between adjacent filaments (ΔS) (i.e. the filaments density), such that the corresponding value of λ nominally falls in the transitional regime.

4.2 Numerical Setup

The solver tackles the LES governing Equations 3.73 and 3.74, using a second order accurate, cell centred finite volume approach described in section 3.7.1. The domain has been divided into tiles of area ΔS^2 and every single filament has been placed with a random uniform distribution in every tile. The mean filament spacing and the height can be set to match any wanted solidity value (λ), thus selecting different nominal regimes of the canopy flow. In the present study, we focus on the transitional regime and the values of λ corresponding to the two canopies were obtained by maintaining a constant filament height (h) and diameter (d), whilst modulating the in-plane solidity (ΔS) to match the transitional criterion $\lambda \approx 0.15$ and $\Delta S/h \simeq 1$ (Monti *et al.*, 2020). The chosen ΔS values lead to two canopy configurations corresponding to $\lambda \in [0.14, 0.25]$ and $\Delta S/h \in [1.31, 0.98]$ (see Table 4.1). As mentioned, the zero velocity condition is enforced stem-by-stem using an Immersed Boundary formulation (IBM) described in (Pinelli *et al.*,

Configuration	λ	$\Delta S/h$	$n_i \times n_k$	$\Delta S/H$	$Re_{\tau,o}$	Δx^+, Δz^+	Δy_w^+	Δy_c^+
T. Sparse (TS)	*0.14*	*1.31*	48×36	$\pi/24$	*730*	*7.5*	*0.34*	*0.34*
T. Dense (TD)	*0.25*	*0.98*	64×48	$\pi/32$	*754*	*8.2*	*0.38*	*0.38*

TS - Transitionally sparse, TD - Transitionally dense, λ is the solidity; $\Delta S/h$ is known as the aspect ratio; $n_i \times n_k$ is the stem density, where n_i and n_k are the number of filament rows in the streamwise and spanwise directions, respectively; Re_τ is the friction Reynolds number based on the friction velocity ($u_{\tau,o}$) computed at the virtual origin. The grid resolution in the streamwise and spanwise directions are denoted by Δx^+ and Δz^+, respectively. The wall normal resolution of the numerical grid in the region near the impermeable wall and canopy top are denoted in Δy_w^+ and Δy_c^+

Table 4.1: Simulation parameters considered in the current investigation

2010). Each filament has a finite, circular cross-sectional area and is discretised using a set of Lagrangian nodes distributed along the filament in the wall-normal direction. The nodes discretising the filament do not need to conform to the underlying Eulerian grid. More specifically, a compact support defining the cross-sectional size of each rod is centred around each Lagrangian node and the body force required to enforce the Dirichlet type boundary condition is computed and spread on each support as a part of the time advancing scheme (Pinelli *et al.*, 2010). The dimension of this compact support depends on the local grid size and defines the hydrodynamic thickness (i.e., the diameter) of the filament. In the current numerical set-up, using a uniform grid in the wall parallel directions, the thickness of each filament is estimated to be of about $d \approx 2.2\Delta x_i$ (Δx_i being the grid size in the streamwise and spanwise directions) (Monti *et al.*, 2019). Concerning the distribution of the filaments in the canopy substrate, we have used a tiled approach, in which the bottom impermeable wall is meshed into square tiles of size $\Delta S/H$. Each tile holds a single filament, and its local position on each individual tile is assigned randomly according to a uniform probability distribution. This approach prevents the introduction of specific patterns that may promote flow channelling effects within the voids between neighbouring filaments.

Concerning the overall LES filter operator, the adopted ILSA model enables the computation of a dynamic yet localised eddy viscosity. In this condition, the external flow in the region outside the canopy can be considered as a coarse Direct Numerical Simulation (DNS) that progressively becomes highly resolved when approaching the

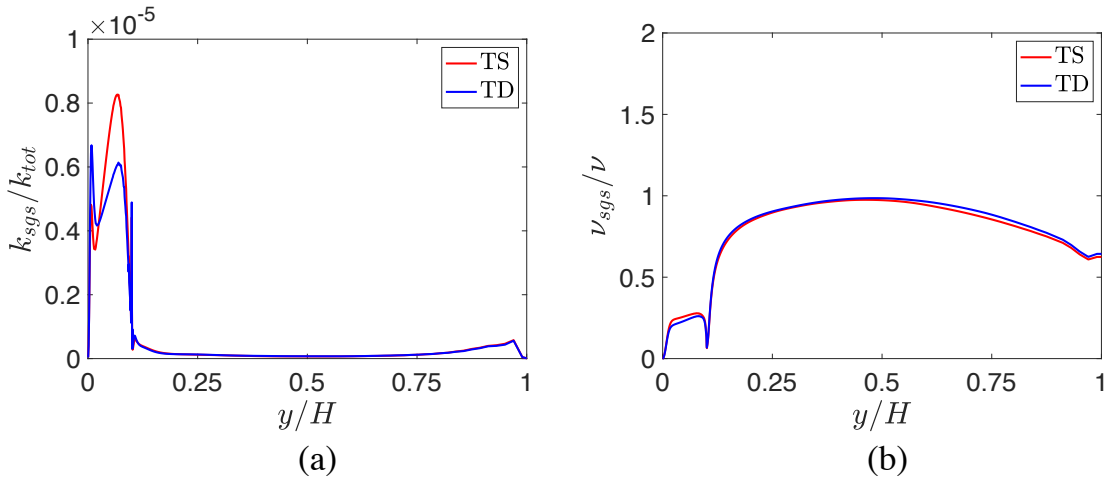


Figure 4.1: (a) Ratio of the sub-grid scale energy to the total fluctuating energy as a function of the wall normal direction (b) Ratio between eddy viscosity and the physical viscosity along the wall normal direction. The parameters have been averaged both in space (i.e., homogenous directions) and time.

canopy layer. In particular, the primary role played by the sub-grid scale stresses in the outer region is limited to a very mild and stabilising numerical dissipation (Monti *et al.*, 2020). Figure 4.1a illustrates the ratio between the sub-grid scale and total energies averaged in time and the wall-parallel directions, as a function of the wall-normal direction. It is evident that this ratio is always below 10^{-5} for all the canopy configurations considered in the current investigation. Further insight into the LES filter activity can be obtained by inspecting Figure 4.1b, which presents the ratio between the eddy viscosity and the physical one as a function of the wall-normal distance. The parameter averaged both in space and time, is always less than one (< 1) for the whole domain, illustrating clearly that the LES filter operates at the end of the turbulence cascade. This *posterior* analysis suggests that any adjustments associated with the coupling between the LES and the IBM can be negated.

The two canopy simulations share the same computational box, with the streamwise length, open channel depth H and spanwise width corresponding to $L_x/H = 2\pi$, $L_y/H = 1$ and $L_z/H = 1.5\pi$, respectively. To mimic an open channel, we have enforced no slip (i.e., zero velocity) and a freeslip (i.e., $\partial_y u = \partial_y w = 0, v = 0$) conditions on the bottom wall and on the top surface, respectively. The homogeneous directions (i.e., streamwise and spanwise) are treated with periodic boundary conditions. Concerning the features

of the numerical grid, we have employed a stretched distribution based on a tangent hyperbolic function in the wall-normal direction. At every time step, a uniform pressure gradient is modulated, such that a constant, time-independent volumetric flow rate is attained, which corresponds to the bulk Reynolds number of $Re_b = U_b H/\nu = 6000$. This choice aligns with other numerical (Monti *et al.*, 2020) and experimental (Ghisalberti & Nepf, 2004) investigations. The numerical grid resolution of all the cases, based on the outer friction scales (i.e. friction velocity computed at the virtual origin of the outer flow) satisfies the standard DNS thresholds (i.e., $\Delta x^+ = \Delta z^+ \leq 9, \Delta y^+ \leq 0.4$). Moreover, the adequacy of the grid has been assessed using a preliminary grid convergence study discussed in (Monti *et al.*, 2020).

4.3 Results and Discussion

In this section, we present the results obtained from statistically converged simulations of the two considered TS and TD canopy configurations. All the figures incorporate results from both canopy configurations: TS results are represented by red lines, while TD cases are represented by blue lines. For comparison, we have also incorporated the results of the canonical smooth wall turbulent channel flow at $Re_\tau = 950$ (Hoyas & Jiménez, 2008), which are shown in black.

We start to review the results by considering the mean velocity distribution scaled with the open channel height (H) and the bulk velocity ($U_b = \frac{1}{H}\int_0^H \langle U \rangle dy$, where the $\langle . \rangle$, is an operator indicating averaging in both time and homogenous directions). The distributions in Figure 4.2, clearly exhibit the existence of two inflectional points, located at the canopy edge (outer) and within the canopy layer (inner), with the location of the latter highly dependent on the actual canopy flow regime (Monti *et al.*, 2020). The outermost inflectional point is induced by the abrupt discontinuity of the drag force at the canopy tip, whilst the internal one is a result of the merging of the mean flow developing by the wall with the velocity distribution underneath the canopy tip (Monti *et al.*, 2019). The mean locations of the two inflectional points can be estimated by considering the mean momentum balance in the streamwise direction.

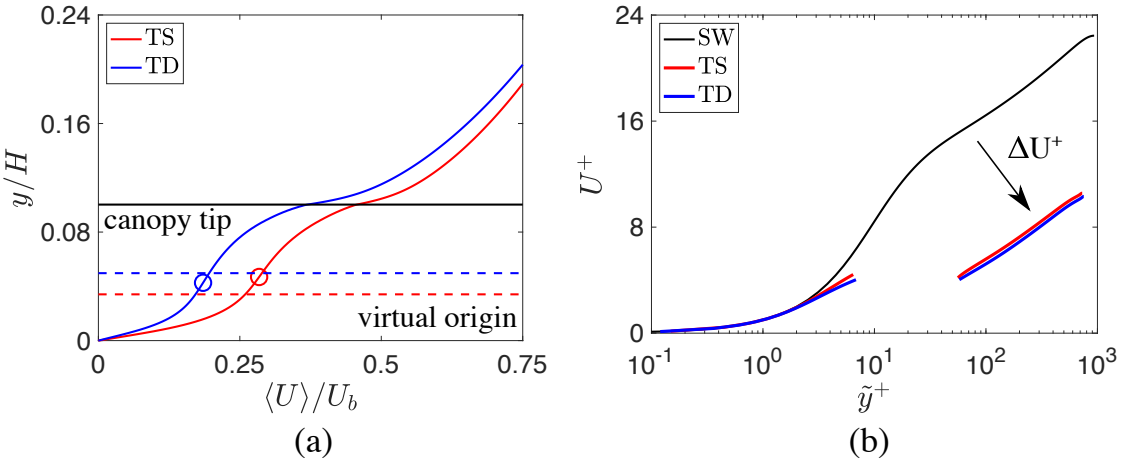


Figure 4.2: Mean velocity profiles (a) in terms of the outer flow units (i.e., H and U_b). The circle symbols presents the mean locations of the internal inflection point and dashed lines represents the virtual origin. The black horizontal line represents the canopy height (h), while the dashed lines represents the position of the virtual origin (see text for definition) (b) in terms of the wall units. The $\tilde{y}^+$ represents the wall normal coordinates made non-dimensional with the inner and outer wall units, based on their origin. See text for colour-band and description on the virtual origin

$$\frac{1}{Re_b}\frac{\partial^2\langle U\rangle}{\partial y^2} = \frac{\partial P}{\partial x} + \frac{\partial\langle u'v'\rangle}{\partial y} + \langle F_D\rangle \tag{4.1}$$

The first three terms in Equation 4.1, represent the mean viscous force, mean streamwise pressure gradient and the mean Reynolds shear stress, respectively. The last term represents the contribution of the overall mean drag imposed by the individual filaments of the canopy. In particular, the mean wall-normal location of the inflection points is determined when $\partial^2\langle U\rangle/\partial y^2 = 0$ is satisfied. Their positions within the canopy are represented by the circles in Figure 4.2a.

The internal and external boundary layers are illustrated in Figure 4.2b. To characterise the inner flow, we use the friction velocity $u_{\tau,in} = \sqrt{\tau_w/\rho}$, based on the wall shear stress at the canopy bed. The profiles exhibit behaviour that matches the typical velocity profile of a canonical turbulent channel flow (Hoyas & Jiménez, 2008). However, this is only limited to the viscous sub-layer, where the skin frictional drag dominates the drag imposed by the filaments (Monti *et al.*, 2020). Moving away from the wall, we observe the modification of the buffer layer generated by the presence of the stems. In particular, this region is dominated by the filament-induced, meandering motion and

the alternating upwash and downwash movements driven by the outer flow. In the tip region, we define an external friction velocity based on the total stress evaluated at the virtual origin (y_{vo}). This can be interpreted as the virtual location of an abstract wall seen by the outer turbulent boundary layer that develops above the canopy, which is assumed to obey the "displaced" logarithmic law (Jiménez, 2004). We compute the wall-normal position of y_{vo} implicitly, by enforcing the canonical velocity log law on the outer layer mean velocity profile,

$$\frac{\langle U \rangle}{u_{\tau,o}} = \frac{1}{\kappa} log\left(\frac{(y - y_{vo})u_{\tau,o}}{\nu}\right) + B - \Delta U^{+} \tag{4.2}$$

where $y - y_{vo}$ is the shifted wall normal coordinates for the outer flow. $u^2_{\tau,o} = \nu \partial_y U_{vo} - u'v'_{vo}$ is the outer (global) friction velocity computed at the virtual origin, κ is the von Kármán constant here set at 0.41 and B is the intercept in a smooth wall configuration. Figure 4.2b reveals a standard turbulent boundary layer logarithmic profile, with a downward shift (ΔU^{+}), suggesting that the canopy exhibits a rough-wall-like behaviour for the outer flow. In the context of rough wall boundary layers, the term ΔU^{+} is often, termed as the roughness function (Hama, 1954). The universality of the logarithmic layer has been previously reported by other authors (Mizuno & Jiménez, 2013; Kwon & Jiménez, 2021). In particular, Kwon & Jiménez (2021), conducted a novel experiment by isolating the multi-scale dynamics of the logarithmic region, which showed a robust and uniform behaviour of the flow structure regardless of the imposed manipulations.

The features of the mean velocity profile and their locations within the canopy, allow us to identify three localised layers: an inner layer, developing between the canopy bed and the inner inflection point; an outer layer spanning the region from the canopy tip down to the position of the virtual origin and lastly, an overlap region sandwiched in-between them. The latter is home to complex interactions between the internal and external boundary layers. The existence of the overlap region depends on the actual canopy regime. In the TS configuration, the virtual origin has penetrated the inner layer (i.e., below the internal inflection point), resulting in the absence of an overlap layer, indicating a strong interaction between the inner and outer layers. However, the virtual origin of the TD configuration has moved away from the canopy bed and is located just

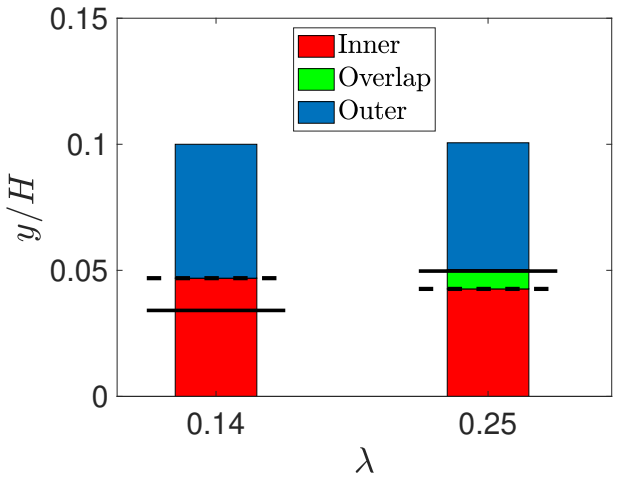


Figure 4.3: Mean locations of the mean velocity features, revealing the extent of the localised layers embedded within the canopy. The dashed and solid horizontal line.

above the inner inflectional point. The location of the latter, in turn, has moved towards the wall, when compared with the TS case, thereby inducing an overlap layer of marginal thickness. Moreover, decreasing the mean filament spacing (ΔS) below the value used for the TD configuration may result in an increase in the thickness of the overlap layer. However, this would represent the inception of a dense canopy flow regime, which is beyond the scope of the current study. From Figure 4.2a and 4.3, it is evident that the mutual signed distance between the two points has a zero in between the TS and TD configurations (i.e., $0.14 < \lambda < 0.25$). By performing a simple linear interpolation, we find that zero corresponds to $\lambda = 0.21$, which is close to the value identified as a possible criterion to establish the inception of the dense regime (Monti *et al.*, 2020). It should be noted that the proposed classification is associated with pressure-driven flows and may not be applicable to canopy flows that concerns with zero-pressure gradient boundary layers, which is outside the scope of the current work (Zhang *et al.*, 2022).

Figure 4.4, presents the diagonal Reynolds stress distributions, made non-dimensional with the outer friction velocity ($u_{\tau,o}$), as a function of the wall-normal distance scaled with the open channel height (H). Away from the canopy, the stress profiles resemble the canonical smooth wall turbulent channel, confirming the outer layer similarity (Townsend, 1976). Overall a good collapse can be observed, apart from the region close to the upper boundary $y/H = 1$, where the differences between an open vs full

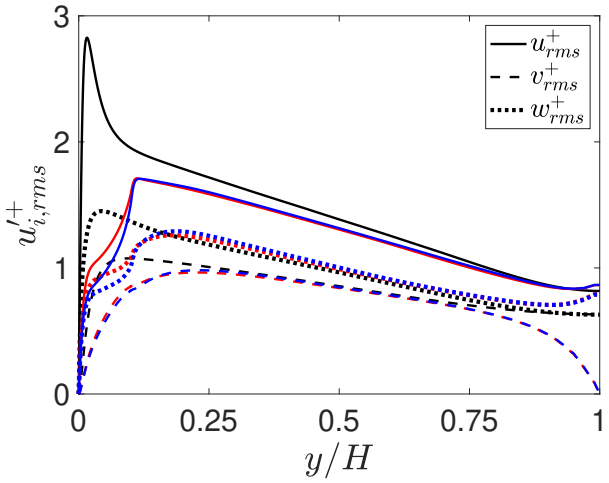


Figure 4.4: Velocity fluctuations distributions made non-dimensional with the outer friction velocity ($u_{\tau,o}$). The solid, dashed and dotted lines represents the streamwise, wall normal and spanwise components. See text for colour-band.

channel persist. This behaviour was similarly reported by Scotti (2006) where the authors analysed turbulent open channel flows developing over transitionally rough surfaces. However, deep inside the canopy, we observe a behaviour highly dependent on the selected canopy configuration. In particular, the streamwise and spanwise components have been dampened by the increased filament number density, while the wall-normal components remain unaffected. Nevertheless, both configurations share the same outer peak intensity for all three components. This indicates there is a need for better scaling in the inner region of the canopy, which would enable us to make a direct comparison of the velocity r.m.s fluctuations. To this end, we consider the integral form of the mean momentum balance (see Equation 4.1) from an arbitrary y location up to the free shear surface of the open channel (i.e., $y = H$).

$$\left(1 - \frac{y}{H}\right)\left|\frac{\partial P}{\partial x}\right| H = \mu \frac{\partial \langle U \rangle}{\partial y} - \langle u'v' \rangle - \int_y^H \langle F_D \rangle \tag{4.3}$$

where $\left|\frac{\partial P}{\partial x}\right|$ represents the absolute value of the mean pressure gradient used to drive flow at a constant flow rate. If the lower limit of the integral is replaced by the location of the canopy bed (i.e., $y = 0$), the balance equation reads as,

$$\left|\frac{\partial P}{\partial x}\right| H = \tau_w + \int_0^H \langle F_D \rangle \tag{4.4}$$

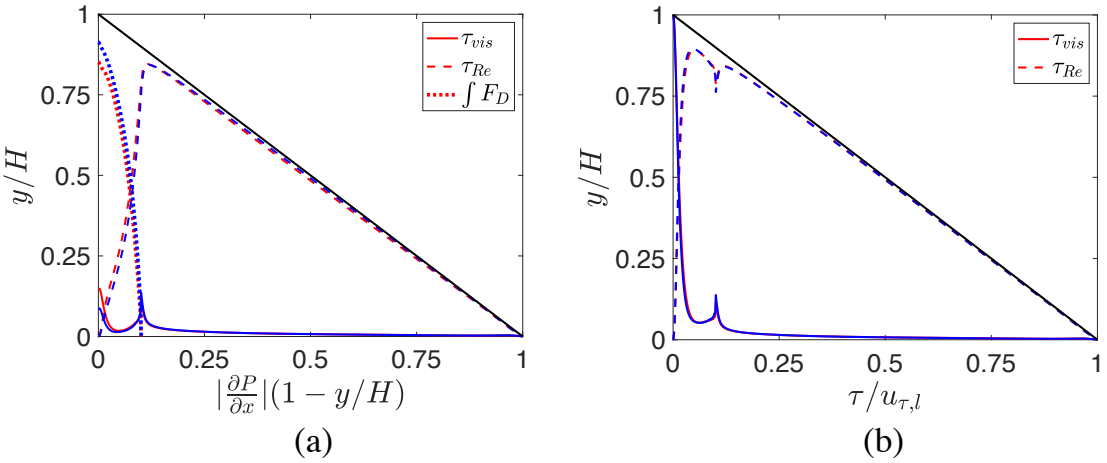


Figure 4.5: (a) Mean momentum balance, with solid, dashed, and dotted lines representing the viscous, Reynolds stress, and the cumulative drag contributions. The solid black line represents the norm of the average pressure gradient. (b) Viscous and Reynolds stresses re-scaled with the local friction velocity $u_{\tau,l}$.

where τ_w is the wall shear stress and $\int_0^H \langle F_D \rangle$ is the cumulative drag contribution and the left-hand-side term represents the norm of the mean pressure gradient. The respective contributions of all the terms appearing in the balance Equation 4.3 are reported in Figure 4.5a. Outside the canopy, the cumulative drag term is zero and the distributions of the viscous and Reynolds stress contributions are similar to those of a smooth wall. Recently, Monti *et al.* (2019) and Sharma & García-Mayoral (2020*a*) studied mildly dense and sparse canopies, respectively observing that the scale of the turbulent fluctuations well with the local total stress, defined as the sum of the viscous and Reynolds stresses. In the current framework, we aim to extend this scaling argument to canopies that fall in the transitional regime, by defining a local friction velocity scale based on the total stresses as,

$$u_{\tau,l} = \sqrt{\frac{H}{H-y}\tau(y)} = \sqrt{\frac{\mu\partial_y\langle U\rangle - \langle u'v'\rangle}{1-y/H}} \tag{4.5}$$

This local scaling yields a non-dimensional linear variation of the total stress when scaled with the local friction velocity. The local friction velocity formulation has also been quite successful in the context of artificially manipulated shear flows, although the total stress did not exhibit a linear variation with the wall-normal direction (Jiménez, 2013; Tuerke & Jiménez, 2013).

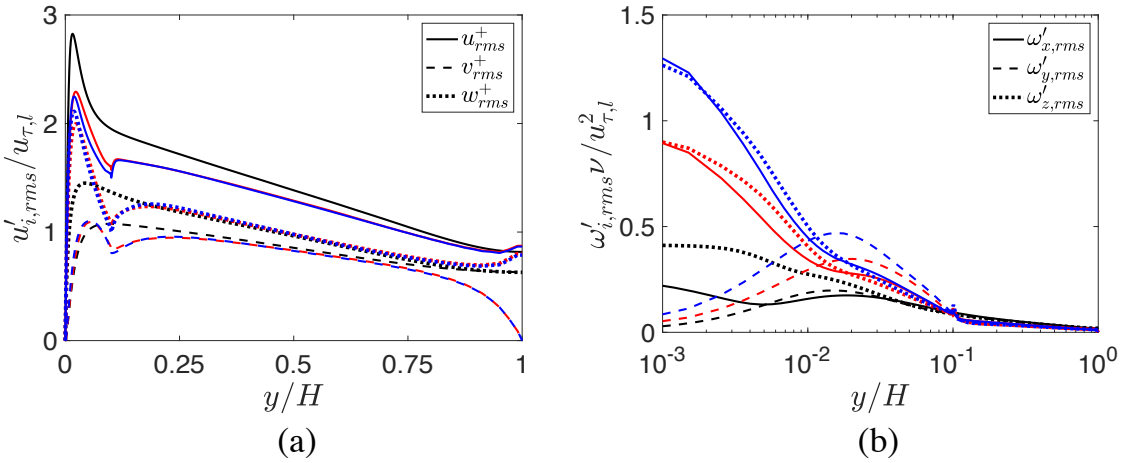


Figure 4.6: (a) Velocity and (b) vorticity fluctuations distributions rescaled with the local friction velocity scale ($u_{\tau,l}$) and the open channel height (H). The solid, dashed and dotted lines represents the streamwise, wall normal and spanwise components. See text for colour-band.

Figure 4.6a, displays the diagonal terms of the Reynolds stress tensor rescaled with the local friction velocity defined in Equation 4.5. In particular, we observe two peaks located in the inner and outer regions of the canopy. The distribution of the stresses outside the canopy once again confirms the negligible role played by the imposed wall conditions on the external flow structures (Scotti, 2006). The behaviour of the wall parallel components in the inner layer indicates the impact of the canopy on the velocity fluctuations, which takes the form of an intensification of the spanwise component and a weakening of its streamwise counterpart. This behaviour appears quite clearly when considering the TD configuration, suggesting the existence of a redistribution mechanism for the velocity fluctuations induced by the presence of the filaments. These act as obstacles and disrupt the streamwise coherence of the inner flow. The role played by the stems is further confirmed by the distribution of the wall-normal component of the velocity fluctuations. The mild deficiency of the proposed scaling in the vicinity of the canopy edge can be attributed to the imbalance between production and dissipation induced by the abrupt change in the drag profile (Monti *et al.*, 2019). In Figure 4.6b, we present the vorticity fluctuations that have been normalised by the local friction velocity (see Equation 4.5) and open channel height (H). The intensity of all three components has substantially increased, across the canopy layer. An interesting behaviour can be observed for the wall-normal component ($\omega^+_{y,rms}$). In particular, the peak for the TS

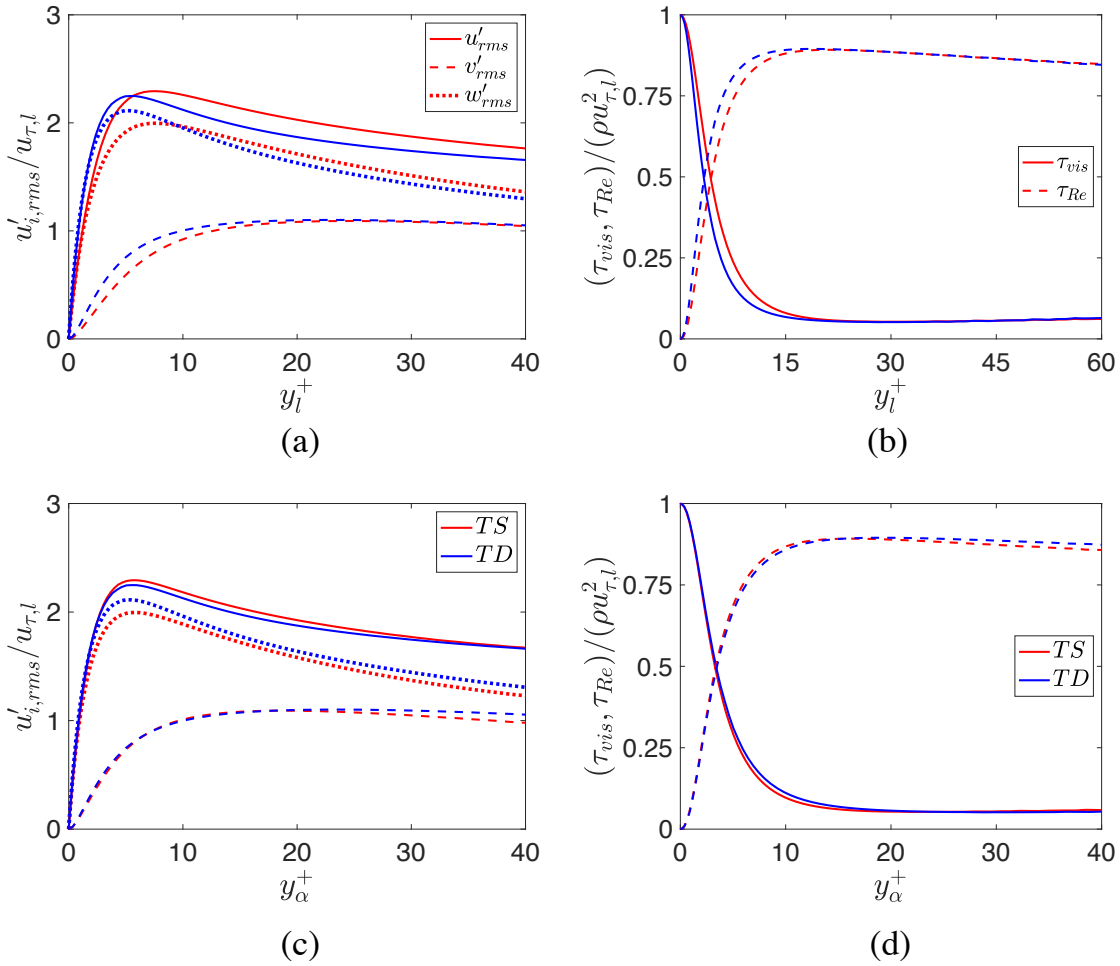


Figure 4.7: Distributions of the velocity fluctuations (a,c) and the stresses as a function of the non-stretched (top row) and stretched (bottom row) viscous units. The solid, dashed and dotted lines in the first columb represents the streamwise, wall normal and spanwise components. The solid and dashed lines in the second column represents the viscous and Reynolds stresses. See text for colour-band.

configuration presents an outward shift, when compared with the smooth wall profiles, similar to a rough wall boundary layer (Abderrahaman-Elena *et al.*, 2019). However, the corresponding peak of the TD configuration presents an inward shift relative to the TS configuration, indicating a departure from the rough-wall-like behaviour. It is noted that the peak locations are highly influenced by the alternating spanwise velocity fluctuations along the streamwise direction, induced by the presence of the filaments.

Before moving into the analysis of the higher dimensional statistics, we discuss the appropriateness of the chosen viscous length scale. Based on the local friction velocity formulation presented in Equation 4.5, we define a local viscous unit as, $\delta_{v,l} = \nu/u_{\tau,l}$. In

Figure 4.7a and 4.7b, we present the profiles of the velocity fluctuations and the stresses versus the local viscous units (i.e., $y_l^+ = y/\delta_{\nu,l}$). While there is a good collapse of the profiles away from the wall, the same cannot be said for the inner region of the canopy. This can be attributed to the several geometrical length scales introduced by the canopy, e.g. average filament spacing (ΔS), height (h), filament diameter (d), mean positions of the virtual origin and the internal inflection point and their signed distances. In the spirit of adopting the proposed scaling to the conditions of the canopy, we employ a non-dimensional stretching factor (α) suggested by Monti *et al.* (2020). Different from their choice, we select the aspect ratio ($\Delta S/h$), which is the most relevant length scale of the canopy regime under scrutiny (Monti *et al.*, 2020; Sharma & García-Mayoral, 2020*b*). The resulting, stretched viscous unit takes on the definition:

$$y_\alpha^+ = \frac{1}{\alpha}\frac{u_{\tau,l}y}{\nu} = \frac{h}{\Delta S}\frac{u_{\tau,l}y}{\nu} \tag{4.6}$$

The robustness of the proposed scaling can be easily seen in Figure 4.7c and 4.7d, where the profiles exhibit a good collapse for the two configurations. From a physical perspective, in the sparser regime, the turbulent eddies of the external boundary layer can easily penetrate the full extent of the canopy since the penetration of the external vortices is only constrained by the distance to the wall (i.e., h). However, as the canopy becomes denser, the interaction with the outer flow weakens and only characteristic vortices with size ΔS are able to penetrate the canopy. Therefore, it is reasonable to incorporate the proposed aspect ratio into the definition 4.6.

To obtain further insight into the emergence and organisation of the large coherent structure prevalent in both the internal and external boundary layers, we turn our attention to the fluctuating velocity field. Following Nikora *et al.* (2007*b*) and Mignot *et al.* (2009), we introduce a double averaging technique to decompose an instantaneous flow quantity (ϕ),

$$\phi(x,y,z,t) = \langle\bar{\phi}\rangle(y) + \tilde{\phi}(x,y,z) + \phi'(x,y,z,t) \tag{4.7}$$

into a space-time mean quantity ($\langle\bar{\phi}\rangle$), spatial fluctuation of the temporal average ($\tilde{\phi}$) and the full turbulent fluctuation (ϕ'). The term $\tilde{\phi}$, which is computed from the time-averaged

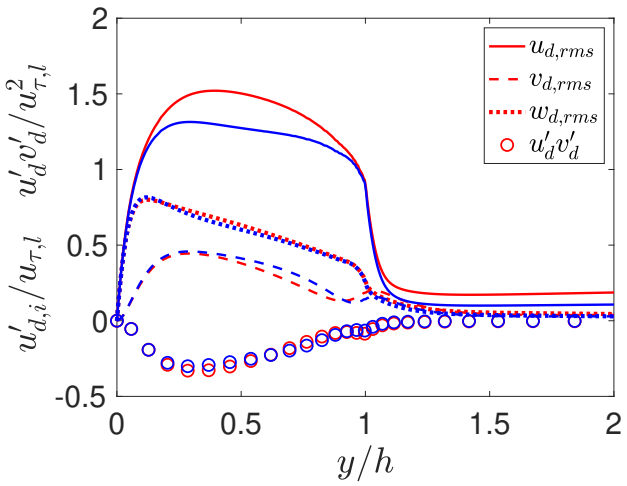


Figure 4.8: Form induced dispersive stresses as a function of wall normal distance normalised with the canopy height. The solid, dashed and dotted lines represents the streamwise, wall normal and spanwise components, while the symbols represents the anisotropic term ($u'_d v'_d$). See text for colour-band.

flow field (i.e., $\tilde{\phi} = \bar{\phi}(x, y, z) - \langle\bar{\phi}\rangle(y)$), is also known as the dispersive component. The usefulness of this triple decomposition mainly concerns the filamentous layer, since the canonical Reynolds decomposition is recovered (because the dispersive terms tend to zero), in the region outside the canopy. This is clearly seen in Figure 4.8, where the form-induced (dispersive) stresses are presented as a function of the wall-normal distance scaled with the filament height. The figure illustrates the streamwise (u'_d), wall-normal (v'_d) and spanwise (w'_d) and the anisotropic ($u'_d v'_d$) components of the dispersive stresses. These stresses are often neglected in the context of canopy flows, however, they play an important role in the momentum transfer within the canopy, especially in the sparse and transitional regimes (Poggi *et al.*, 2004*a*). Consistent with previous rough-wall studies (Mignot *et al.*, 2009; Yuan & Piomelli, 2014), the wall-normal and spanwise components in Figure 4.8 have a lower intensity relative to the corresponding streamwise component. Apart from the latter, which is comparable to the Reynolds stresses, the form-induced stress profiles for both canopy configurations agree well with each other. In particular, the magnitude of the u'_d peak for the TD case has decreased, in agreement with the behaviour observed by Poggi *et al.* (2004*a*).

The presence of the filamentous layer induces a meandering motion, amplifying the signature of the spanwise velocity fluctuation within the canopy. The instantaneous

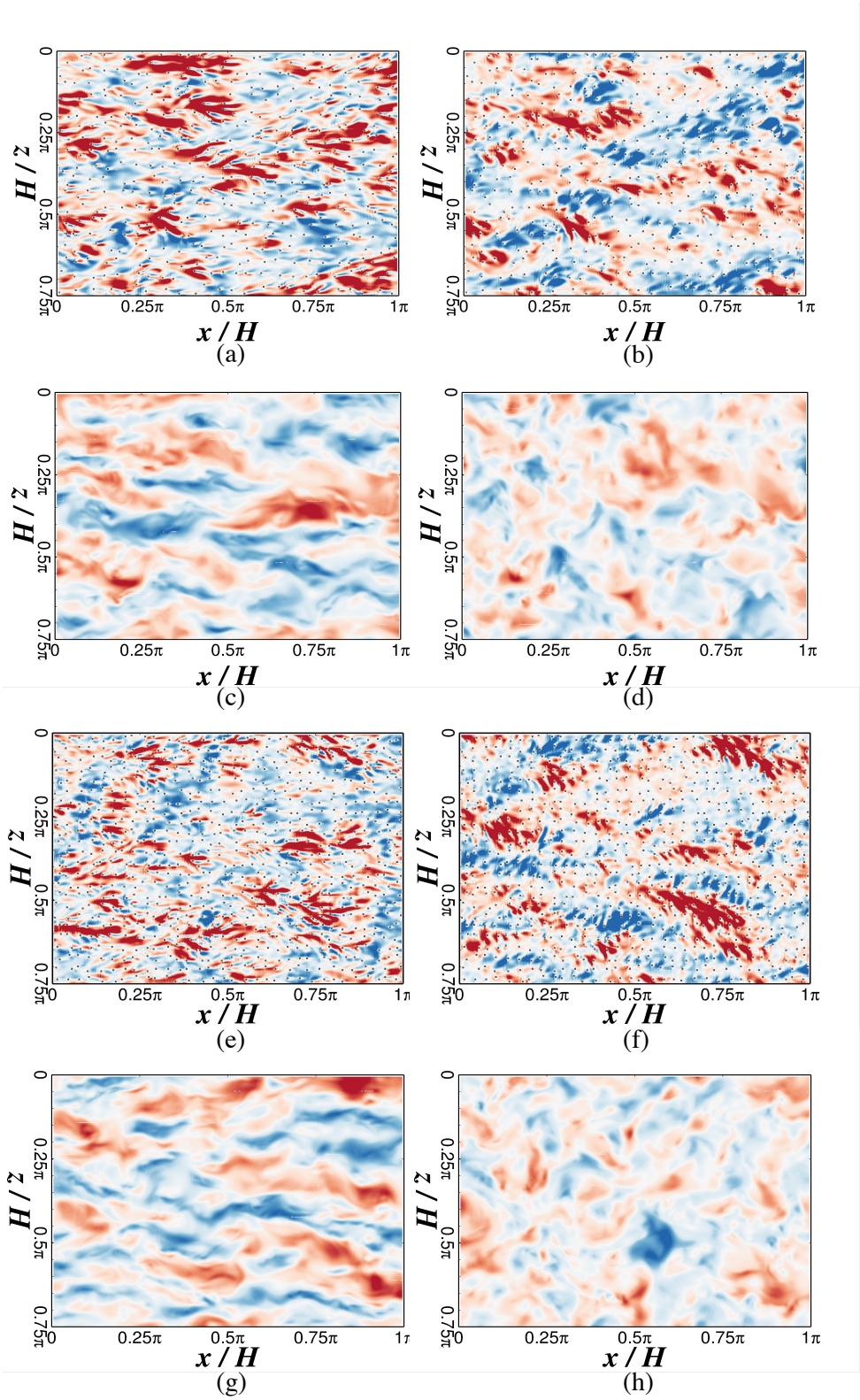


Figure 4.9: Wall parallel instantaneous snapshots located at $y/H = 0.02$ (a), (b), (e), (f) and at $y/H = 0.15$ (c), (d), (g), (h). The first and third columns represents the streamwise fluctuations, while the The second and fourth columns represents the spanwise fluctuations (u'^{+}, $w'^{+} \in [-4, 4]$). The top and bottom row represents the TS and TD configurations, respectively.

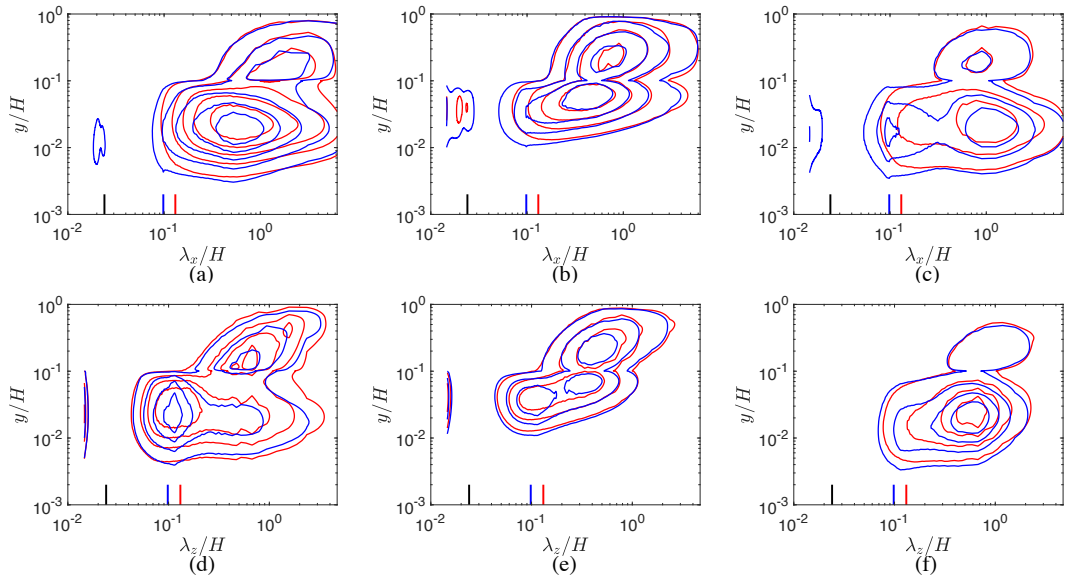


Figure 4.10: Pre-multiplied spectra of the velocity fluctuations, as a function of the wall normal distance and the streamwise (top row) and spanwise wavelength (bottom row) scaled with the outer units. The first, second and third columns represents the streamwise, wall normal and spanwise components, respectively. The short vertical lines presents the wavelength of the mean filament spacing corresponding to the two canopy configurations, while the black line represents the wavelength equivalent of filament diameter.

velocity fluctuations (u' and w') presented in Figure 4.9, have been sampled at two wall parallel planes locations, one deep inside the canopy and the other in the vicinity of the canopy tip. In particular, Figure 4.9a, 4.9b, 4.9e and 4.9f clearly illustrate the sinuous deviation of the flow in the intra-canopy region, due to the presence of the filaments and its eventual contribution towards the spanwise velocity fluctuations. Furthermore, the intra-canopy flow also inherits a footprint of the quasi-streamwise vortices that populate the external flow, which can be attributed to the negligible or very mild decouple between the inner and outer flow in the transitional regime. A close examination of the streamwise component of the TD configuration reveals an interesting feature. In particular, Figure 4.9e, contains the weak traces of a spanwise coherent motion, resembling the Kelvin Helmholtz instability that is typically found in dense canopies. The spanwise modulation of the streamwise velocity fluctuation deep inside the canopy was originally reported by Monti *et al.* (2020), in the context of the fully dense regime.

The organisation of the coherent structures observed in the instantaneous snapshots can be further analysed by, considering the spectral energy content. To this end, the

pre-multiplied spectra of the fluctuating velocity components are presented in Figure 4.10, as a function of the wall-normal distance (y/H) and wavelengths along both homogeneous directions (i.e. streamwise λ_x/H and spanwise λ_z/H). The panels in Figure 4.10, reveal the presence of two primary fluctuating peaks located in the inner and outer regions of the canopy for both configurations. Concerning the internal maxima in the canopy layer (i.e., $y/H \leq 0.1$), we observe its occurrence at three wavelengths. In particular, the left-most peaks, occurring at short wavelengths, are comparable to the geometrical length scales of the canopy, including the filament diameter and spacing (i.e., $\lambda_x, \lambda_z = [d, \Delta S]H$). This can be associated with an obstacle-induced, flow deviation and the formation of a wake behind each filament. In Figure 4.11, we present pre-multiplied spectra as function of the λ_x and λ_z wavelengths, at three wall-normal locations that corresponds to the inner region ($y = 0.02H$), the canopy edge ($y/H = h$) and the outer region ($y/H = 0.15$). The right-most peak of u' and w' in Figure 4.10, which is comparable with Figure 4.11, corresponds to the large wavelength, typically of the order $\lambda_x, \lambda_z \sim O(H)$. This extremum can be associated with the large-scale structures of the outer flow that preferentially penetrate the canopy through the wall-normal component, similarly observed in the instantaneous planar snapshots offered in Figure 4.9. A closer examination of panel *a* in Figure 4.11 reveals an interesting behaviour of the pre-multiplied spectra of the streamwise component. First, the extent of the maxima corresponding to large wavelengths has decreased relative to the TS configuration, indicating a weaker footprint of the outer logarithmic structures deep inside the canopy. This can also be clearly seen in the pre-multiplied spectrum of the v' (see panel b of Figure 4.11). Second, the spectra of u' of the TD case, highlight the presence of a peak at wavelength $\lambda_x = 0.5H$ and $\lambda_z = H$, with the streamwise wavelength similar to the distance from the canopy bed to the inner inflection point. The association of the respective maxima with the large-scale wavelengths, suggests the emergence of a different physical mechanism that would be responsible for its inception. When focusing on the instantaneous snapshots (panels *e* and *f* in Figure 4.9) and the spectral decomposition (panels *a* and *c* in Figure 4.11), we indeed observe the signature of a new coherent motion embedded in the background of large scale structures. In

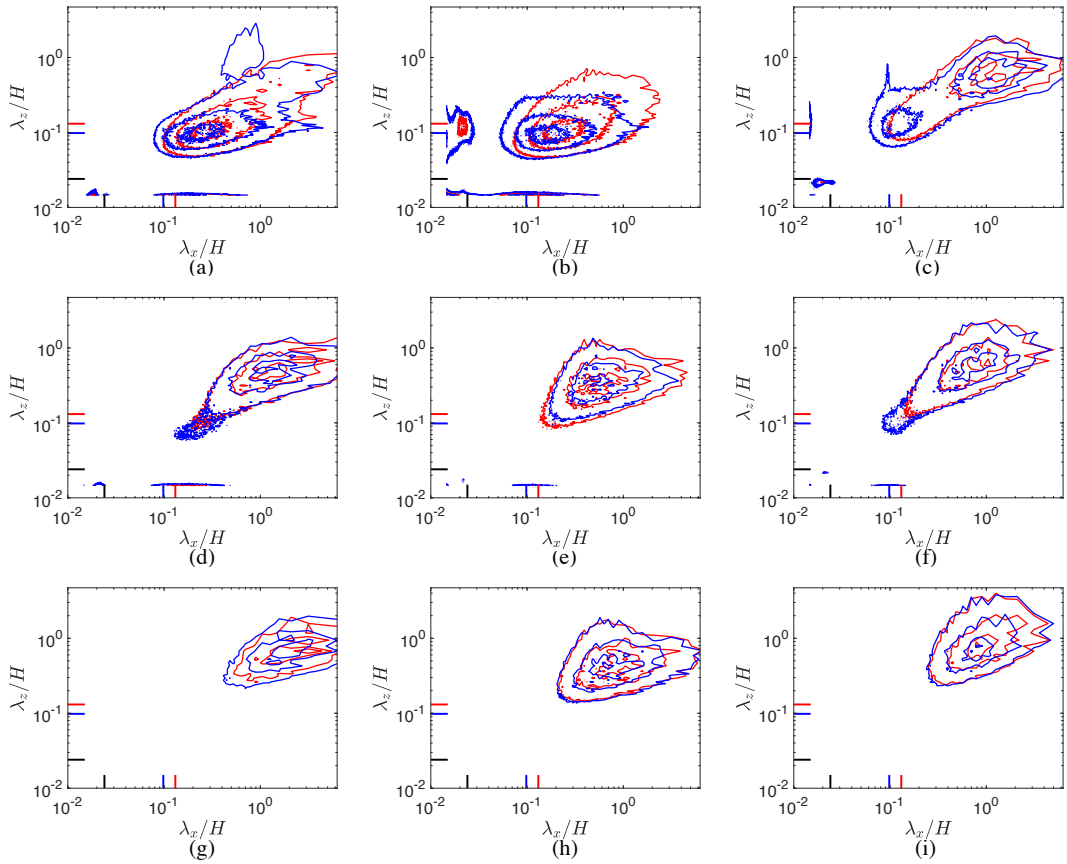


Figure 4.11: Pre-multiplied spectra of the velocity fluctuations, as a function of the streamwise and spanwise wavelength scaled with the outer units. The three rows (top to bottom) corresponds to three wall normal locations $y = 0.02H, h, 0.15H$. Panels (a, d and f), (b, e and h) and (c, f and i), represents the streamwise, wall normal and spanwise components, respectively. See Figure 4.10 for the definitions of the colour lines.

particular, the u' is organised with a spanwise coherency, while the w' is more organised along the diagonal direction. The panels extracted at the canopy edge and the outer flow clearly illustrate that the observed flow structure progressively vanishes when moving away from the wall, indicating a partial decoupling of the inner and outer flows.

Next, we discuss the insurgence of the peak observed in the outer region. To deepen the discussion, we also consider the cospectra shown in Figure 4.12. All the panels of Figure 4.10 and the bottom row of Figure 4.11, reveal the existence of a maximum associated with a large spatial scale. In particular, the external maxima of u' corresponds to a very long streamwise wavelength with a modulation in the spanwise direction (see panels a and d of Figure 4.10). These outer large-scale structures are characterised by velocity streaks that are typically found in the logarithmic region in wall-bounded

flows (Jiménez, 2013). Moreover, the peaks of v' and w' detected just above the canopy in panels *e* and *f* of Figure 4.10, confirm the presence of quasi-streamwise vortices that flank large scale streaky structures. The occurrence of these vorticity structures is clearly evident in the instantaneous iso-surfaces of the streamwise velocity fluctuations, presented in Figure 4.13. Apart from the typical logarithmic structures, the occurrence of a set of spanwise rollers in the context of canopies that fall into the transitional regime still remains an open question. When dealing with dense canopies, the inflection point of the mean velocity is known to trigger a KH-like instability that leads to the formation of large-scale spanwise coherent rollers. It should be noted that these rollers are not well-defined vorticity structures, which can be easily detected (Finnigan *et al.*, 2009) through snapshots. However, the wall-normal velocity fluctuation is a good indicator of the presence of these vorticity rollers (Sharma & García-Mayoral, 2020*b*). This is the case for the two-dimensional pre-multiplied spectra of the v' extracted at the canopy edge (see panel *e* of Figure 4.11) from where we observe a spanwise coherent spectral peak occurring within a narrow streamwise wavelength band, for both canopy configurations. Alternatively, the emergence of the set of spanwise rollers centred around the edge of the canopy can be detected by the outer peaks of the one-dimensional pre-multiplied cospectra of the Reynolds stress, as shown in Figure 4.12. Another indication of the presence of the rollers can be evinced by the streamlines drawn on the lateral plane of Figure 4.13, which have been obtained by averaging the velocity fluctuations along the spanwise direction. The occurrence of such spanwise oriented vorticity structures has been previously reported by other authors in the context of porous substrates (Jimenez *et al.*, 2001; Rosti *et al.*, 2018*a*).

4.4 Concluding Remarks

In conclusion, we have investigated the regime transition of canopy flows. The respective regime, defined as the separation between the sparse-dense asymptotic regimes (Nepf, 2012), occurs when the solidity takes on the value $\lambda \approx 0.15$ (Monti *et al.*, 2020). By leveraging an efficient IBM formulation, we have fully resolved the canopy layer, enabling us to obtain a detailed characterization of the intra-canopy flow. The two configurations

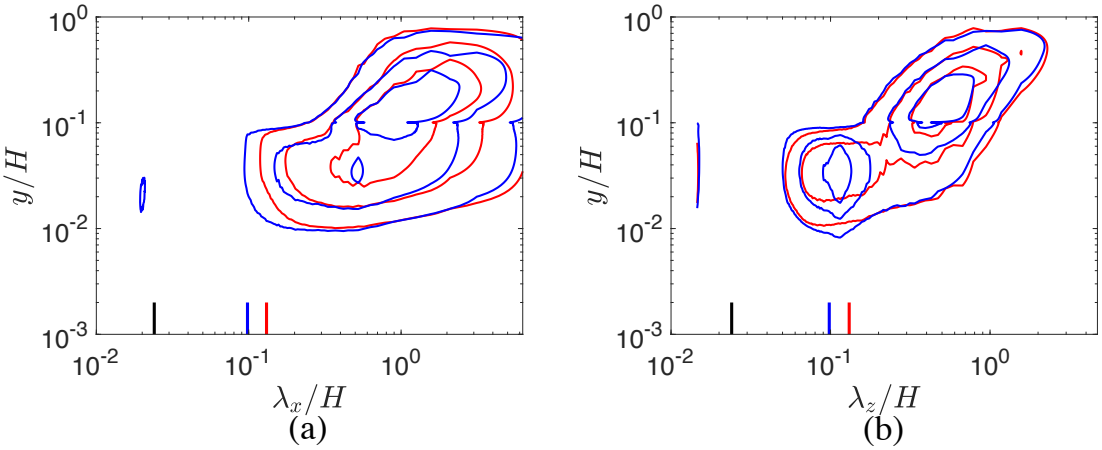


Figure 4.12: Magnitude of the pre-multiplied co-spectra of the $u'v'$ as a function of the wall normal direction scaled in outer units. The left and right panels represents the dependence on the streamwise (λ_x/H) and spanwise (λ_z/H) wavelength, respectively. See Figure 4.10 for the definitions of the colour lines.

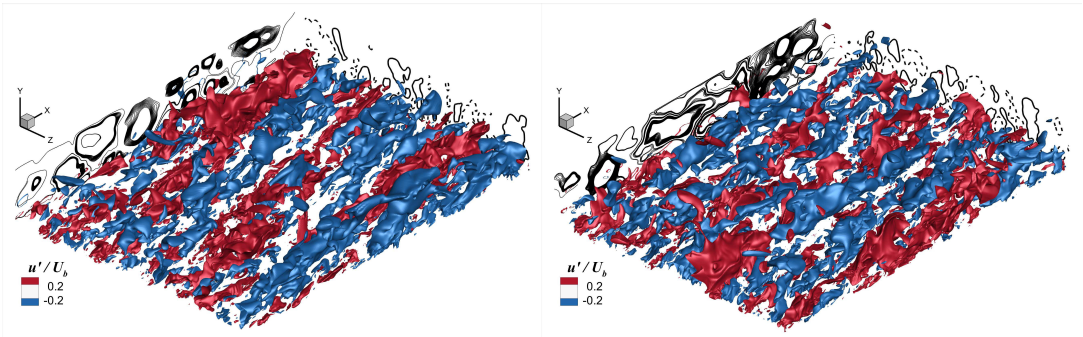


Figure 4.13: Instantaneous iso-surfaces of the streamwise velocity fluctuations for the TS (a) and TD (b) configurations. The longitudinal plane presents contours of positive (solid) and negative (dashed) (w') that have been averaged along the streamwise direction. The streamlines drawn at the end lateral plane have been obtained by averaging the u' and v' along the spanwise direction

considered in this chapter were obtained by modifying the average distance between neighbouring stems (ΔS). Initially, the emergence of the transition regime in our simulations was confirmed. According to Monti *et al.* (2020) the signed distance between the internal inflection point and the virtual origin establishes the transition regime. In particular, the condition that infers its inception (i.e., the collapse of the mean location of the internal inflection point and the virtual origin) was satisfied when the canopy aspect ratio is unity. In this condition, the canopy layer is divided into two layers of

similar thickness, inducing a decouple between the innermost and outermost layers. Thus, the interactions between two layers are restricted to communication along the wall-normal directions (i.e., sweeps and ejection induced by the outer flow). We have also extended the scaling arguments associated with the sparse and dense conditions to the transitional regime. In particular, the local friction velocity based on the viscous and Reynolds stresses presented a good scaling for the velocity fluctuation distributions.

The character and the structure of the turbulent flow field in both the internal and external layers of the canopy were analysed with the aid of a triple decomposition technique. In particular, the former is dominated by various structures corresponding to a wide range of length scales. We identified the existence of a spanwise coherent motion of the streamwise velocity fluctuations deep inside the canopy that is embedded in the background of larger structures that emerge from the outer flow. Previously, this behaviour was only reported in the context of a fully dense canopy (Monti *et al.*, 2020). This is the first indication that highlights the importance of ΔS, as the primary length scale that governs the transition between the two asymptotic regimes. On the other hand, the external layer is populated by highly elongated velocity streaks that are bounded by the quasi-streamwise vortices and a system of spanwise coherent vorticity structures. The latter is triggered by a Kelvin-Helmholtz-like instability as a result of an inflected mean velocity profile. Previously, these rollers have been reported by authors in the context of dense canopy flows, flows over permeable substrates, and roughness elements.

5

On the effects of in-plane solidity on the different regimes of canopy flows

Contents

5.1 Introduction 85
5.2 Numerical Setup 87
5.3 Results and Discussion 90
5.3.1 Mean flow characteristics 90
5.3.2 Canopy layer: scaling laws 96
5.3.3 Heuristic model 99
5.3.4 Statistical characterisation of the flow 104
5.3.5 Structure of canopy flows 114
5.4 Concluding Remarks 140

5.1 Introduction

The inception of highly resolved simulations, *á-la* DNS allow to address some unanswered questions on canopy flows. In particular, the conditions associated with the insurgence and the characterisation of different behaviours of the flow in the various regions of the canopy and their modulation by the ongoing canopy regimes still represent an open research area that has not been fully explored by previous works. Apart from a general characterisation, also the role played by the frontal solidity and the in-plane

solidity on the different regimes of canopy flows is not well understood yet. The effects of the frontal solidity were recently investigated in the framework of a parametric study by Monti *et al.* (2020), where the canopy height was systematically increased whilst maintaining a constant in-plane solidity. In this case the shortest and the tallest canopies represented the two asymptotic regimes while intermediate heights constituted the transitional regime. Differently, in this chapter we have turned our attention to the effects of the in-plane solidity (i.e., ΔS) on the different regimes of canopy flows. In other words, the focus is on the way the parameter λ can be modified (i.e. by either changing the height or the stem density), and on the impact that this choice has on the resulting canopy flow regime. In addition, the existence of a robust scaling law (i.e, non-dimensional parameter) apart from the solidity λ, that would provide a prior prediction of the respective canopy regimes based on the geometrical properties, has not well documented (Monti *et al.*, 2020)

The present study has been conducted using a series of highly resolved simulations of turbulent flows in an open channel flow bounded by a canopy composed of circular, rigid cylinders (*the filaments*) flush mounted perpendicular to the impermeable wall. By using an immersed boundary formulation, the canopy is resolved filament-by-filament imposing a zero velocity condition on each cylinder. The in-plane solidity of the canopy (i.e., ΔS) is systematically modulated such that the canopies with the largest and lowest stem densities nominally correspond to the solidity of a sparse (i.e., $\lambda << 0.1$) and dense (i.e., $\lambda >> 0.1$) asymptotic regimes (Nepf, 2012). All the other, intermediate cases would, a-priori fall within the *transitional regime* scenario. In particular, we present the results of the fluctuating field by employing a triple decomposition technique that would allow us to focus on the full fluctuating field by eliminating the influence of the filaments. The organisation of the chapter is as follows: Section 5.2 describes the numerical technique that we have adopted to undertake the simulations, Section 5.3 highlights the results of five different canopy configurations via the statistical characterisation and the instantaneous realisations of the flow fields. Lastly section 5.4 highlights some of the concluding remarks of the overall chapter.

5.2 Numerical Setup

We have conducted high fidelity numerical simulations of turbulent flows developing above rigid canopies using SUSA, an in-house developed, incompressible Navier-Stokes solver (see Chapter 3). In this study, we will present results from the simulations of five cases. All of them share the same computational domain corresponding to the one used in Monti *et al.* (2020); Bailey & Stoll (2016). In particular, the streamwise length, the open channel height and the spanwise width of the channel are set to $L_x/H = 2\pi$, $L_y/H = 1$ and $L_x/H = 3\pi/2$, respectively. The adequacy of the selected domain size was confirmed by Monti *et al.* (2019) that showed how the large scale turbulent structures are captured by the computational box (i.e. the velocity correlations drop to small values at domain half size in the stream and spanwise directions). For all simulations, we set the origin in the wall normal direction at $y/H = 0$ (the location of the bottom impermeable wall, the *canopy bed).* With this choice, the filaments form a canopy which height is h/H. To model an open channel flow, we use a zero-velocity condition at $y/H = 0$ and a free-slip condition (i.e., $\partial_y u = \partial_y w = 0, v = 0$) at the top surface $y/H = 1$. In the homogenous directions x and z, we have employed periodic boundary conditions, a choice justified by the experimental observations of Ghisalberti & Nepf (2004). The flow in the computational box is driven by a uniform pressure gradient applied in the streamwise direction. At each time step, the uniform pressure gradient is computed, by imposing a constant, time independent volumetric flow rate. All the simulations that we have performed share the same imposed flow rate leading to a bulk Reynolds number of $Re_b = U_b H/\nu = 6000$. This value has been chosen to allow direct comparison with the results of Monti *et al.* (2020) and because closely matches the one adopted in the experimental works of Ghisalberti & Nepf (2004); Shimizu *et al.* (1991).

Similar to previous investigations (Monti *et al.*, 2020; Thakkar *et al.*, 2018), the spatial distribution of the filaments is based on a *tiled-approach*: the bottom impermeable wall is partitioned into non overlapping, uniform square tiles with a ΔS edge (see Figure **??**). For each tile we assign a single filament, vertically mounted at a random position (extracted from a uniform distribution) within the tile. This choice minimises the possibility of

Case	λ	$\Delta S/h$	$n_i \times n_k$	$Re_{\tau,o}$	Δx_o^+	Δz_o^+	$\Delta y_{w,o}^+$	$\Delta y_{c,o}^+$	*Symbol*
SR	*0.08*	*1.74*	36×27	*676*	*7.5*	*7.5*	*0.34*	*0.34*	∇
TR	*0.14*	*1.31*	48×36	*730*	*8.2*	*8.2*	*0.38*	*0.38*	$\square$
MD	*0.25*	*0.98*	64×48	*754*	*8.6*	*8.6*	*0.39*	*0.39*	$\triangle$
RD	*0.32*	*0.87*	72×54	*755*	*8.7*	*8.7*	*0.39*	*0.39*	$+$
DR	*0.56*	*0.65*	96×72	*716*	*8.4*	*8.4*	*0.38*	*0.38*	o

Table 5.1: Simulation parameters considered in the current investigation: (λ) is the solidity; $\Delta S/h$ is the canopy *aspect ratio*; $n_i \times n_k$ is the filaments count ratio, where n_i and n_k are the number of filament rows in the streamwise and spanwise directions, respectively; $Re_{\tau,o}$ is the friction Reynolds number based on the friction velocity ($u_{\tau,o}$) computed at the virtual origin (to be introduced later). Δy_w^+ and Δy_c^+ are the grid spacings, in viscous units, within the region next to the impermeable wall

generating filaments clusters or repeated patterns that may produce channelling effects in the canopy layer (Stoesser *et al.*, 2009; Sharma & García-Mayoral, 2020*a*).

From the definition of the canopy solidity (i.e., $\lambda = dh/\Delta S^2$), it is noted that using filaments with uniform cross section, a simple change in the canopy height (h) or in the size of the square tiles (ΔS) would lead to a variation in the λ value. Thus, the systematic variation of the two parameters would allow to isolate and investigate the effects the two geometrical parameters on the emergence of different regimes of canopy flows and the supposed universality of λ as a regime indicator. In the present study, the solidity has been changed only by varying the tile size ΔS. Thus the present work can be considered to be complementary to the one by Monti *et al.* (2020) where the λ value was altered by uniquely adjusting the canopy height. As done in the aforementioned research, also here we consider variations of λ that nominally lead to different canopy regimes. In particular, by maintaining a constant canopy height and filament cross section (i.e., $h/H = 0.1$ and $d/H = 0.024$), the largest and the smallest tile size (i.e. the filaments spacing) nominally lead to a sparse or to a dense regime (Nepf, 2012), respectively. The intermediate spacings are associated with the transition regime.

Concerning the space discretisation, we have used a Cartesian mesh with a uniform nodes distribution in the wall parallel directions and a stretched arrangement in the wall normal direction. The stretched grid, obtained with a tangent hyperbolic mapping, allows to cluster more points near the canopy bed and in the vicinity of the canopy

Case	*Nominal Regime*	*Solidity(λ)*	*Height (h/H)*	*Symbol*
SRM	*Mildly Sparse*	*0.07*	*0.05*	◆
TRM	*Transitional*	*0.14*	*0.10*	■
MDM	*Mildly Dense*	*0.35*	*0.25*	▲
DRM	*Dense*	*0.56*	*0.40*	●

Table 5.2: Parameters of the canopy configurations investigated by Monti *et al.* (2020). All the canopies shared the same mean filament spacing of $\Delta S/H = \pi/24$.

tip region. As the estimated boundary layer thickness ($\delta \approx H - h$) is the same across all the configurations, we have used a single computational mesh for all the cases reported in Table 5.1 with the number of grid points in x, y and z set to $N_x = 576$, $N_y = 230$ and $N_z = 432$, respectively. The numerical grid resolutions in wall units, based on the friction velocity computed using the total stress at the virtual origin (i.e., $u_{\tau,o} = \sqrt{\nu \partial \langle U \rangle / \partial y - \langle uv \rangle}$), are reported in Table 5.1. Note that the subscript 'o' used in the table, refers to parameters that have been made non-dimensional using the frictional velocity of the outer logarithmic boundary layer (Monti *et al.*, 2019). In particular, the resolution along the wall parallel directions based on outer flow units (i.e., $\Delta x_o^+ = \Delta x \cdot u_{\tau,o}/\nu$) used for all the configurations satisfies the condition $\Delta x_o^+ = \Delta z_o^+ \leq 9$. The employed stretching function in the wall normal direction is calibrated to preserve a resolution of $\Delta y_o^+ < 0.4$ in the localised layers next to the impermeable wall and embedding the canopy tip, respectively (see Table 5.1). The grid resolution reported above, is within the standard values used for DNS of typical wall bounded turbulent flows (Kim *et al.*, 1987; Lee & Moser, 2015*b*). If the canopy bed friction velocity is used to determine the wall units, the chosen mesh delivers a resolution of $\Delta x_i^+ = \Delta z_i^+ \leq 3$ and $\Delta y_i^+ \leq 0.16$. Further details concerning the numerical grid distribution, the mesh convergence analysis and the suitability of the numerical scheme can be found in Monti *et al.* (2019). Finally, it should be mentioned that all the results presented in the next sections have been obtained using statistically converged simulations with the statistical data collected over $900tU_b/H$ time units, approximately corresponding to 150 full washouts.

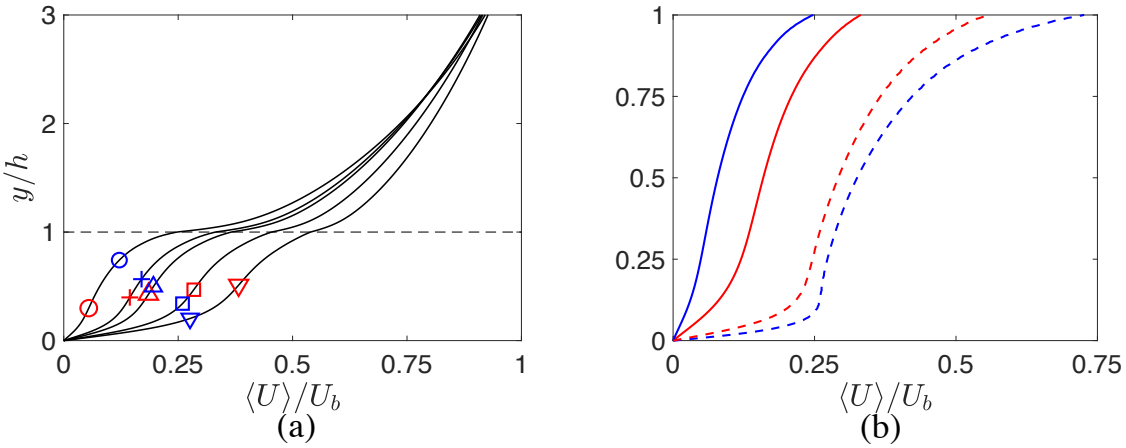


Figure 5.1: Left panel (a): Mean velocity profiles made non dimensional with the half channel height H and the bulk velocity U_b. See Table 5.1 for symbols. The red and blue symbols represents the internal inflection point and the virtual origin, respectively. Right panel (b): Direct comparison with the mean profiles inside the canopy obtained by Monti *et al.* (2020) (dashed lines) for the same solidity values: blue is the present DR case and red is the RD case, respectively.

5.3 Results and Discussion

In this section, we present the results obtained from the simulations of the five canopy flows characterised by the parameters of Table 5.1. The main body of the discussion is dedicated to the direct comparison of the flow statistics and structures across the different cases considered here and the ones obtained by Monti *et al.* (2020) (see Table 5.2). Initially, we discuss the basic averaged quantities and their variations as a function of the in-plane solidity. We also explore the robustness and appropriateness of well-known non-dimensional parameters for the a-priori identification of the canopy flow regime and in particular of the shape of the mean velocity profiles (Nepf, 2012). In the subsequent subsections, we focus mainly on higher order statistics and on the analysis of the coherent structures that emerge or disappear on the onset of different regimes of canopy flows.

5.3.1 Mean flow characteristics

.

We start by considering the effect of varying the in-plane solidity on the mean velocity profile. Figure 5.1-a presents the mean velocity distributions made dimensionless

with the open channel height (H) and the bulk velocity ($U_b = \frac{1}{H}\int_0^H \langle U \rangle dy$, where $\langle . \rangle$, represents the triple, i.e. time and homogenous directions, averaging operator). The variations of the mean velocity distribution associated with different solidity (λ) values are quite evident, especially in the intra-canopy region (i.e., $y/H \in [0, 0.1]$). In the canopy region, as the solidity is increased the mean velocity profiles shows an increased retardation with an enhanced concave shape. The SR case exhibits a the smallest slowdown among the velocity distributions, the TR, MD and RD cases show a mild retardation while the DR configuration presents a substantial decrease of the mean velocity accompanied by a curvature enhancement. When the present DR profile is compared with the one obtained by Monti *et al.* (2020) at the same λ value (see figure 5.1-b), the difference in shape is quite evident. In particular, the velocity gradient in the wall region is much milder in the present case with a smoother change of curvature with increasing y/H. The strong gradient in the wall region and the appearance of a *kink* in the velocity profile, just below the inner inflection point, reported by Monti *et al.* (2020), is absent in our mean velocity profile. The same authors have attributed the insurgence of the kink to the strong inrushes (jet-like) of wall normal velocity directed towards the wall (Banyassady & Piomelli, 2015) and then deflected in the x and z directions as a consequence of continuity. Although the two dense cases share the same solidity λ the absence/presence of the kink is a first indication that the underlying dynamics in the canopy region may be of different nature. It is also interesting to note that overall mean velocity profile of the present DR case is similar to the distributions reported in the context of turbulent wall flows bounded by porous media (Breugem *et al.*, 2006; Rosti *et al.*, 2015; Kuwata & Suga, 2017; Gómez-de Segura & García-Mayoral, 2019). This analogy between canopy flows in the limiting condition $\Delta S/h << 1$ and flows developing above anisotropic porous layers, also suggested by other authors (Nepf, 2012; Monti *et al.*, 2020; Sharma & García-Mayoral, 2020*b*), is further explored by assuming that the actual DR canopy can be interpreted as an anisotropic porous medium with permeability tensor $\mathcal{K}$ which principal components $\mathcal{K}_x^+$, $\mathcal{K}_y^+$ and $\mathcal{K}_z^+$ are characterised by $\mathcal{K}_y^+ > \mathcal{K}_x^+, \mathcal{K}_z^+$. Due to the homogeneous filament distribution in the wall parallel directions, we can also assume $\mathcal{K}_x^+ = \mathcal{K}_z^+$ (Gómez-de Segura & García-Mayoral, 2019), while $\mathcal{K}_y^+$ is set by

the mean spacings of the filaments therefore determining the degree of penetration of the external flow and, ultimately the shape of the mean velocity profile. Some authors (Kuwata & Suga, 2017; Suga *et al.*, 2018) have proposed the use of the pore length scale D_{px} as a surrogate for characterising the permeability. This argument implies that the λ value is inversely proportional to the Frobenius norm of the permeability tensor $\boldsymbol{\mathcal{K}}$. Increasing the sparsity of the canopy (i.e., $\lambda < 0.04$) increases the entries of the permeability tensor asymptotically to infinity as the resistance imposed by the filamentous layer becomes negligible. Conversely, moving towards denser regimes ($\lambda >> 0.1$), the permeability tensor entries would systematically decrease as the solidity is increased. In the limiting condition $\lambda \rightarrow 1$, the magnitude of the permeability tensor elements must converge to $\boldsymbol{\mathcal{K}} \rightarrow 0$, satisfying the impermeability constraint of an impenetrable substrate. The porous layer analogy provides an explanation for the increasingly retarded behaviour of the mean velocity profiles in the intra canopy region, observed in Figure 5.1, as the streamwise directional permeability of the canopy is decreased.

When considering non sparse canopy flow regime (i.e., $\lambda > 0.04$), the mean velocity profile features three notable points within the filamentous layer (i.e. for $y \leq h$ as shown in the right panel of Figure 5.1): two inflection points and the virtual origin of the outer flow (Poggi *et al.*, 2004*b*; Nepf, 2012; Monti *et al.*, 2019). The latter can be interpreted as the location of the virtual wall, i.e. as seen by the outer turbulent boundary layer that develops above the canopy. The occurrence of a shifted boundary layer is commonly observed in the framework of boundary layers that develops over various textured surfaces (Jiménez, 2004; Bottaro, 2019). In the context of rough wall boundary layers, this shift was characterised as the zero-plane displacement (Raupach *et al.*, 1991), which was computed by considering the centroid of moment of the mean drag profile, i.e. the mean thickness of momentum absorbed underneath the surface (Jackson, 1981). We determine the location of the virtual origin (y_{vo}), by enforcing the canonical logarithmic boundary formulation on the outer layer mean velocity profile (Monti *et al.*, 2020) as:

$$\frac{\langle U \rangle}{u_{\tau\, out}} = \frac{1}{\kappa} log\left(\frac{y_{out}\ u_{\tau\, out}}{\nu}\right) + B \tag{5.1}$$

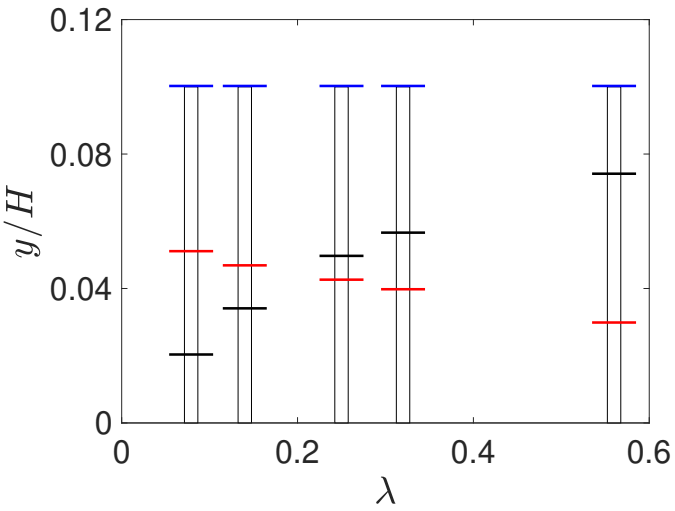


Figure 5.2: Mean locations of the features observed in the mean velocity profiles: inner inflection point (red horizontal line); virtual origin (black horizontal line) and the outer inflection point (blue horizontal line) as a function of the solidity λ. Note that the canopy becomes sparser (smaller λ) when increasing the mean filament spacing ΔS.

where $y_{out} = y - y_{vo}$ is the shifted wall normal coordinate (reference at the virtual origin) and κ is the von Kármán constant. Equation 5.1 incorporates the standard modification to the boundary layer log-law accounting for the shift due to the presence of the textures (e.g. roughness) (Jiménez, 2004). In the present work, the friction velocity ($u_{\tau,out}$) in the above equation is computed from the total stress at the location of the virtual origin as the sum of the viscous stresses and the Reynolds shear stress:

$$u_{\tau,out} = \sqrt{\frac{\tau(y_{vo})}{\rho}} = \sqrt{\nu \frac{\partial \langle U \rangle}{\partial y}_{vo} - \langle u'v' \rangle_{vo}} \tag{5.2}$$

If the total stress profile is known, then the wall normal location of the virtual origin for each canopy configuration can be determined by solving equation 5.1 which is an implicit equation for the virtual origin location (Monti *et al.*, 2019).

The mean velocity profiles reported in Figure 5.1 show an inflection point (outer) located at the top of the canopy and another, internal inflection point close to the wall. The former is attributed to the sudden discontinuity of the drag force profile by the canopy tip. The other, internal inflection point is the result of the merging of the close-to-the-wall velocity profile with the mean velocity distribution characterising the region closer to the canopy tip (Monti *et al.*, 2020). The locations of the inner inflection point

can be found by determining the locations of the zeros of the second derivative of the mean velocity appearing in the mean momentum balance in the streamwise direction:

$$\frac{1}{Re_b}\frac{\partial^2\langle U\rangle}{\partial y^2} = \frac{\partial P}{\partial x} + \frac{\partial\langle u'v'\rangle}{\partial y} + \langle F_D\rangle \tag{5.3}$$

The first, second and third terms in Equation 5.3, represent the mean of the viscous force, streamwise pressure gradient and the Reynolds shear stress, respectively. The final term represents the contribution of the overall mean drag imposed by the filaments of the canopy. Since the filaments are mounted normal to the bottom wall, the last term in 5.3 is mainly due to the cylinders form drag with a weak wall shear stress contribution.

Based on the locations of the virtual origin and the inflectional points, the canopy (in a non sparse regime) can be divided into three zonal layers (Monti *et al.*, 2020). The first zone, termed as the *inner* layer, develops between the canopy bed and the location of the mean internal inflection point. The *outer layer*, going from the virtual origin to the canopy tip can be interpreted as the canopy region directly affected by the dynamics of the external flow. The region sandwiched in between the inner and the outer layers, can be seen as an *overlap* zone where complex interactions between the inner and outer flows take place. The existence and the extent of the overlap layer depends on the ongoing canopy flow regime.

The locations of the virtual origin and of the inflectional points for the five canopy configurations considered in this work are shown in Figure 5.2. The wall normal locations of these characteristic points can be used to infer the ongoing canopy flow regime (Monti *et al.*, 2020). In the case of sparse canopies, defined by $\Delta S/h \gg 1$ (Poggi *et al.*, 2004*b*; Sharma & García-Mayoral, 2020*a*), the virtual origin asymptotically moves towards the canopy bed (i.e., $y_{vo}/H \to 0$), and correspondingly the position of the internal inflection point collapses onto the canopy tip. This limiting condition is analogous to a rough-wall boundary layer (Jiménez, 2004). Even the sparsest canopies considered in this study (SR and TR) do not fall into this extreme conditions although in these cases, the wall normal positions of the virtual origin lie below the inner inflection point. In this situation, the external boundary layer penetrates into the inner layer determining the absence of an overlap region, and the outer flow would actually be affected directly by the canopy bed.

When the average filament distance is systematically decreased, the canopy transitions from a sparse regime into a dense one. Figure 5.2 shows that the signed distance between the inner inflection point and virtual origin is a function of the solidity. As λ is increased, the location of the virtual origin starts to move away from the canopy bed, while the inner inflection point moves towards it. As a result from figure 5.2, we conclude that the signed distance between these points has a zero in the range $0.14 < \lambda < 0.25$. The value of λ for which the two points collapse one into the other can be used as a sharp criterion for predicting the inception of the dense canopy flow regime (Monti *et al.*, 2020). In dense configurations, the virtual origin occupies in the upper half of the canopy (i.e. $y_{vo}/h > 0.5$), while the inner inflection point is located in the bottom half of the canopy (i.e. $y_{vo}/h < 0.5$). As the canopy density increases, the size of the overlap region thickness also increases suggesting a decoupling effect of the inner and the outer layers (Monti *et al.*, 2020; Sharma & García-Mayoral, 2020*b*). In the most dense case that we have studied (i.e. case DR), the virtual origin and the internal inflection point are located near the canopy tip and bed, respectively. This situation leads to the conjecture that the outer flow behaves like a shear flow over a rough wall, while the innermost flow develops a local boundary layer in the vicinity of the bed. This decoupling can also be discussed in terms of the permeability analogy. As mentioned above, in the limiting condition where $\lambda \longrightarrow 1$, the overall magnitude of the permeability tensor would converge to $|\boldsymbol{\mathcal{K}}| \longrightarrow 0$, therefore the location of the virtual origin would move towards the canopy tip while the inner inflectional point would collapse onto the canopy bed, asymptotically recovering a canonical smooth wall turbulent boundary layer.

Figure 5.3a and 5.3b show the locations of the inner inflection point and of the virtual origin measured from the canopy tip (i.e. the outer inflection point). The figures incorporate data from Monti *et al.* (2020) as well (see Table 5.2 for symbols). In particular, these data show that the parameter $h - y_{vo}$ and the location of the internal inflection point saturates to a constant value as λ is increased (i.e., canopy becomes denser). This asymptotic behaviour can be explained by considering the specific situation in which the filaments spacing is kept constant (i.e., $\Delta S/H = \pi/24$) while the canopy height is systematically increased. In this scenario the inner and outer layer decouple more and

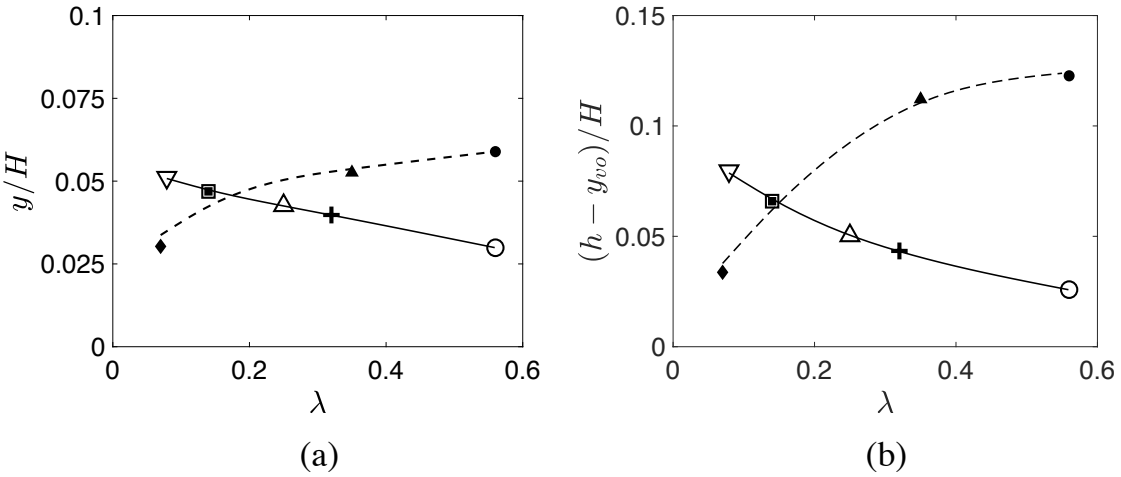


Figure 5.3: Left: (a) mean locations of the inner inflection point as a function of solidity λ. Right: (b) mean locations of the virtual origin measured from the canopy tip as a function of λ. Both parameters are made non dimensional using the half channel height H. The solid lines are best fits for the current data, while the dashed lines fit the results from Monti *et al.* (2020). For symbols meaning please refer to Table 5.1 for symbols.

more until reaching conditions in which the canopy height (or the solidity λ, in this case) becomes irrelevant on the flow behaviour. Differently, in the current framework where λ is changed by increasing the number density of the filaments, no asymptotic behaviour is detected. This non-saturating behaviour will clearly come to an end when an almost solid wall is assembled by a very dense filaments clustering, when $\lambda \to \infty$. The quantities examined so far have been made dimensionless using an outer scaling (e.g. lengths with channel depth H). Not surprisingly, this choice does not help in collapsing the data or in unveiling universal features. In the next section, we will look at alternative scaling laws to characterise the flow behaviour with particular emphasis on the role of the solidity λ.

5.3.2 Canopy layer: scaling laws

The selection of the non-dimensional geometrical parameters able to characterise the flow within a textured substrate has been previously considered by a number of authors in the context of rough surfaces and permeable layers (Nikuradse, 1933; Schlichting, 1937; Rosti *et al.*, 2015; Gómez-de Segura & García-Mayoral, 2019). In flows over rigid, submerged canopies, the regime transition is determined by the variations of λ. The value of λ can be changed by modifying either the frontal or the in-plane solidity. The

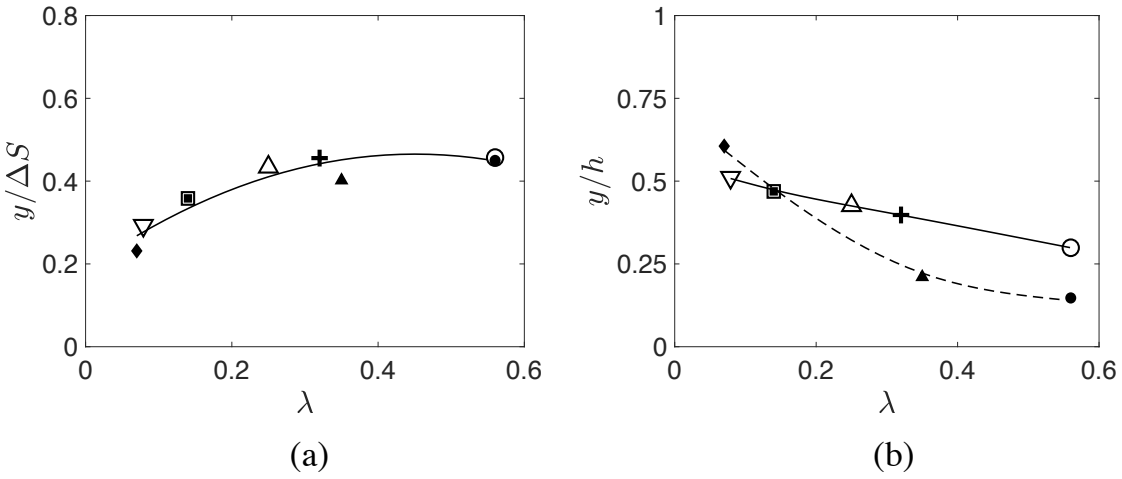


Figure 5.4: Mean location of the inner inflection point as a function of the aspect ratio λ. The mean locations are scaled by the mean filament spacing ΔS and the canopy height h (symbols as in table 5.1). The solid line represents a polynomial best fit through the internal inflection points for all canopy data.

effects of changing frontal solidity through variations of the canopy height h/H has been explored in Monti *et al.* (2020). Here, we consider the variations of λ obtained by changing the value of the canopy aspect ratio $\Delta S/h$, i.e. the ratio between the average distance between filaments and the canopy height. It should be noted that the value of λ could also be modulated by changing the value of the ratio between the stems diameters d and h. However, the impact of d/h becomes marginal when considering slender elements (i.e., $d/h \ll 1$) that are more representative of a vegetative canopies. In this study we set for all simulation $d/h = 0.24$ and just focus on the effect of the filaments packing or number density, i.e. on the effects of the ratio $\Delta S/h$.

Figure 5.4 shows the locations of the internal inflection point of the mean velocity profile (i.e. the height of the inner region) scaled with ΔS and h, plotted versus λ. Panel (a) shows a full collapse between the cases sharing the same λ value, independently of the way in which its variations is obtained (either changing ΔS or h). It is noticed that for ΔS going to zero y should behave like $y \sim \Delta S$ to maintain a finite value of the $y/\Delta S$. Differently, panel (b) shows that y/h starts to diverge in the two cases as the canopy becomes denser. This is consistent with the observation that for ΔS going to zero (i.e. λ increasing) the wall becomes solid and y/h must go to zero as well (see the linear decreasing behaviour associated with the open symbols), while for h becoming

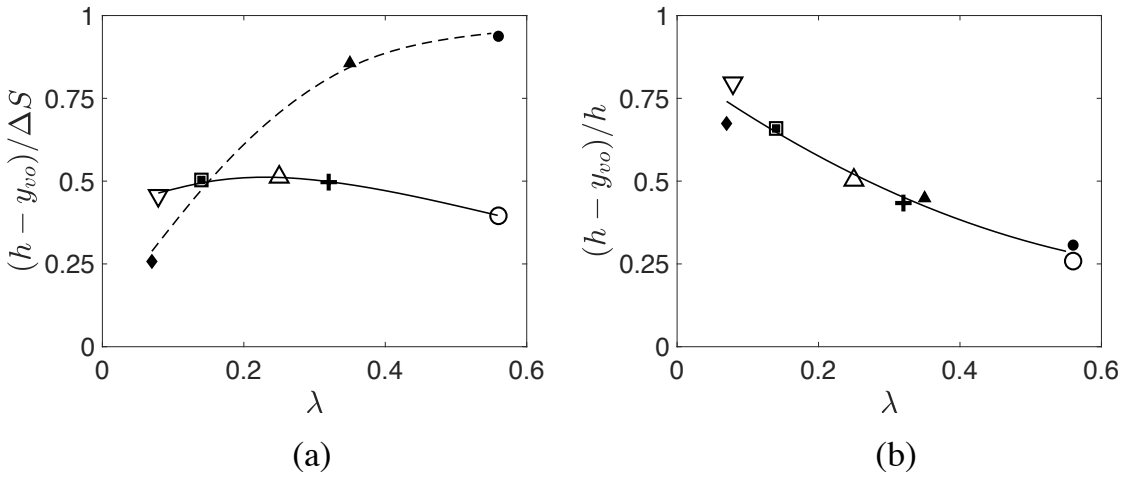


Figure 5.5: Mean location of the virtual origin measured from the canopy tip, as a function of solidity (λ). Panel (a) shows the scaling with ΔS, while panel (b) presents the scaling with the canopy height h (Symbos as in table 5.1. The solid line represents a polynomial fit passing through the virtual origin positions of the full canopy database.

very large the behaviour of the inner region becomes independent of the value of h (or λ) and therefore y/h reaches an asymptotic value.

Next, we look at the characterisation of the outer canopy layer. In particular, figure 5.5 shows the extent of the penetration of the outer flow measured by the distance of the virtual origin from the canopy tip as a function of λ. Differently from the thickness of the inner layer, the thickness of the outer one scales with the canopy height h rather than with the spacing ΔS. Looking at the open symbols distribution in panel (a), it is noticed that the outer thickness keeps roughly the same size as the filament average spacing suggesting that it is ΔS that sets the size of the eddies allowed to penetrate the canopy (Monti *et al.*, 2020). On the other hand, when ΔS is kept constant, the penetration is dictated by h and eventually saturates to unity as the canopy height increases towards the densest regime. Looking at panel (b), it appears to be clear that when $h - y_{vo}$ is scaled with h, a good collapse is observed independently of the way in which the variations of λ has been enforced. This result can be explained by thinking of $(h - y_{vo})/h$ as the fraction of the canopy that the eddies (allowed to penetrate the filamentous layer) are displaced inside the canopy. In other words, ΔS sets the sizes of the eddies allowed to enter the canopy, while h establishes the depth of such penetration. Further discussion

on the size of the characteristic eddies hosted in the canopy and on the variation of the position of the virtual origin will be presented in the following subsection 5.3.3.

In summary, both the profiles of the inner inflection points and of the virtual origin position show a clear dependence with the solidity λ. However, to obtain a data collapse, the inner inflection point locations need to be scaled with the spacing ΔS while the outer flow penetrations, measured through the locations of the virtual origin, collapse when made dimensionless with the canopy height. In turns, this suggests that the nature of the inner flow is set by ΔS, while the flow character of region of the canopy exposed to the outer flow is determined by the canopy height h.

5.3.3 Heuristic model

We next introduce a conceptual model that provides a simple explanation of the variations of the position of the virtual origin of the mean velocity profile (Monti *et al.*, 2020). We will will also discuss the influence of the mean filament spacing on the upwash/downwash events produced inside the canopy by the outer turbulent eddies and discuss how this effect may determine the transition between different canopy flow regimes (Nepf, 2012). The discussion will be based on the effects on the flow induced by a systematic decrease of the average filaments distance ΔS. Since the height of the canopy h is kept constant, the variation of ΔS allows to interpret the canopy as a high-pass filter, with varying pass band, acting on the external eddies. This approach is different from the one used in Monti *et al.* (2020) where the spacing was kept fixed while the filament height was systematically increased thus modulating the penetration length rather than the filter pass band.

We start by considering the sketch in figure 5.6 visualising the relation between the filaments spacing, the canopy height and the size of an eddy. The figure shows that it is the ratio $(\Delta S - d)/h$ that sets the size of the eddies allowed to penetrate and the depth of their penetration. In the case of slender canopies (i.e. $d/h \ll 1$), it is sufficient to consider the magnitude of $\Delta S/h$ to predict the depth of the outer flow penetration and therefore the onset of one of the two asymptotic canopy regimes. In particular, when $\Delta S/h > 1$ (left panel of figure 5.6), the typical width of the canopy voids is larger than

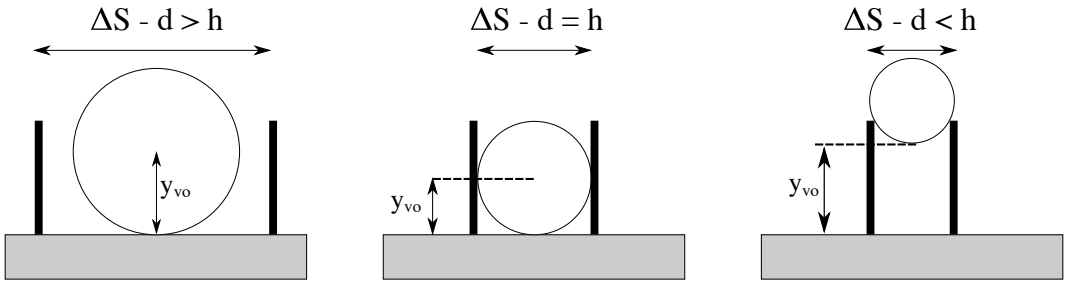


Figure 5.6: Sketch of the largest possible vortex size that can penetrate the canopy from the outer layer and its corresponding location of the virtual origin from the bottom wall. The idealised vortex is presented as a characteristic eddy with diameter $\Delta S - d$.

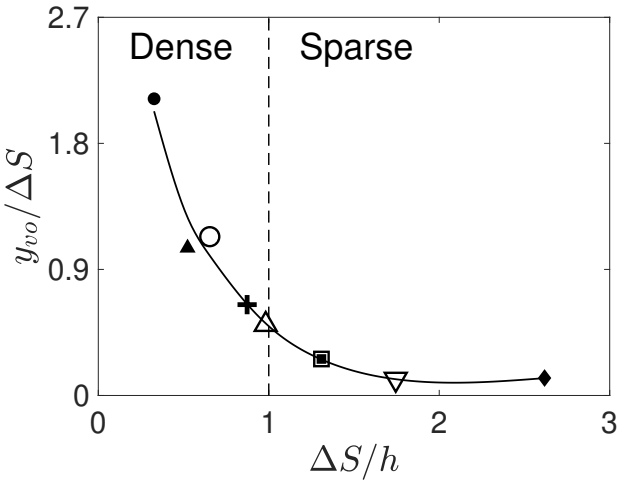


Figure 5.7: Mean location of the virtual origin scaled with the mean filament spacing (ΔS), as a function of the aspect ratio ($\Delta S/h$). See Table 5.1 for symbols.

the size of the characteristic eddy (i.e., $\Delta S > \phi_{eddy}$). In this condition, the mean filament spacing does not set any upper bound on the size of the eddies able to penetrates the canopy (Monti *et al.*, 2020), and the mean location of the virtual origin (y_{vo}) is set by the average distance between the core of the eddy and the bottom impermeable wall. This situation is similar to the one of found for the k-type rough surface (Jiménez, 2004).

Conversely, when $\Delta S/h < 1$ or $\Delta S - d < h$, the outer flow is highly constrained by the mean filament spacing, leading to a flow regime associated with a dense condition. In this situation, only outer structures with size smaller than ΔS can be accommodated in the void regions ($\phi_{eddy} < \Delta S$) of the canopy (see Figure 5.6). When an external eddy has a size larger than ΔS, its interaction with the filaments would lead to a local deformation leading to a penetration length smaller than ΔS (see figure 5.6 (right)).

Thus, when ΔS becomes small (compared to the external eddies size), the position of the virtual origin, seen by the outer flow, moves towards the interface at a distance of $O(\Delta S)$ from the tip of the canopy. This heuristic reasoning leads to conjecture that the mean location of y_{vo} scales directly with ΔS. This presumption is confirmed in Figure 5.7, showing the evolution of the location of the virtual origin, made dimensionless with ΔS versus $\Delta S/h$. The dependence of the virtual origin on the average spacing was previously put forward by MacDonald *et al.* (2018), in the context of turbulent flows that develops over spanwise aligned bars.

Between the two asymptotic conditions (i.e dense and sparse), a transitional condition achieved whenever the canopy aspect ratio is order one (i.e., $\Delta S/h \simeq 1$), will develop. In this situation, the void regions can be idealised as a set of square cavities hosting eddies of size $\phi_{eddy} \simeq \Delta S$. This condition is similar to the one corresponding to turbulent flows over d-type rough surfaces (Perry *et al.*, 1969; Leonardi *et al.*, 2007; MacDonald *et al.*, 2016). From a geometrical perspective, since the distance from the core of an idealised eddy to the bottom wall is half of the filament height, the mean location of the virtual origin would be at $y_{vo}/h = y_{vo}/\Delta S = 0.5$. When considering the MD case, characterised by $\Delta S/h \approx 1$, it is found that the virtual origin is indeed located at the mid-point of the canopy height (see Figure 5.7), indicating the robustness of the proposed transition criterion.

A visual validation of the proposed model can be obtained by considering the instantaneous contours of the streamwise and wall normal vorticity fluctuations on a $y - z$ cross-section of the channel, as shown in figure 5.8. The right and left columns of figure 5.8 represent the streamwise and wall normal vorticity fluctuations components, respectively. Each row from top to bottom represents configurations with increasing solidity or equivalently decreasing aspect ratio. All the figures clearly show the influence of the filtering operation imposed by the canopy on the external flow field. In the sparser regime (i.e., SR and TR), the outer flow fully penetrates the canopy layer and reach the bottom wall. Conversely, the dense regime configurations (i.e., MD, RD and DR) show that it is ΔS that dictates the penetration depth of the outer vortical structures. For the denser cases, we also observe localised fragmentations of large scale vortical structures

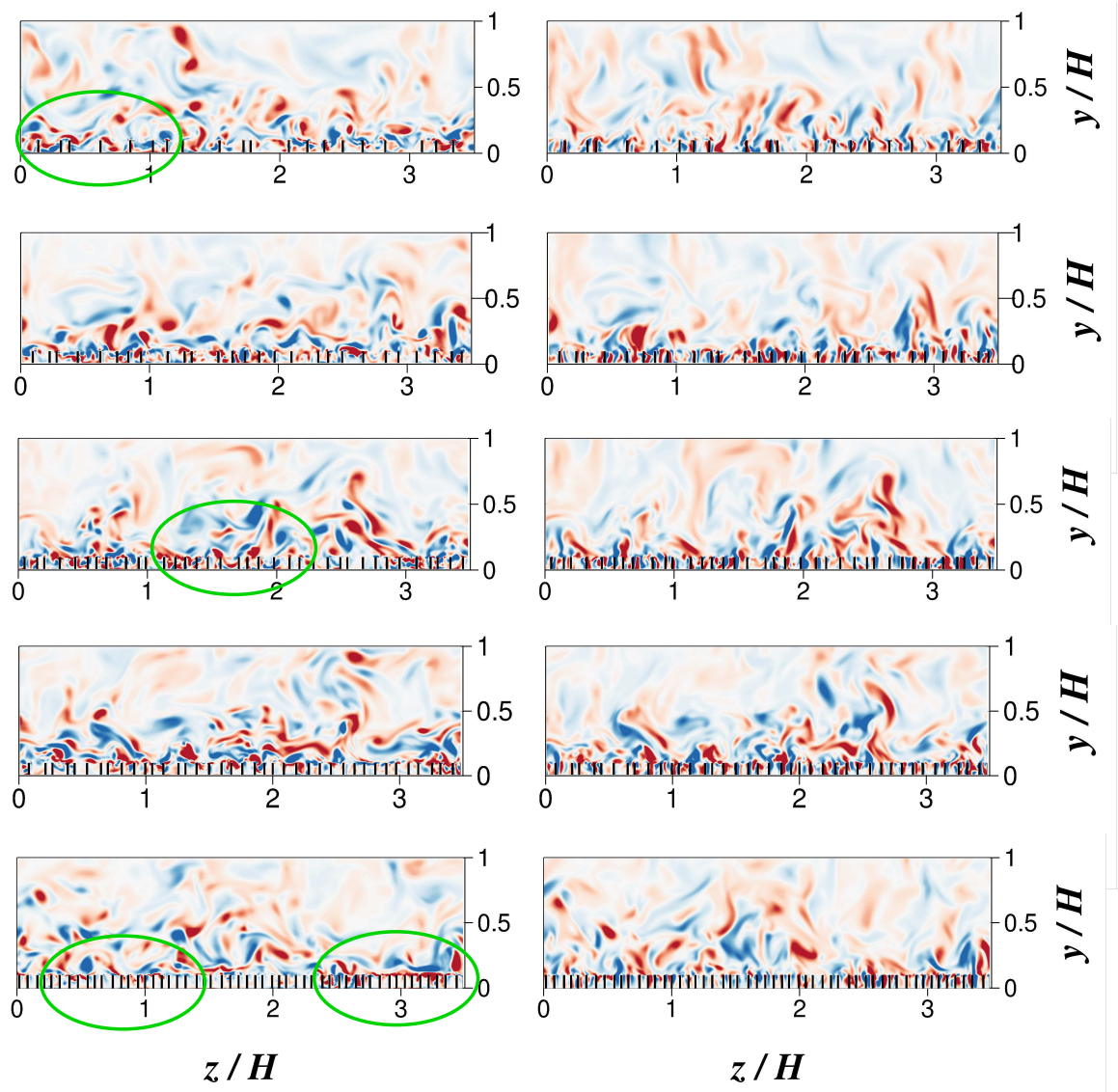


Figure 5.8: Contours of the instantaneous vorticity fluctuations extracted from a $y-z$ cross plane: on the left column ω_x' (i.e. streamwise component) and on the right ω_y' (i.e. wall-normal component). Each row, from top to bottom represents an increasing solidity value (see table 5.1). The colour code, from red to blue represents positive to negative values. The vorticity fluctuations have been made non dimensional with the outer flow variables (i.e., H and U_b), and the corresponding dimensionless vorticity fluctuations $\omega_x' H/U_b$ and $\omega_y' H/U_b$ are both within the range $[-8, 8]$

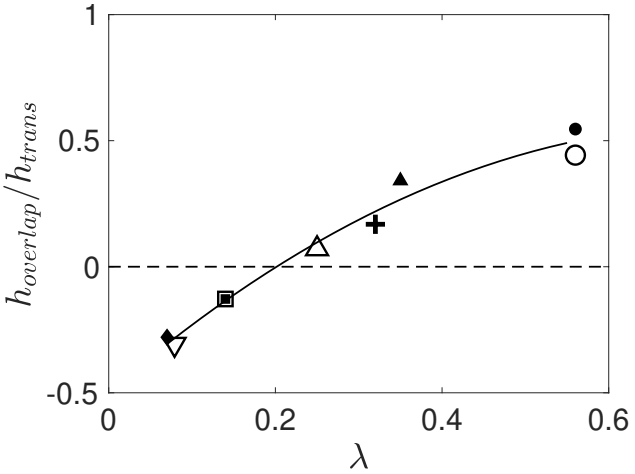


Figure 5.9: Extent of the overlap region, re-scaled with the mean thickness of the transitional layer as a function of λ . The solid line represents the polynomial fit. See Table 5.1 for symbols.

at the canopy interface leading to a partial penetration of the eddies limited to the region closer to the canopy tip (in agreement with the behaviour predicted by the model).

Having established the criterion for the inception of the dense regime (i.e. when $\Delta S - d \simeq h$), we can now provide a sharp estimate of the mean filament spacing (and of the solidity value λ) corresponding to the canopy flow transition. By incorporating the specific geometrical parameters of the canopy used in the current investigation (i.e., $h/H = 0.1$ and $d/h = 0.24$), we obtain $\Delta S/H = 0.124$, which corresponds to $\lambda \simeq 0.15$ or equivalently $\Delta S/h = 1.24$. The value of the transitional λ obtained by varying ΔS for a constant canopy height is almost identical to the one obtained by Monti *et al.* (2020) by modifying systematically the canopy height with a fixed value of ΔS. Moreover, the value $\lambda \simeq 0.15$ is commonly accepted as the threshold that distinguishes between sparse and dense regimes in the context of k-type rough surfaces (Schlichting, 1937; MacDonald *et al.*, 2016). An upper bound for the transition value can be estimated by assuming very slender filaments (i.e. $d/h \ll 1$). The matching condition in such a scenario would simplify to $\Delta S \simeq h$, leading to $\lambda = 0.24$ or equivalently $\Delta S/h = 1$. Alternatively, one could determine the transition value of the solidity empirically, by evaluating the value of λ leading to a zero thickness of the overlap layer (i.e. the distance between the mean virtual origin and the inner inflection point of the mean velocity profile) as done in figure 5.9. From the latter, one can evince that the transition takes place for $\lambda \simeq 0.2$ or equivalently for $\Delta S/h \simeq 1.1$, values falling within the range given above.

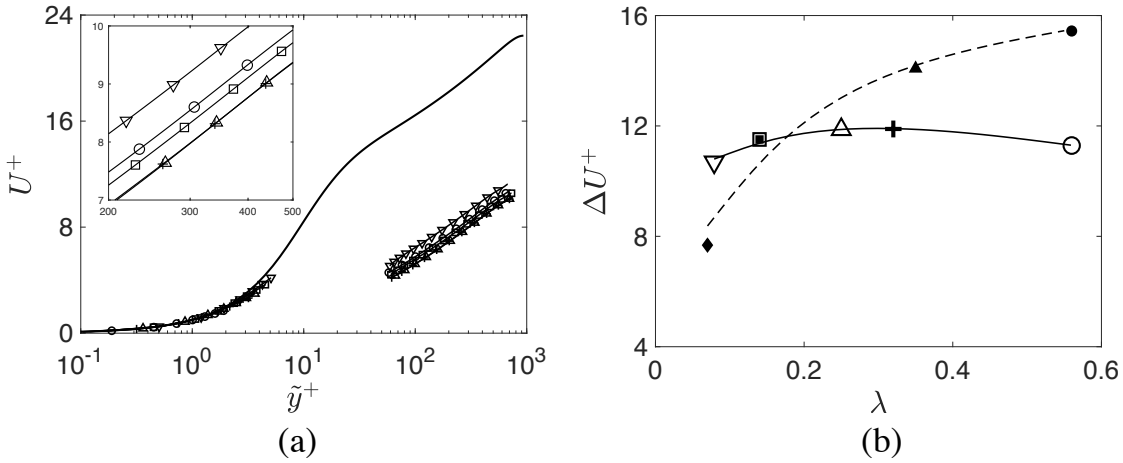


Figure 5.10: Left (a): Mean velocity profiles normalised with the two friction velocities (see text). The abscissa $\tilde{y}^+$ represents the wall normal coordinates in wall units determined using either the inner or the outer friction velocity and considering either the wall or the virtual origin as the zero of the wall-normal axis: $\tilde{y}^+ = yu_{\tau,in}/\nu$ and $\tilde{y}^+ = (y - y_{vo})u_{\tau,out}/\nu$. The solid line without symbols refers to the profile of a canonical smooth wall channel flow at $Re_\tau = 950$ (Hoyas & Jiménez, 2008). The sub-plot positioned at the left, top corner is a magnification the profiles in the logarithmic region. On the right panel (b), the roughness function (Hama, 1954) is plotted as a function of λ for all considered canopies. The solid line represents a polynomial fit for cases obtained varying ΔS (current investigation), while the dashed line represents a polynomial fit for the cases considered in Monti *et al.* (2020). See Table 5.1 for the symbols meaning.

5.3.4 Statistical characterisation of the flow

We start by considering the mean velocity profiles by comparing with the canonical logarithmic law. We will then focus on the characterisation of the diagonal Reynolds stresses. We will also identify the scaling enabling direct comparison of statistical quantities among different canopy configurations. To present the mean velocity distribution, we separate the flow within the filaments layer from the *shifted* external flow developing above the virtual origin. Figure 5.10a shows the mean velocity distribution in semi-logarithmic scale for all the considered solidity values. The mean velocity profiles have been made non-dimensional using two *friction* velocities computed at two wall normal locations: on the impermeable wall (i.e. $y = 0$), using the friction velocity $u_{\tau,in} = \sqrt{\tau_w/\rho}$, and at the virtual origin (i.e. $y = y_{vo}$) using $u_{\tau,out} = \sqrt{\tau(y_{vo})/\rho}$, where τ_w is the wall shear stress at the bed and $\tau(y_{vo})$ is the total stress at the virtual origin (i.e. $\tau(y_{vo}) = \mu\partial\langle u\rangle/\partial y|_{y=y_{vo}} - \rho\langle u'v'\rangle$).

Figure 5.10a reveals that, independently of the solidity value, all the profiles collapse

within the first few wall units $\tilde{y}^+$ indicating the dominance of the wall friction over the filaments drag even for more densely packed canopies. Moving further away from the wall, the modulation imposed by filaments on the mean velocity distribution becomes visible. In particular, the large value of the wall normal permeability has an important impact on the internal flow allowing strong in-rush of wall-normal momentum. This effect is coupled with the wakes generated across the filaments. Outside the canopy, the external profile scaled with the outer friction velocity (i.e., $u_{\tau,out}$) and corresponding viscous length scale (i.e., $\delta_{v,out} = u_{\tau,out}/\nu$), follows a logarithmic distribution with the effect of the canopy reflecting into a shift in the logarithmic region (see subplot in Figure 5.10a). In general, the logarithmic law for the turbulent boundary layer that develops over textured surfaces can be written as,

$$U^+_{out} = \frac{1}{\kappa} log(y^+_{out}) + 5.5 - \Delta U^+ \tag{5.4}$$

The first three terms in (5.4) represent the canonical log-law for a smooth wall . The last term, ΔU^+, known as the roughness function in the context of rough wall boundary layers (Hama, 1954; Jiménez, 2004), is a wall-offset in the logarithmic region that takes into account the momentum deficit/surplus due to the presence of textures on the wall. It is noticed that a drag reduction is characterised by an upward shift (i.e. $\Delta U^+ > 0$) while downward shifts (i.e. $\Delta U^+ < 0$) are associated with an increment in drag. Examples in the context of permeable substrates can be found in Rosti *et al.* (2018*a*); Gómez-de Segura & García-Mayoral (2019), while for rough wall boundary layers see Bechert *et al.* (2000*a*); Jiménez (2004). Figure 5.10a, shows that all the considered canopy configurations present a drag increment and that the magnitude of the roughness function is highly dependent on λ. A negative value of ΔU^+ in (5.4) is in agreement with previous studies on flow bounded by anisotropic porous media that have generally associated a drag increase with porous media characterised by a dominating wall normal permeability component ($\phi_{yx} > 1$). The relaxation of the impermeability condition at the wall leads to an increase in the Reynolds stresses at the interface inducing the onset of vorticity structures that are highly correlated in the spanwise direction (Rosti *et al.*, 2018*a*; Gómez-de Segura & García-Mayoral, 2019), a situation that resembles the observed generation

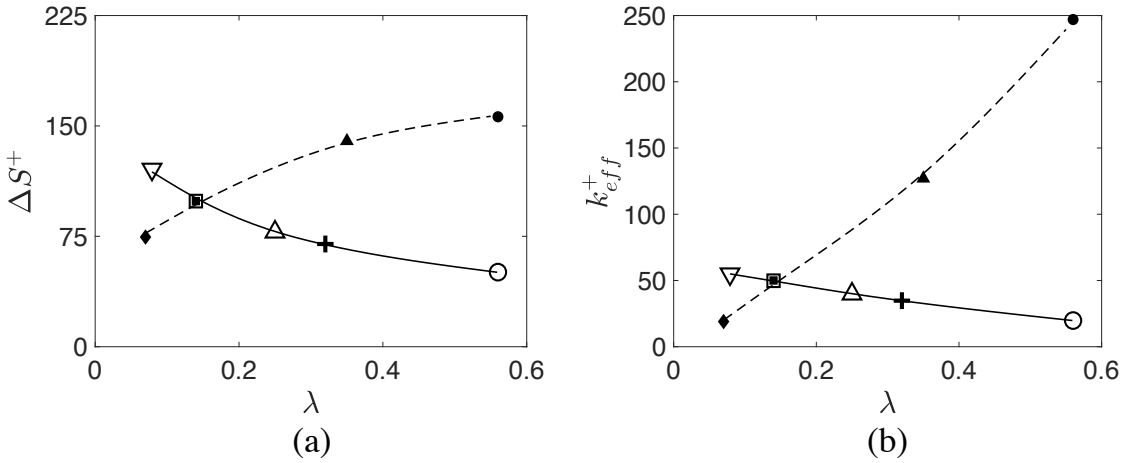


Figure 5.11: Mean filament spacing (a) and effective canopy height (b) expressed in outer wall units ($u_{\tau,out}$), as a function of λ for all considered canopies. See Table 5.1 for symbols.

of spanwise rollers in the context of canopy flows (Nepf, 2012; Finnigan, 2000). Figure 5.10b shows ΔU^+ as a function of the solidity λ for the present cases and the ones studied by Monti *et al.* (2020). Differently from the asymptotic saturation observed when λ is varied by changing the canopy height, in the present case figure 5.10b (solid line) reveals a quadratic behaviour of ΔU^+ with increased λ values. In particular, it is noticed that maximum friction is obtained for the MD case, corresponding to the transitional threshold value $\Delta S/h = 1$. A similar friction distribution was also reported by MacDonald *et al.* (2016) in the context of a wall carved with a three dimensional sinusoidal pattern with varying roughness solidity (λ_r). The authors report that in the sparse regime, the drag increases monotonically with λ_r reaching a maximum value corresponding to the onset of the dense regime. The subsequent decrease of ΔU^+ for increasingly denser regimes was attributed to the shielding effect of the upstream elements and the decoupling effect of the inner and outer boundary layers. Similarly, in the present case the canopy seen by the outer flow can be modelled as a textured wall with cylindrical roughness elements $k_{eff} = h - y_{vo}$ tall extruding from a virtual wall located at $y = y_{vo}$ with an average spacing of ΔS. Alternatively the canopy can also be modelled as an anisotropic porous layer with a porous Reynolds number ΔS^+ given by equation 5.5 (Rosti *et al.*, 2015; Kuwata & Suga, 2017; Suga *et al.*, 2018; Rosti *et al.*, 2018*a*).

In summary, the canopy seen by the external flow can be interpreted as a rough

wall whose roughness elements mean spacing and effective height, expressed in outer wall units, are given by:

$$\Delta S^+ = \frac{\Delta S u_{\tau,out}}{\nu}, \quad k^+_{eff} = \frac{k_{eff} u_{\tau,out}}{\nu} \tag{5.5}$$

The values of ΔS^+ and k^+_{eff} for all the canopies configurations considered here and in Monti *et al.* (2020) are plotted in figure 5.11a and 5.11b, as a function of the solidity λ. Figure 5.11 shows a very different behaviour for solidity values varied using the height or the mean spacing. In particular, the distributions of ΔS^+ and k^+_{eff} found for the canopies considered in Monti *et al.* (2020) show a monotonous increase with λ with a possible saturation of the porous Reynolds number for very dense cases. In these cases, as the canopy becomes denser (i.e., $k^+_{eff} >> 1$), the drag imposed by the elements dominates over the viscous one, which is often associated with the fully rough regime of a *k*-type rough surface (Jiménez, 2004; Flack & Schultz, 2014). Differently, in the present case where λ is increased by shortening the average filaments spacing, a decrease in both ΔS^+ and k^+_{eff} is observed for increasing values of λ. An explanation of this behaviour can be based on the heuristic model introduced in 5.3.3 that suggests a decoupling of the external flow from the flow developing within the canopy region for densely packed canopies. Figure 5.11a and 5.11b, show that the effective canopy height and mean spacing for the densest considered case (i.e. the DR case) are $\Delta S^+ \approx 50$ and $k^+_{eff} \approx 20$, respectively. These values correspond to the condition for the breakdown of the drag reduction regime in walls covered with riblets (Bechert *et al.*, 2000*a*; Garcia-Mayoral & Jimenez, 2011). A decreasing effective height and drag in the dense regime (i.e., when $\lambda > 0.15$), can be related to the departure from a fully rough regime and the onset of a transitionally rough regime as previously reported in Jiménez (2004) and in Thakkar *et al.* (2018). The transitional regime is characterised by a complex dynamical interplay between the drag offered by the roughness elements and the viscous drag (Flack, 2018). The *equivalent sand roughness* (k_s), another way of characterising the effect of non-smooth walls (Schlichting, 1937; Bradshaw, 2000; Jiménez, 2004), was introduced as an abstract measure of the height of a closely packed grains of sand that would produce the same frictional drag in the fully regime (i.e., $k^+_s \geq 70$) (Nikuradse, 1933). Based on

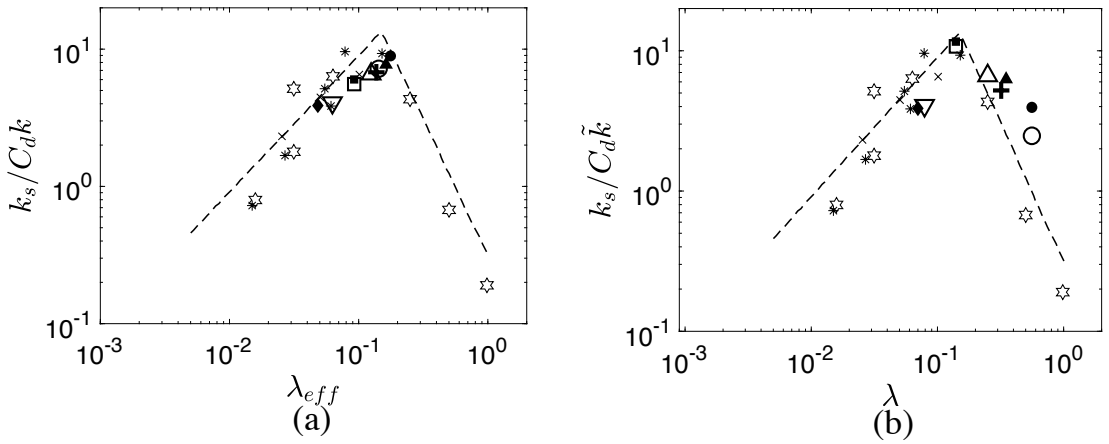


Figure 5.12: Non dimensional form of equivalent sand roughness (k_s/k) as a function of the effective solidity (λ_{eff}) (a) and solidity (λ) (b). The value of k_s/k have been rescaled with a filament drag coefficient C_d (Jiménez, 2004) computed at the mid-location of the filaments, where the localised flow is unaffected by the fixed and free ends. The dashed lines are from Jiménez (2004). See Table 5.1 for symbols. Other symbols represents non-circular roughness elements: $*$ - spanwise fences (Schlichting, 1937); 'x' - spanwise fences (Webb *et al.*, 1971); .

the collapse of the roughness function in the fully rough asymptotic condition (Flack & Schultz, 2014), k_s can be defined via a modified law of the wall (Jiménez, 2004) as:

$$U^+_{out} = \frac{1}{\kappa} log\left(\frac{y - y_{vo}}{k_s}\right) + 8.5 \tag{5.6}$$

The ratio of k_s/k (where k is the roughness element height) and the roughness solidity λ_f turn out to be strongly related. As for the canopy flows considered here, large or small solidity values promote two different k-type regimes, respectively termed as *dense* and *sparse* (Schlichting, 1937; Raupach *et al.*, 1991; Jiménez, 2004). In particular, for surfaces with roughness solidity $\lambda_f \leq 0.15$, the value of k_s/k increases linearly with $log(\lambda_f)$, while when $\lambda_f > 0.15$, the shielding effect of the roughness elements starts to kick in leading to a decrease of k_s/k. In the framework of rigid canopy flows, Monti *et al.* (2020) considered the outer portion of the canopy as a k-type rough surface with effective roughness height $k = k_{eff} = h - y_{vo}$ and effective solidity $\lambda_{eff} = dk/\Delta S^2$.

Figure 5.12a shows the relationship between k_s/k and λ_{eff} across all cases. In the figure, the value k_s/k has been corrected with the drag coefficient computed at the filament mid length (Jiménez, 2004). From the figure, it appears that k_s/k increases monotonically with λ_{eff}, suggesting that all the considered canopies belong to the

sparse k-type regime with only the *canopy-dense* cases (i.e., RD, DR, MDM and DRM) in transitional condition.

Although the notion of equivalent sand roughness can be useful to link the outer behaviour of the canopy flow with classical experiments on rough walls, the present results suggest that the sole consideration of the external canopy flow is not sufficient to characterise the overall effect of the canopy on the flow developing above the canopy tip. Due to the closely packed arrangement of the filaments, similarly with the dense k-type regime, we also expect the shielding effects to come into play on the onset of the dense regime. These observations lead to propose an alternative scaling able to capture the full effect of the canopy onto the outer flow. In particular, it is proposed to incorporate the effects of the canopy wall layer (i.e., region extending from canopy bed to y_{vo}) and the outer layer of the canopy into a newly defined roughness height $\tilde{k}$ as,

$$\tilde{k} = \begin{cases} h - y_{vo}, & \text{if } \lambda < 0.15 \\ y_{vo}, & \text{if } \lambda \geq 0.15 \end{cases} \tag{5.7}$$

Note that the modified roughness height depends on the respective canopy flow regime. The definition (5.7), in the dense regime, is suggested by the shrinkage of the outer layer of the canopy resulting in the decoupling of the external and internal boundary layers. In this conditions the canopy wall layer can be interpreted as a highly dense rough surface with the origin of the displaced external boundary layer, closely located below the roughness crest (MacDonald *et al.*, 2016, 2018). Incorporating the effect of the canopy wall layer into the ratio $k_s/\tilde{k}$ (as a function of the full canopy solidity λ), enables to capture the full spectrum of the transitional behaviour of the canopy (see figure 5.12b). The SRM, SR and TR cases belong to the sparse k-type regime where the effect of roughness increases linearly with λ with a maximum reached at the transition threshold (i.e., for $\lambda = 0.15$). On the other hand, due to the sheltering effect of the filaments in the denser cases (i.e., MD, MDM, RD, DR and DRM), the value of $k_s/\tilde{k}$ decreases as the solidity is increased. It should be noted that the data scatter visible in figure 5.12, was attributed to the inconsistent way in which the drag coefficient was introduced (Jiménez, 2004). However, the proposed scaling reveals to be reasonably successful in characterising the canopy in the sparse-dense roughness map.

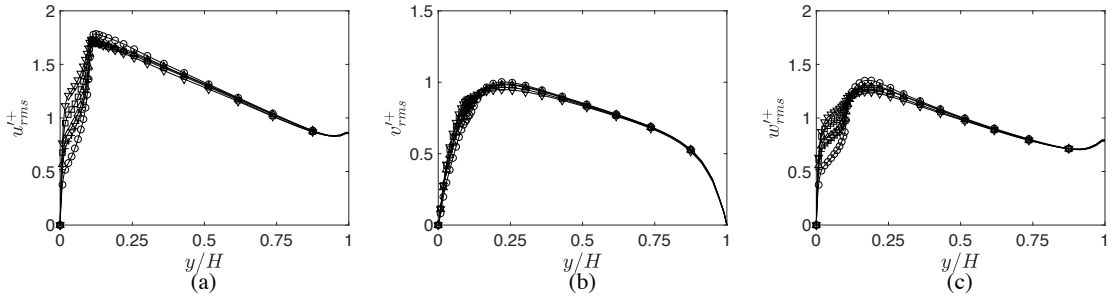


Figure 5.13: Diagonal Reynolds stresses plotted as a function of the wall normal coordinate in external units (H). The stresses are scaled with the *outer* friction velocity (top row) computed at the virtual origin ((5.2)). Left to right the panels represent the streamwise (a), the wall normal (b) and the spanwise (c) components, respectively. See table 5.1 for symbols.

Next, we turn our attention to the distribution of the diagonal Reynolds stress and the associated viscous scales that enables a direct comparison among the various canopy configurations delivering further insights on the properties of the turbulent flow. Figure 5.13, shows the profiles of the *rms* of the velocity fluctuations. These have been scaled with the outer friction velocity, based on the total stress evaluated at the virtual origin (see Equation 5.2). The profiles collapse in the region outside the canopy, confirming the outer layer similarity hypothesis (Townsend, 1976), while the inner layer presents a substantial modulation in both the streamwise and spanwise components induced by the in-plane solidity. Differently, the modulation observed in the wall normal component is weaker. The streamwise and spanwise components of the DR case distributions share strong similarities with the respective components reported in DNS studies of turbulent shear flows over porous media (Breugem *et al.*, 2006; Rosti *et al.*, 2015; Gómez-de Segura & García-Mayoral, 2019). It is possible to mitigate the mentioned modulation by choosing a *local* velocity scale based on the total stress as

$$u_{\tau,l} = \sqrt{\frac{\nu \partial \langle U \rangle / \partial y - \langle u'v' \rangle}{1 - y/H}} \tag{5.8}$$

This choice corresponds to the scaling proposed in the context of canopy flows (Monti *et al.*, 2019; Sharma & García-Mayoral, 2020*a*) and in the case of manipulated wall bounded turbulent flows (Jiménez, 2013; Tuerke & Jiménez, 2013). The friction velocity (5.8), incorporating the pressure gradient and the overall effects of drag due to the filaments, leads to the recovery of a linear variation of the total, dimensionless stress

profile. The diagonal stress profiles made non-dimensional with the *local* friction velocity (5.8) are presented in figure 5.14. We observe a good collapse of the profiles that exhibit a smooth-wall like trend, particularly in the canopy region (Sharma & García-Mayoral, 2020*a*). The diagonal Reynolds stresses profiles shown in figure 5.14 feature an almost bi-modal distribution, with two peaks located in the inner and in the outer regions. The magnitude of the former increases with λ for all three components. We next focus on the choice of a relevant length scale considering both an outer (i.e., the open channel height H) and an inner length scale. (5.8). The latter may depend on the three length scales that determine the geometry of the canopy (i.e., d, h and ΔS) and can be reduced to the influence of two if the filaments are sufficiently slender (i.e., $d/h << 1$) to disregard the effect of the filament diameter. In this case, when only the spacing and height of the canopy matter, it is possible to follow the approach suggested by Monti *et al.* (2020) by introducing a dimensionless stretching factor

$$y^+_\alpha = \frac{1}{\alpha}\frac{u_{\tau,l}y}{\nu} \qquad \text{where } \alpha = [h/H, \Delta S/H] \tag{5.9}$$

In (5.9), if the stretching factor is set to unity, we recover a *local* friction Reynolds number (i.e. $Re_{\tau,l} = u_{\tau,l}y/\nu$), while the choice between either $\alpha = h/H$ or $\alpha = \Delta S/H$ depends on the expected flow canopy regime. Monti *et al.* (2020), suggest that the appropriate stretching factor for the sparser configurations, is the non-dimensional form of the average filament spacing, while the dimensionless canopy height is more relevant for the dense regime. We have tested the proposed scaling obtaining the *rms* velocity distributions shown in figure 5.15a. From the figure, it appears that the profiles plotted as a function of of y^+_h do not exhibit a unified behaviour despite the fact that the MD, RD and DR configurations fall in the dense regime (a common value of α set to h/H for all the dense cases). On the other hand, we observe a good collapse of the profiles when α is set to the value $\Delta S/H$, with the exception of the DR case, which will be discussed later. This behaviour suggests that $\alpha = \Delta S/H$ is a good choice for the stretching factor across all configurations from the full sparse-dense asymptotic regimes. A final verification of the proposed scaling is provided in figure 5.15d, where

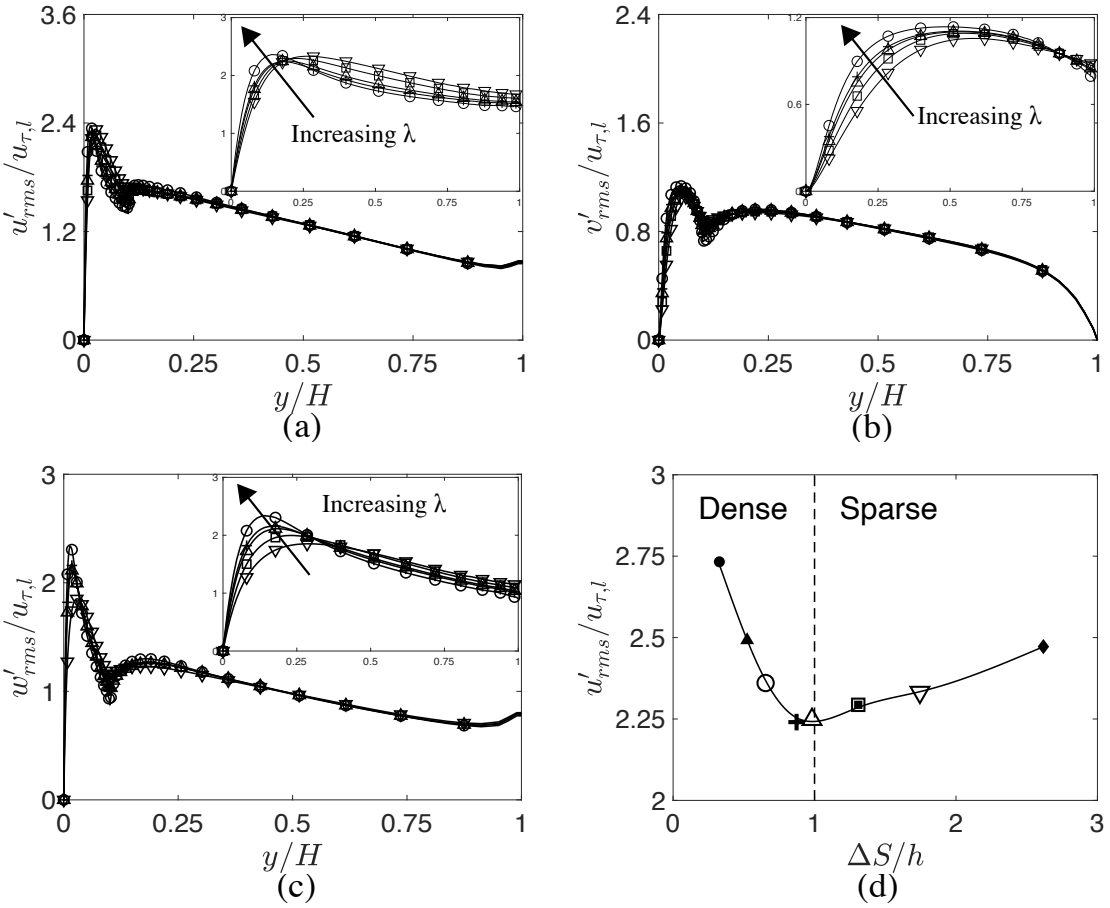


Figure 5.14: Diagonal Reynolds stresses, scaled with the local friction velocity, plotted as a function of the wall normal direction of the external units (H). The subplots on the top right corner of each panel show the distributions within by the canopy layer. The *a*, *b* and *c* panels represent the streamwise, the wall normal and spanwise component, respectively. Panel *d* shows the magnitude of the internal peak as a function of $\Delta S/h$. See Table 5.1 for symbols.

the contributions from the Reynolds shear and viscous stresses do show a full collapse for all the configurations considered in this work.

We finalise this section by discussing in more details the Reynolds stress distributions across the different configurations. We first consider the wall normal component. A closer examination of the inner layer shown in the subplot of figure 5.14b, reveals a monotonic increase of the peak magnitude, as the value of λ is increased. However, moving towards the canopy tip, a collapse of the distributions is observed. This can be attributed to the fact the wall normal component of the velocity fluctuations is generally unaffected by the stem number density. Differently, increasing canopy heights led to increasing magnitudes of both the internal and the canopy tip peaks (Monti

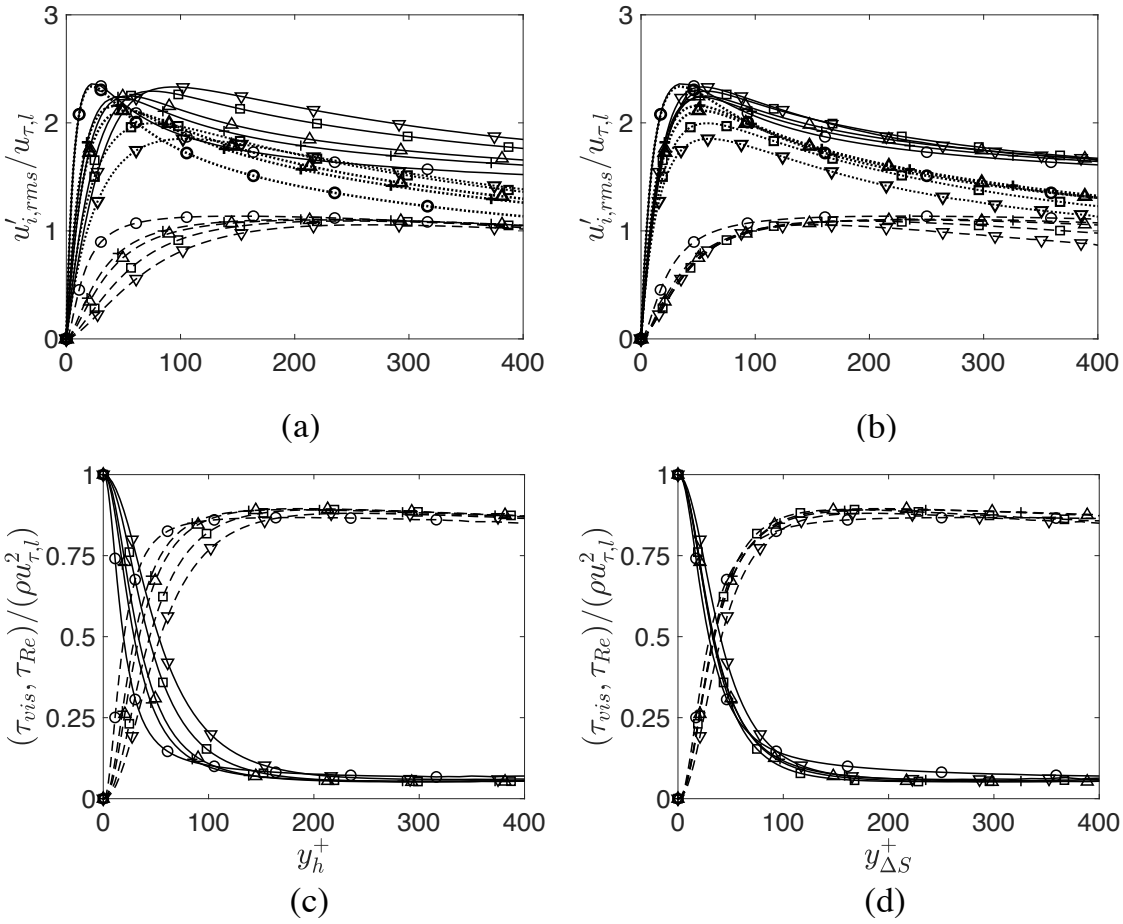


Figure 5.15: Top: Wall normal distributions of the diagonal Reynolds stresses represented as a function of the two stretching factors: h (a) and ΔS (b). The profiles have been normalised by the local friction velocity as in equation 6.3. The solid, dashed and dotted lines represents the streamwise, wall normal and spanwise components, respectively. See Table 5.1 for symbols.

et al., 2020). This indicates that the sweeps and ejections from and to the outer layer are mainly controlled by the wall normal distance to the impermeable canopy bed. Concerning the outer region, the profiles for all the configurations collapse into one curve as in the case of smooth wall turbulent channel flows (Hoyas & Jiménez, 2008), verifying the outer layer similarity.

Next we focus on the wall parallel component and the modulation imposed by the varying filament spacing. The spanwise component distributions are presented in figure 5.14c, where they are plotted as a function of the canopy height. It is noticed that the internal peak presents a monotonic increase in magnitude moving towards the canopy bed as the canopy solidity is increased. This behaviour can be attributed to the increase

of the intensity of the spanwise deviations of the outer logarithmic structures that leave their footprints within the canopy through sweeps and ejections (Monti *et al.*, 2019). Finally, the streamwise component variations present an interesting behaviour, that does not monotonically follow the increase in the value of λ. In figure 5.14d, we present the magnitude of the streamwise peak across all canopies configurations, as a function of the canopy aspect ratio. In sparser regimes, we notice a decrease in the magnitude with $\Delta S/h$, with a minimum located at the transitional threshold $\Delta S/h = 1$. Differently, in denser regimes, we observe an abrupt increase in the magnitude of the peak that simultaneously moves towards the canopy bed. This feature, observed in the denser regimes, suggests the presence of another mechanism that accompanies the onset of the dense regime. Similar behaviours have been reported in the context of transitionally rough surfaces, when the roughness solidity is increased (Abderrahaman-Elena & García-Mayoral, 2016; Abderrahaman-Elena *et al.*, 2019). A more detailed discussion of this mechanism will be provided in the following sections. It is also observed that in the DR configuration, the peaks of the *rms* of the fluctuating velocity components share the same value. This feature is probably the result of the streamwise/spanwise deviations of the flow within the canopy that becomes dominant and 2D uniform in closely packed conditions. Thus, it can be stated that in the densest conditions within the canopy, the flow decouples becoming almost isotropic in the two wall-parallel directions.

5.3.5 Structure of canopy flows

We next focus on the inception and organisation of the coherent structures populating both the intra-canopy and the outer regions identifying the role played by the canopy in-plane solidity. We start by discussing the time averaged flow field determined by using a spatial (i.e. tile based) ensemble averaging procedure. Later, we will focus on the full fluctuating flow field, obtained via triple decomposition and we will consider the energy content of the velocity fluctuations via a spectral decomposition and the 3D autocorrelation functions. We start by considering the time averaged flow fields which have been determined by using the methodology proposed by Monti *et al.* (2020). This technique computes the mean flow field around a filament by considering all the

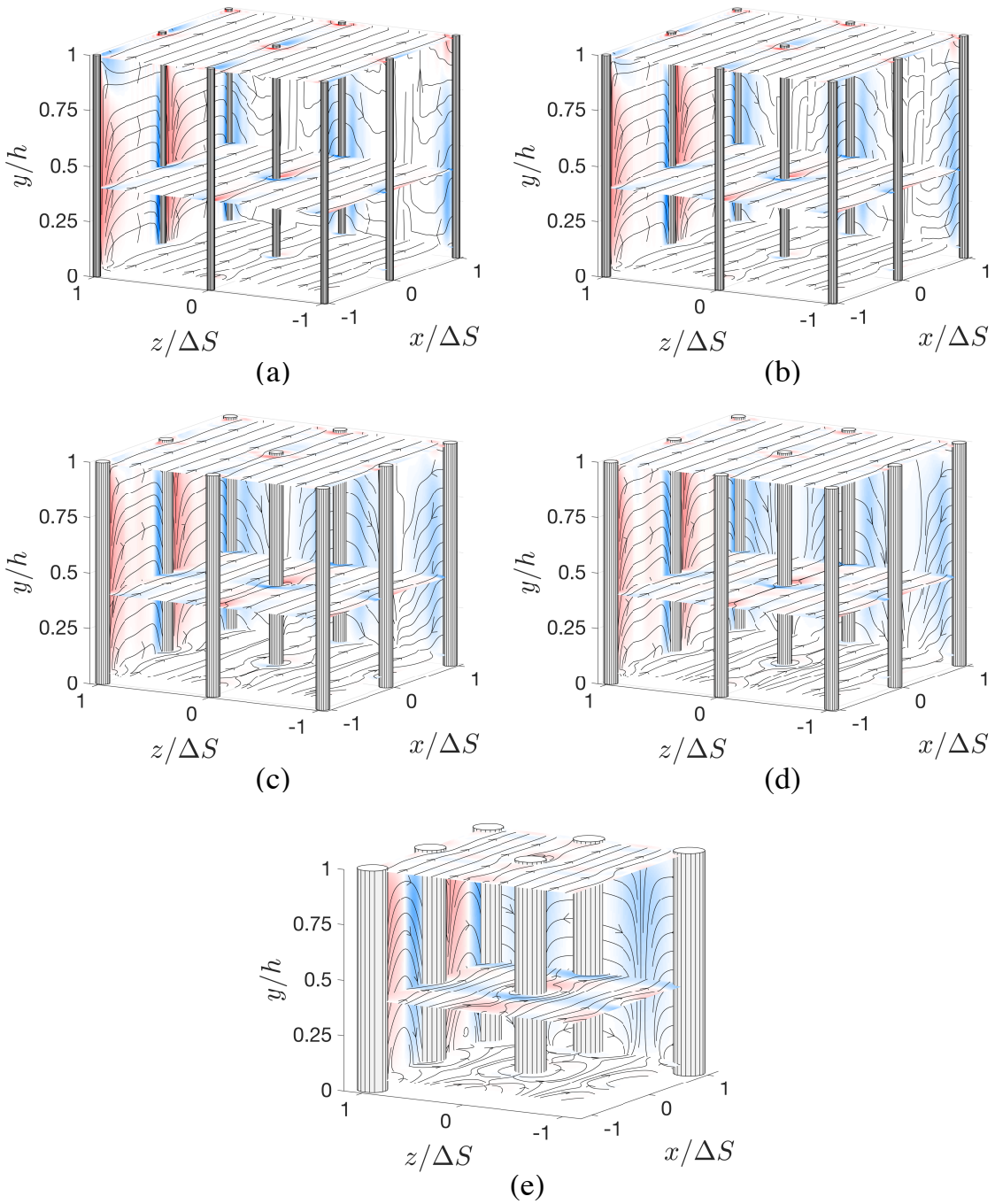


Figure 5.16: Time and tile-ensemble averaged flow fields (see text for description of the averaging procedure) in the intra-canopy region corresponding to the five canopy configurations. The panels a, b, c, d and e correspond to the SR, TR, MD, RD and DR cases respectively. The iso-contours represented in the cross-planes and wall parallel planes, corresponds to the wall normal velocity, with blue and red regions representing negative and positive values within the range $[-0.3, 0.8]/U_b$. The wall parallel planes correspond to the wall normal locations of 5%, 45%, and 95% of the canopy height. The streamlines have been computed using the tile-ensemble averaged flow field.

3D lattices that can be formed by joining nine volumes surrounding any individual tile (i.e. the tile holding each individual filament). To determine the mean flow field, we proceed through three stages: firstly the flow field time average is computed by accumulating the snapshots produced during a full simulation, in a second step the mean flow field is broken into nine volumes that surround each individual filament (i.e. parallelepipeds having the filament set at the origin with a size of 2 tiles in the stream and spanwise directions and an height of H), and finally all the flows corresponding to each volume are ensemble averaged. It should be noted that the decreasing the tile size ΔS, results in more compact tiles limiting the dispersion of the filament positions thus leading to a more organised and homogeneously distributed canopy. The mean flow fields, computed using the above procedure are presented in Figure 5.16 showing both the mean streamlines and the iso-contours of the wall normal velocity that allow to detect localised regions of mean sweeps and ejections. It should be noted that the filaments located at $(x/\Delta S, z/\Delta S) = (-1, 0)$ and $(0, -1)$ of the DR configuration (see Figure 5.16e), have been removed for visual clarity. In the sparser regime (panels *a* and *b*), the wall parallel plane cut at the canopy tip shows a mean ejection and sweep on the frontal and rear sides of the filaments. However, deeper inside the canopy, we observe an opposite behaviour with the transition occurring at a wall normal location of $y/h \approx 0.8$ indicating that the outer flow penetrates the canopy (sweeps) by the rear side of each upstream filament. Closer to the wall, the mean flow deflects around the downstream filament with a partial fraction of the flow ejecting from the stoss side of the filament, inducing a strong deviation of the mean streamlines particularly, in the near wall region. It is also observed that the footprint of the mean sweeps observed at the vicinity of the canopy tip progressively decreases as the canopy sparsity is decreased (see Figure 5.16b, 5.16c and 5.16d). The denser configurations, especially the configurations in the mildly dense regime (i.e., MD and RD), exhibit very weak sweeps on the rear sides of the filaments, indicating a behaviour independent of the distance from the canopy edge (Monti *et al.*, 2020). Another interesting feature can be detected in the DR configuration (see Figure 5.16e) in which the mean streamlines show the presence of a mean vortex occupying the void region in between two neighbouring filaments. The wall normal

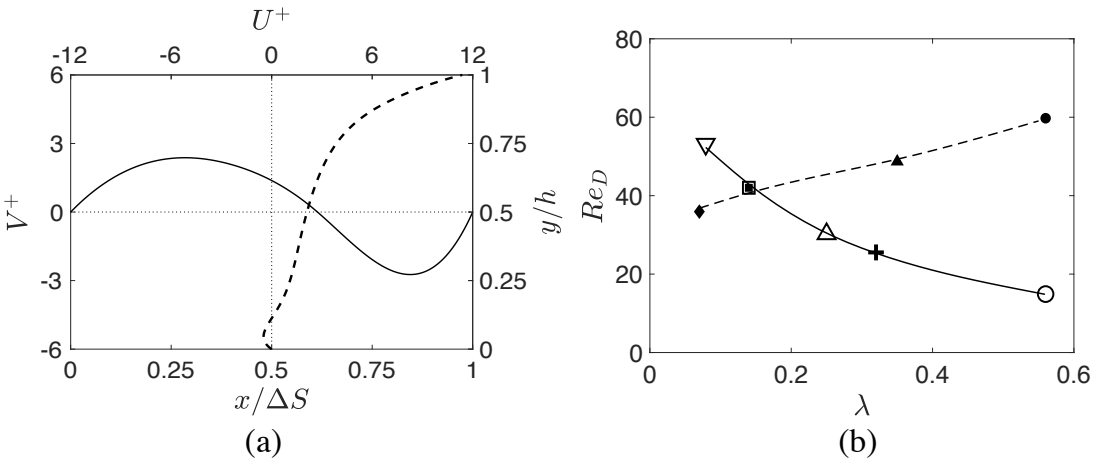


Figure 5.17: Velocity distributions for the DR case seen as a cavity flow (a). Dashed and solid black lines represents streamwise and wall normal distributions. (b) The filament Reynolds number distribution based on the bulk velocity in the canopy layer and the filament diameter for both the actual simulations (solid line) and for the ones conducted in Monti *et al.* (2020) (dashed line). See Table 5.1 for symbols.

position and extent of this mean vortex reinforce the hypothesis of flow decoupling inside the canopy in denser regimes. Indeed, figure 5.16e shows very weak or almost absent mean sweeps at the canopy tip leaving the inner layer almost without any direct kinematic communication with the outer flow. This situation leads to the emergence of a mean vortex standing by the wall, whose diameter is determined by the average filament distance and local Reynolds number. A similar situation has been previously reported in the context of *d*-type rough surfaces (Perry *et al.*, 1969; Jiménez, 2004; Leonardi *et al.*, 2007), that as already mentioned, share several similarities with the present DR configuration (MacDonald *et al.*, 2018). Concerning the mildly dense regime (MD and RD configurations), it is noted that their mean flows are comparable to the fully dense configuration (DRM) of Monti *et al.* (2020). In this condition, the internal and external flows are characterised by a partial decoupling with a moderate interaction between the inner and the outer flows inhibiting the emergence of a stable vortex. The emergence of a mean vortex in the DR configuration can be conceptually understood by interpreting the void region between two adjacent filaments, as a cavity (Prasad & Koseff, 1989; Hou *et al.*, 1995). The non-dimensional numbers that determines the features of cavity flows are its geometrical aspect ratio (i.e., $\Delta S/h$) and the Reynolds number. In the present case, it is the high shear at the canopy tip that drives a cavity-like flow which Reynolds number

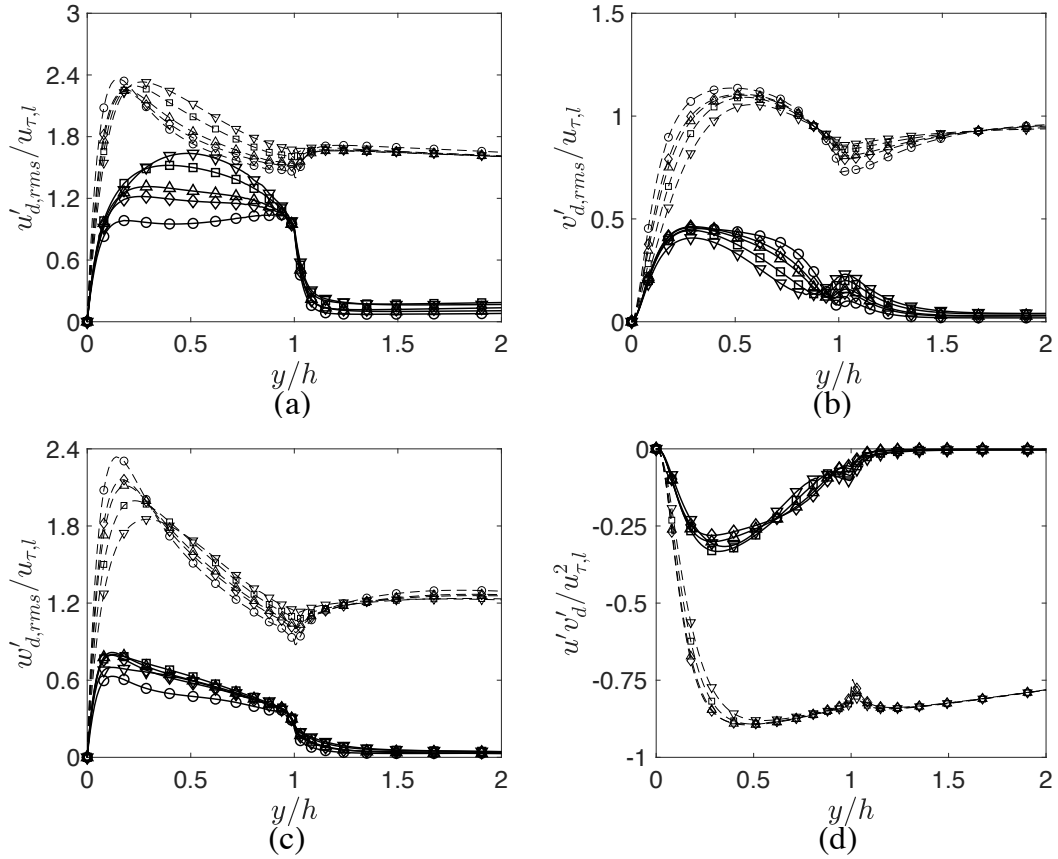


Figure 5.18: Components of the dispersive (form-induced) stresses as a function of the wall normal direction. Panels (a), (b), (c) and (d) represent the streamwise, the wall normal, the spanwise and the anisotropic terms, respectively. The dispersive fluctuations are made non-dimensional with the local friction velocity defined in Equation 6.3, while the wall normal coordinate is scaled with the canopy height. Dashed lines are denoted by the respective velocity fluctuations normalised by the local friction velocity. See Table 5.1 for symbols.

can be related to the local filament Reynolds number. The latter is based on the canopy (internal) bulk velocity (i.e., $U_{b,h} = 1/h \int_0^h \langle U \rangle dy$) and filament diameter and it is shown in figure 5.17b) for various solidity values. As expected, the filament Reynolds number decreases with increasing stem density. In Figure 5.17a, we present the streamwise and wall normal velocity rescaled with the internal friction velocity (i.e., $u_{\tau,in} = (\tau_w/\rho)^1/2$, the relevant velocity scale in the intra-canopy region), versus both the wall parallel distance between adjacent filaments, and the wall normal distance from the canopy bed.

Another mechanism that can be evinced from the mean flows is the sheltering effect exerted by the filaments, which is generally associated with the dense regime (Poggi *et al.*, 2004*b*). To discuss this effect we focus on the mean streamlines shown on the

wall-parallel plane located at the vicinity canopy tip (i.e., $y/h = 0.95$) in figure 5.16. In the sparser conditions (SR and TR configurations), the streamlines deflect around the filament and rejoin past it. In the case of denser canopies, the mean streamlines on the rear side of the filament do not rejoin after the filament on the plane indicating that the filaments now exert a stronger sheltering effect. This behaviour is particularly visible in the DR case. As already mentioned in the previous section, an increased sheltering is accompanied by a decrease in ΔU^+ (see Figure 6.6b), a phenomenon reported by other authors in the context of rough surfaces composed of densely packed elements (Jiménez, 2004; Yang *et al.*, 2016; MacDonald *et al.*, 2016).

Next, we turn our attention to the structure of the fluctuating flow field, both in the internal and external layers of the canopy. Following previous studies (Pedras & de Lemos, 2000; Nikora *et al.*, 2007*a*,*b*; Abderrahaman-Elena *et al.*, 2019; Sharma & García-Mayoral, 2020*b*), we have employed a modified version of the triple decomposition technique, which was originally proposed by Reynolds & Hussain (1972). The adopted technique enables to isolate the full fluctuating flow field from the local influence of the filaments, which is embedded in the mean flow field that was previously discussed. The decomposition is given by:

$$u(x, y, z, t) = \langle \overline{u}(y) \rangle + \tilde{u}(x, y, z) + u'(x, y, z, t) \tag{5.10}$$

$$\tilde{u}(x, y, z) = \overline{u}(x, y, z) - \langle \overline{u}(y) \rangle \tag{5.11}$$

where the instantaneous flow field $u(x, y, z, t)$ is decomposed into a time and spatially averaged field $\langle \overline{u}(y) \rangle$, dependent solely on the wall normal distance, a time averaged, spatially heterogeneous field $\tilde{u}(x, y, z)$, incorporating the dispersive components, and the full time and space fluctuating field $u'(x, y, z, t)$. The triple decomposition allows to analyse in depth the intra-canopy flow where the random assignment of the filament position introduces a spatial heterogeneity in the wall parallel direction. In the region outside the canopy, the triple decomposition should converge to the canonical Reynolds decomposition, typically used in unobstructed flows (Kim *et al.*, 1987).

We start by looking at the dispersive stresses that play an important role on the sparse-dense transition of canopy flows (Finnigan & Shaw, 2008). In Figure 5.18, we

present the three main diagonals ($u'^{+}_{d,rms}$, $v'^{+}_{d,rms}$ and $w'^{+}_{d,rms}$ representing streamwise, wall normal and spanwise directions, respectively) and off-diagonal ($u'v'^{+}_{d,rms}$) terms of the dispersive stress tensor (made dimensionless using the local friction velocity 5.8), versus the wall normal distance, normalised with h. We observe that as λ is increased, the peak intensity of the wall parallel dispersive (form induced) stresses decreases consistently with the results of previous studies (Poggi & Katul, 2008; Sharma & García-Mayoral, 2020*b*). The wall normal component presents an opposite trend, which can be attributed to the rapid mixing induced by the DR configuration (see Figure 5.16). Interestingly, above the canopy we can observe a localised region where the wall parallel dispersive stresses are non-negligible. This region is often associated with the so-called *roughness sub-layer*, an abstract volume characterised by a highly three dimensional field influenced by the geometrical scales of the roughness elements. We also notice that the peaks of the $v'_{d,rms}$ and $w'_{d,rms}$ (see Figure 5.18b and 5.18c), are shifted towards the canopy bed, suggesting that the dispersive stresses are larger within the bottom half of the canopy, in agreement with the hypothesis postulated by Poggi *et al.* (2004*a*). Differently, the $u'_{d,rms}$ peak is located at the mid-location of the filament height.

Next, we look at the fluctuating flow field within the canopy region, home to complex processes which are central to the onset of different canopy regimes. In between them, we explore the possibility of the emergence of another mechanism occurring deep inside the canopy, as firstly put forward by Monti *et al.* (2020). In particular, the authors reported the occurrence of a spanwise modulation of the streamwise velocity fluctuations, in the most dense configuration that they have analysed (i.e., their DRM case). They conjectured that the modulation was due to a partial decoupling of the internal and external layers of the canopy. This phenomenon was often overlooked by previous studies (Finnigan *et al.*, 2009; Bailey & Stoll, 2016), maybe because of a limitation of their numerical methodology that did not allow for a stem by stem resolution inside the canopy. We wish to verify that the coherent motion conjectured by Monti *et al.* (2020) may also occur in the present set of simulations where we track the inception of the dense regime by decreasing the average filament spacing rather than the canopy height. Figure 5.19 presents instantaneous snapshots of the velocity fluctuations in

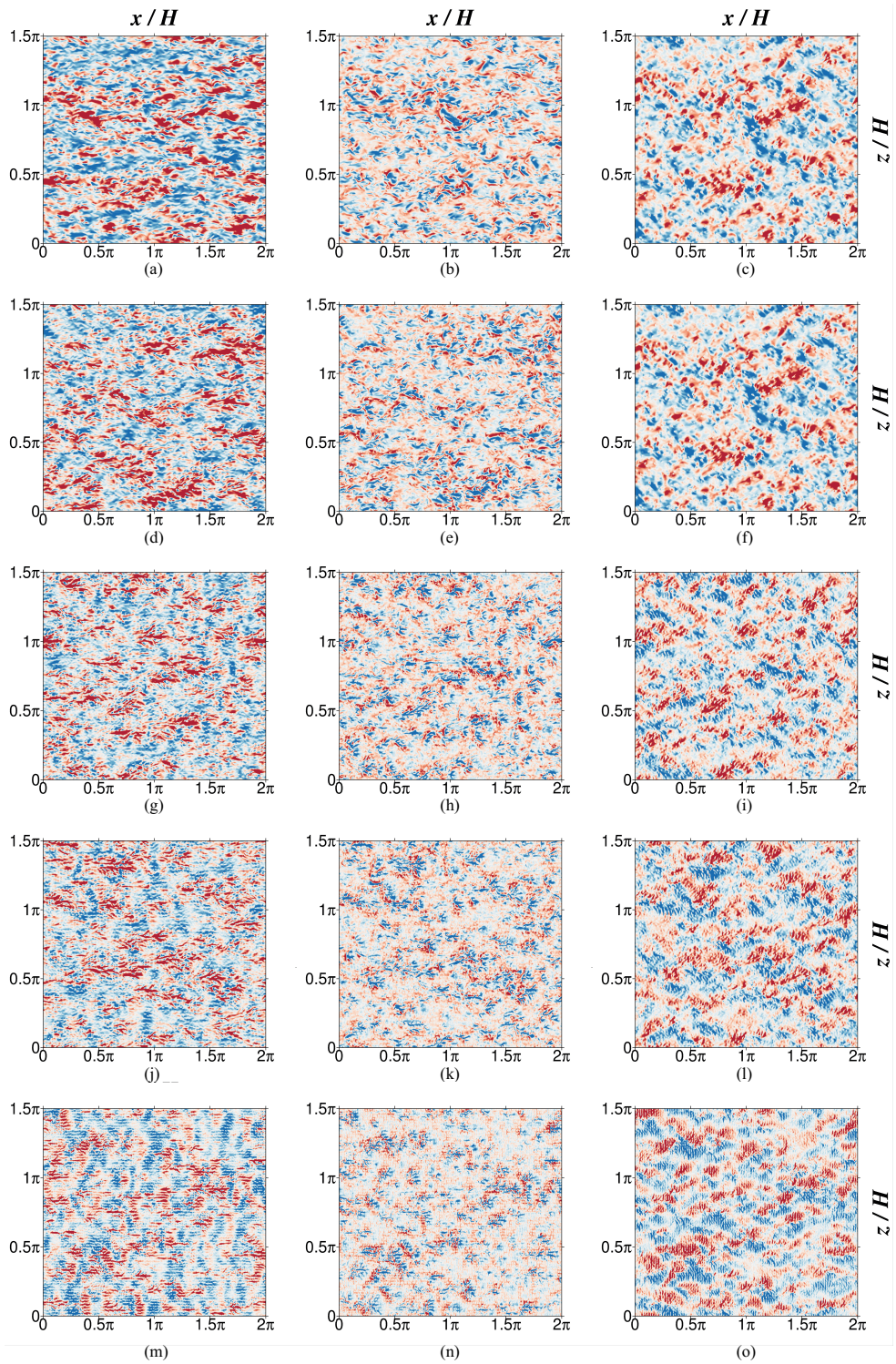


Figure 5.19: Instantaneous realisations of the non dimensional velocity fluctuations in the wall parallel plane located at the inner inflection point. The panels in the rows from left to right represent the three velocity components u', v' and w'. The panels in the columns, top to bottom, display the cases ordered by increasing solidity. The iso-contours have been scaled with the local friction velocity. The colour codes, ranging from red to blue, represent positive to negative values. The velocity ranges are $u'^{+} \in [-3, 3]$, $v'^{+} \in [-2, 2]$ and $w'^{+} \in [-3, 3]$.

the $x-z$ planes (i.e. wall-parallel planes) sampled at wall distances matching the locations of the respective internal inflection points. From the contours, it appears that in the sparser configurations (i.e., SR and TR), the velocity fluctuations are organised in coherent regions that inherit the structure of the external, streamwise oriented vortices. Theses larger patterns coexist with small-scale fluctuations induced by the meandering motions of the fluid around the filaments. As the canopy sparsity is decreased, the modulation of the internal flow field becomes evident. In particular, panel *j* and *m* reveal the presence of a strong spanwise oriented wave-like structure. This movement is embedded within the organised patterns generated by the quasi-streamwise vortices of the MD and RD cases (see panels *g* and *j*). Monti *et al.* (2020), suggested that the spanwise coherent motion, reminding a Kelvin-Helmholtz like instability, is induced by the high wall-normal permeability promoting a directional penetration of the external structures in the form of wall normal jets. Inside the canopy, these penetrations generate streamwise and spanwise modulations as a consequence of the bed impermeability and the solenoidal condition. For the present set of simulations, we have already mentioned that in the denser cases, as in the DR one, a clear decoupling between the inner and the outer layer of the canopy establishes. This suggests that the aforementioned penetration may loose some of its importance when the solidity is increased by packing the filaments as it is also clear from the sequence of panels in the middle column of 5.19 where it clearly appears that the intensity of the wall-normal velocity fluctuations fades away as the canopy get denser. The variation and the organisation of the coherent motions populating the canopy layer can be determined by considering higher order statistics of the full fluctuating field. We start by turning our attention to the two-dimensional two-point auto-correlation function in the streamwise (i.e., with separation Δx) and spanwise (i.e., with separation Δz) directions: i.e.

$$R_{u_i'u_i'} = \frac{u_i'(0,y,0)u_i'(\Delta x,y,\Delta z)}{u_i'^2(0,y,0)} \tag{5.12}$$

The iso-values of positive (0.1) and negative (-0.1) correlation coefficients are presented in Figure 5.20 from where we can have a good insight about the structure of the velocity fields associated with the different regimes. Looking at the central column of the

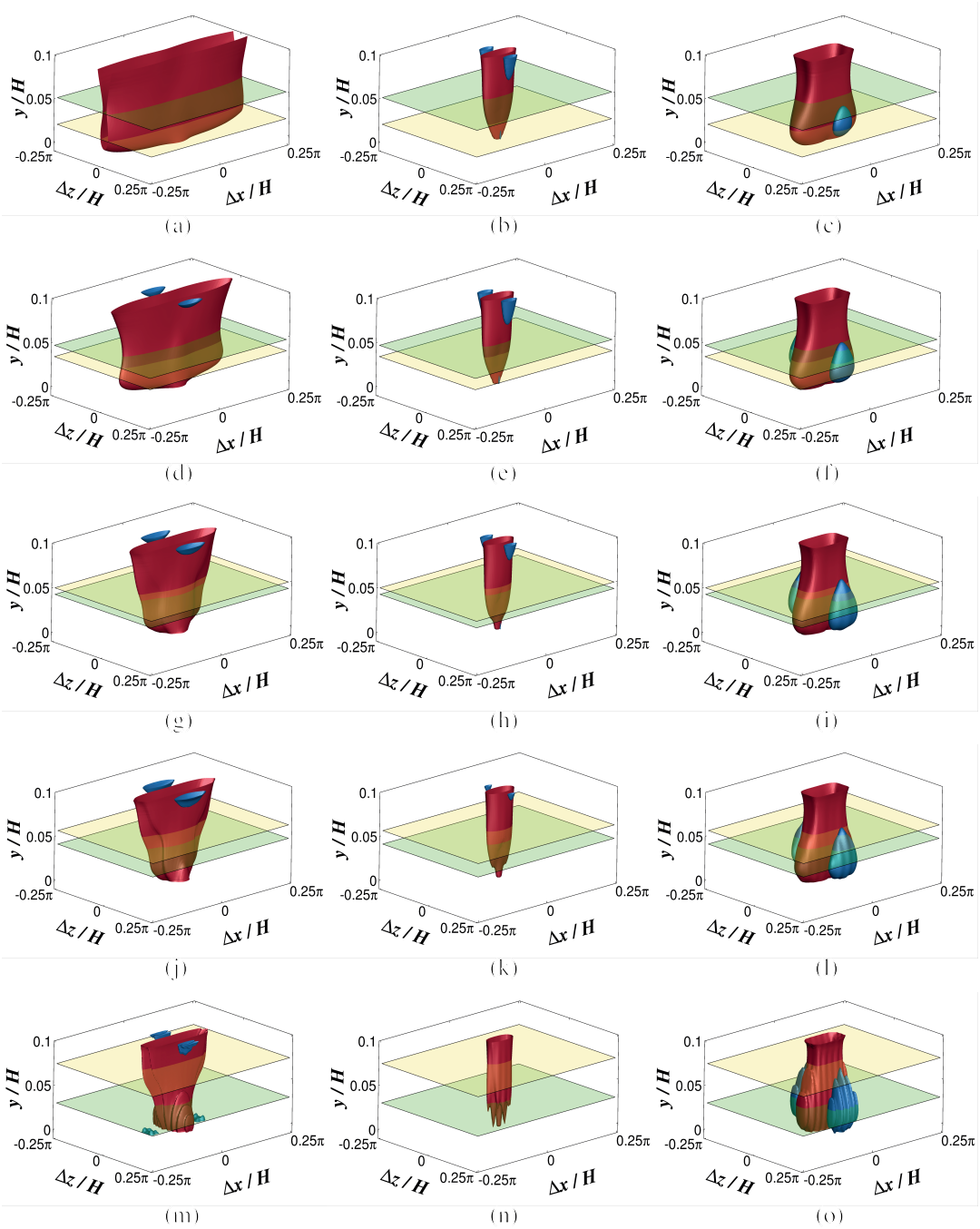


Figure 5.20: Iso-surface of the two-dimensional two-point velocity auto-correlation function shown as a function of the wall-normal distance in the intra-canopy region. The panels in the rows from left to right correspond to the three velocity components, streamwise, wall normal and spanwise, respectively. The panels in the columns, top to bottom, display the cases ordered by increasing solidity. The red and blue iso-surfaces represent the regions of positive and negative correlations. The green translucent slice shows the mean location of the inner inflection point while the yellow one indicates the position of the virtual origin.

panels in 5.20, it is noticed that the red iso-surface which is related with the positive wall normal component correlation does not show any substantial modification as the canopy sparsity is decreased except in the case of the DR configuration that exhibits a spiky-like structure in the region below the inner inflection point (i.e. the green surface). Interestingly, the negatively correlated iso-surface (i.e., the blue region) diminishes in size for increasing values of λ until it totally disappears in the most dense case. Differently, the spanwise correlation function (right column of Figure 5.20), reveals that the negative correlation iso-surfaces feature a lobe spanning almost all the interior of the canopy with a size that increases with the solidity value. On the other hand, the extent of the positively correlated iso-surfaces remains unchanged. The streamwise correlation function (left column of Figure 5.20) presents the most interesting behaviour, showing that the increase in the in-plane solidity leads to a modification of the coherence length and direction. In particular, the SR case show a long-scale correlation in the streamwise direction above and across the canopy corresponding to the snapshot captured in the top, left panel of figure 5.19. This consistent behaviour is associated with the quasi-streamwise vortices that penetrate the canopy from the outer the logarithmic region via unconstrained (very high wall-normal permeability) sweep events. It should be noted that the structure visible in top, left panel of figure 5.20 is open-ended in the streamwise direction as a consequence of the size that has been chosen to compute auto-correlation function. As the canopy sparsity decreases, the penetration of the external vortices allowed into the canopy is discriminated by ΔS. Indeed, the DR configuration reveals the shortest streamwise coherence length at the top of the canopy. As discussed previously in section 5.3.3, the external structures approaching the canopy-tip are exposed to large deformations losing their streamwise coherence. On the onset of the dense regime, the streamwise correlation function exhibits a strong dependency on the wall normal direction coordinate. In particular, we notice a decrease in the streamwise coherence as the distance from bottom impermeable wall decreases. Differently the spanwise coherence gains more importance in the vicinity of the wall. We also observe that in the densest case, the plane located at the inflection point reveals two detached regions of negative correlation developing in the spanwise direction (see Figure 5.20m). This

feature corresponds to the wave like structure also visible in the instantaneous snapshots of Figure 5.19m, suggesting the potential, coherent motions at the vicinity of the internal inflectional point would be characterised by a set of spanwise oriented vortices. These can only be detected when the influence of the outer turbulent structures is removed from the canopy layer. Differently to the structures generated by the inflectional instability occurring at the canopy tip, which losses part of its coherency by merging with the outer logarithmic structures (Monti *et al.*, 2019), the spanwise coherency of the internal ones is preserved by the complete decoupling of the internal and external canopy regions. We also expect these internal vortices to be influenced by the blocking effect of the canopy bed. It is indeed observed that with the exception of the densest case, the streamwise correlation function exhibits a kink in the spanwise direction for all the canopy configurations. We can conclude that the turbulent flow field in the canopy layer is mainly fed by the outer layer structures penetrating the filaments bundle coupled with the canopy sparsity which generates wall normal jets that impinges the bottom impermeable wall. These jets only operates by feeding structures confined next to the inflectional point of the mean velocity profile.

Further insight into the overall structure of the fluctuating flow field can be obtained by considering the spectral energy content of the fluctuating velocity components. In Figure 5.21 and 5.22, we present the one-dimensional pre-multiplied spectra, re-scaled with the local friction velocity (see Equation 5.8), as a function of the streamwise and spanwise wavelengths, respectively. The spectra is organised as a 5×3 matrix, with the columns corresponding to the three velocity components and the rows ordered according to increasing values of λ (i..e. the sparsest at the top and the densest at the bottom). All the panels in Figure 5.21 and 5.22, feature two peaks, located below and above the canopy tip, corresponding to the wavelengths $\lambda_x/H \simeq 1$ and $\lambda_z/H \simeq 1$. In particular, the outer spectral peaks are related with well known coherent structures populating the external flow: the streaks of the streamwise velocity field with the associated quasi-streamwise vortices, and the spanwise oriented rollers, ubiquitous in canopy flows. A more detailed account of the outer structures will be provided later. Concerning the internal spectral peak (i.e., found for wall distances $y/H \leq 0.1$), we can identify two different situations

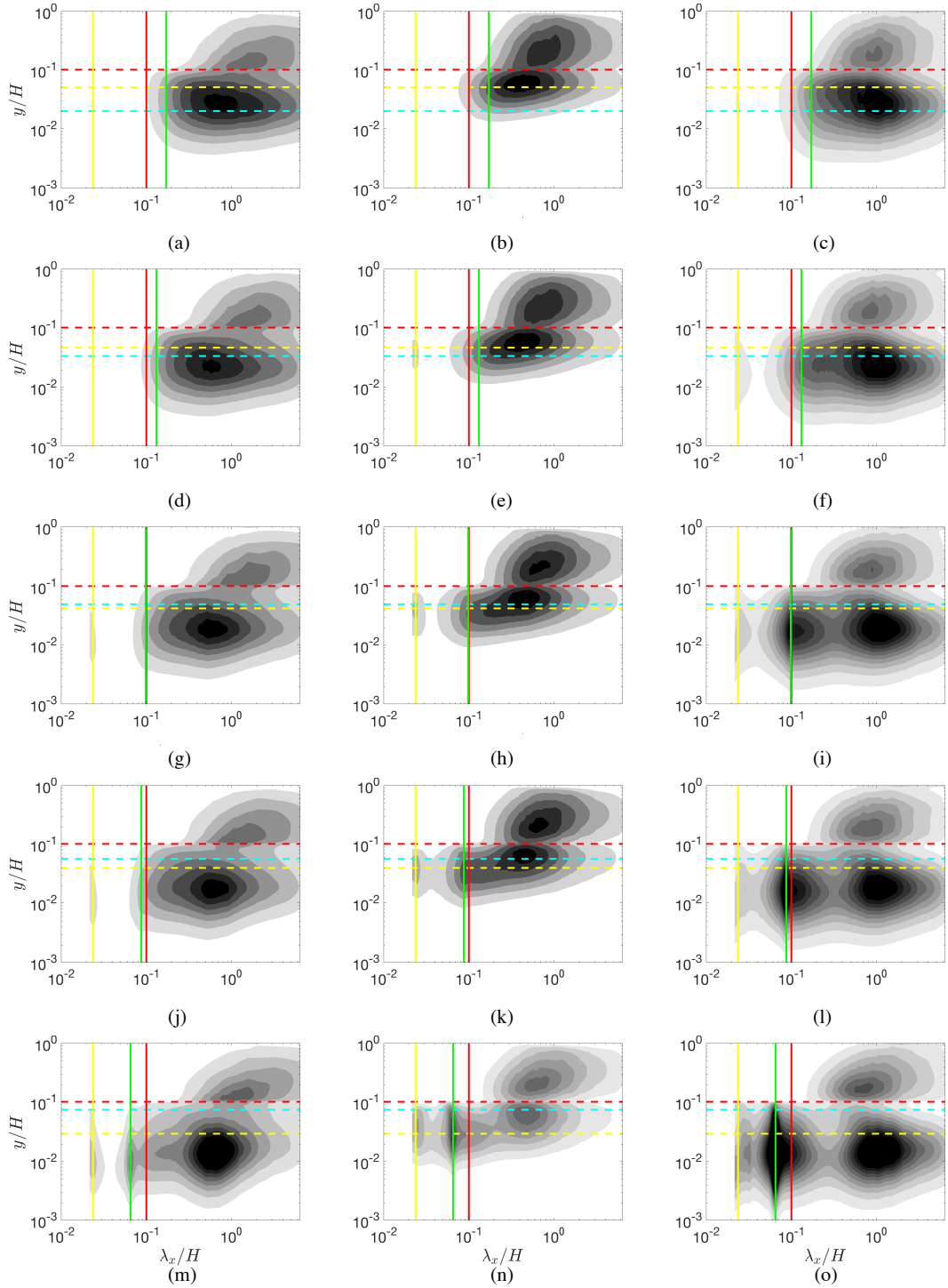


Figure 5.21: Premultiplied spectra of the fluctuating velocity components represented as a function of the streamwise wavelength (λ_x/H) and wall normal distance (y/H). The rows, left to right refer to the three velocity components, with the first column (a,d,g,j and m), second column (b,e,h,k and n) and third column (c,f,i,l and o) representing the pre-multiplied spectra $\kappa_x\Phi_{u'u'}/u^2_{\tau,l}$, $\kappa_x\Phi_{v'v'}/u^2_{\tau,l}$ and $\kappa_x\Phi_{w'w'}/u^2_{\tau,l}$, respectively. Solidity decreases moving from top to bottom.

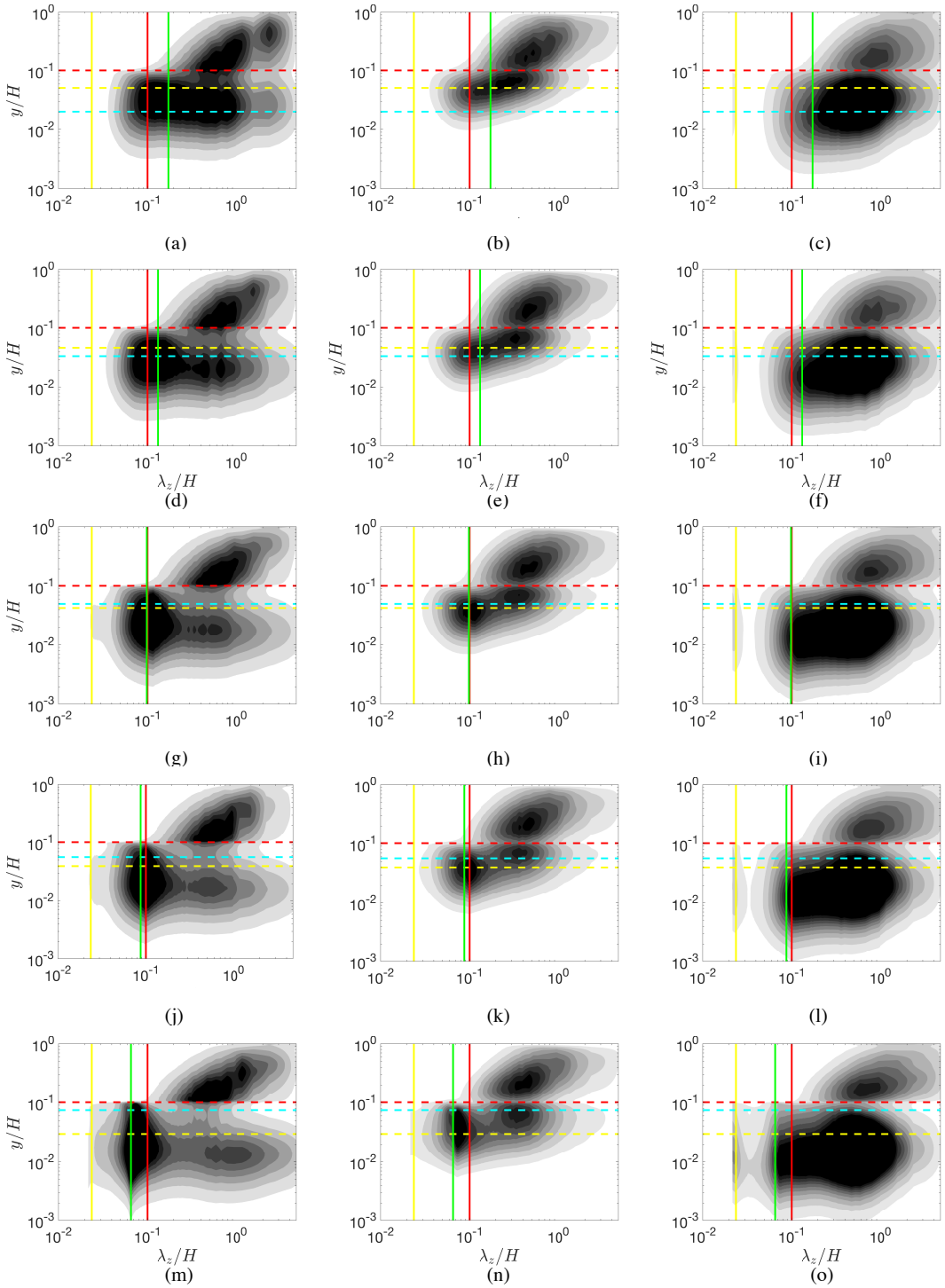


Figure 5.22: Premultiplied spectra of the fluctuating velocity components $\kappa_z\Phi_{u'u'}/u^2_{\tau,l}$, $\kappa_z\Phi_{v'v'}/u^2_{\tau,l}$ and $\kappa_z\Phi_{w'w'}/u^2_{\tau,l}$ represented as a function of the spanwise wavelength (λ_z/H) and wall normal distance (y/H). Panels ordered as in figure 5.21.

arising in different canopy flow regimes. In the sparser regimes, the inner peaks in Figures 5.21a, 5.21b and 5.21c, corresponding to $\lambda_x/H = 1$, do not correspond to any of the wavelengths associated with the canopy geometrical parameters. In the spanwise direction, the wavelengths correspond to lengths ranging from $\lambda_z/H = h, \Delta S$ to $\lambda_z/H = 1$. It is also noted that the internal spectral peaks share a common wavelength with the outer peaks. This mirroring behaviour was already observed in the instantaneous snapshots of Figure 5.19 and in the two-dimensional auto-correlation functions of Figure 5.20. As the value of λ is increased, we observe the emergence of a peak in all the three components corresponding to the wavelength associated with the diameter of the filaments (i.e., $\lambda_x/H = \lambda_z/H = d$). The intensity of this peak is maximum for the DR configuration, highlighting the importance of the wake behind the filament at the inception of the dense regime. The overall behaviour suggests that the influence of the individual filaments cannot be neglected, as the canopy becomes denser, i.e. when the wavelength associated with the diameter becomes comparable to the mean filament spacing (when $\Delta S/d \approx 6$) as it happens in the most dense configuration. For increasing values of the solidity, we notice that the internal peak of the spectral energy content splits into two maxima for all the three velocity components. The leftmost peak is associated with the average filament spacing (i.e., $\lambda_x/H = \lambda_z/H = \Delta S$), while the rightmost peak mirrors the outer peak. It is also observed that the wall normal location of the rightmost internal peak, always sits below the location of the internal inflection point, suggesting this location sets the features of the motion occurring in the inner layer of the canopy. The occurrence of the internal peak associated with wavelengths matching the values of ΔS is related to the observed meandering motion, imposed by the presence of the filaments, as evident by the branching of the peaks observed in the instantaneous realisations of the dense regime (see Figure 5.19 $g - o$). In the densest configuration, the increased intensity of the u' and w' components (see Figure 5.21m and 5.21o), indicates that the meandering motion between filaments becomes more important because of the increased stem number density. The rightmost peak of u' and w' in the intra-canopy region, observed in both Figures 5.21 and 5.22, represents processes at play at large wavelengths (i.e., $\lambda_x/H \simeq \lambda_z/H \simeq 1$) related with the dominant

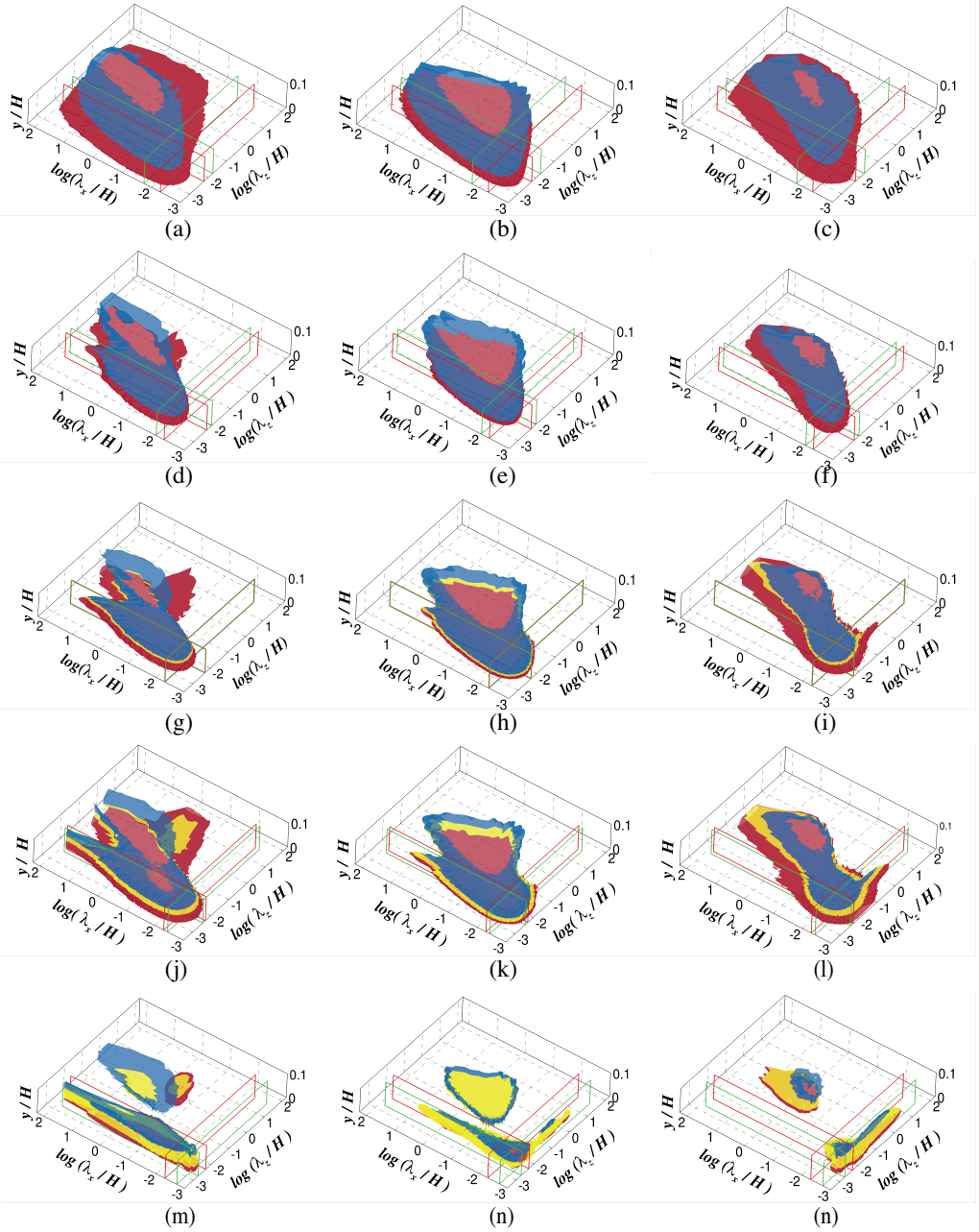


Figure 5.23: Iso-surfaces of two-dimensional pre-multiplied spectra of the fluctuating velocity components represented as a function of the wall paralell wavelengths (λ_x/H and λ_z/H) and wall normal distance (y/H). The first column (*a*,*d*,*g*,*j* and *m*), the second column (*b*,*e*,*h*,*k* and *n*) and third column (*c*,*f*,*i*,*l* and *o*) represent the $\kappa_x\kappa_z\Phi_{u'u'}/u^2_{\tau,l}$, $\kappa_x\kappa_z\Phi_{v'v'}/u^2_{\tau,l}$ and $\kappa_x\kappa_z\Phi_{w'w'}/u^2_{\tau,l}$ premultipled spectra respectively. The rows top to bottom, correspond to decreasing in-plane solidity. See text for the meaning of the lines and colours. Note that the isosurfaces are open-ended in the wall normal direction because the region above the canopy is not considered in the panels.

outer structures. As also anticipated previously, the instantaneous snapshots of Figure 5.19 ($g-l$) and the two-dimensional auto-correlation function shown in Figure 5.20 ($g-l$), reveal that in the mildly dense regime, within the intra-canopy region, there is a superposition of two physical mechanisms: one being related with the effect of the outer, quasi-streamwise vortices, that scales well with the external length scale; the other being the result of a weaker signature of a spanwise oriented motion, that is driven by the wall-normal jets. It is also observed that the peaks of u' and w' correlate with the peak of v' in the outer region of the canopy layer. Monti *et al.* (2020), attributed this behaviour to the energetic sweeps of the outer layer vortices into the canopy due to the weak wall normal permeability and their subsequent deflection when reaching the bottom wall to verify the both the wall impermeability and the solenoidal constraints. Differently, for the present DR case, we observe an overall decrease in the intensity of the v' peak (see Figure 5.21m) indicating that filament clustering determines a decrease in the wall normal permeability and, as a consequence, the role of the outer vortices becomes marginal in determining the dynamics of the intra-canopy region. Further insight into the overall structure of the intra-canopy layer can be obtained by considering the two-dimensional spectral decomposition of the fluctuating flow field. In Figure 5.23, we present the two-dimensional premultiplied spectra in the streamwise and spanwise direction as a function of the wall normal distance from the canopy bed. The resulting iso-surfaces are made non-dimensional with the local friction velocity. Each surface is split in wall parallel bands identified with different colours. Specifically, the portion of the surfaces coloured in red correspond to the inner region, while the blue indicates a portion of the surface in the outer layer. The yellow coloured regions fall within the overlap region. To accommodate the short wavelength fluctuations, we use in log axes for the streamwise and spanwise wavelengths. The red and green lines indicate the wavelengths associated with the canopy height and the mean filament spacing. In the sparser conditions, shown in panels a, b and c of figure 5.23, we observe that the iso-surfaces span the full extent of the canopy, with the spectra exhibiting a flat peak across a wide range of wavelengths extending from the $\lambda_x/H = \lambda_z/H = 1$ to the wavelengths associated with the geometrical parameters of the canopy. In particular, the

peaks of u' and w' in the inner region are characterised by a large range of wavelengths, while the v' peak features a more compact shape almost independent of the wall normal distance. As already mentioned, the peaks observed in the spectral decomposition can be classified into two leading contributions: energy associated with large-scale external vortices that penetrates the canopy layer; and small scale contributions generated by the meandering motion imposed by the presence of the filaments. As the canopy becomes denser, the iso-surfaces of the premultiplied spectra shapes in a more complex way, with the respective peaks featuring a more marked scale separation depending on the value of the solidity λ. For higher values of λ, the shapes change also along the wall normal direction indicating that the energy content of the velocity fluctuations increasingly depends on the wall normal distance from the canopy bed as the filaments separation decreases. Apart from the large scale spectral contributions occurring at $\lambda_x/H \simeq 1$ (blue and yellow region), we identify an interesting feature in Figure 5.23 g-n, where an elongated peak, with a wavelength window of $\lambda_x/H, \lambda_z/H \in [h, \Delta S]$, appears in all the three components of the pre-multiplied spectra. This feature is clearly related to the small scale motions taking place within the canopy, i.e. velocity fluctuations generated by the interaction with the filaments. The footprint of these motions in the spectrum of v' component appears as two peaks elongated in both the wall parallel directions (i.e., a L-shaped structure in panel 5.23n). The corresponding energy in the u' and w' components, presents a single elongated peak along the streamwise and spanwise directions, respectively. These maxima further extend when increasing values of λ are considered. A mildly elongated peak is also observed in the u' component of the TR case in panel 5.23d. Although the TR configuration nominally falls in the sparse regime, this feature can be attributed to the transitional effects already present for this value of λ. The organisation of this spectral feature and its common wavelength range, indicates the existence of a correlation among the three components of the velocity fluctuations, which are responsible for the momentum exchange occurring in the intra-canopy region. The elongated footprints observed in the u' and w' components can also be interpreted as the *legs* of a main spectral structure present in the wall normal component. These *legs* can be attributed to the high wall normal permeability and suggest a momentum

redistribution in the wall parallel directions, as already pointed out previously. However, the footprint peak of v' in the inner layer progressively decreases as λ is increased reaching a significant behaviour in the DR case. It is noted that the L-shaped structure of the v' component mainly occupies the outer and the overlap layer, while the wall parallel peaks extend across the full canopy height as the outer vortices cannot to reach the bottom wall as a result of the decreasing in-plane solidity. A closer examination of the spectral structure of the DR case (see Figre 5.23m, 5.23n and 5.23o), reveals a marked scale separation occurring in the intra-canopy region. This separation concerns all three components of pre-multiplied spectra. The phenomenon has been previously reported in the context of high Reynolds number flows over smooth wall flows (Lee & Moser, 2015*b*). In particular, the u' component presents three isolated peaks occurring at different wavelengths, while the v' and w' components exhibit peaks that correspond to large and small scale contributions. The most interesting feature in the absence of the v' peak in the inner layer of the canopy, highlighting again the decoupling hypothesis previously illustrated. In summary, we can state that the inner layer of DR case is mainly governed by a two-dimensional planar flow, dominated by the wall parallel velocity components.

Concerning the conjectured internal coherent motions, the one-dimensional pre-multiplied spectra do not provide any clear identification. Panels m-o in figure 5.23 show that in the DR case, the large scale contributions are limited to the upper region of the canopy (i.e., the overlap and outer layer), while the small scale contributions are observed only in the wavelength window $\lambda_x/H, \lambda_z/H \in [h, \Delta S]$. On the other hand, Figure 5.23m shows the presence of an isolated spectral extremum shared between the inner and the overlap layers. This peak may be related to the aforementioned internal inflection point because no v' peak is detected, while a w' peak corresponding to the same spanwise wavelength does appear. Another feature that confirms the existence of a travelling spanwise oriented structure within the intra-canopy region is provided by the premultiplied cospectra of the streamwise and spanwise velocity components (MacDonald *et al.*, 2018; Monti *et al.*, 2020) shown in figure 5.24. In the latter, the magnitude of the pre-multiplied cospectra of u' and v', is plotted as a function of the wavelength in the x and z directions. From the cospectra, we observe a decrease in

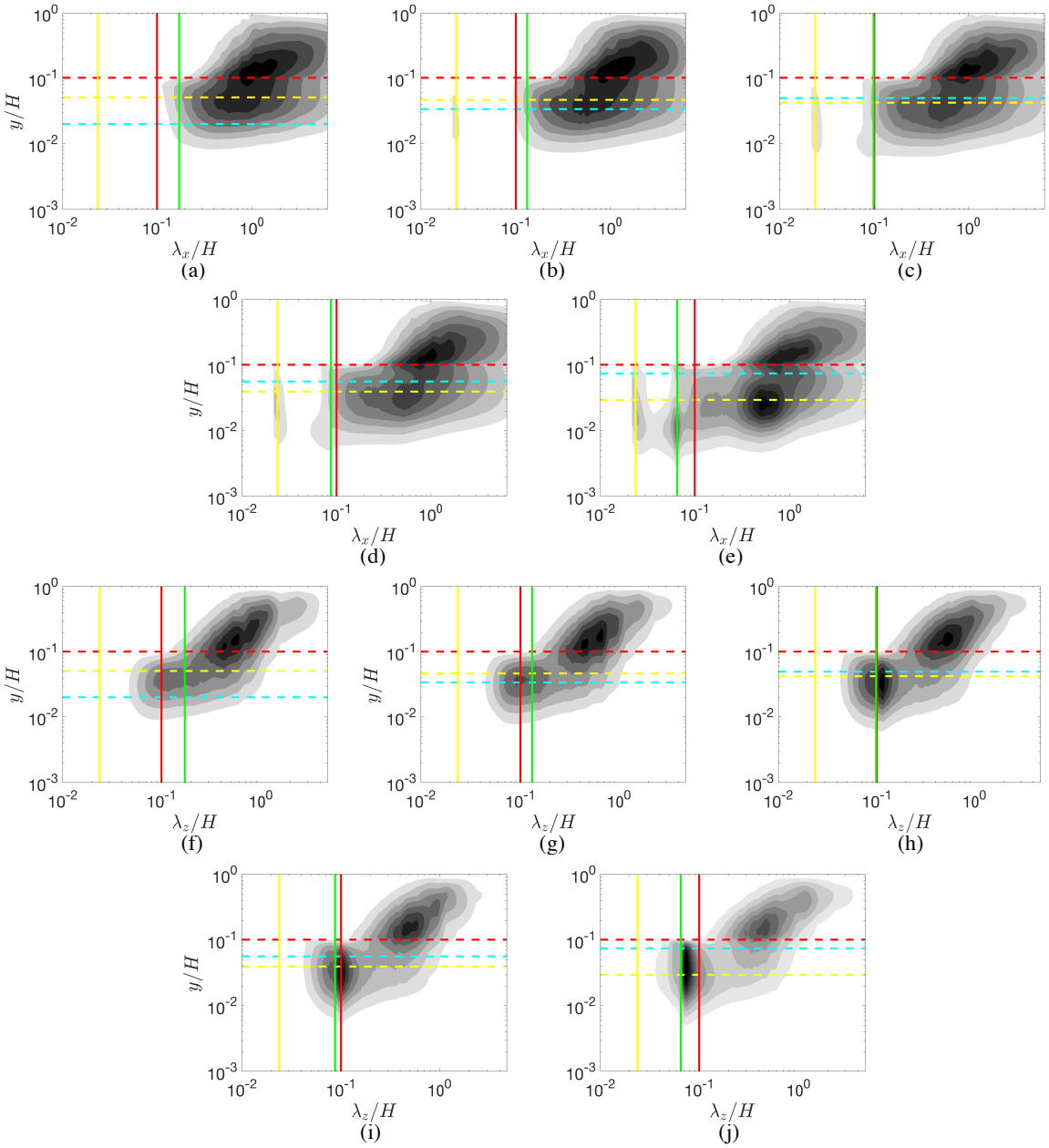


Figure 5.24: Magnitude of premultiplied cospectra for the streamwise and the wall normal velocity fluctuations as a function of the streamwise and spanwise wavelengths. Panels a-e represent the streamwise wavelength for increasing values of λ. Panels f-j represent the streamwise wavelength ordered with λ as in the a-e cases. The contours are extracted within the range $[0, 0.4]$ using a 0.02 increment.

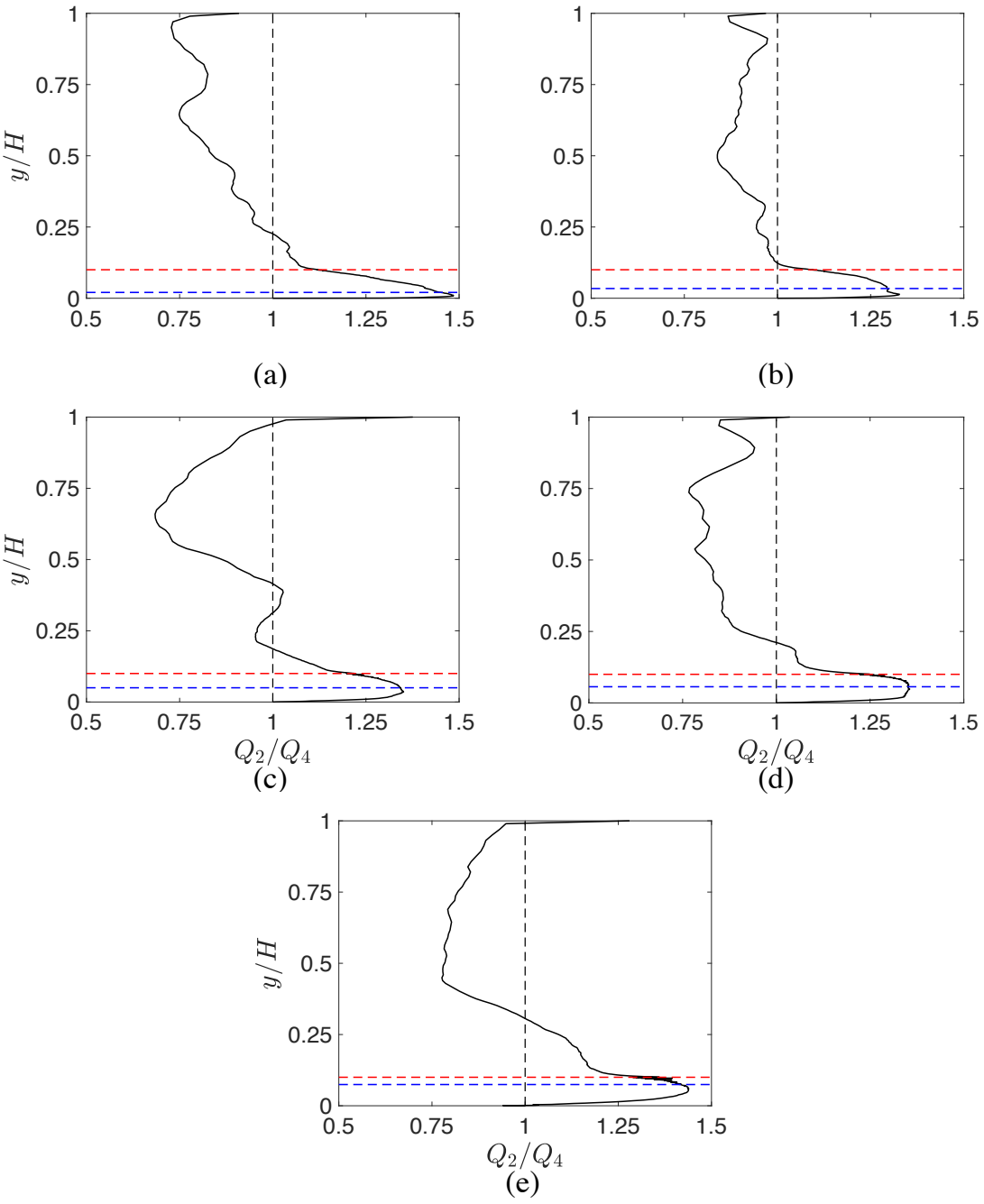


Figure 5.25: Ratio between the number of events occurring in the 2^{nd} and in the 4^{th} quadrant corresponding to the ejection and sweep events, as a function of the wall normal direction. The red and blue dashed lines indicate the location of the canopy tip and the virtual origin, respectively. The figures a-e are arranged according to the ascending order of λ

the intensity of the internal peak, when moving from the sparsest to the mildly dense condition. This peak asymptotically moves towards the location of the internal inflection point as λ is increased. Breaking this trend, the DR case shows an abrupt increase in the intensity of the internal peak that therefore cannot be attributed to the leak of external energy within the inner layer. Another tool that can be used to study the generation of the Reynolds shear stresses (i.e. $\langle u'v' \rangle$) the quadrant decomposition analysis (Ong & Wallace, 1998; Wallace, 2016), incorporating the directional information of the sweep ejection events events. Following previous studies (Bailey & Stoll, 2013, 2016), we consider the ratio between the number of 2^{nd} and 4^{th} quadrant events (i.e., ratio between the number of ejections and sweeps) occurring across the full extent of the open channel, both inside and outside the canopy. Figure 5.25, shows the profiles of the ratio between ejection ($Q2 : u' < 0, v' > 0$) and sweep ($Q4 : u' > 0, v' < 0$) events as a function of the wall normal distance from the canopy bed. The profiles were determined by computing the ratio of the number of ejection and sweep events (i.e., N_{Q2} and N_{Q4}) at each $x-z$ plane for all y nodes of the grid. The region outside canopy ($y/h >> 1$) is clearly dominated by the sweep events as normally observed in wall bounded turbulent flows (Jiménez, 2018). Nonetheless, the modulation imposed by the various canopy regimes becomes more and more significant as the canopy tip is approached. In the sparser conditions, the canopy tip interface (i.e., red dashed line) is characterised by the presence of both sweeps and ejections due to the weak effect of the in-plane solidity in discriminating between the events generated in the external flow. As a denser conditions are considered a shift of the profiles towards an ejection dominated condition is observed. It is also observed that all the configurations considered in the current investigation share a common behaviour in the region inside the canopy with a dominance of the ejection events, suggesting that the internal peaks of the cospectra of Figure 5.24 are mainly fed by dominant ejection events followed by weaker sweep events. As anticipated, we now return to the analysis of the external boundary layer that develops above the canopy. It is well known that the mean velocity profile of canopy flows, exhibits an inflection point located at the canopy tip. This feature is known to induce a Kelvin-Helmholtz like instability that leads to the formation of large-scale spanwise coherent structures (Raupach *et al.*, 1996; Finnigan,

2000; Nepf, 2012) that according to Finnigan *et al.* (2009) promote the appearance of *head-up*/*head down* hairpin vortices through a series of non-linear interactions. The emergence of spanwise oriented rollers have also been previously reported by authors, in the context of permeable substrates with relaxed vertical permeability (Jimenez *et al.*, 2001; Rosti *et al.*, 2018*a*; Gómez-de Segura & García-Mayoral, 2019) and corrugated walls (Garcia-Mayoral & Jimenez, 2011; Endrikat *et al.*, 2021). The occurrence of these vorticity rollers can be identified by considering the two-dimensional spectral content of the wall normal velocity fluctuations in the region above the canopy tip (Sharma & García-Mayoral, 2020*b*). Alternatively, the outer peak of the pre-multiplied cospectra of the u' and v' component given in Figure 5.24 can also be used to reveal the presence of the spanwise rollers (MacDonald *et al.*, 2018; Monti *et al.*, 2020). Figure 5.26, represents two-dimensional pre-multiplied spectra of the wall normal component ($k_x k_z \Phi_{v'v'}/u^2_{\tau,l}$) at the wall normal location of $y^+_{out} = 60$ for all considered solidity values. The spectra have been made non-dimensional with the local friction velocity (see definition 5.8), while the wavelengths are scaled with the open channel height H. It should be noted that the location of $y^+_{out} = 60$, corresponds to a location outside the canopy tip at a constant distance from the location of the virtual origin (which differs from case to case). Figure 5.26 shows that for all configurations, the premultiplied spectrum $k_x k_z \Phi_{v'v'}/u^2_{\tau,l}$ exhibits a spanwise elongated peak occurring within a narrow band of streamwise wavelengths. This feature indicates the presence of structures characterised by a strong coherence in the spanwise direction. Those structures are also visible when considering snapshots of the flow field. In particular, the presence of the rollers becomes particularly evident when looking at the lateral panel of Figure 5.28, where we have plotted the streamlines of the instantaneous mean flow on the $x - y$ plane obtained by averaging across the spanwise direction each individual time snapshot. It should be noted that the spanwise rollers emerging from the Kelvin-Helmholtz instability are not well defined vorticity structures (Finnigan *et al.*, 2009; Bailey & Stoll, 2016) and cannot be identified by considering the q-criterion alone. As already mentioned, in the conceptual model of Finnigan *et al.* (2009) the final shape of the rollers is determined by a series of non-linear interaction between the rollers. Differently, Monti *et al.* (2019) suggested that

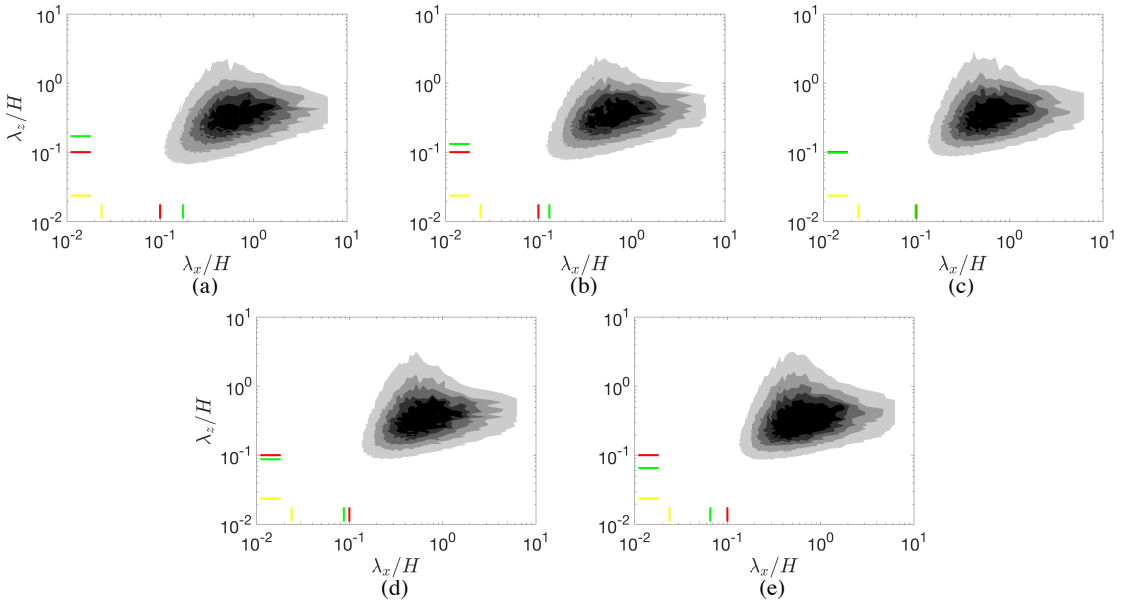


Figure 5.26: Two-dimensional pre-multiplied spectra of the wall normal fluctuating velocity component extracted at $y^+_{out} = 60$, as a function of the streamwise (λ_x/H) and spanwise (λ_z/H) wavelength, scaled with the open channel height H. The panels ($a - e$) highlights the spectral content for the configurations with increasing in-plane solidity (i.e., SR to DR cases).

the spanwise roller formed as a result of the inflected mean velocity profile, looses part of its coherence due to its interaction with the strong sweep/ejections generated by the outer quasi-streamwise vortices. The emergence of a Kelvin-Helmholtz type instability due to an inflected mean velocity profile, shares several similarities with a plane mixing layer. This resemblance, enticed many authors to adopt a mixing layer analogy to analyse the coherent structures that appear by the canopy tip (Raupach *et al.*, 1996; Finnigan, 2000; Nepf, 2012). In particular, these authors postulated that the streamwise periodicity wavelength (Λ_x) of the spanwise rollers observed in the context of a dense canopy, scaled with the shear length scale (L_s, see Equation 2.4), falls within the range of $7 < \Lambda_x/L_s < 10$. Raupach *et al.* (1996), by compiling several experimental studies, proposed a sharper estimate of $\Lambda_x \simeq 8.1L_s$. The streamwise wavelengths of the associated spanwise elongated peak observed in Figure 5.26, versus the shear length for all canopy configurations are presented in Figure 5.27a. This figure includes both the present results and the ones reported by Monti *et al.* (2020). The lack of collapse on the estimate proposed by Raupach *et al.* (1996), indicates that the validity of the approximation is limited to sufficiently tall canopies, falling in the dense

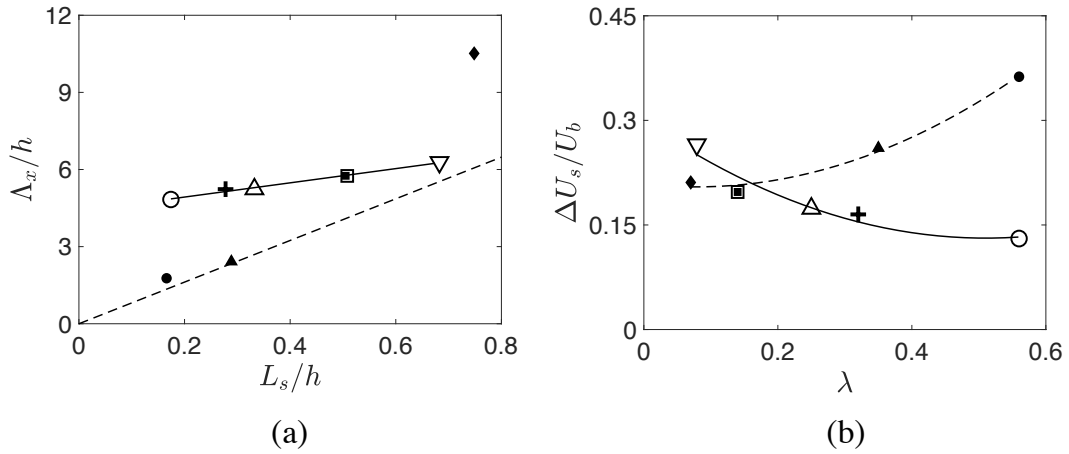


Figure 5.27: (a) Streamwise wavelength of the large scale spanwise coherent motions (made dimensionless with the canopy height h) above the canopy tip as a function of the shear length scale. The solid lines correspond to the current simulations, while the dashed line correspond to the estimate proposed by Raupach *et al.* (1996).(b) Velocity difference within the canopy outer layer scaled by the bulk velocity, shown as a function of the solidity. Solid lines obtained in the current investigation, and dashed lines obtained in the study by Monti *et al.* (2020). See Table 5.1 for symbols.

regime. Monti *et al.* (2020), suggested that the strong interaction of the intra-canopy layer with the outer layer, leads to an inconsistency of the estimate when in sparser regimes (i.e., SRM and TRM cases). However, in the framework of the simulations carried out for this work, we observe a different behaviour, with the wavelength of the sparsest configuration (i.e., SR case) being very close to the estimated value predicted by Raupach *et al.* (1996). The general inconsistency mentioned above can be attributed to the formulations used in the different contexts. In particular, in the set up of the mixing layer analogy, Raupach *et al.* (1996), define the thickness of the layer as the distance across which the mean streamwise velocity goes from U_o, the velocity in the low-speed side of the canopy to U_h, the velocity at the canopy tip. The computation of U_h presents no ambiguity, while the one of U_o proposed by Raupach *et al.* (1996) does, since in their definition of $L_s = U_h/(dU/dy)_{y=h}$, it is assumed that the velocity profile reaches a negligible value within a distance L_s from the tip (i.e. $U_o = 0$) without the need of a canopy bed (i.e. very tall canopies). To extend the analogy to a more general framework that incorporates sparser canopies, in this work we have used the same Taylor's expansion from the canopy tip as in Raupach *et al.* (1996), but slightly modified

as $U_o = U_h - L_s \cdot (dU/dy)_{y=h}$ using as U_o the mean velocity computed at the virtual origin (i.e. resulting in $L_s = \Delta U_s/(dU/dy)_{y=h}$, where $\Delta U_s = U_h - U_{vo}$). Figure 5.27b, presents the mean velocity difference $\Delta U_s = U(h) - U(y_{vo})$ as a function of λ. We observe that the SR, MDM and DRM cases present a higher magnitude of the velocity difference, when compared the with the other cases. Therefore, we can suggest that the validity of the shear length scale (see Equation 2.4) as an estimate for the vorticity thickness, is limited to canopies that are characterised by large velocity difference with a threshold magnitude of $\Delta U_s/U_b \approx 0.26$. It is noticed that the sparse canopies considered by Monti *et al.* (2020) do not verify this condition. We close this section with few more comments about the topology of the flow structure above the canopy tip. The external region is populated by quasi-streamwise vortices flanked by low and high momentum streaks (see Figure 5.28). These are responsible of the outer peaks observed in the pre-multiplied spectra. In particular, the presence of streaky u', spanwise alternating patterns and the quasi-streamwise vortices detected in the external region suggests that the outer layer features a velocity field structure shared by many others wall-bounded turbulent flows in the logarithmic region, thus verifying the wall similarity's hypothesis of Townsend (1976). A further examination of the q-criterion surfaces of the dense regime shown in Figure 5.28, reveals the occurrence of coherent structures resembling the head-up hairpin structures typical of turbulent boundary layers. The emergence of these structures was not reported by Monti *et al.* (2020). They attributed the absence of these structures to the constraint induced by the short distance between the canopy tip and the interface of the open channel. As already mentioned, several authors (Finnigan *et al.*, 2009; Bailey & Stoll, 2016), have described the emergence of head-up and head-down hairpin structures associated with the non-linear evolution of the spanwise rollers. In the current set of simulations, only the DR case exhibits a set of structures similar to head-up hair pins. The emergence of these structures in a single canopy configuration, can be attributed to the increase in shear at the top of the as a result of the increase in stem number density, sharing similarities with an anisotropic porous and rough layer.

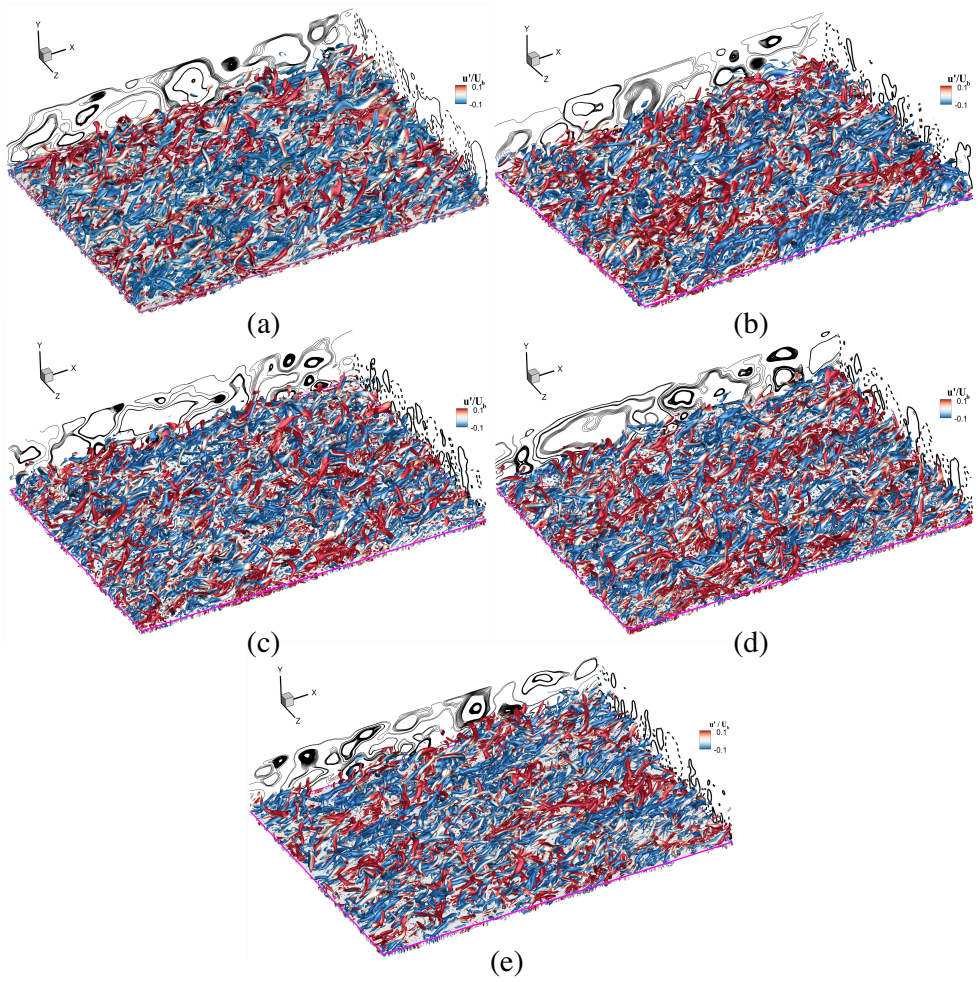


Figure 5.28: Instantaneous iso-surfaces of the q-criterion of the second invariant of the velocity tensor. The panels from a to e correspond to decreasing canopy sparsity values (i.e., SR to DR cases). The panel on the far lateral side shows the streamlines that have been determined by considering the spanwise averaged velocity fluctuations (i.e., $\langle u \rangle_z$ and $\langle v \rangle_z$). The panel located at the downstream end of the domain shows contours of positive (solid lines) and negative (dashed lines) spanwise fluctuations that have been obtained after a streamwise average operation. The iso-surfaces have been coloured by the fluctuating streamwise velocity values. The pink line in the $x - z$ plane indicates the canopy height.

5.4 Concluding Remarks

In this section, we draw some conclusions from the current chapter, in which we have conducted a parametric study of submerged canopies of varying stem number density (or equivalently mean stem spacing ΔS). The canopy embedded in an open turbulent channel is characterised by slender, rigid, circular cylindrical elements that are mounted to an impermeable wall. In this condition, we can identify a couple of hydrodynamic

regimes (i.e., sparse and dense) based on the value of solidity (λ). In contrast to a previous study by Monti *et al.* (2020), where the authors investigated the effect of canopy height on the different regimes of canopy flow, in this study, we focus on the average spacing between stems. The primary outcomes of the current study, alongside the findings of Monti *et al.* (2020), are summarised as follows.

Initially, it was found that the sparse and mildly dense canopies share several common features with the canopies of the same solidity. However, the overall flow in the intra-canopy region is highly dominated by stem number density since the latter essentially governs the norm of the entries of the permeability tensor that characterises the canopy substrate. On the other hand, the fully dense regime showcases much different behaviour. In particular, the two dense canopies with the same $\lambda = 0.56$ (obtained by increasing canopy height and decreasing the mean filament spacing, respectively) presented dynamics that are of different natures. The inner/outer layer interaction in the case of a tall submerged canopy highly depends on the wall-normal sweeps originating in the external flow. The interaction of the sweeps with the canopy leads to the generation of wall-normal jets of size ΔS that are responsible for transferring momentum to the wall parallel velocity components in the near wall region. We have shown that this momentum redistribution process is partially inhibited when the stem number density is increased.

Next, we focused on the transition that occurs between the sparse-dense asymptotic regimes (Nepf, 2012). It was found that this transition is primarily governed by the canopy aspect ratio, defined as the ratio between the mean filament spacing and the filament height. Our simulations have proved that in the transitional condition ($\Delta S/h = 1$), the virtual origin and the internal inflection point collapses on to the same mean location, segregating the canopy into two layers, that decouples as ΔS is increased. Thus, the nature of the flow occurring within dense canopies is governed by the average distance between filaments. The appropriate length scales that better characterise the localised flow layers in the canopy were also investigated. In the inner region, it was found that ΔS governs the nature of the flow, irrespective of the way in which λ was varied. Conversely, the external layer thickness scales well with the canopy height

scales. Nevertheless, it is the mean filament spacing that sets the size of the eddies that are allowed to penetrate the canopy.

Concerning the coherent structures that populate the flow domain, we can identify two types of structures based on the inner and outer localised layers. Initially, we focus on the structures that occupy the region outside the canopy. In line with previous studies, we observed that the inflection point in the mean located at the edge of the canopy triggers a Kelvin-Helmholtz instability that generates localised vorticity rollers. These structures enhance the momentum flux into the canopy along the wall-normal direction. In addition to these rollers, the external flow is populated by the canonical logarithmic structures, which generate strong sweeps and ejection events that interact with the canopy layer. For instance, during a strong sweep event, these structures are swept towards the canopy and their coherence is broken up by the canopy stems that are spaced at ΔS. This behaviour leads to the formation of wall-normal jets of size ΔS that are directed towards the canopy bed. These energy-carrying jets interact with the bottom impermeable wall to redistribute its momentum to the wall-parallel direction, giving rise to coherent motions of streamwise and spanwise velocity fluctuations. A fraction of the oncoming momentum is also pushed away from the wall, giving rise to regions of high Reynolds stresses. This process, essentially driven by the external flow, sets the location of the internal inflection point of the mean velocity profile. These mechanisms become active at the onset of the transitional condition. On the other hand, in the sparse, transitional, and mildly dense scenarios, the external structures in the logarithmic region are able to penetrate and occupy the canopy region. As the solidity is increased, the footprint of these external structures diminishes, inducing a decoupling between the inner and outer layers of the canopy. At the onset of the fully dense regime, inner layer dynamics are completely isolated from the influence of external structures, producing a large-scale separation.

6

On the effects of filaments inclination on canopy flows

Contents

6.1 Introduction 143
6.2 Numerical Setup 145
6.3 Results and Discussion 147
6.3.1 A new phenomenological model 151
6.3.2 Statistical characterisation of canopy flows 154
6.3.3 Virtual origin framework in the roughness regime 160
6.3.4 Prediction of drag change via the virtual origins 169
6.3.5 Structure of the canopy flow regimes 173
6.4 Concluding Remarks 187

6.1 Introduction

The elements embedded in the majority of the naturally occurring aquatic canopies often assume a streamlined posture that is oriented along the dominant flow direction. The canopies with the resulting posture shield the near-bed region, leading to a decrease in the sediment resuspension and control of the nutrient and oxygen exchange (Hurd, 2000). In addition to these physiological processes, the overall posture of the filament that composes the canopy plays a key role in decreasing the drag experienced by the

outer flow (Luhar & Nepf, 2011), by inducing a mutual sheltering effect of canopy elements (Raupach *et al.*, 1991). A streamlined filament's coordinate system is defined by two components: the length along the filament direction (s) and the angle of the filament relative to the wall-normal axis (θ°). The former can be subdivided further into two sections (Chen *et al.*, 2011): a lower sheath region, where the filament is nearly upright due to the clamped boundary condition at the base, and a middle inclined region, in which the filament assumes a streamlined shape based on the angle θ°. The change in the posture directly modulates the angle of canopy inclination relative to the wall-normal direction and eventually the frontal projected height of the filament, potentially decreasing the overall drag experienced by the canopy (Vogel, 1984). For example, increasing θ° (while maintaining a constant ΔS, l and d) reduces the overall height of the canopy and, as a result, the value of λ, which may induce a regime change in the respective canopy (i.e., $\lambda < 0.15$). In this condition, the simple model (based on the wall-normal permeability of the turbulent eddies) used to describe the transitional regime may not be applicable due to the geometrical constraint imposed by the filament inclination (Monti *et al.*, 2022). This condition can be envisaged as a localised modulation of the wall-normal permeability. Furthermore, the introduction of partial shielding may also give rise to new regimes that have been unexplored in the previous literature.

In the present study, we address these points by considering a series of high-fidelity simulations of open channel turbulent flows bounded by a canopy, which is characterised by a set of solid, rigid cylindrical filaments. To minimise the complexity associated with the mean posture of the filament, we consider a simple linearised filament model, which is characterised by the aforementioned sheath and inclined regions. The former is characterised by a perpendicular filament that is flush mounted to the bottom impermeable wall, while the latter features the filament inclination at a certain θ° along the streamwise direction. The height of this sheath region accounts for 10% of the total filament length and it is fixed for all the configurations. The angle of inclination will vary from $\theta^\circ = 0$, which corresponds to the fully dense configuration in Chapter 5, up to $\theta^\circ = 90$, a condition that is associated with the sparse regime (i.e., $\lambda = 0.05$).

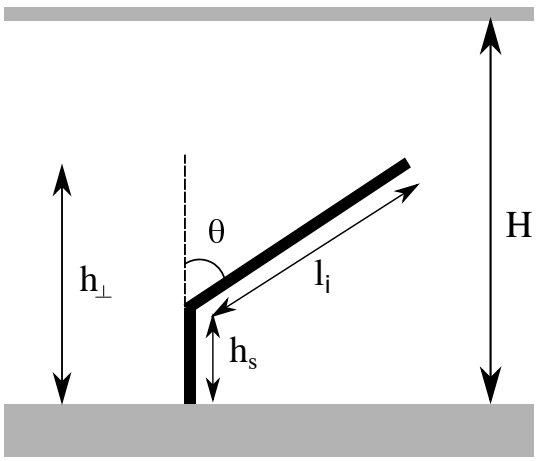


Figure 6.1: Sketch of the inclined canopy configurations considered in the current investigation. The overall shape of the filament is defined by the angle of inclination (θ°), sheath region (h_s), length of the inclined region (l_i) and the frontal projected height (h)

6.2 Numerical Setup

The high-fidelity simulations of rigid inclined canopies were conducted using a Navier Stokes + IBM solver that was described in Chapter 3. The canopies considered in the current study are composed of slender solid cylindrical filaments, flush-mounted to the bottom impermeable wall. We have uniformly distributed the filaments on the impermeable wall by partitioning the latter into non-overlapping square tiles of size ΔS. The local position of the filament base within the boundary of the tile, follows a random distribution. This approach prevents the generation of flow channelling effects in the canopy layer.

Inspired by the naturally occurring aquatic canopies, we consider an idealised set of rigid canopy configurations where the overall filament geometry is defined by a sheath and an inclined region. The former remains perpendicular to the impermeable wall, while the latter is governed by the angle of inclination (θ°), which is the free parameter of the current investigation (see Figure 6.1). The systematic variation in θ° leads to a modulation in the frontal and vertical projected lengths of filament. Therefore, the solidity for a canopy composed of finite cross sectional filaments reads as,

$$\lambda = \lambda_\perp = \frac{h_\perp d}{\Delta S^2} \tag{6.1}$$

Config.	θ°	$h_\perp/H$	λ	$\Delta S/h_\perp$	$Re_{\tau,o}$	$\Delta x_o^+, \Delta z_o^+$	$\Delta y_{w,o}^+, \Delta y_{h,o}^+$	*Symbol*
NI	*0*	*0.1*	*0.56*	*0.66*	*717*	*8.4*	*0.38*	∇
WI	*33.5*	*0.085*	*0.48*	*0.77*	*597*	*7*	*0.32*	$\square$
MI	*48.25*	*0.07*	*0.39*	*0.94*	*544*	*6.3*	*0.27*	$\triangle$
RSI	*60*	*0.055*	*0.31*	*1.19*	*478*	*5.47*	*0.25*	$+$
SI	*77.5*	*0.03*	*0.17*	*2.18*	*334*	*3.7*	*0.17*	o
VSI	*90*	*0.01*	*0.05*	*6.55*	*317*	*3.5*	*0.16*	$\pentagon$
SOC	-	-	-	-	*326*	*3.6*	*0.16*	-

Table 6.1: Simulation parameters considered in the current investigation. The filament distribution is maintained at $n_i \times n_k = 96 \times 72$, where n_i and n_k are the number of filament rows in the streamwise and spanwise directions, respectively; $Re_{\tau,o}$ is the friction Reynolds number based on the friction velocity ($u_{\tau,o}$) computed at the virtual origin. The grid resolution in the streamwise and spanwise directions are denoted by Δx^+ and Δz^+, respectively. The wall normal resolution of the numerical grid in the region near the impermeable wall and canopy top are denoted in Δy_w^+ and Δy_h^+

where $h_\perp = h_s + l_i cos\theta^\circ$, is the frontal projected height of the filament, which is a function of the angle of inclination, that increases in the positive clockwise direction. In particular, we chose six cases spanning from $\theta^\circ = [0, 90]$. such that the lowest and the largest angles would correspond to the sparse dense asymptotic regimes (Nepf, 2012). The other geometrical parameters were selected such that the nearly upright configuration ($\theta^\circ = 0$) matches the fully dense regime ($\lambda = 0.56$) of chapter 5. The total length of the filament is maintained at $l = h_s + l_i = 0.1H$, where the height of the sheath region is $h_s = 0.1l$ and the filament length in the inclined region $l_i = 0.9l$, respectively, while a constant geometrical ratio of $d/\Delta S = 0.367$ was maintained.

All the canopy configurations were simulated on Cartesian mesh, which is characterised by a uniform distribution along the homogenous directions (wall parallel) and a tangent hyperbolic stretched distribution in the wall-normal direction. The latter enables the concentration of more grid nodes at the regions of high shear (i.e, canopy bed and tip). Similar to previous work by Bailey (2016) and Monti (2020), all configurations share the same computational box of size $L_x/H = 2pi$, $L_y/H = 1$, and $L_z/H = 1.5pi$, but the streamwise length was doubled (i.e., $L_x/H = 4\pi$) for the configurations with $\theta^\circ = 77, 90$, allowing the computational box to capture large scale coherent structures. The total number of grid nodes is equal to $N_z = 432$,

and $N_x = 576, 1152$ for $\theta^\circ = [0, 30, 48.15, 60][77, 90]$, while nodes in the wall-normal direction range from $N_y \in [216, 260]$. As a result, the numerical grid resolution in wall units (see Table 6.1), satisfies the threshold highlighted in canonical wall-bounded turbulent flows (Kim *et al.*, 1987). The former was computed based on the outer friction velocity that corresponds to the total stress evaluated at the virtual origin (i.e., $u_{\tau,out} = \sqrt{\nu \partial \langle U \rangle / \partial y - \langle uv \rangle}$). Further discussion on the viscous scales is presented in §6.3. We have also conducted a simulation of a smooth wall turbulent open-channel flow. The latter is treated with the same boundary conditions used in the canopy flow simulations. The selected domain shares several similarities with the extremely inclined canopies. For a smooth wall turbulent flow, the numerical grid resolution in wall units (made non-dimensional using the friction velocity at the wall, $u_\tau = \sqrt{\tau_w / \rho}$) is adequate. The former is presented in Table 6.1.

Concerning the treatment of the boundary conditions, we have employed a periodic condition along the wall-parallel directions; a no-slip condition on the bottom impermeable wall and a free slip condition on the top surface, mimicking an open channel flow. The flow in the domain is driven by a uniform pressure gradient, that is applied along the streamwise direction. At each time step, the pressure gradient is adjusted to obtain a time-independent constant volumetric flow rate which corresponds to a bulk Reynolds number of $Re_b = U_b H / \nu = 6000$. This value closely matches with that of Monti *et al.* (2020), enabling direct comparisons with the different canopy configurations.

6.3 Results and Discussion

The results accumulated from the six statistically converged simulations are presented in this section. The main body of the discussion is based on the direct comparisons of the statistical quantities and the structures of the turbulent flow field. This part of the thesis is structured as follows: initially, we will focus on the mean velocity distributions and the effect of the inclination on the positional variation of the aforementioned mean velocity profile features. Then we will shift our focus to the higher order statistics and turbulent coherent structures that exist in the various regimes. The overall discussion

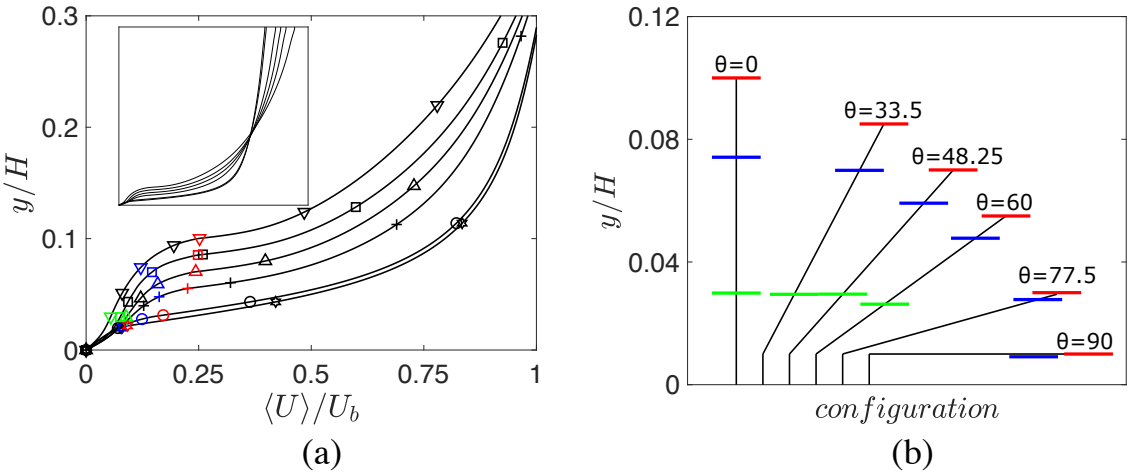


Figure 6.2: (a) Mean velocity profile scaled with the open channel height (H) and bulk velocity (U_b), (b) Mean locaitons of the outer inflection point (red), virtual origin (blue) and internal inflection point (green), for the various configurations considered in the current study. See Table 6.1 for symbols.

will be expanded by incorporating the Monti *et al.* (2020) results and those presented in Chapter 5, which will be represented by red and blue x lines/symbols, respectively.

First, we turn our attention to the effect of the canopy inclination on the mean velocity profile. As mentioned above, the modulation in θ° corresponds to a two-fold change in the frontal projected height ($h_\perp$) and the vertically projected length ($l_\parallel$) of the canopy. Therefore, we expect a simple streamwise inclination to have a completely different impact on the distributions, when compared with the perpendicular canopies (Monti *et al.*, 2020). The distributions of the mean velocity normalised with the open channel height (H) and the bulk velocity ($U_b = 1/H \int_0^H \langle U \rangle dy$) are shown in Figure 6.2a, with the red-colored symbols representing the edge of the canopy, or equivalently the outer inflectional point. The mean velocity distribution for all the configurations below the edge of the canopy is characterised by a convex profile, with the effect of the filament inclination limited to the convexity in that region. In particular, an increase in θ° results in the decreasing curvature of the convex profile, indicating a speeding up of the mean flow in the intra-canopy region. This diminishing footprint of the profile convexity can also be associated with the geometrical constraint induced by the filament inclination (Monti *et al.*, 2022). This can be further discussed qualitatively by considering the positional variations of the mean velocity profile features.

The mean velocity distribution for the nearly upright filament configuration (i.e., $\theta^\circ = 0$) exhibits three distinct features: a couple of inflection points (Nepf, 2012) located at the tip of the filament and deep inside the canopy, respectively, and lastly, a virtual origin for the outer flow. The former can be computed by considering the zeros in the mean momentum balance (Monti *et al.*, 2019), while the latter, interpreted as the abstract wall seen by the outer flow, is computed by enforcing the canonical logarithmic (shifted) boundary layer formulation (Jiménez, 2004) on the outer mean velocity profile. Figure 6.2b shows the mean positions of these features for all configurations, where the blue, red, and green horizontal lines represent the virtual origin (y_{vo}), external, and internal (y_{ip}) inflection points, respectively. It can be observed that the position of the virtual origin moves closer to the tip of the filament as the angle of inclination is increased. For the extremely inclined configurations (i.e., $\theta^\circ = 77.5, 90$), the virtual origin lies just below the canopy tip, indicating the decreasing extent of the outer flow region within the canopy layer. On the other hand, the effect of the filament inclination on the internal inflection point reveals a rather radical behavioural change when compared with the virtual origin. In particular, the wall-normal position of the internal inflection point remains relatively unaffected by the low and mild angle of inclination (i.e., $\theta^\circ = 0, 33.5, 48.25$). However, on the onset of the $\theta^\circ = 60$, the inner inflection point advances towards the canopy bed, triggering a potential departure from the typical dense canopy regime. Interestingly, the internal inflection point is completely absent for the extremely inclined configurations. suggesting that there exists some kind of physical mechanism that comes into play, in between $\theta^\circ = 60$ and $\theta^\circ = 77.5$, configurations which revoke the internal layer of the canopy.

Further insight into the behaviour of the mean velocity features can be obtained by drawing comparisons with the canopies composed of perpendicular filaments. The transition from a quasi-sparse to a fully dense regime occurs when the canopy aspect ratio is unity ($\Delta S/h = 1$), and the mean position of the virtual origin and internal inflection point collapses at the same wall-normal location (i.e., $y_{vo} \approx y_{ip} \approx 0.5h$) (see chapter 5). Conversely, the positional variation of the virtual origin and internal inflection point in the present investigation exhibits different behaviourism. The mean

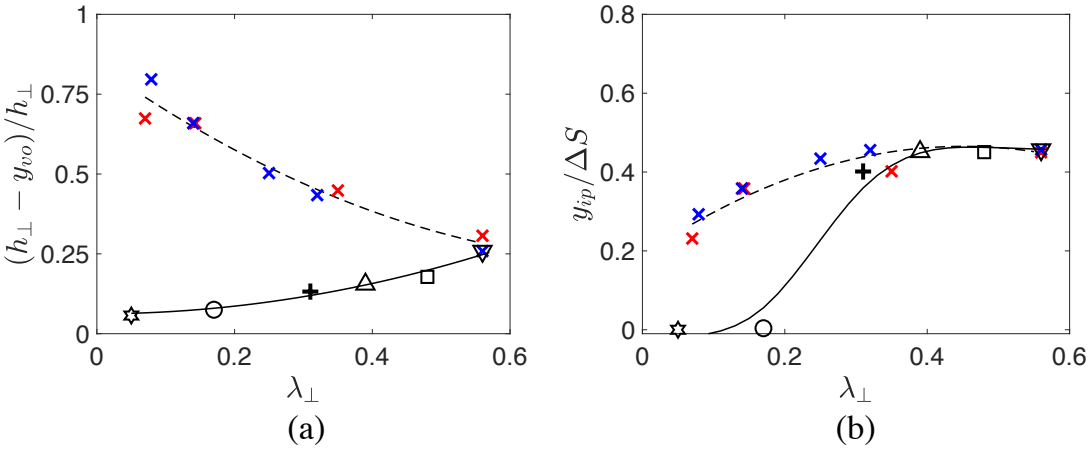


Figure 6.3: (a) Extent of the outer layer within the canopy normalised by the frontal projected height of the canopy, (b) Thickness of the internal layer scaled with the mean filament spacing. See Table 6.1 for symbols. Red and blue symbols represents the data extracted from Monti *et al.* (2020) and chapter 5, respectively.

locations of the former and latter do not converge towards a single point as the angle of inclination increases, even though selected canopies fall within the range of the transitional threshold (i.e., $[\Delta S/h_\perp]_{\theta^\circ=0} < 1 < [\Delta S/h_\perp]_{\theta^\circ=90}$ or equivalently $\lambda_{\theta^\circ=0} < 0.15 < \lambda_{\theta^\circ=90}$), indicating that the canonical sparse-dense asymptotic regimes are insignificant. Concerning the scaling of the localised layers within the canopy, it was suggested in chapter 5 that the internal and external layers of a perpendicular canopy are better characterised by the mean filament spacing (ΔS) and height (h). Following this, we normalised the thickness of the internal layer with ΔS, while the thickness of the outer layer ($h_\perp - y_{vo}$) is scaled with the frontal projected height of the filament ($h_\perp$). These values are shown in Figure 6.3, along with the results from the entire perpendicular canopy database (represented by coloured x symbols). For the mild inclination configurations, the extent of the internal layer (see Figure 6.3b) reveals a good collapse, with the trend obtained for the perpendicular canopies. This suggests the inclined canopies share certain similarities with the dense regime of perpendicular canopies. Figure 6.3b, on the other hand, shows an abrupt departure at the onset of the extremely inclined configurations $\theta^\circ = 77.5, 90$. Conversely, the normalised thickness of the external layer (see Figure 6.3a) presents a rather radical change in the behaviour, even for a very low angle of inclination. This is a clear indication of the insignificant

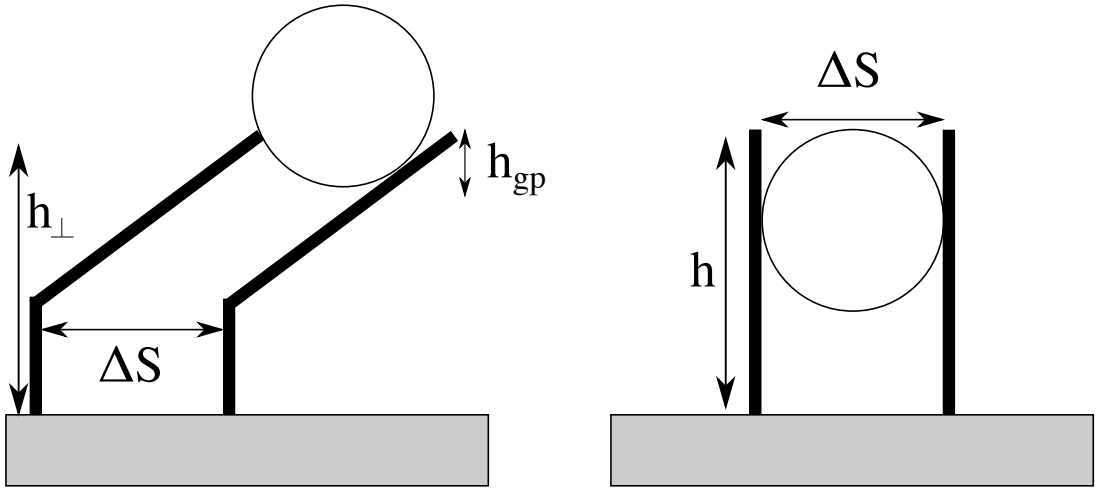


Figure 6.4: Phenomenological model that proposes a new geometrical length scale to the characterise the penetration of the external flow.

role played by the frontal projected height of the filament in characterising the external layer thickness within the canopy. Therefore, we can postulate that there exists an alternative length scale that can better characterise the outer flow region. Furthermore, the observed behaviours also cast questions over λ as the governing non-dimensional parameter in the context of canopy flows (Nepf, 2012).

6.3.1 A new phenomenological model

In this section, we propose a new conceptual model, intending to explain the penetration of the outer eddies into canopies composed of inclined filaments. The extent of the outer layer within the canopy can be interpreted as the level of penetration of the eddies, that populate the external boundary layer (Monti *et al.*, 2020). In the context of perpendicular canopies, outer characteristic eddies of diameter ϕ can penetrate the void region between two adjacent filaments via the wall-normal direction (see Figure 6.4 right). The mean filament spacing (i.e., $\phi \leq \Delta S$), which is considered the canopy's most dominant length scale, governs the mutual upwash/downwash of outer flow eddies. In this condition, the canopy can be envisaged as an an-isotropic porous medium with high wall normal permeability (Monti *et al.*, 2020). As a result, the wall-normal progression of an outer eddy $\phi = \Delta S$ that has penetrated the canopy layer scales well with canopy height (h), as illustrated in Figure 6.3a.

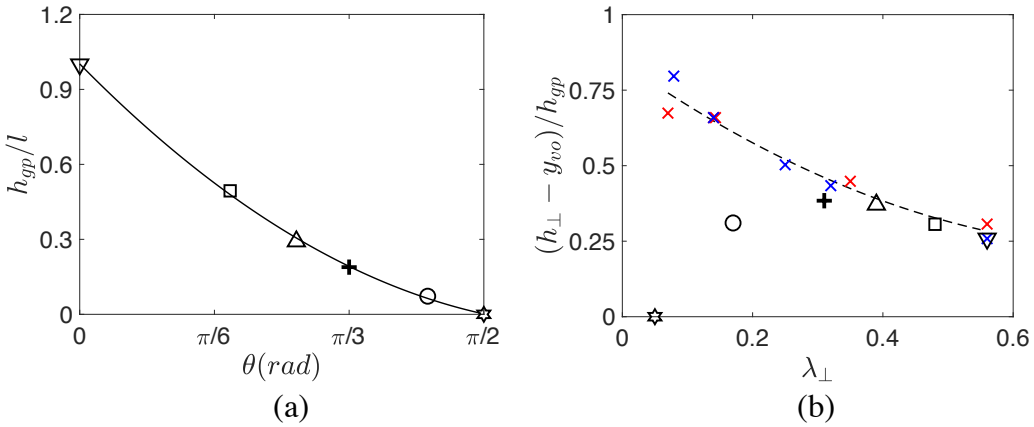


Figure 6.5: (a) Geometrical penetration depth scaled with the filament length (l) as a function of the angle of inclination in radians. (b) The extent of the outer layer within the canopy normalised by the newly proposed geometrical penetration depth. See Table 6.1 for symbols.

The fundamental basis of the above physical mechanism fails at the onset of inclined canopies, due to the geometrical constraint imposed by the inclining filaments. Differently from perpendicular canopies, the introduction of a simple filament inclination impedes the motion of the characteristic eddies along the wall-normal direction. In particular, an eddy with size $\phi = \Delta S$, that crosses the interface at the edge of the canopy, is obscured by the inclined region of the downstream filament, as represented in Figure 6.4. In this condition, the external boundary layer that develops over the canopy substrate does not see the full extent of the filament, due to the sheltering effect. Instead, the outer flow sees only a small fraction of the overall canopy layer. We can compute the thickness of the effective portion of the canopy, by introducing a simple geometrical argument. In particular, we define a new length scale called *geometrical penetration depth* (h_{gp}), to account for the constrained wall normal penetration of these outer eddies. For canopies composed of nearly upright filaments ($\theta^\circ \approx 0$), h_{gp} takes on the value of the canopy height. However, on the onset of inclined filaments, the geometrical penetration depth must diminish to account for the constrained penetration. Thus, it transforms into a function based on the average filament distance (ΔS) and the inclination angle (θ°). For the configurations considered in the current we compute it as, $h_{gp} = \Delta S/2tan(\theta^\circ)$. However, in the limit of $\theta^\circ \longrightarrow 90$ (i.e., fully inclined filaments), the geometrical penetration depth goes to zero (i.e., $h_{gp} \longrightarrow 0$), satisfying the conceptual

model. Figure 6.5a illustrates the non-dimensional geometrical penetration depth scaled with the filament length for the varying angles of inclination (in radians). The same figure also includes a polynomial curve-fit of the data points that decays for the increasing angles of inclination, in agreement with the conceptual model. The equation of the fit is given as, $h_{gp}/l = 0.2611\theta^2 - 1.047\theta + 1.002$, with the fit quality parameters $\sigma = 0.0037$ and $R^2 = 0.9993$. It should be noted that the geometrical penetration depth is only valid for the canopies that are characterised by a positive angle of inclination since configurations with $\theta^\circ < 0$, enhances the level of penetration within the canopy (Monti *et al.*, 2022). Furthermore, the proposed length scale can only be applied to scenarios that correspond to the fully dense regime, in which the penetration is governed by the mean filament spacing.

The appropriateness of the proposed length scale can be verified by once again considering the thickness of the external flow embedded within the canopy. Figure 6.5b, presents the outer layer extent normalised by the geometrical penetration depth. It should be noted that for $\theta^\circ = 90$ configuration (i.e., fully inclined), $h_{gp} = 0$ and $h_\perp - y_{vo} \approx 0$, therefore in Figure 6.5, we have enforced $(h_\perp - y_{vo})/h_{gp} = 0$. While the perpendicular configurations remain unaffected, the inclined canopies reveal an interesting behaviour. In particular, when scaled with h_{gp}, the low and mildly inclined configurations ($\theta^\circ = [30, 48.25, 60]$) collapse on the trend obtained for the perpendicular canopies, a behaviour similarly observed for the internal layer (see Figure 6.3b). This suggests that the two morphologies (i.e., perpendicular and mildly inclined) share several similarities in the physical characteristics that define both the internal and external layers of the canopy. However, when compared to the other configurations, the extremely inclined configurations (i.e., $\theta^\circ = 77.5, 90$) exhibit inconsistent behaviour, despite the fact that the proposed length scale incorporates the effects of constrained penetration. This is a clear indication that the extremely inclined configurations belong to a different regime that does not nominally fall into either of the sparse-dense asymptotic regimes (Poggi *et al.*, 2004*b*; Nepf, 2012). The following sections will shed further light on this new regime by evaluating the higher-order statistical distributions.

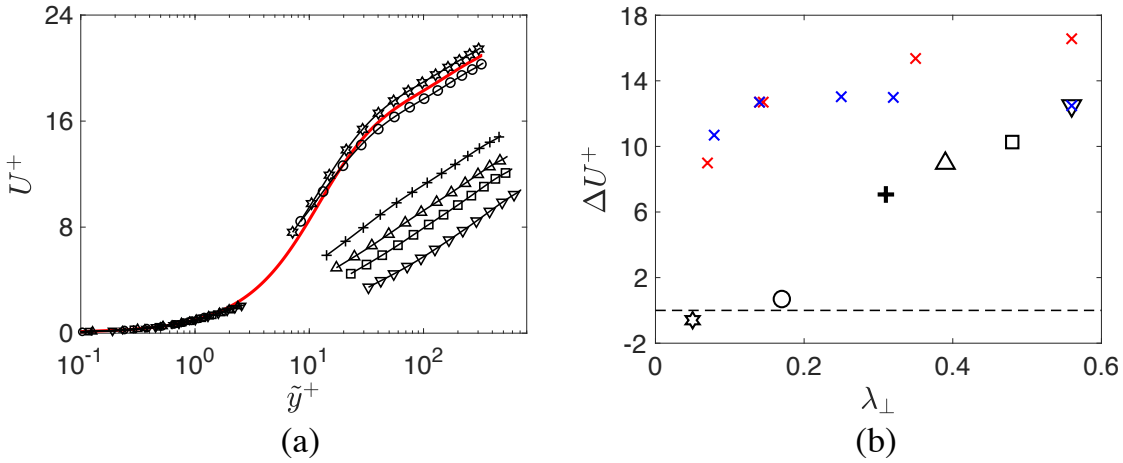


Figure 6.6: (a) Mean velocity profile normalised with two friction velocity (i.e., inner and outer). The $\tilde{y}^+$ represents wall normal coordinate non-dimensionalised by the respective friction velocities. The solid red line represents the canonical smooth wall open turbulent channel flow. (b) Resistance function plotted against the solidity of the canopy configurations, . See Table 6.1 for symbols.

6.3.2 Statistical characterisation of canopy flows

In this section, we turn our attention to the characterisation of the turbulent flow that develops within and above the canopy substrate, in terms of their mean flow and Reynolds stress distributions, and higher order statistics based on the fluctuating flow field.

First, we kick start the discussion by considering the semi-logarithmic formulation of the mean velocity profile. In particular, we identify two layers corresponding to their origins: an internal and an external layer. While the origin for the internal layers corresponds to the canopy bed, the external layer is associated with an abstract plane located at y_{vo}, which typically resides below the tip of the canopy. The occurrence of a shifted outer boundary layer has been previously reported by authors in the context of rough wall boundary layers (Jiménez, 2004), permeable substrates (Rosti *et al.*, 2018*a*) and canopy flows (Monti *et al.*, 2019). Therefore, we define an internal friction velocity based on the wall shear stress at the canopy bed (i.e., $u_{\tau,in} = \sqrt{\tau_w/\rho}$) and an external friction velocity based on the total stress evaluated at the virtual origin (i.e., $u_{\tau,out} = \sqrt{\nu(\partial\langle U\rangle/\partial y)_{vo} - \langle uv\rangle_{vo}}$).

The mean velocity distributions scaled with a couple of friction velocities are represented in Figure 6.6a. The profile obtained for a smooth wall open-channel turbulent

flow at $Re_\tau = 326$ is also included in the same figure. In the internal region, all the configurations reveal a good collapse with the smooth wall profile, up to $\tilde{y}^+ \approx 5$. This suggests that the region in close proximity to the canopy bed is highly dominated by the wall frictional drag, and does not depend on the canopy morphology, although the filaments in that region are characterised by the sheath layer. When moving away from the viscous sublayer, we observe the distinct effects of the filament inclination, particularly on the buffer layer, which is well known to be independent of the outer flow (Jiménez & Pinelli, 1999). In particular, the buffer layer dynamics have been completely modulated by the presence of an inclined filament layer, which promotes a meandering motion in the wall's parallel directions. However, this meandering signature diminishes with the increasing angle of inclination as a result of the decreasing frontal projected height of the filaments. For the extremely inclined cases (i.e., $\theta^\circ = 77.5, 90$), the latter in wall units (obtained by normalising with the outer friction velocity) is in the range of $7 < h_\perp^+ < 12$). A Similar behaviour was recently reported by Thakkar *et al.* (2018), where the authors investigated turbulent flows that develop over rough surfaces that span the hydrodynamically smooth to the fully rough regime ($3 < k_s^+ < 100$, where k_s^+ is the non-dimensional equivalent sand-grain height). On the other hand, the logarithmic region presented in Figure 6.6a, follows a universal logarithmic distribution, exhibiting the robustness of the corresponding layer irrespective of the imposed manipulations (Kwon & Jiménez, 2021). In particular, the effect of filament inclination is limited to the shift in the mean velocity distribution in the logarithmic region. Thus the logarithmic law for the turbulent flow that develops over textured surfaces (Jiménez, 2004) can be written as,

$$U_{out}^+ = \frac{1}{\kappa} log(y_{out}^+) + 5.5 - \Delta U^+ \tag{6.2}$$

where $y_{out} = y - y_{vo}$ is the shifted wall normal coordinates, $\kappa = 0.41$ is the classical von Kármán constant and $B = 5.5$ is the intercept in the context of a smooth wall flow. Note the subscript *out* denotes the quantities that have been made non-dimensional with the outer friction velocity. The first three terms on the right-hand side of the above equation represent the canonical formulation of the turbulent boundary layer that develops over a smooth wall. We define ΔU^+ as the resistance function, which is a wall offset

included in the logarithmic formulation to characterise the momentum deficit/surplus induced by the respective textures on the wall (Hama, 1954). The parameter ΔU^+ was predominantly used by previous authors in the studies associated with the turbulent flow over rough surfaces (Jiménez, 2004; Garcia-Mayoral & Jimenez, 2011) and permeable substrates (Rosti *et al.*, 2018*a*; Gómez-de Segura & García-Mayoral, 2019). In general, a downward shift (i.e., $\Delta U^+ > 0$) represents a drag incremental scenario, with the drag reducing condition often associated with an upward shift, i.e., $\Delta U^+ < 0$. In the context of permeable substrates and ribletted surfaces, the former is typically characterised by a drag increasing mechanism, i.e., the occurrence of a KH type instability due to the high wall normal permeability (Garcia-Mayoral & Jimenez, 2011; Gómez-de Segura & García-Mayoral, 2019; Endrikat *et al.*, 2021). Similarly, we observe this for the configurations selected in the current study (see Figure 6.6a). In particular, the canopies spanning the low and mild inclinations present a downward shift, indicating a substantial increase in the drag experienced by the outer flow. Therefore, these canopies can be envisaged as porous media with high wall-normal permeability. It can be hypothesised that the latter decreases with the increasing θ° due to the geometrical constraint induced by the inclining filaments. On the other hand, the extremely inclined configurations reveal a profile reminiscent of the smooth wall data, suggesting that the overall drag induced by the canopy is comparable to a canonical turbulent channel flow (Moser *et al.*, 1999). Interestingly the $\theta^\circ = 90$ configuration presents an upward shift, indicating a drag decrease when compared with a smooth wall. It can be easily seen that the value of ΔU^+ decreases monotonically with the increased angles of inclination, with the extremely inclined filaments presenting a negative value. Therefore, based on ΔU^+, we can identify two asymptotic regimes: a canopy regime ($\theta^\circ = 0, 30, 48.25, 60$), where the resistance function is comparable to a typical canopy flow, and a roughness regime ($\theta^\circ = 77.5, 90$), which presents a drag reminiscent of a rough wall boundary layer (Jiménez, 2004). Furthermore, it is evident that in between the two extremely inclined canopies, there exists a transition at $\Delta U^+ = 0$, which marks the departure from a drag increasing to a drag decreasing scenario. In this condition, the drag offered by the canopy is equivalent to the skin frictional drag on the smooth wall. The angle corresponding to

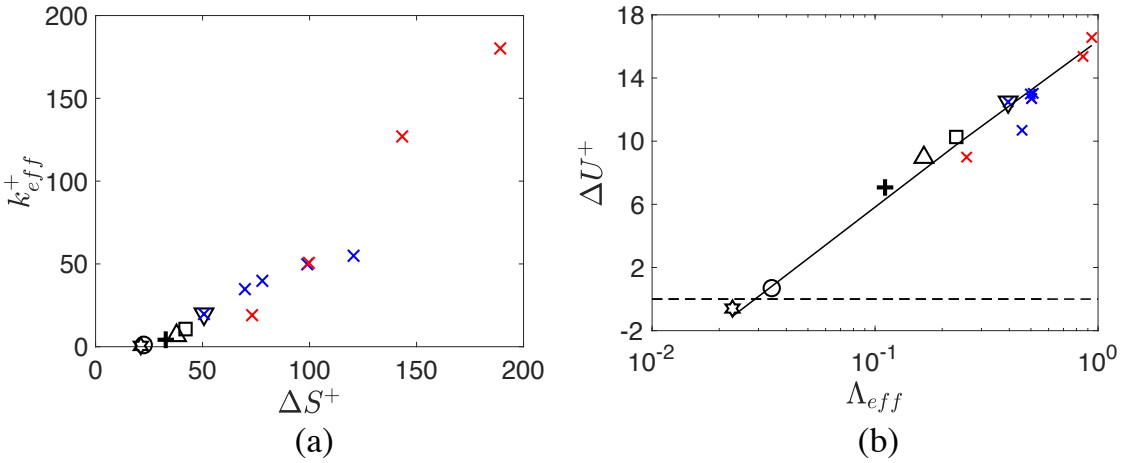


Figure 6.7: (a) Non dimensional effective canopy height vs non-dimensional spacing. (b) Resistance function ΔU^+ related to the effective canopy aspect ratio Λ_{eff}. See Table 6.1 for symbols.

this transition can be estimated as $\theta^\circ \approx 84$, via a simple linear interpolation. Although we have identified a drag-reducing condition, a qualitative description of the true nature of its drag reduction will be provided in §6.3.3.

Alongside the perpendicular canopies, the value of the resistance function in terms of the canopy solidity is presented in Figure 6.6b. In particular, we observe a scattered distribution, with the canopies of similar solidity exhibiting completely different values ΔU^+. This indicates the lack of robustness of λ in characterising the different regimes in canopy flows, presenting the need for a new non-dimensional parameter. Following the observations from chapter 5, we define an effective canopy aspect ratio $\Lambda_{eff} = k_{eff}/\Delta S$, where $k_{eff} = h_\perp - y_{vo}$ is the effective canopy seen by the outer flow, a length scale representative of the level of penetration from the external boundary layer. The choice of k_{eff} is motivated by the fact that the frontal projected height of the filament fails to characterise inclined canopies since the outer flow does not see the full extent of the canopy but rather a small portion of it. On the other hand, the influence of the internal layer has been implicitly incorporated in Λ_{eff}, via the ΔS term, as it is the relevant length scale deep inside the canopy. Figure 6.7a presents a non-dimensional (scaled with the outer friction velocity and kinematic viscosity) form of the effective canopy height versus the mean filament spacing. It is evident, that the increasing inclination angle yields a decrease in both k^+_{eff} and ΔS^+, with the minimum observed for the

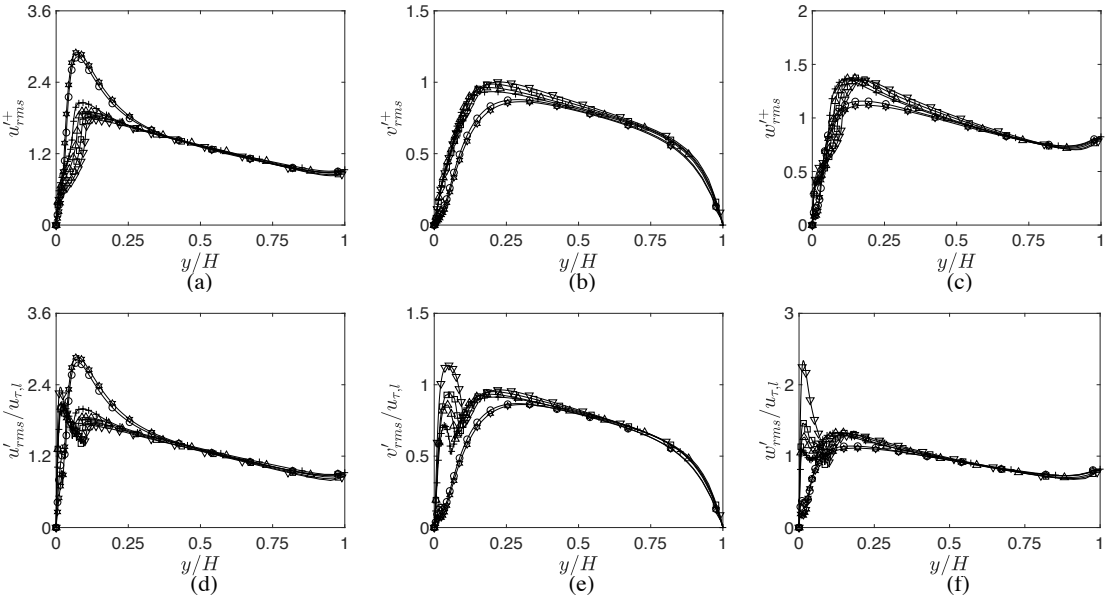


Figure 6.8: Diagonal terms of the Reynolds stresses normalised by the outer friction velocity (top row) and the local friction velocity scale (bottom row), as given in Equation 6.3. The columns from left to right represents the streamwise, wall normal and spanwise components, respectively. See Table 6.1 for symbols.

$\theta^\circ = 90$ configuration. When considering the full canopy database, including both the perpendicular and inclined ones, the effective canopy height increases monotonically with the mean filament spacing, suggesting the suitability of the proposed length scales. Based on this, we represent the resistance function in terms of the effective canopy aspect ratio in Figure 6.7b. Independently of the filament morphology, we can observe a logarithmic behaviour, indicating the robustness of the chosen parameter. This behaviour essentially, associates the resistance function with the internal and external layers of the canopy via the Λ_{eff}, although ΔU^+ was computed by considering the mean velocity distribution in the logarithmic region.

Next, we move on to the characterisation of the velocity fluctuations, as they contain important information regarding the influence of the filament inclination on the surrounding turbulent flow. Figure 6.8 shows the profiles of the diagonal terms of the Reynolds stresses as a function of wall-normal distance. In particular the distributions in the top row of Figure 6.8 have been normalised by the outer friction velocity ($u_{\tau,out}$). The distributions in the outer region present a good collapse, verifying the outer layer similarity, which was originally proposed by Townsend (1976). Therefore, the external

flow can be interpreted as a rough wall boundary layer developing over a virtual wall (Scotti, 2006). However, the comparison of the profiles in the inner region becomes complex due to the presence of the filaments. In this region, the scaling based on the outer friction velocity fails to characterise the canopy layer. Thus, we select a local friction velocity scale based on the total stress, given as

$$u_{\tau,l} = \sqrt{\frac{\nu \partial \langle U \rangle / \partial y - \langle u'v' \rangle}{1 - y/H}} \tag{6.3}$$

In the above formulation, viscous shear stresses are denoted by $\nu \partial \langle U \rangle / \partial y$, while the Reynolds stresses are represented by $\langle u'v' \rangle$. This scaling has been previously used by authors in the context of sparse (Sharma & García-Mayoral, 2020*a*), transitional and dense (Monti *et al.*, 2020) canopies, and manipulated shear flows (Jiménez, 2013; Tuerke & Jiménez, 2013). By observing the profiles normalised by the above formulation (see bottom row of Figure 6.8), we can identify a smooth wall-like behaviour with a good collapse, particularly in the inner region of the canopy, enabling a direct comparison among the configurations. The scaling presented by both friction velocities (i.e., outer and local) converges in the region that spans the external boundary layer that develops above the canopy due to the absence of the filaments in that region.

Lastly, we focus on the discussion on the mean behaviour of the velocity fluctuations. The distributions reveal a couple of peaks located inside and outside the canopy substrate. For the streamwise fluctuating velocity component, the peak associated with the outer region is likely to correspond with the canonical streaky structures. The latter has also been reported in the context of manipulated walls (Rosti *et al.*, 2018*a*). In particular, we observe an increase in the outer peak intensity with the increasing angle of inclination, suggesting a strengthening of these streaky structures. Conversely, the wall-normal and spanwise outer peaks see a decrease in intensity with the increasing values of θ°. It is well-known that these parameters are representative of the outer quasi-streamwise vortices (Jiménez, 2013). In the current context, the decrease in the peak intensity can be associated with the weakening of these vortices above the canopy layer, due to the decreasing penetration of the outer flow. Concerning the internal layer, we observe the opposite behaviour for the peak of the streamwise velocity

fluctuation. In particular the peak intensity of u'_{rms} decreases with the increasing filament inclination. The presence of the peak deep inside the canopy may associate itself with the aforementioned streaky structures. However, the presence of filaments disrupts the near-wall regenerative cycle and the development of the streaky structures (Jiménez & Pinelli, 1999). Therefore, this peak can be associated with the meandering motion induced by the wall parallel deviations of the intra-canopy flow on the onset of filament, which can be perceived as the structures formed by the flow past bi-periodic cylinders (Monti *et al.*, 2022). This can also be verified by the intra-canopy distributions of the spanwise component, which presents behaviour very similar to its streamwise counterpart. For the $\theta^\circ = 0$ configuration, the internal distributions of both the streamwise and spanwise components share the same peak intensity. The internal peak of v_{rms} similar to the wall parallel components, decreases in intensity with the increasing angles of inclination. This is indicative of the decrease in the level of penetration of the external flow due to the increasing filament inclination. For the extremely inclined configurations, the internal distributions for all three components do not feature an internal peak, presenting a departure from the behaviour exhibited by the low and mildly configurations, Instead, the overall behaviour of the profiles for the roughness regime is an almost smooth wall like (Moser *et al.*, 1999). Further insight into the modulation presented by $\theta^\circ = 77.5, 90$ configurations and their comparison with the canonical turbulent channel flow will be provided in the following subsection.

6.3.3 Virtual origin framework in the roughness regime

We turn our attention to the roughness regime of the inclined configurations, which presents a drag that is comparable to a smooth wall flow. In this scenario, the extremely inclined canopies can be perceived as a surface composed of small textures (i.e., $h_\perp^+ < 10$) capable of modulating the drag experienced by the near wall flow (Garcia-Mayoral *et al.*, 2019). In particular, these textures manipulate the near wall cycle (Jiménez & Pinelli, 1999) by impeding the cross-flow component as opposed to its streamwise counterpart (Luchini *et al.*, 1991). This has been the fundamental basis in many successful passive drag reduction techniques, including riblets (Bechert *et al.*, 1997) and superhydrophobic

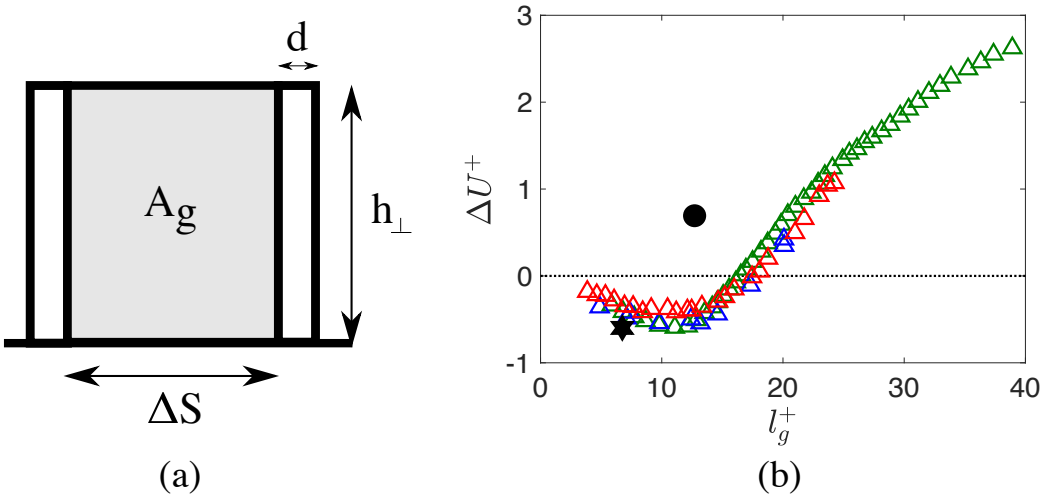


Figure 6.9: (a) Frontal projection of the canopy, which is characterised by geometrical parameters used to compute the groove cross sectional area, as defined by Garcia-Mayoral & Jimenez (2011). (b) Drag change (resistance function) represented against the non-dimensional square root of the groove cross sectional area. The symbols of the extremely inclined cases are filled for clarity. The green, blue and red coloured triangular symbols represents triangular, v-shaped and bladed riblets, respectively. The data were extracted from Endrikat *et al.* (2021).

surfaces (Rothstein, 2010). Therefore, we will be considering a unifying framework, that will enable us to make direct comparisons with smooth wall turbulent flows. To be consistent with the small textured surfaces reported in previous literature, from here on we will refer to the resistance function ΔU^+ as the drag change, relative to the smooth wall, open-channel turbulent flow simulated at the same nominal bulk Reynolds number (see §6.2).

The filamentous substrate, characterised by a high angle of inclination in the streamwise direction and high filament number density (see Table 6.1), exhibits a high shielding effect on the downstream filaments. Alternatively, the resulting surface can be envisaged as rows of streamwise interconnected filaments that are distributed in the spanwise direction with a spacing defined by ΔS, mimicking a ribletted surface. Motivated by this similarity, we make a direct comparison between the extremely inclined canopy configurations and the classical ribletted surfaces. In general, the drag-reducing surfaces covered with riblets are well characterised by the non-dimensional parameter, defined by the groove cross-sectional area (see Figure 6.9) (Garcia-Mayoral & Jimenez, 2011). This parameter is computed by considering the two-dimensional frontal

projected area of the valley in between two neighbouring riblets (i.e., $l_g^+ = \sqrt{A_g^+}$, made non-dimensional by considering the friction velocity u_τ). The optimum drag minimum typically occurs at $l_g^+ \approx 10.7$, with the increasing riblets size inducing a degradation in the drag reducing performance and eventually leading to the inception of the breakdown of the viscous regime ($l_g^+ > 17$) (Endrikat *et al.*, 2021). In the current framework, we can compute l_g^+, with the frontal height of the filament $h_\perp$, spacing ΔS and the outer friction velocity $u_{\tau,out}$ defined in the previous subsection. In Figure 6.9 we present the drag change as a function l_g^+ for both the extremely inclined configurations, along with riblets of varying morphologies and viscous scaled cross-sectional areas. When compared with the riblets, it is evident that the drag change ΔU^+ for the $\theta^\circ = 77.5$ configuration is much larger and lies in the viscous breakdown regime. The $\theta^\circ = 90$ configuration, on the other hand, exhibits a good collapse with the trend obtained for the riblets, implying that the drag-reducing properties associated with the latter can be used to describe the physical mechanisms present in the respective canopy. Luchini *et al.* (1991) proposed the concept of protrusion height to quantify the drag change of a ribletted surface. In particular, the protrusion height is defined as the offset between the height of the virtual origin seen by the mean flow and that perceived by the turbulent fluctuations, or equivalently, the quasi-streamwise vortices of the near wall cycle (Luchini, 1996). The latter is known to induce a shear in the spanwise direction, which is responsible for the generation of skin frictional drag (Jiménez, 1994). Therefore, drag-reducing riblets essentially impede the penetration of turbulence and displace the quasi-streamwise vortices away from the virtual origin of the mean flow, leading to a decrease in the local mixing and thereby the skin frictional drag. In the drag-increasing regime, these vortices would perceive a much deeper origin than the mean flow, resulting in intense localised mixing near the wall (Luchini *et al.*, 1991).

More recently, Ibrahim *et al.* (2021), proposed a virtual origin framework to quantify the drag change effects of small surface textures on the near wall turbulence. The authors, by drawing inspiration from the seminal work of Luchini (1996), suggested that the shift ΔU^+ in the mean velocity profile is an appropriate parameter to measure the drag change induced by small texture, since the former can be assumed to be independent of

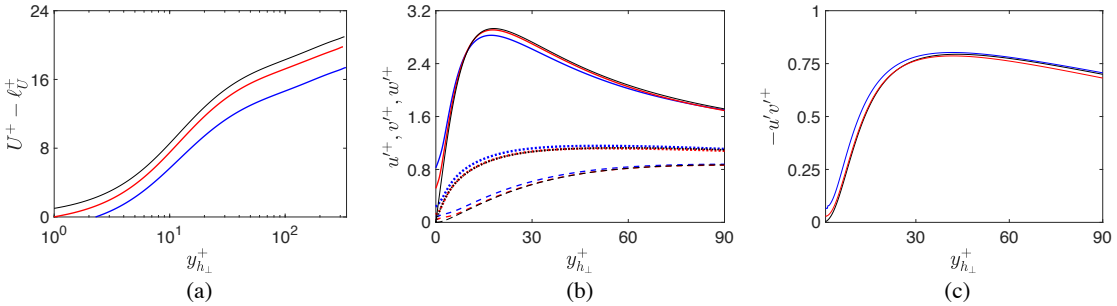


Figure 6.10: Conventional way of presenting turbulence statistics, (a) Mean velocity profile, (b) r.m.s velocity fluctuations, (c) Reynolds shear stress with the origin located at canopy edge. The black, blue and red colours represents the smooth wall open channel at $Re_\tau = 326$, $\theta^\circ = 77.5$ and $\theta^\circ = 90$, configurations, respectively. The solid, dashed and dotted lines of (b) and (d), represents the streamwise, wall normal and spanwise components, respectively.

the Reynolds number (Spalart & McLean, 2011; Garcia-Mayoral *et al.*, 2019). Therefore, the proposed framework quantifies the drag change as,

$$\Delta U^+ = \ell_U^+ - \ell_T^+ \tag{6.4}$$

where ℓ_U^+ is the virtual origin for the mean flow and ℓ_T^+ is the imaginary smooth wall perceived by the near-wall turbulence. The above formulation is based on the physical idea that the small-scale surface texturing results in a displacement of the quasi-streamwise vortices due to the diminished transverse shear (spanwise velocity is linear) and impermeability constraint (wall-normal velocity is quadratic) at the boundary (Gómez-de Segura & García-Mayoral, 2020). Thus, the turbulence is essentially shifted by a distance ℓ_T^+, and remains smooth wall-like. Furthermore, the friction velocity used to scale all the physical quantities must also be evaluated at this origin (i.e., $u_\tau = \sqrt{\tau}|_{y=-\ell_T}$) (Gómez-de Segura & García-Mayoral, 2020; Ibrahim *et al.*, 2021).

For the extremely inclined configurations considered in the current study, we define an alternative wall normal coordinate, in which the origin is located at the tip of the filament ($y_{h_\perp} = y - h_\perp$), therefore the presence of any virtual origin would lie below the canopy edge (i.e., $y^+_{h_\perp} = -\ell_U^+$ or $y^+_{h_\perp} = -\ell_T^+$). As seen in the previous subsections, we have already computed the position of the virtual origin with respect to the canopy tip, and the corresponding *outer* friction velocity. The respective virtual origin can be interpreted as the smooth wall perceived by the turbulence (i.e., $\ell_T^+ = h_\perp^+ - y_{vo}^+$), since we

have evaluated it based on the canonical logarithmic law. However, Ibrahim *et al.* (2021), established the virtual origin for the Reynolds shear stress as the appropriate choice for the origin of turbulence (i.e., $\ell_T^+ = \ell_{uv}^+$). The choice of the turbulence origin stems from the fact that the mean momentum balance in the context of a smooth wall flow is dominated by the viscous and Reynolds shear stress terms, with the latter $\langle u'v' \rangle^+ = 0$ at the wall. Based on this argument, for flows that remain smooth wall-like (under the influence of turbulence displacements), the suitable origin would correspond to the plane at which $\langle u'v' \rangle^+$ perceives a smooth wall. Therefore, we can evaluate both methods of determining the position of the abstract origin for the turbulence. Following Ibrahim *et al.* (2021), we determine the shift that better fits the Reynolds stress profile to a smooth wall data in the region at the close proximity of the wall (i.e., $10 < y_{h_\perp}^+ < 25$), to be $\ell_{uv}^+ = 1.2$ and $\ell_{uv}^+ = 0.5$ for the $\theta^\circ = 77.5$ and $\theta^\circ = 90$ configurations, respectively. These values are well within the threshold defined by $\ell_T^+ \leq 5$ (Garcia-Mayoral *et al.*, 2019). Interestingly, the obtained values also match well with the turbulence origin computed via the logarithmic formulation mentioned above (i.e., $\ell_T^+ = h_\perp^+ - y_{vo}^+ = \ell_{uv}^+$), thus complimenting the validity of both techniques. Therefore, the abstract origin of the turbulence can be determined either by considering the logarithmic formulation in the outer region or shift in the Reynolds shear stress profile.

The conventional way of portraying turbulence statistics in the context of passive flow control techniques (i.e., riblets, superhydrophobic surfaces), defines the wall-normal origin at the crest of the surface textures ($y^+ = 0$) (Garcia-Mayoral *et al.*, 2019). Thus, in Figure 6.10, we present the mean flow distribution after subtracting l_U^+. The latter is computed by considering the slip velocity at the texture edge, i.e., $l_U^+ = U_{slip}^+ = U^+(y_{h_\perp} = 0)$, since the streamwise velocity gradient closer to the smooth wall in internal units is equal to unity. The figure reveals a distinct difference between the inclined canopies and the smooth wall data. As shown in Figure 6.10b and 6.10c, we observed a shift in the velocity fluctuations and Reynolds shear stress distributions towards $y_{h_\perp} = 0$. This suggests that the overall near-wall turbulence structure has been either modified or dampened by the presence of the small textures, suggesting that the turbulence is no longer comparable to a smooth wall. However, the physical arguments proposed

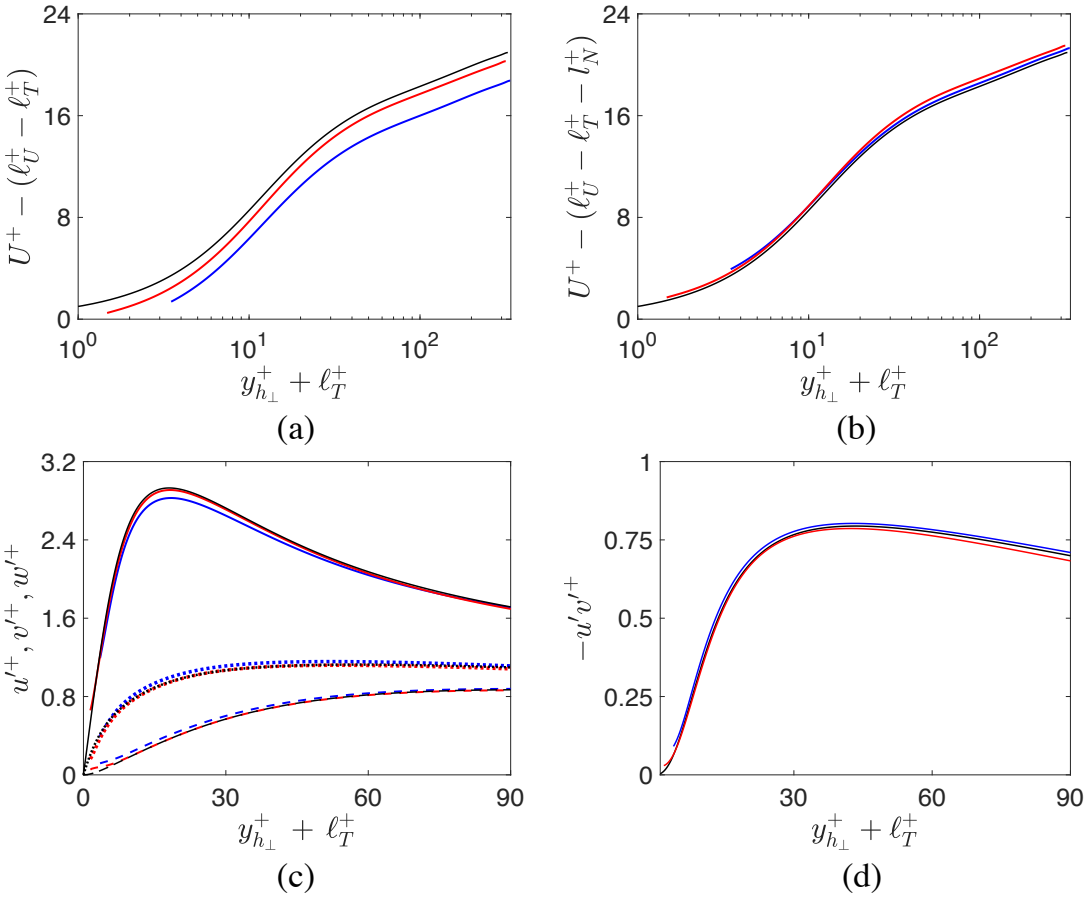


Figure 6.11: Turbulence statistics that have been shifted by the origin for turbulence (ℓ_T^+). Mean velocity profile shifted by drag change (a) and the modified drag change (b), r.m.s velocity fluctuations (c), Reynolds shear stress (d). The black, blue and red colours represents the smooth wall open channel at $Re_\tau = 326$, $\theta^\circ = 77.5$ and $\theta^\circ = 90$, configurations, respectively. The solid, dashed and dotted lines of (b) and (d), represents the streamwise, wall normal and spanwise components, respectively.

in the virtual origin framework (Ibrahim *et al.*, 2021) postulate that these differences can be incorporated by considering a simple offset to the origin. In this condition, the wall-normal coordinate is modulated such that it measures from the virtual origin for the turbulence ($y_{h_\perp}^+ = -\ell_T^+$). Figure 6.11a, 6.11c and 6.11d present the profiles of the mean velocity, velocity fluctuations and Reynolds shear stress, versus the modified wall normal coordinates. Apart from the mean velocity, these distributions reveal an excellent collapse with the smooth wall data, suggesting that the sustained turbulence in the extremely inclined canopy simulations essentially remains unaltered when compared to a flow over a smooth wall (Ibrahim *et al.*, 2021). The offset ℓ_T^+ fully describes the effects of

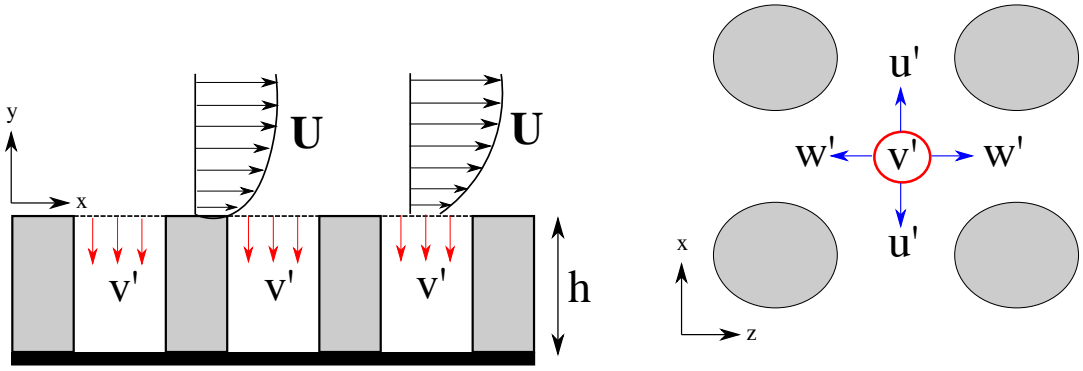


Figure 6.12: Sketch of idealised concept that leads to the introduction of the transpiration term in Equation 6.5. Left - side view of the variation in the mean velocity along the streamwise direction, inducing a transpiration into the filamentous layer. Right - top view of the canopy that redistributes the influx momentum in the wall parallel directions.

the virtual origins on the near-wall turbulence dynamics (Garcia-Mayoral *et al.*, 2019).

The minor differences observed in the mean velocity for both configurations suggest that the drag change described in Equation 6.4, is underestimated. The reason for this inconsistency can be attributed to the fact that the proposed formulation does not account for the localised effects of textures/filaments. In particular, the textured surfaces used in the investigation by Ibrahim *et al.* (2021), were not fully resolved. Instead, the authors employed a Robin boundary condition to represent the effects of the roughness elements on the overlying flow, similar to a homogenised approach (Bottaro, 2019; Lācis *et al.*, 2020; Khorasani *et al.*, 2022). However, when we consider a fully resolved textured surface or equivalently the filamentous layer in the current framework, the outer flow does not perceive an impermeable wall. Instead, the streamwise flow experiences an alternating no-slip condition on the top of the textures and a slip condition in the volume that occupies the void region in between adjacent textures (see Figure 6.12), which cannot be neglected. The spanwise flow, primarily induced by the quasi-streamwise vortices, also experiences the same phenomenon. Thus, the variation of the flow along both the streamwise and spanwise directions must induce a relative vertical flux at the top of the canopy to satisfy the mass conservation condition. Therefore, we modify the "drag change" law as,

$$\Delta U^+ = \ell_U^+ - \ell_T^+ - \ell_N^+ \tag{6.5}$$

where the first two terms represent the original formulation and $\ell_N^+ = \ell_u^+ \ell_w^+ / \ell_v^+$ is a non-linear term called the *transpirational virtual origin* that accounts for the virtual origin of all three fluctuating velocity components, which are essential in characterising the drag induced by complex surface topology. From a physical perspective, the streamwise and spanwise slip at the tip of the canopy yields a flux through the vertical planes normal to the wall-parallel directions. According to the laws of mass conservation, this additional flux must be then balanced with non-zero transpiration via the horizontal plane parallel to the bottom impermeable wall, located at the edge of the canopy. Recently, a similar physical phenomenon was reported in the context of canopy flows, in which the transpiration was characterised as a set of wall-normal jets that impinges the canopy bed (Monti *et al.*, 2020). Inside the canopy, the wall-normal jets must deflect in the wall-parallel directions to conserve the momentum and the solenoidal condition as depicted in the conceptual sketch in Figure 6.12. Thus, the transpirational condition at the canopy tip induces a momentum redistribution within the canopy. These physical arguments lead to the non-linear term being dependent on the virtual origins of the fluctuating velocity components. Thus, we compute virtual origins ℓ_u^+, ℓ_w^+ and ℓ_v^+ following the same technique employed to determine the virtual origin of the Reynolds shear stresses. In general, the virtual origin computed by considering the profiles of u' and w' is equivalent to their relative slip lengths (Garcia-Mayoral *et al.*, 2019). However, the $v'_{r.m.s.}$ profile is quite complex, thus the virtual origin (ℓ_v) is determined by extrapolating the best fit of the r.m.s. profile of v', is comparable to a transpiration length (or equivalently the wall-normal slip length). These observations suggest that the term ℓ_N accounts for the combined effect of the transpiration and the wall parallel redistribution of the momentum influx at the tip of the canopy.

In Figure 6.11b, we shift the mean velocity distribution with the modified drag change and observe an excellent collapse with the smooth wall data. This suggests that the drag change is predicted accurately by considering a combination of the virtual origins of the turbulence and the transpiration. Nevertheless, it can be hypothesised that the apparent effects of the extremely inclined filaments are similar to those of the small-scale textures, and are essentially characterised by the displacement of the

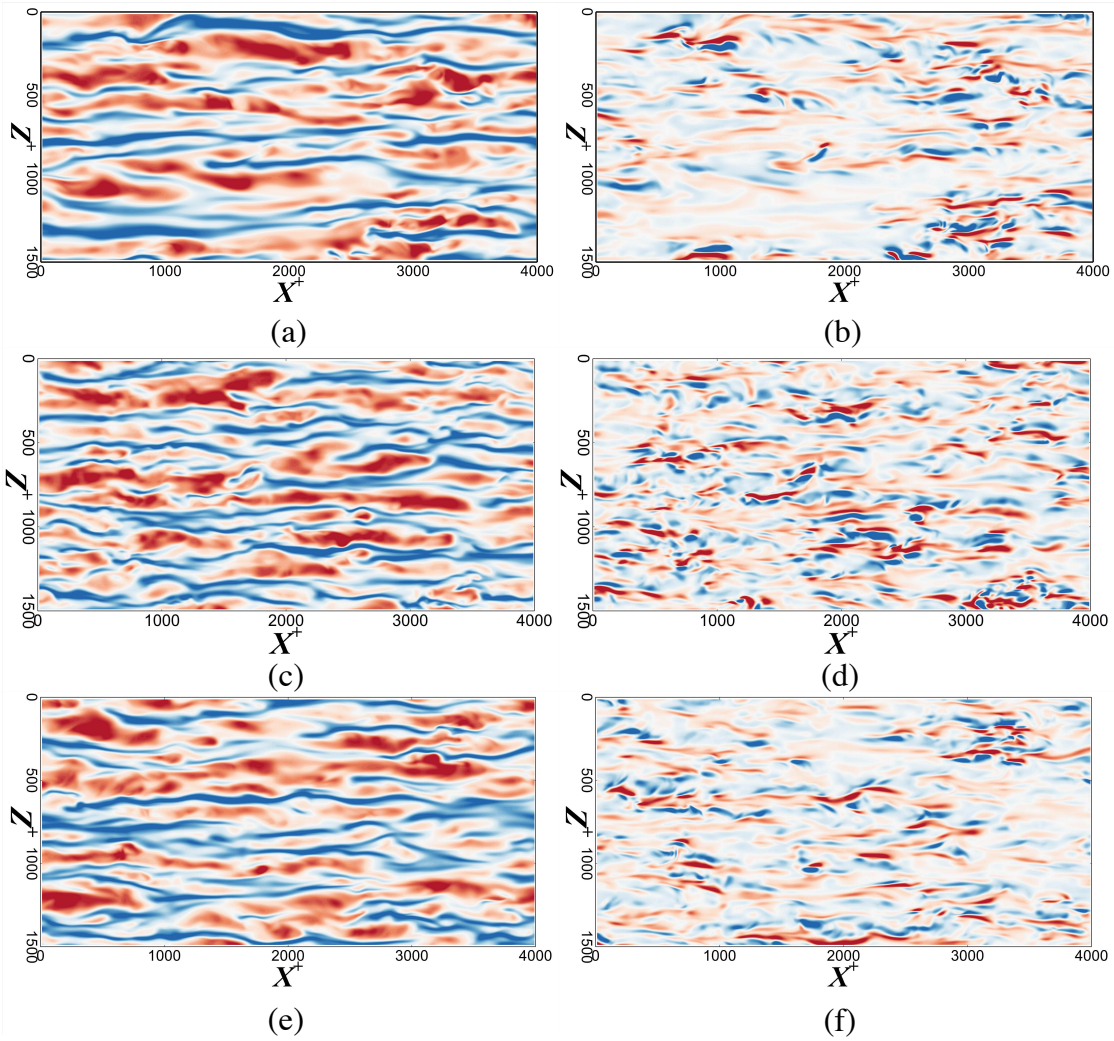


Figure 6.13: Instantaneous realisations of the streamwise (first column) and wall normal (second column) components located at a wall parallel plane of $y^+_{h_\perp} + \ell^+_T = 20$. The rows from top to bottom corresponds to the smooth wall open channel, $\theta^\circ = 77.5$ and $\theta^\circ = 90$, configurations, respectively. The colour band from red to blue represents positive to negative. The velocity fluctuations were made non-dimensional with the $u_{\tau,out}$ and ν, with a depicted range of $u'^+ \in [-5, 5]$ and $v'^+ \in [-1, 1]$.

near-wall cycle away from the wall. Additionally, this can also be verified by examining the instantaneous snapshots of the extremely inclined canopy flows, and the smooth wall flow. Figure 6.13 compares the u'^+ and v'^+ for the extremely inclined configurations with the smooth wall open channel located at the $y^+_{h_\perp} + \ell^+_T = 20$. The figure corroborates the proposed hypothesis since there is no visual evidence of modulation in the overall flow when compared with the smooth open channel flow.

Nominal Regime	θ°	U_s^+	ℓ_T^+	ℓ_u^+	ℓ_v^+	ℓ_w^+	ΔU^+
Negligible Inclination	*0*	*1.9*	*20.3*	*12.9*	*77.4*	*22.2*	*12.5*
Weak Inclination	*33.5*	*2.3*	*9.9*	*8.6*	*43.8*	*21.1*	*10.3*
Mild Inclination	*48.3*	*2.5*	*6.4*	*8.0*	*31.6*	*19.1*	*9.0*
Relatively Strong Inclination	*60*	*2.7*	*3.8*	*6.9*	*19.6*	*11.6*	*7.1*
Strong Inclination	*77.5*	*3.0*	*1.2*	*3.6*	*5.6*	*3.8*	*0.7*
Very Strong Inclination	*90*	*1.7*	*0.5*	*1.7*	*1.7*	*1.3*	*-0.6*

Table 6.2: Parameters used in the virtual origin framework (Ibrahim *et al.*, 2021). The slip velocity at the tip of the canopy is defined by U_s^+, while ℓ_T^+ represents the virtual origin for the turbulence. The virtual origin for the velocity fluctuations are given by ℓ_u^+, ℓ_v^+ and ℓ_w^+, respectively. The drag is computed via the formulation presented in Equation 6.5.

6.3.4 Prediction of drag change via the virtual origins

In this section, we extend the virtual origin framework to the canopy regime, which presents a significant departure from a smooth wall-like flow. The presence of the filamentous layer induces additional drag-increasing dynamical mechanisms, such that the effect of the respective texture cannot be represented solely by the virtual origin model (Ibrahim *et al.*, 2021). However, the fundamental idea leading to the virtual origin framework relies on the fact that the r.m.s distributions of the diagonal Reynolds stress terms remain comparable to a smooth wall flow. For this condition, the near-wall turbulence cycle must not be disrupted. Ibrahim *et al.* (2021) reported that the virtual origin framework holds as long as it satisfies the condition, $\ell_T^+ \leq 5$. Beyond this threshold, the underlying assumptions are no longer valid since the increasing size of the individual textures extends beyond the realm of the viscous sublayer (Pope, 2000). This condition, often termed the transitional roughness is characterised by a complex interaction between the viscous and pressure drag offered by the textural elements (Flack, 2018; Thakkar *et al.*, 2018). Further increase in the roughness size yields the fully rough asymptotic regime, in which drag modification is essentially dominated by the pressure drag (Jiménez, 2004). In the current investigation, apart from the $\theta^\circ = 60$ configuration, the remaining cases do not satisfy this threshold. Indeed the low and mildly inclined canopy configurations fall outside the scope of the virtual origin framework. However, it should be noted that we are not attempting to prove that this regime is similar to a

smooth wall flow. Instead, we aim to predict the drag change induced by the filaments, via the virtual origins for the fluctuating velocity components. Thus, we expect the modulation introduced in the form of a non-linear term to the overall drag change, to extend the virtual origin framework beyond $\ell_T^+ \approx 5$.

First, using the technique demonstrated in the previous subsection, we compute the virtual origins for the turbulence ℓ_T^+ and fluctuating velocity components (ℓ_u^+, ℓ_v^+, and ℓ_w^+) for all configurations in the canopy regime. The obtained values are presented in Table 6.2. Once again ℓ_{uv}^+ matches well with the values computed via the logarithmic formulation, suggesting that the latter can be considered as the origin for turbulence, although the employed formulation contains the mean velocity term. Then the resulting non-linear transpirational virtual origin can be determined. From Table 6.2, it is evident that the non-dimensional virtual origins increase with the increasing angle of inclination. This suggests that the outer flow of the low and mildly inclined canopies perceives a much deeper origin. Within the remit of the same argument, the origin of the mean flow should also exhibit the behaviour. For the nearly upright configuration, we observe a large difference between the virtual origin for the mean flow and turbulence. In this condition, the mean flow origin computed via the slip velocity ($\ell_U^+ = U_s^+$) becomes insignificant, when compared with the turbulence and velocity fluctuations origins. Therefore, we need to define the virtual origin for the streamwise velocity fluctuations (ℓ_u^+) as the alternative origin for the streamwise flow for the cases where $U_s^+ \ll \ell_T^+$. The reason for the observed inconsistency can be attributed to the breakdown of the linear velocity mean profile since the streamwise velocity gradient in wall units is no longer equal to unity (Luchini, 1996; Garcia-Mayoral *et al.*, 2019). Note that the substitution of mean flow origin ℓ_U^+ with the origin for the streamwise velocity fluctuations is only limited to configurations that are associated with the $U_s^+ \ll \ell_T^+$ condition.

Figure 6.14a, presents the mean velocity distribution that has been shifted by the modified formulation. The resulting profile collapses well with the smooth wall data, illustrating the robustness of Equation 6.5 in describing the overall drag change induced by the filamentous surface. Note that the low and mildly inclined configurations do not extend into lower values of $y_{h_\perp}^+$, since we have chosen the tip of the canopy as an origin in

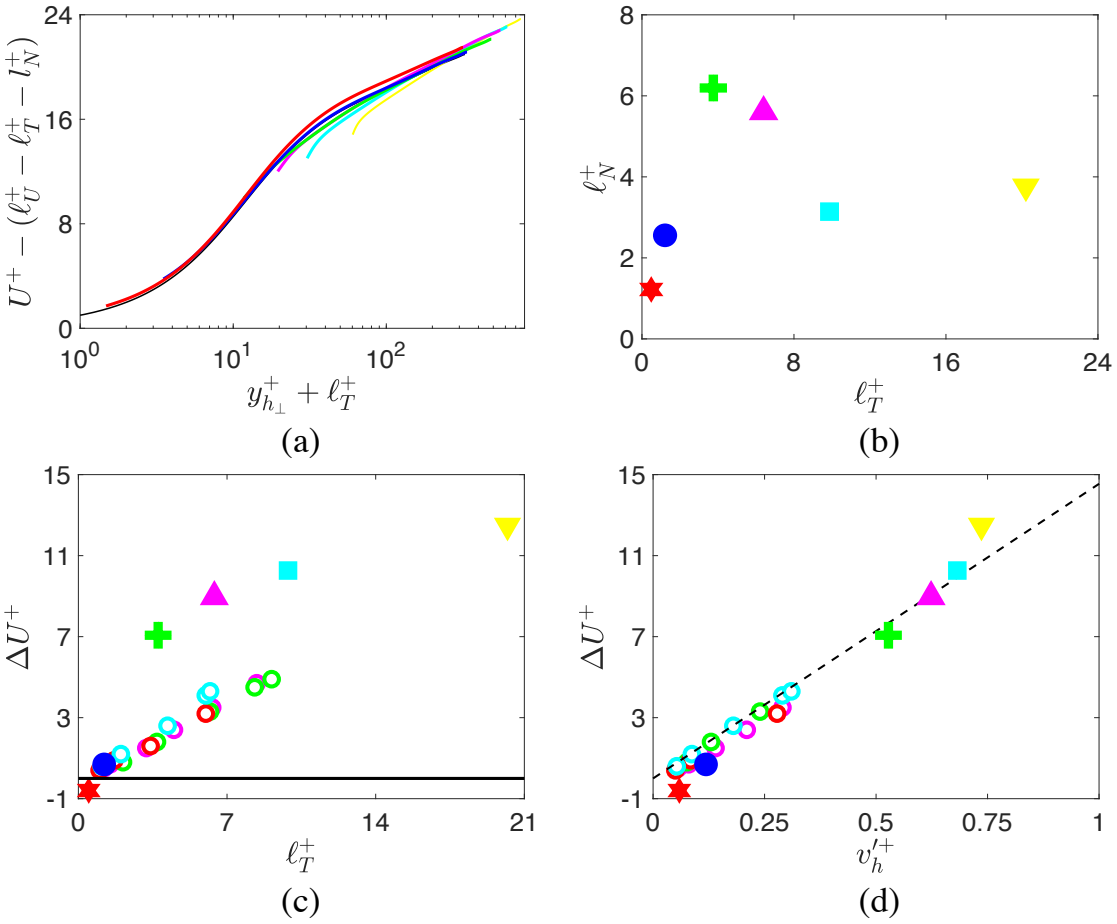


Figure 6.14: (a) Mean velocity profile according to the drag change proposed in Equation 6.5, (b) transpirational virtual origin as a function of the origin for the turbulence, (c) drag change as a function of the abstract origin for the turbulence and (d) drag change as a function of the transpirational velocity at the tip of the canopy. The colours of the solid line can be associated with the symbols as given in Table 6.1. The black horizontal line represents $\Delta U^+ = 0$. The dashed line represents a linear relationship $\Delta U^+ = 13.42 v_h^+$ according to Orlandi & Leonardi (2008). The coloured *o* symbols represents data extracted from Abderrahaman-Elena *et al.* (2019), O - colocated posts, O - colocated posts with varying heights, O - staggered posts (streamwise) and O - staggered posts (spanwise).

the wall-normal direction. Figure 6.14c presents the predicted drag change as a function of the virtual origin for the turbulence for all the canopy configurations. The figure also includes the results obtained for several textured surfaces from Abderrahaman-Elena *et al.* (2019). In particular, the authors performed several DNS of turbulent channel flow surfaces covered with a homogenous distribution of colocated posts, that nominally fall in the transitionally rough regime. More recently, Thakkar *et al.* (2018), by conducting a series of DNS of rough wall turbulent channel flow, identified the occurrence of

a couple of sub-regimes within the remit of the transitionally rough regime. Based on the value of the equivalent sand grain roughness height (k_s^+), the authors called these sub-regimes as the lower ($0 \leq k_s^+ \leq 13.05$) and an upper ($13.05 < k_s^+ < 78.3$) transitionally rough regime.

The $\theta^\circ = 77$ configuration collapses with the trend observed for the colocated and staggered posts, indicating that the respective canopy configuration behaves as a transitionally rough surface. We can infer from the magnitude of the ΔU^+ that the $\theta^\circ = 77$ configuration is in the lower transitionally rough regime, where the drag modulation provided by the inclining filaments is still governed by viscous drag. This is also further verified by the collapse of the r.m.s profiles of the velocity fluctuations with the open-channel turbulent flow (see Figure 6.11), suggesting that the overall flow is reminiscent of a smooth wall flow. Conversely, the decreasing angles of inclination yield a deeper turbulence origin. For the same value of ℓ_T^+, the mildly and low inclined canopies present a larger drag change when compared with the surfaces covered with colocated posts, indicating a departure from the roughness (transitional) regime to the canopy regime. Alternatively, Orlandi & Leonardi (2008) found a strong linear correlation between the drag change and the wall-normal velocity fluctuation (i.e., transpiration intensity $v_h'^+$) at the tip of the texture. The resulting scaling removes any dependence of the drag change on the spatial morphology of the respective textures that populate the surface. For example, height, density, shape, etc. Figure 6.14d illustrates the drag change as a function of the transpirational intensity evaluated at the tip of the canopy. The figure presents an excellent collapse, with the $v_h'^+$ capturing the increasing drag change with the increasing texture size. The excellent correlation between the drag change and wall-normal velocity was also shown by Rosti & Brandt (2017), for the case of turbulent flow that develops over viscous hyper-elastic walls. The observed linear relationship suggests that the departure from the roughness (transitionally) regime to the canopy flow-like regime is fully characterised by the enhanced transpiration occurring at the edge of the canopy.

This effect is also evident in the non-linear term (i.e., transpirational virtual origin ℓ_N^+) of the proposed modified drag change (see Figure 6.14b). In particular, ℓ_N^+ increases with

the increasing values of ℓ_T^+ and features a maximum for the mildly inclined configurations. A further increase in ℓ_T^+ results in the asymptotic saturation of ℓ_N^+, which is indicative of the canopy regime. Similar behaviour was reported in the seminal work of Nikuradse (1933). In their pioneering investigation, the inner surface of the pipe was covered with a sand grain. The height of the latter (k_s^+) was systematically varied such that the roughness spans the full transition from a hydrodynamically smooth to a fully rough regime. Based on the proposed logarithmic formulation for a rough wall boundary layer, often known as Nikuradse's scaling i.e., $U^+ = A + 5.75log_{10}(r/k_s)$, they suggested that the effect of the roughness is captured by the additive constant. Similar to the behaviour of ℓ_N^+, the latter exhibits a maximum in the transitionally rough regime and asymptotically saturates to $A \approx 8.5$ at the onset of the fully rough regime (Thakkar *et al.*, 2018). In this condition, the onset of the canopy regime can be perceived as the inception of the fully rough regime in the context of roughness studies.

Lastly, we focus on the actual total drag experienced by the flow. In the current investigation, we have conducted all the simulations by considering the same nominal bulk Reynolds number, $Re_b = 6000$, yielding a constant volumetric flow rate. This in turn facilitates the direct comparison of the smooth wall case with the inclined canopies, enabling us to measure the total drag from the average pressure gradient. In particular, the drag reduction of the extremely inclined canopy configurations can be quantified by the ratio $DR = (G_{px} - G_{px,s})/G_{px,s}$, where G_{px} and $G_{px,s}$ are the mean pressure changes in the streamwise direction for the inclined canopies and the smooth wall configurations, respectively. For the $\theta^\circ = 90$ configuration, we obtain a total drag reduction of $DR = 3.2\%$, while the $\theta^\circ = 77$ yields a total drag reduction of $DR = -12.1\%$, where the negative indicates an increase in the total drag. The modest DR performance of the fully inclined configurations can be associated with the limitations of the drag-reducing capabilities in riblets (Garcia-Mayoral & Jimenez, 2011).

6.3.5 Structure of the canopy flow regimes

In this section, we turn our attention to the structures of the flow that occupy the various configurations considered in the current investigation. The structures that populate

the turbulent flow field are evaluated by determining the spectral decomposition and the auto-correlation function of the fluctuating velocities. Because we have already established that the extremely inclined configurations are reminiscent of smooth wall flow, the results for the $\theta^\circ = 90$ configuration have been omitted for brevity in this section. Following Nikora *et al.* (2007*a*), we extract the full fluctuating field by employing a triple decomposition technique, as given below,

$$u(x, y, z, t) = \langle \overline{u}(y) \rangle + \tilde{u}(x, y, z) + u'(x, y, z, t) \tag{6.6}$$

$$\tilde{u}(x, y, z) = \overline{u}(x, y, z) - \langle \overline{u}(y) \rangle \tag{6.7}$$

where instantaneous velocity $u(x, y, z, t,)$ is decomposed into a time and spatial averaged component ($\langle \overline{u}(y) \rangle$), a temporal averaged spatially fluctuating component $\tilde{u}(x, y, z)$ and a full space-time fluctuating velocity field $u'(x, y, z, t)$. The $\tilde{u}(x, y, z)$ term also commonly referred to as the dispersive velocity, accounts for the localised effect of the filaments. In the region outside the canopy, this term goes to zero and the canonical Reynolds decomposition is recovered.

We start by focusing on the spectral energy content of the fluctuating velocity components in the wavelength domain. Figure 6.15 and 6.16 represent the one-dimensional pre-multiplied spectra as a function of the wall-normal distance, and the streamwise and spanwise wavelengths, respectively. The panels in the figure are ordered as a matrix of 5×3, with each column representing the streamwise, wall-normal and spanwise velocity fluctuations, while the rows from top to bottom correspond to the increasing angles of inclination from $\theta^\circ = 0$. The wall-normal distance and wavelengths have been made non-dimensional with the open channel height, while the spectral energy content has to be re-scaled with the local friction velocity defined in Equation 6.3. Moreover, the organisation of the coherent motions appearing in the flow is qualitatively investigated by considering the two-point autocorrelation function. We compute the latter as a function of streamwise and spanwise separation length. For example, the autocorrelation function in the streamwise direction is given as,

$$R_{u_i' u_i'} = \frac{u_i'(0, y, 0) u_i'(\Delta x, y, 0)}{u_i'^2(0, y, 0)} \tag{6.8}$$

where Δx is the separation distance along the streamwise direction. We present the $R_{u_i'u_i'}$ as a function of the streamwise and spanwise separation distance in Figure 6.18 and 6.19, respectively. The figures are ordered in the same manner as the one directional pre-multiplied spectra.

Both Figures 6.15 and 6.16 reveals the emergence of two peaks occurring in the inner and outer layer, respectively. The outer peak, occurring in all three fluctuating velocity components corresponding to a wavelength of $\lambda_x/H = 1$ and $\lambda_z/H = 1$, can be identified as large-scale coherent structures. In particular, the streamwise velocity fluctuation presents a clear outer peak (just above the tip of the canopy) associated with a very long streamwise wavelength. The corresponding structures occur in the form of elongated velocity streaks that are typically found in the logarithmic region of wall-bounded turbulent flows. The occurrence of these streaky structures has been previously reported in the context of canopy flows (Monti *et al.*, 2020). The u' peak of the pre-multiplied spectra, obtained for the different values of $\theta°$, clearly scales well with the outer flow units. In particular, we observe an increase in the intensity of the outer peak with the increasing angles of inclination. This suggests the strengthening of the quasi velocity streaks. By observing the streamwise two-point autocorrelation function in Figure 6.18, we notice the monotonic increase in the streamwise coherent length in the region just outside the canopy marked by the green horizontal line. The longest streamwise coherent length is observed for the $\theta° = 77$, which was previously established as a smooth wall-like flow. This behaviour suggests that the coherency of the canonical streaky structures increases, yielding a more organised motion with a less meandering shape. This can also be verified by observing the instantaneous wall parallel realisations of u' in Figure 6.13. The latter reveals the presence of streamwise oriented streaky structures that extends at a spanwise distance of $\Delta z^+ \approx 100$ (Kim *et al.*, 1987). Previously, this behaviour was reported as a drag-reducing condition in the context of permeable substrates (Rosti *et al.*, 2018*a*; Gómez-de Segura & García-Mayoral, 2019). The velocity streaks are also generally flanked by a set of quasi-streamwise vortices (Monti *et al.*, 2020). Their presence can be confirmed by the outer peaks of v' and w' in the pre-multiplied spectra presented in Figure 6.16 and auto-correlation function in Figure 6.19.

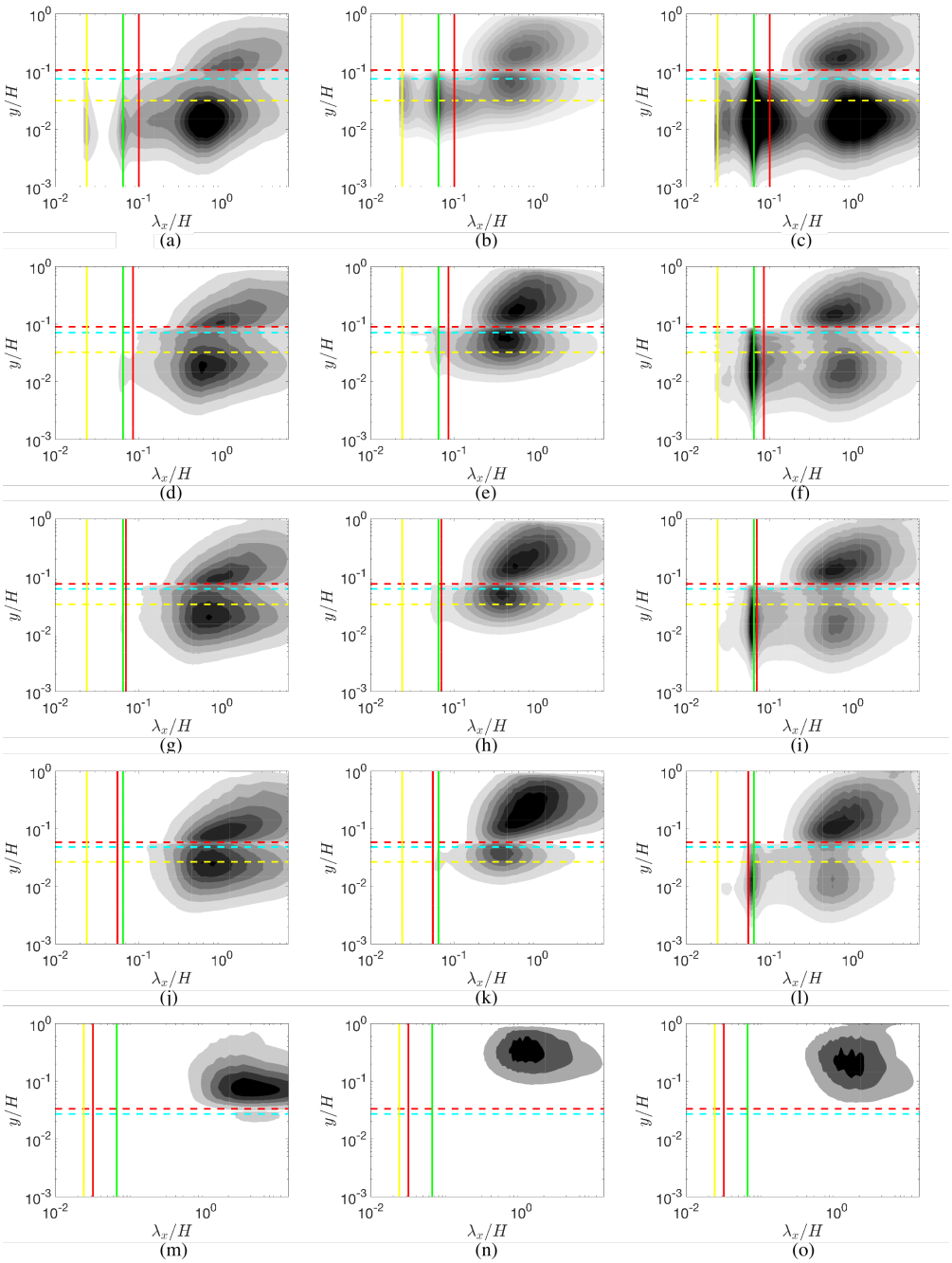


Figure 6.15: One dimensional pre-multiplied spectra as a function of the wall normal (y/H) direction and the streamwise wavelength (λ_x/H). The rows from top to bottom represents the ascending order of increasing θ. The columns from left to right represents $k_x\phi_{u'u'}/u^2_{\tau,l}$ with a range of [0, 0.8] and incremental of 0.1, $k_x\phi_{v'v'}/u^2_{\tau,l}$ with a range of [0, 0.3] and incremental of 0.02, and $k_x\phi_{w'w'}/u^2_{\tau,l}$ with a range of [0, 0.4] and incremental of 0.04. The yellow, green and red vertical lines represents the wavelength at $\lambda_x/H = d$, $\lambda_x/H = \Delta S$ and $\lambda_x/H = h$, respectively. The red, yellow and cyan horizontal dashed lines represents $y/H = h$, $y/H = y_{ip}$ and $y/H = y_{vo}$, respectively.

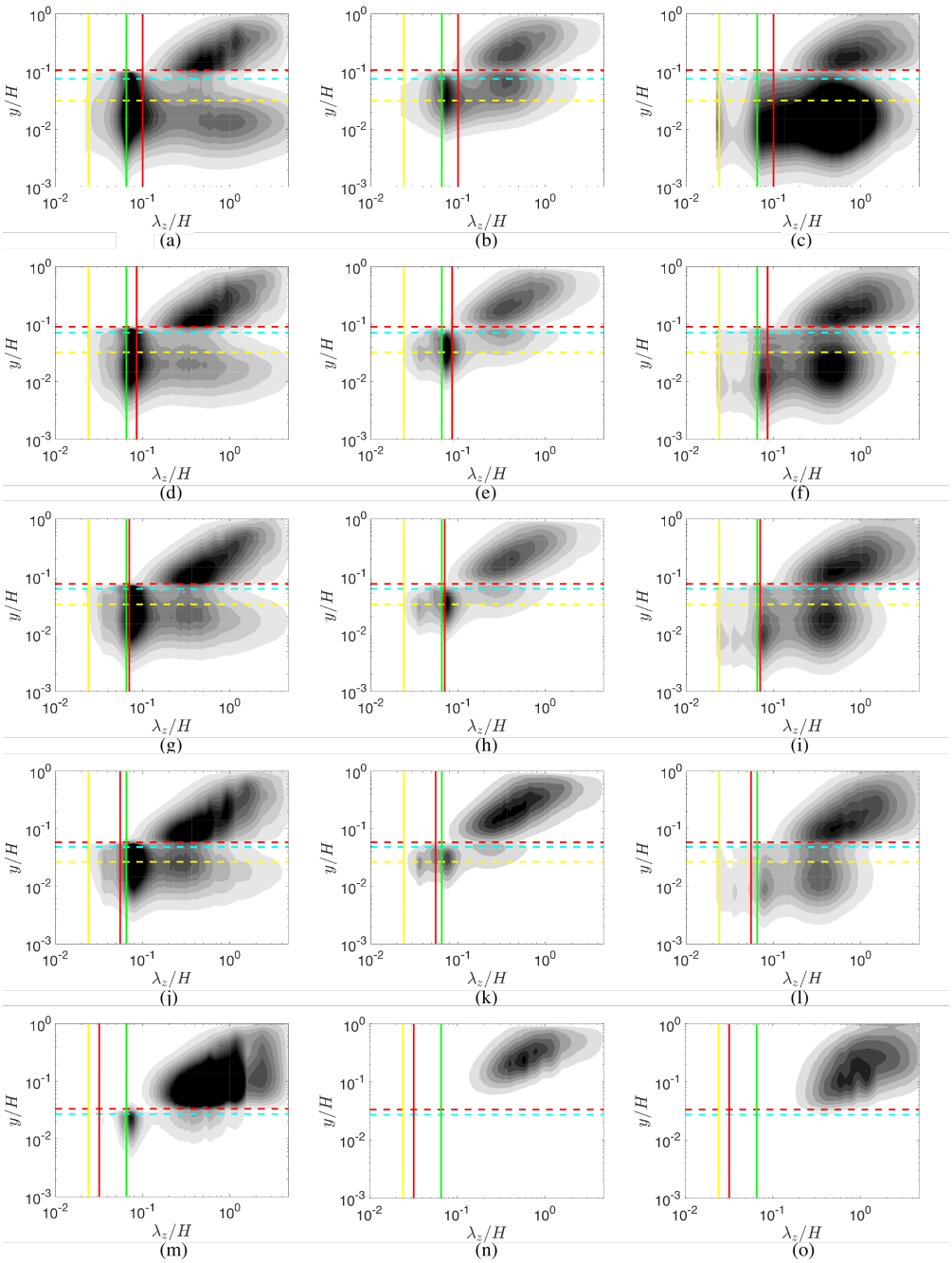


Figure 6.16: One dimensional pre-multiplied spectra as a function of the wall normal (y/H) direction and the streamwise wavelength (λ_z/H). The rows from top to bottom represents the ascending order of increasing θ°. The columns from left to right represents $k_z\phi_{u'u'}/u^2_{\tau,l}$ with a range of [0, 1] and incremental of 0.1, $k_z\phi_{v'v'}/u^2_{\tau,l}$ with a range of [0, 0.4] and incremental of 0.04, and $k_z\phi_{w'w'}/u^2_{\tau,l}$ with a range of [0, 0.5] and incremental of 0.05. Coloured lines have the same meaning as in Figure 6.15.

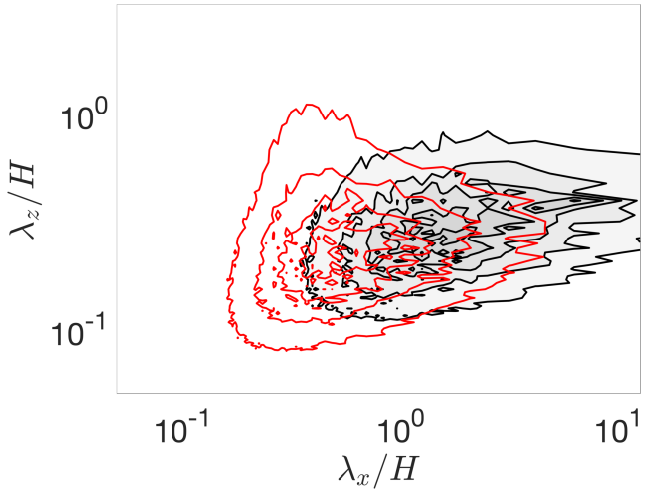


Figure 6.17: Two dimensional pre-multiplied spectra of $k_x k_z \phi_{v'v'}/u^2_{\tau,l}$ as a function of the streamwise and spanwise wavelengths, extracted at a wall parallel plane located at $y^+_{out} = 20$. The black lines with filled contour represents the $\theta = 77$, while the red lines represents $\theta = 60$ configuration.

On the other hand, in the canopy regime (i.e., decreasing $\theta°$), it can be noticed that the streamwise correlation of u' goes to zero at a shorter distance (see Figure 6.19) when compared with the $\theta° = 77$ configuration, indicating a breaking up of the streamwise coherency of the u' correlation function. This behaviour is accompanied by an abrupt decrease in the v' correlation along the streamwise direction (see the second column of Figure 6.18). This suggests the existence of another physical mechanism at the edge of the canopy. It is known that the inflectional point located at the tip of the canopy induces Kelvin Helmholtz (KH) type instability, leading to the generation of large-scale spanwise coherent rollers. The spanwise vortices manifest at the edge of the canopy, inducing a mutual upwash and downwash of momentum into the canopy via the wall-normal component (v'). This is evident by the organisation of the outer and inner peaks of the v' pre-multiplied spectra, which in turn is the preferable mode of communication between the two layers. Another reason for the emergence of rollers can be attributed to the non-zero transpiration at the edge of the canopy (Jimenez *et al.*, 2001). This can also be confirmed by the outer peak of the $u'v'$ in Figure 6.20, which presents the magnitude of the pre-multiplied cospectra. However, these spanwise oriented rollers are not clear vorticity structures that can be detected easily (Finnigan *et al.*, 2009),

since they lose part of their coherence due to the strong sweep events from the large-scale structures that populate the outer flow (Monti *et al.*, 2019). Nevertheless, the occurrence of these vortices has been often associated with drag-increasing scenarios by previous authors in the context of permeable substrates (Rosti *et al.*, 2018*a*) and ribletted surfaces (Endrikat *et al.*, 2021). Concerning the effect of filament inclination, we observe a decrease in the footprint of the v' peak at the edge of the canopy, as θ° is increased, with the peak being absent for the $\theta^\circ = 77$ configuration. This suggests that the decreasing transpiration as a result of the inclining filaments mitigates the occurrence of the KH instability, or at least suppresses the formation of spanwise oriented vortices. The latter can be easily recognised by the two-dimensional pre-multiplied spectrum of v' given in Figure 6.17. In particular, for the $\theta^\circ = 60$, the figure illustrates a v' peak corresponding to a large spanwise wavelength and shorter streamwise wavelength. This feature indicating the onset of the spanwise coherent structures was also previously reported in the context of ribletted surfaces (Garcia-Mayoral & Jimenez, 2011). However, this feature is absent when the angle of inclination is increased, indicating the suppression of the KH instability. The overall spectral structure, characterised by long streamwise wavelengths, is reminiscent of a smooth wall flow. This behaviour has also been reported by Rosti *et al.* (2018*a*), for porous layers that are characterised by a decreasing wall normal permeability.

Next, we turn our attention to the internal layer of the canopy. The discussion of the turbulent field of the inner layer is also facilitated with the wall parallel snapshots of the fluctuating velocity field located at the location of the internal inflection point, presented in Figure 6.21. The latter is organised as a 4×3 matrix with the rows depicting the inclined configurations spanning from $\theta^\circ = 0$ to $\theta^\circ = 60$, while the columns represent the streamwise, wall-normal and spanwise components of the fluctuating field.

First, we consider the $\theta^\circ = 0$ configuration. The one-dimensional pre-multiplied spectra reveal the occurrence of two peaks in the internal layer of the canopy for both streamwise and spanwise wavelengths. The leftmost peak corresponds to a wavelength of $\lambda_x/H = \lambda_z/H = \Delta S$ is associated with the small-scale contributions that sustain in the form of high momentum meandering motion in between the filaments, which is

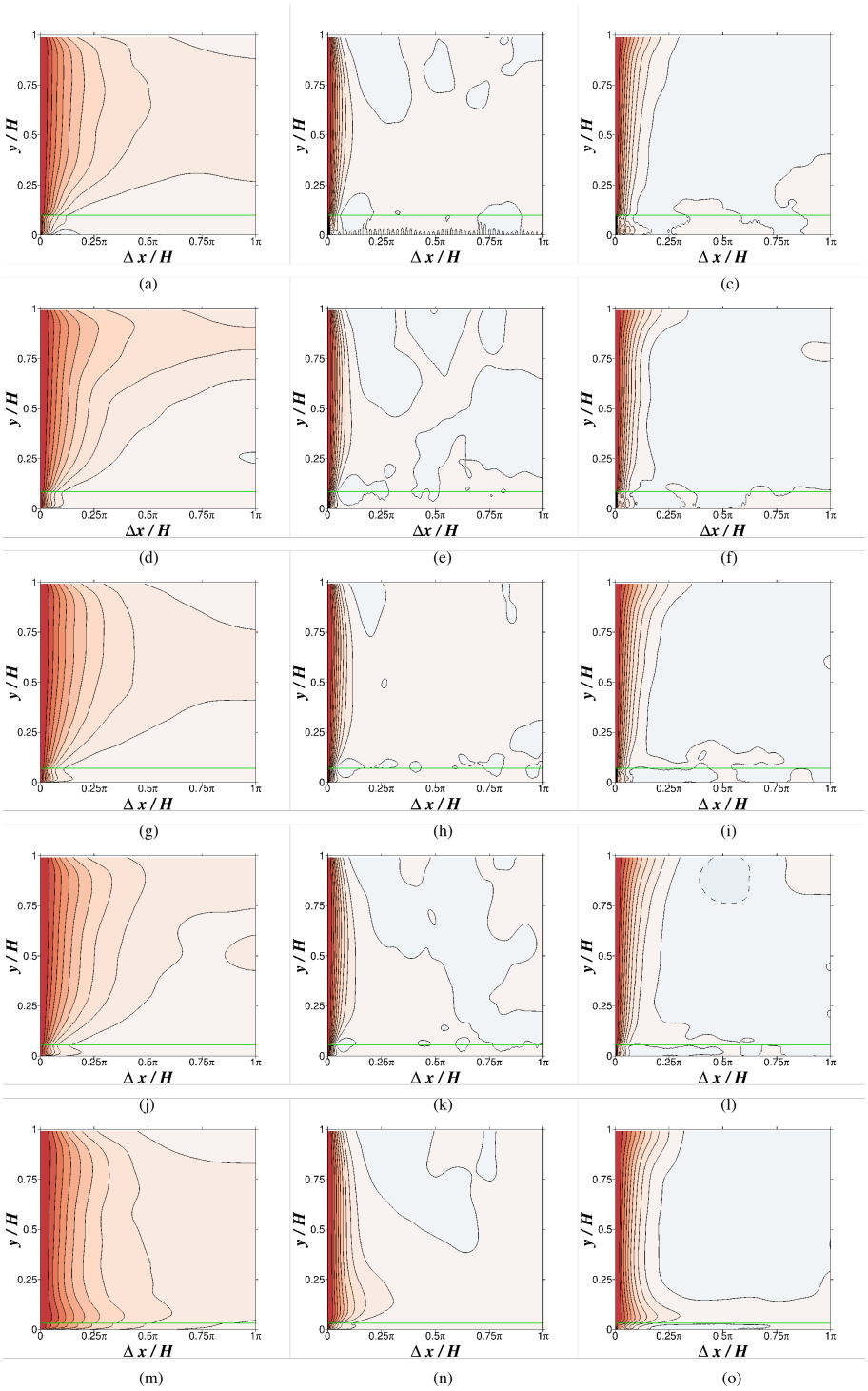


Figure 6.18: Contour maps representing the two-point autocorrelation functions of the velocity fluctuations in the streamwise direction. The columns left to the right showcases the autocorrelation for u', v'. The contours levels are denoted by [-0.4,1], associated with the blue to red region with an increment of 0.1.The negative values are plotted with a dashed line. The green horizontal line denotes the height of the canopy.

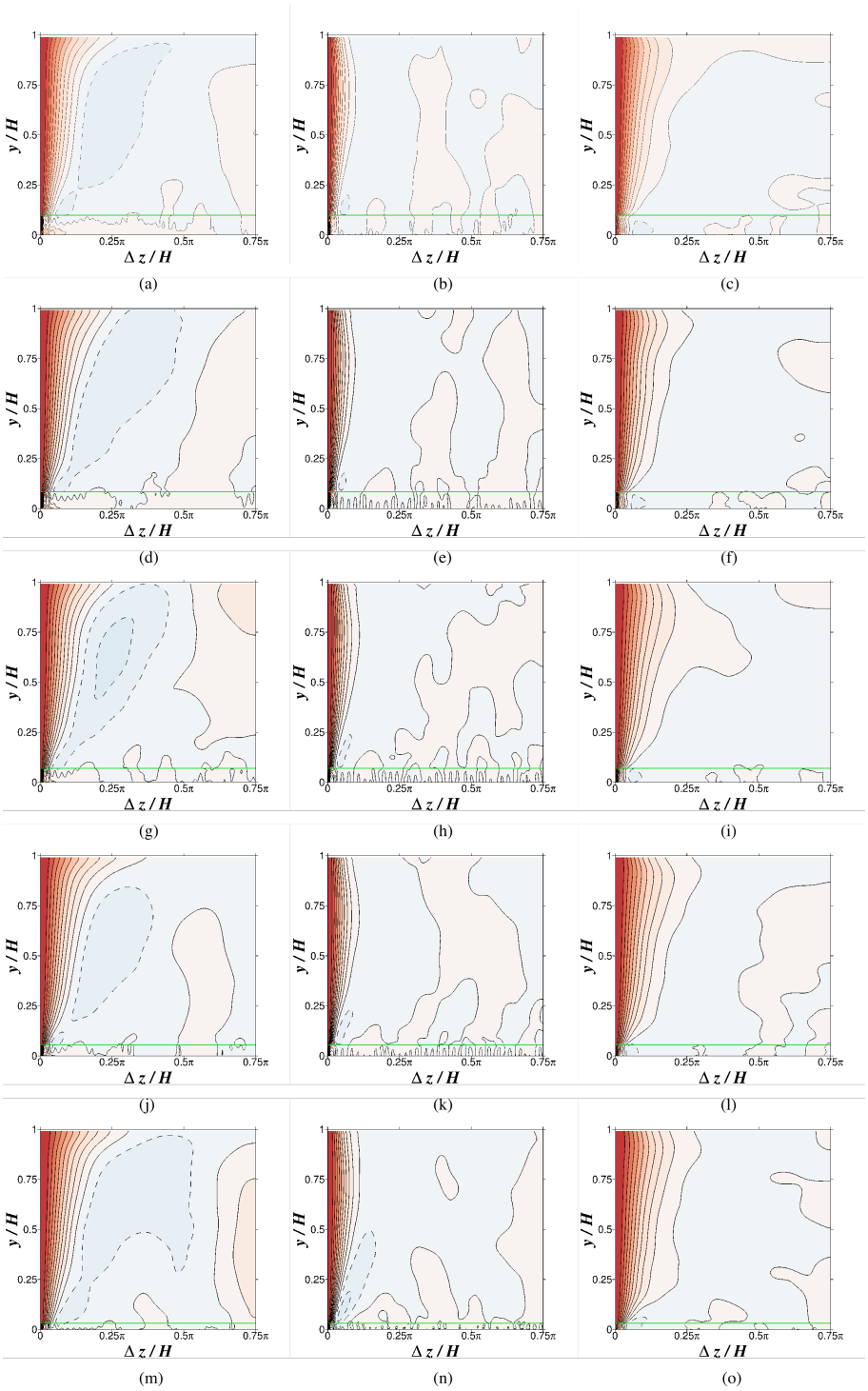


Figure 6.19: IContour maps representing the two-point autocorrelation functions of the velocity fluctuations in the spanwise direction. The columns left to the right showcases the autocorrelation for u', v'. The contours levels are denoted by [-0.4,1], associated with the blue to red region with an increment of 0.1.The negative values are plotted with a dashed line. The green horizontal line denotes the height of the canopy.

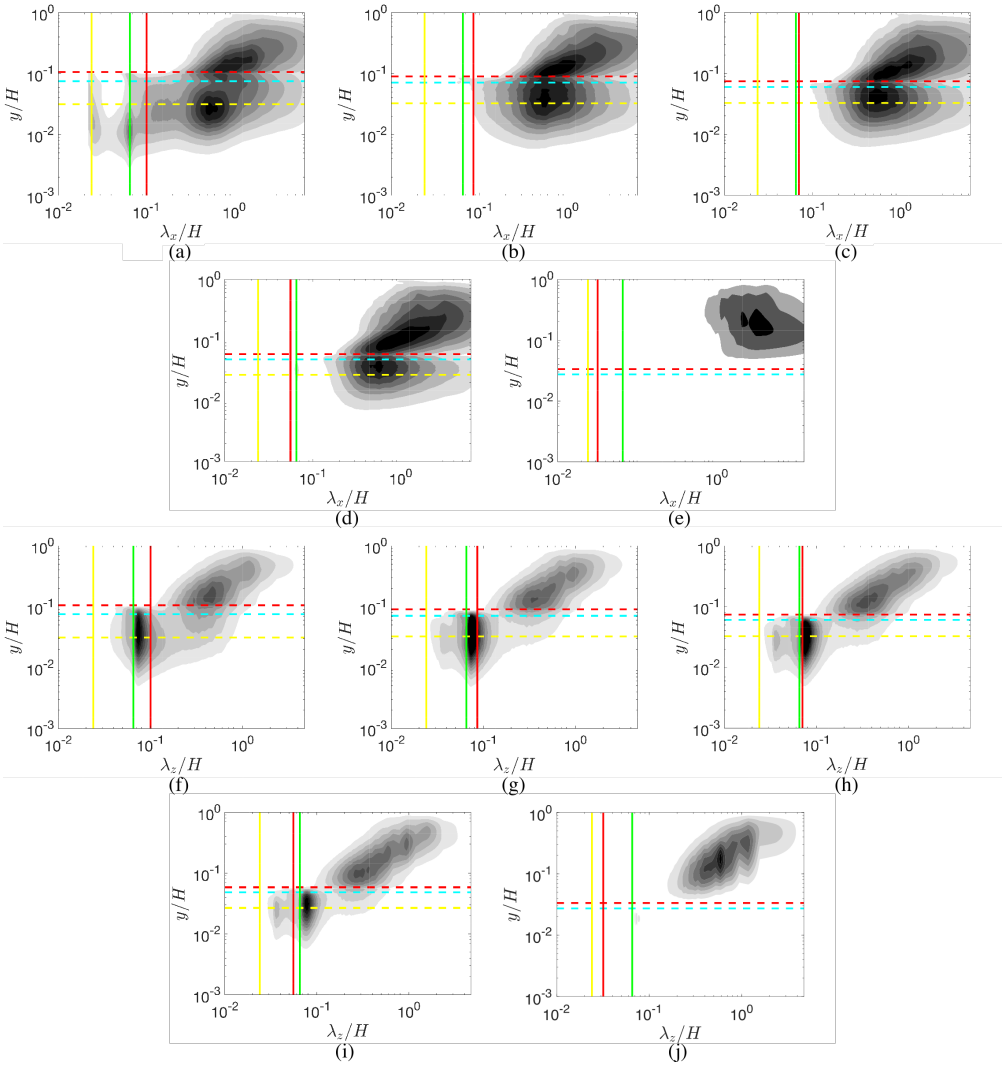


Figure 6.20: Magnitude of one dimensional pre-multiplied cospectra ($k_x|\phi_{u'v'}|/u^2_{\tau,l}$ and $k_z|\phi_{u'v'}|/u^2_{\tau,l}$) as a function of the wall normal (y/H) direction, the streamwise (λ_x/H) and spanwise (λ_z/H) wavelength. The top two rows concerns the λ_x/H and the last two rows represents λ_z/H. The panels from left to right has been ordered in the increasing values of $\theta°$. The $k_x|\phi_{u'v'}|/u^2_{\tau,l}$ with a range of [0, 0.2] and incremental of 0.02, and $k_z|\phi_{u'v'}|/u^2_{\tau,l}$ with a range of [0, 0.5] and incremental of 0.05, Coloured lines have the same meaning as in Figure 6.15.

primarily governed by their localised spacing. From the panels in the top row of Figure 6.15 and 6.16, we also observe an alternative small-scale contribution in the form of filament wake, which is characterised by a wavelength of $\lambda_x/H = \lambda_z/H = d$. In the fully dense regime, the effect of the filament diameter cannot be neglected since the ratio $\Delta S/d \approx 6$. Conversely, the rightmost peak, corresponding to a wavelength of $\lambda_x/H = \lambda_z/H = 1$, is associated with the large-scale contributions arising from the penetration of the high momentum outer flow turbulent structures. Indeed the relevant

length scales deep inside the canopy are the geometrical scales of the canopy, yet the peak for u' and w' resides below the location of the internal inflection point, while the wall-normal extent of the v' peak is limited to the location of the virtual origin. Apart from the obvious weak shear developing over the impermeable wall, this suggests that the $u'$and w' terms have a different physical mechanism when compared with the v' term. In the previous chapter, it was reported that in a fully dense regime, the inner and outer layers decouple due to the strong scale separation induced by the lower ΔS. Thus, the penetrated outer flow structures do not extend to the canopy bed, instead, they manifest above the virtual origin (denoted by the cyan horizontal dashed line of Figure 6.15 and 6.16). This is also evident by the lack of or negligible large-scale contributions in the instantaneous snapshots of the fully dense regime presented in Figure 6.21. In the sparser regime, these outer structures occupy the full extent of the canopy layer and coexist with the small-scale contributions, although the former dominates the internal layer (Monti *et al.*, 2020). In the dense regime, the ΔS induces a geometrical constraint at the tip of the canopy, that filters out the penetration of large-scale structures. This constraint breaks the coherence of the outer large-scale structures and results in the generation of jets that are oriented along the wall-normal direction of the filament. This mechanism, induced at the onset of the tip of the canopy, penetrates the canopy layer due to the high wall normal permeability, similar to the transpirational phenomenological model presented in the previous subsection. The wall-normal jets of size ΔS, different to the larger structures, penetrate from the outer region and reach the proximity of the canopy bed. This is clearly evident from pre-multiplied spectra of v' presented in panel *b* from Figure 6.15 and 6.16, and the contour of the instantaneous planer snapshot of the wall-normal velocity fluctuation in Figure 6.21b. These jets, upon encountering the impermeable wall and the solenoidal condition, generate regions of positive and negative spatial gradients of wall parallel velocity fluctuations in the region surrounding the circumference of the wall-normal jet. In particular, this mechanism generates a positive and negative u' in the region upstream and downstream of the wall-normal jet, while the same can be said for the w' in the lateral sides. The flow is then pushed away from the wall creating regions of $u'v'$ vortices. The accumulation of the consecutive jets,

i.e., the merging of these gradient varying regions, gives rise to a $u'v'$ Reynolds shear stress peak, which in turn sets the location of the internal inflection point (Monti *et al.*, 2022). This can be verified by the internal peak of the magnitude of the cospectra of $u'v'$ presented in Figure 6.20. In particular, panels a and f of the same figure illustrate a peak that corresponds to the mean location of the inner inflection point, denoted by the yellow horizontal dashed line. This redistribution of momentum along the wall in parallel directions feeds directly into the flow by the canopy bed, inducing a spanwise modulation of u' and a streamwise modulation of w'.

Next, we focus on the effect of the filament inclination on the structure of the turbulent flow field within the canopy layer. As established in the previous subsections, the level of penetration from the outer flow decreases with the increasing angles of inclination. Apart from the obvious geometrical constraint of ΔS at the canopy tip, the inclining filaments further restrict the wall-normal progression of the outer turbulent structures. Thus, canopies composed of inclined filament not only break up the coherence of these outer vortices but also impede the progression of the wall-normal jets, shielding the region closer to the impermeable wall. We expect the inclining filament to have a greater influence on the v' component since it is directly related to the level of penetration. We verify this by considering the one-dimensional pre-multiplied spectra and the magnitude of the pre-multiplied cospectra within the canopy. These are presented in Figure 6.15, 6.16 and 6.20, enabling a direct comparison among the various inclined configurations. Aside from the $\theta^\circ = 77$ configuration, the overall structure of the w' spectra is similar for all the remaining canopies, with a couple of peaks present in the canopy region. However, the difference due to the filament inclination is remarkably evident in the v' component, while the u' component presents a minor modulation in the pre-multiplied spectra as a function of λ_z. In particular, by observing the pre-multiplied spectra in panels e, h and k of Figure 6.15 and 6.16 for the increasing angles of inclination, we notice the diminishing signature of the v' spectral structure in the canopy layer, particularly at the wavelength of $\lambda_x/H = \lambda_z/H = \Delta S$. This behaviour, accompanied by the absence of a peak in the u' component for the same wavelength in Figure 6.15, suggests that the wall-normal jets generated by the outer turbulent structures are

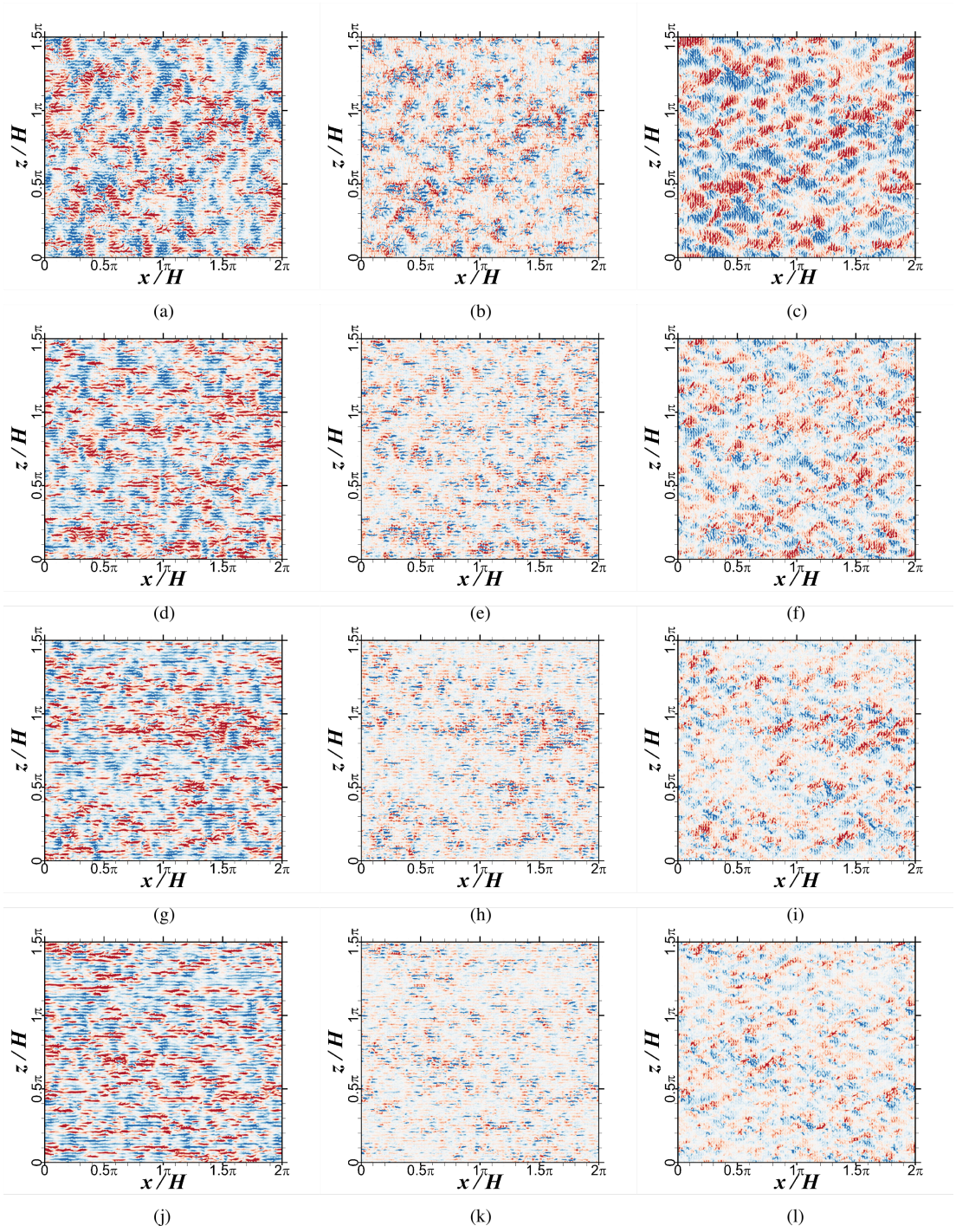


Figure 6.21: Instantaneous realisations of the streamwise (first column) and wall normal (second column) and spanwise (third column) components located at a wall parallel plane of $y/H = y_{ip}$. The rows from top to bottom corresponds to the $\theta^\circ = 0$, $\theta^\circ = 33.5$, $\theta^\circ = 48.25$, $\theta^\circ = 60$, configurations, respectively. The colour band from red to blue represents positive to negative. The velocity fluctuations were made non-dimensional with the local friction velocity formulation (see Equation 6.3), with a depicted range of $u'^+ \in [-3, 3]$, $v'^+ \in [-2, 2]$ and $w'^+ \in [-3, 3]$.

obstructed by the inclining filaments. These wall normal jets, instead of reaching the bottom impermeable wall as seen for an upright canopy, impinges the inclining filaments and deflects along the spanwise direction, giving rise to the leftmost peak of the w' component (see the third column in Figure 6.15). This behaviour can also be confirmed by considering the intensity of the spectral energy content of the fluctuating velocity components. Deep inside the canopy, we observe a decrease in the magnitude of spectral energy intensity for all three fluctuating components (see Figure 6.15 and 6.16). This is inflicted by the absence of the wall-normal jets, which then would lead to the deficit in the momentum influx at the tip of the canopy. Simultaneously, the spectral peak located outside the canopy layer presents an increase in the intensity for the increasing angles of inclination. Moreover, we can verify this physical mechanism by visually inspecting the instantaneous wall parallel snapshots corresponding to the internal inflectional instability illustrated in Figure 6.21. In particular, the second column from the same figure reveals the decrease in the wall-normal velocity fluctuation intensity for the systematic increment of the inclination angle. This in turn results in a decrease in the intensity of wall parallel fluctuating velocity components, since the absence of wall-normal jets inhibits the momentum redistribution seen in the fully upright canopies. The effect of the momentum deficit is translated into the coherent motion occurring in the inner layer of the canopy. It is evident that the flow in the inner region is characterised by a spanwise modulation of u' and a streamwise modulation of w' loses part of its coherency as the filament is inclined along the streamwise direction. This establishes the role played by the wall-normal jets in coupling the inner and outer layers, via a momentum transfer.

Finally, we consider the extremely inclined configuration of $\theta^\circ = 77$, which presents a radical behavioural change when compared with the rest of the inclined canopies. The majority of the one-dimensional pre-multiplied spectra do not exhibit a peak below the tip of the canopy, with the exception of the spectra of u' as a function of both λ_x/H and λ_z/H. In particular, the internal u' peak observed in panel m of Figure 6.15, is characterised by a very long streamwise wavelength ($\lambda_x/H \approx 3$) and a short spanwise wavelength, which corresponds to the mean filament spacing $\lambda_z/H \approx \Delta S$ (see panel m of Figure 6.16). The occurrence of the latter can be explained by considering the virtual

origin framework discussed in the previous subsection. For the extremely inclined configurations, we have already established that the virtual origin for the streamwise velocity fluctuations is much larger when compared with the turbulence origin (i.e., $\ell_u^+ > \ell_T^+$). The latter essentially describes the origin of the quasi-near-wall cycle, which is detected by the v' and w' spectral peaks as a function of the spanwise wavelength. The absence of these peaks inside the canopy suggests that the quasi-streamwise velocity streaks perceive a much deeper virtual origin. Thus, the internal peak of u' can be interpreted as a small portion of the elongated streaky structures that get trapped in between the filaments that are defined by their spacing.

6.4 Concluding Remarks

In conclusion, we have carried out a detailed parametric study of rigid, slender inclined canopies of varying angles of inclination relative to the bottom impermeable wall. Indeed, the angle of inclination is directly related to the frontal projected height, which in turn modifies the value of solidity. Thus, a simple variation in the filament orientation (or equivalently, inclination) would lead to different hydrodynamic regimes of canopy flows. Therefore, the shielding effect of the inclining canopy is responsible for the inception of the different regimes. In this condition, the external boundary layer does not see the entire depth of the canopy, which is the case in the context of a perpendicular canopy. Instead, the outer flow only perceives a portion of the canopy, which we term the geometrical penetration depth, since the penetration of the external turbulent eddies is now constrained by the inclining filaments. These physical mechanisms led to a modulation imposed on the drag change (i.e., ΔU^+) experienced by the external boundary layer. Based on this, it was found that there are two regimes: a canopy regime (i.e., low and mildly inclined canopies), where the overall behaviour is comparable to perpendicular canopies ($\Delta U^+ >> 0$) and a roughness regime constituting extremely inclined configurations, in which the mean velocity profile is analogous to a rough wall boundary layer. We have also shown that the extremely inclined canopies behave as transitionally rough surfaces ($\Delta U^+ \simeq 0$), with the $\theta^\circ = 90$ presenting a total drag reduction. In between the two extremely inclined configurations, there exists a condition

at which the overall drag of the canopy is comparable to the skin frictional drag of a smooth channel (ΔU^+). The angle of inclination associated with this condition, was estimated to be $\theta^\circ \approx 84$, which corresponds to a solidity of $\lambda \approx 0.1$.

We have shown that the extremely inclined canopies can be perceived as a surface composed of small-scale textures, which do not directly interact with the turbulence above the respective substrate. Instead, the primary role of these textures is limited to the displacement of the near-wall cycle. Inspired by canonical riblets, this fundamental principle was translated to the concept of protrusion height, which is defined as the difference between the virtual walls seen by the mean flow and the near-wall turbulent flow (Luchini, 1996). This concept was generalised into a unifying virtual origin framework (Ibrahim *et al.*, 2021) for turbulent flows that develop over small-scale roughness. Our simulations seem to verify the virtual origin framework, by collapsing with the smooth wall profiles when shifted by the turbulence virtual origin. However, the drag change (ΔU^+) is underestimated. To overcome this, we have modified the drag change law based on a mass conservation argument. This modification, termed the transpirational virtual origin, predicts the drag change accurately, even in the canopy regime.

With the aid of a spectral decomposition and autocorrelation function, we have identified various coherent structures and their modulations induced by the inclining canopy. We have already established that the behaviour of the low and mildly inclined configurations is similar to the one observed in the context of perpendicular canopies. Therefore, the external flow is populated by the spanwise coherent structures that are embedded in the background of canonical logarithmic structures. The former is generated by a Kelvin Helmholtz instability that is triggered by the inflection point in the mean velocity profile. In the dense regime, it is known that the inner/outer layer interaction is characterised by the energy-carrying jets that are directed along the wall-normal direction. These jets interact with the wall to redistribute part of its momentum to the wall-parallel directions, giving rise to coherent motions of u' and w'. As the angle of inclination is increased, it was observed that these jets lose part of their energy due to the geometrical constraint induced by the inclining filaments, which also translates to

the loss in the coherence of the inner flow. At the limit of extremely inclined canopies, these jets are completely eliminated and the external flow developing above the canopy substrate is reminiscent of a smooth wall flow with the absence of the KH rollers.

7
Relevance and Outlook

Surfaces covered by arrayed, filamentous layers anchored to a substrate and exposed to viscous flows are ubiquitous in the surrounding world (i.e., natural and artificial contexts). Thus, the study of canopy flows has a high potential in impacting a wide range of applications ranging from natural crop vegetations, coastal and waterway engineering, management of flood risks, and manipulating river channel bed, to technological advances in the fields of aeronautics and automotive to enable smart surfaces capable achieving several functions: skin frictional drag reduction, separation control, enhanced mixing and also mass and heat transfer in different industrial processes. The key findings of the current thesis will have a two-fold academic and industrial impact with numerical advances to deliver physical insights into turbulent shear flows that develop over intermediate/dense rigid coatings. Although the conducted research is mainly of fundamental nature, developing a parametric map setting a correspondence between textured coating properties and the resulting turbulent flows will lead to applications with an important societal impact. Developing drag-reducing surfaces that goes beyond the actual limit $10 - 15\%$ will reduce consumption on vehicles, thus increasing battery life or diminishing greenhouse gasses emissions; controlling the coherence of large scale vortices and their interaction with sharp edges can also lead to the expectation of new routes to reduce aerodynamic noise; controlling separation on strongly unsteady flows using passive and adaptive coatings could lead to the design

of aerodynamically robust drones able to secure stable flight when submitted to large atmospheric fluctuations. A successful outcome of these types of surfaces will lead to a boost in the number of new activities tackling the manufacturing and maintenance of the coatings and their extended use for the control of many other industrial and biological flows, including flows of bioengineering interest. For example, the functionality of many human organs depends on the interaction of ciliated walls with biological fluid flows. More specifically, in Chapter 6 we have shown that fully inclined canopies are capable of decreasing the skin frictional drag experienced by the external turbulent boundary layer. On the other hand, the perpendicular canopies studied in Chapter 5 can be perceived as pin fins used in the context of heat transfer. In general, the ever-increasing expectations of modern electronics have led to a number of issues: increasing functionality, power requirements, and the need for more components in compact packaging. Therefore, engineers are tasked with designing efficient thermal management systems that are capable of handling power requirements. In particular, pin fins have a lower thermal resistance when compared with plate fins, making the former an excellent candidate for heat sinks (Bejan & Morega, 1993). In this context, it is imperative to obtain a deep understanding of the turbulent flow developing around each pin since it influences the overall efficiency of the heat transfer process. More recently, energy harvesting techniques using piezoelectric materials have received recent limelight. In particular, piezoelectric transducers are capable of transforming the energy absorbed by the surrounding environment into electrical energy that is used for actuation or stored in batteries for later use (Elahi *et al.*, 2018). Thus, a flexible filamentous surface coupled with a piezoelectric material can lead to an excellent energy harvesting device since the substrate would generate an electrical charge by undergoing strong deflections in response to the surrounding turbulent flow. This is essentially a fluid-structure interaction problem that is once again governed by the overlying turbulent flow and the properties of the soft filamentous surface. Thus, the overall results from the present thesis can be considered as a contribution towards understanding the turbulent flow field developing above and within a substrate composed of slender filaments.

In the past, canopy flows have been extensively studied in the context of vegetative crops and terrestrial forests. These studies have mainly focused on untangling the physics behind many hydrological and biological processes. For example, the transfer of momentum (Finnigan, 2000), mitigation of uprooting under strong currents (De Langre *et al.*, 2012), weather forecasting (Barlow & Coceal, 2008), exchanging radiation energy, carbon dioxide (Baldocchi *et al.*, 2001), heat, and other scaler quantities with the vegetative layer and overlying flow. Submerged vegetation observed in riverbeds and coastal regions also presents a compelling case for canopy flows. These aquatic canopies create a habitat for many species by significantly affecting the stream, controlling sediment transport and nutrient and oxygen exchange (Hurd, 2000). All the processes highlighted above highly depend on the hydrodynamic interaction of the viscous flow and the canopy of interest (Nepf, 2012). Therefore, the key findings of the present thesis complement the rich experimental and numerical literature that has been accumulated in archival research over the past few decades. The knowledge of the overall structure of the mean velocity and the sustained turbulence above and within the vegetative canopies has been significantly improved. This is an important attribute since it allows engineers and hydrologists to broaden their understanding and unlock the key parameters that govern different processes, which are essentially associated with the overall flow structure. For instance, the uptake of the nutrients significantly depends on the boundary layer that develops around each canopy element (Hurd, 2000). Our canopy-resolving simulations offer an efficient methodology for capturing the stem-based flow scale, which would enable the study of nutrient uptake by a single plant or community of plants. This numerical technique also allowed us to investigate the coherent motions occurring deep inside the canopy, which significantly affect the suspension and redistribution of the previously deposited sediment particles (sediment resuspension). Thus, the results obtained from the current thesis can be inferred to model the behaviour of the sediment particles by the canopy bed. Furthermore, we have established that the primary role played by the inclining filaments is to shield the canopy bed, which is of important relevance to sediment resuspension. Along this line, the transport and capture of pollen located at the tip of the plant in many submerged canopies is also mediated by the

fluid medium rather than the animal (Ackerman, 2000). In particular, the pollination process of about 20% of angiosperm families depends on either wind (anemophily) or water (hydrophily) pollination, which is significantly affected by the dispersive effects of the flow. In the current thesis, we have highlighted the importance of these dispersive stresses and the flow patterns that arise due to the spatial heterogeneity of the canopy. This is not very dissimilar to scenarios associated with turbulent flows laden with inertial particles, an area of research formally known as multiphase flows (Balachandar & Eaton, 2010). In the past, the study of particle-laden flows has been an almost impossible task due to the number of complexities associated with such flows. For instance, the different particle and fluid properties, multiway coupling between the particles and fluid flow, and the existence of a large difference in scales lead to a large number of governing free parameters in such flows. The renewed interest in particle-laden flows is mainly driven by the relevance of the problem and the advances in novel experimental measurements and simulation capabilities (Brandt & Coletti, 2022). Thus, the study of particle-laden flows in conjunction with canopy flows will pave the way for new avenues of research and collaborations, expanding the knowledge boundaries of canopy flows. This will enable engineers and hydrologists to design canopies that maximise pollination and decrease soil erosion, leading to efficient vegetation strategies.

In the current thesis, we have fully resolved the canopy layer with the aid of the Immersed Boundary formulation. Although still in their infancy, investigations using LES and DNS techniques to study different canopy morphologies have emerged recently (Monti *et al.*, 2019; Sharma & García-Mayoral, 2020*a*; Tschisgale *et al.*, 2021; Monti *et al.*, 2022). In the context of flow over rough surfaces, many DNS studies have been reported in archival research aimed at understanding the modulations imposed on the turbulent flow by the presence of roughness elements (Orlandi & Leonardi, 2008; Garcia-Mayoral & Jimenez, 2011; Abderrahaman-Elena *et al.*, 2019). In the studies highlighted above, the geometrical representations of the surface textures have been fully resolved, such that the flow physics is captured even at the surface texture scale. While this approach has several advantages, conducting parametric studies with the aid of fully resolved simulations incorporating the multi-scale nature of the problem is almost an impossible

task due to the high computational cost incurred by the individual simulations. Thus, in recent times, researchers have actively pursued effective approaches to capture the average homogenous effect of the texture on the macro-scale processes (i.e., overlying flow) (Bottaro, 2019; Lācis *et al.*, 2020; Khorasani *et al.*, 2022). In this condition, one can replace the textured surface with an effective representation (boundary condition), thus mitigating the need for geometrical details of the textured surface. However, it should be noted that these homogenisation approaches are advantageous in capturing the free flow above the surface, but fail to characterise the flow in the vicinity of the individual textures. Nevertheless, this approach enables researchers to study the impact of the canopy layer on the outer layer seamlessly, without the need to fully resolve the filamentous surface. For instance, in the current thesis it is found that the filament orientation significantly influences the external boundary layer, therefore, one could use these effective boundary conditions to mimic various canopy morphologies and orientations. Thus, the canopy resolving simulations of the present thesis can be used as reference cases to validate these effective representations. This will enable a much larger parameter space exploration with a fraction of the required computational effort.

8
Conclusions

Contents

8.1 Regime transition in canopy flows 198
8.2 Effect of filament spacing in canopy flows 200
8.3 Effect of filament inclination in canopy flows 204
8.4 Future Work 207

The present doctoral dissertation is centred around the numerical investigation of turbulent flows that develop over various rigid filamentous canopies. The highly-resolved simulations were used as a tool to unravel the underlying physical mechanisms that dominate the different flow regimes, emerging from the interaction of a turbulent parallel shear flow with canopies of different morphologies (i.e., perpendicular and inclined). All the canopy scenarios were studied in the context of an open channel flow at a bulk Reynolds number of $Re_b = 6000$ (based on the open channel height and bulk velocity). The bottom impermeable wall of the open channel is populated by a filamentous layer, whose configuration encompasses various nominal canopy flow regimes (i.e., sparse, transitional, and dense). Thus, the main aim of the present thesis has been to explore the influence of the canopy geometrical parameters on the different regimes of canopy flows and flow behaviours that characterise each regime. The geometrical parameters of a canopy, composed of slender, cylindrical filaments,

define a complex large parameter space. In particular, the assessment of the transitional regime that exists in between the sparse-dense asymptotic regimes was one of the primary objectives of the research. Alongside, a more intricate objective concerns the establishment of a criterion for the inception of the transition regime by considering the geometrical parameters of the canopy. The exercise was carried out in particular by taking into account the average filament spacing (ΔS) and angle of inclination (θ°). The former is generally considered the most dominant length scale of the canopy since it governs the size of the eddy that is hoisted in the canopy layer. On the other hand, θ° defines the frontal projected height of the canopy and the level of penetration from the external turbulent boundary layer, which in turn governs the interaction between the inner and outer layers of the canopy.

The numerical approach employed in the current thesis is based on a modification of an existing immersed boundary method that has been formulated and validated on both a model case and experimental data. By leveraging the numerical efficiency and accuracy of the developed numerical technique, the different regimes of canopy flows are explored by considering a simulation in which the physical boundary values (Dirichlet type boundary condition) are imposed on every single filament. In the subsequent sections, the conclusions for the various canopy scenarios are presented.

8.1 Regime transition in canopy flows

In the first results and discussion chapter, we have investigated the turbulent flow that develops above a rigid filamentous surfaces in the framework of the so-called *transitional regime*. Two canopy configurations that nominally fall in this regime were selected. Differently from previous investigations that were focusing on the frontal area (i.e. the canopy height), the solidity λ has been modified solely by decreasing the average distance between the adjacent filaments (or increasing the stem number density), yielding configurations residing above and below the sharp transitional threshold (i.e., $\lambda \simeq 0.15$) (Monti *et al.*, 2020). The main conclusions of our work can be summarised as follows..

Firstly, we have confirmed the occurrence of a regime transition occurring within the range bounded by the two considered configurations. The signature of such transition

is identified as in (Monti *et al.*, 2020) by the signed distance between the internal inflectional point and the virtual origin occurring when the canopy aspect ratio is unity (i.e., $\Delta S \approx h$). In this condition, we have shown that the mean position of the internal inflection point and the virtual collapses onto a single location ($y_{vo}, y_{inf} \simeq 0.5h$), dividing the canopy into two layers (see Figure 4.3). This induces a decouple between the innermost and outermost boundary layers, whose interactions are limited to the sweep and ejections generated by the outer flow via the wall normal component. This outer/inner communication potentially weakens as the average filament spacing is further decreased (or equivalently increasing solidity), enhancing a stronger decoupling in the limiting condition $\Delta S \rightarrow 0$. Secondly, we have identified and characterised the flow topology across the whole canopy flow in transitional regime. This area is dominated by large scale structures and to the authors knowledge this is the first time, that the presence and the character of these structures in transitional regime has been put forward with conclusive and quantitative evidence across the canopy layers. The analysis has been mainly conducted by looking at the spectral energy content of the velocity fluctuations allowing to identify the different structures of the velocity fields, particularly in the region bounded by the canopy. In particular, we have reported the existence of a spanwise modulation of the streamwise velocity fluctuations hidden in the background of larger energetic structures, triggered by the innermost inflection point (see Figure 4.9 and 4.11). Previously, this phenomenon unique to the fully dense scenario was only reported for a single canopy configuration ($\lambda = 0.56$) (Monti *et al.*, 2020). Its weak inception at a relatively low value of λ, establishes the importance of ΔS as the primary length scale that governs the interaction between the inner and outer boundary layers and eventually the transition between two asymptotic regimes.

Concerning the structure of the external boundary layer developing over a transitional canopy, this is characterised by highly elongated velocity streaks bounded by intense quasi streamwise vortices (see Figure 4.13). The outer layer is also home to a system of spanwise oriented vorticity structures in the form of a Kelvin Helmholtz type instability that emerge as a result of the inflected mean velocity profile. These large structures have been previously reported by several other authors, in the context

of obstructed flows (i.e., dense canopy flows, flows over porous media and roughness elements, e.g. riblets in non-linear regime).

Finally, we have also extended the scaling arguments presented in the context of sparse and dense canopies to the transitional regime, where the mean drag offered by the filaments is comparable to the skin frictional drag of the canopy bed (Nepf, 2012). In particular, the velocity fluctuations scaled with the local friction velocity computed as a sum of the viscous and Reynolds stresses, presents a good collapse of the velocity profiles. In the outer region, the these profiles agree well with the results obtained for turbulent channel flow at moderately high Reynolds number (see Figure 4.6).

8.2 Effect of filament spacing in canopy flows

We have conducted a series of detailed numerical simulations of turbulent open channel flows developing over submerged canopies made of rigid, slender, circular cylindrical stems mounted perpendicular to an impermeable wall. In these conditions, the hydrodynamic regime is basically set by two geometrical parameters: the stems height (h) and the mean filament spacing (ΔS). For slender filaments (i.e. filaments with a diameter d verifying $d/h << 1$), the non-dimensional combination of the canopy geometrical parameters $\lambda = dh/\Delta S^2$ (termed as the *solidity*) has generally be considered as a sufficient indicator enabling the prediction of the flow regime establishing inside and above the canopy. In a previous, companion study Monti *et al.* (2020) have studied the impact of the canopy height on the onset of the different regimes without modifying the average spacing ΔS between the stems. In this study, we have been looking at the other, complementary approach: to change the value of λ by keeping the height of the stems constant while changing the number density of the canopy (i.e. changing the value of ΔS). The present study, combined with the outcomes of the previous work by Monti *et al.* (2020), has led to the following main results: *i)* the elaboration of a conceptual model capturing the essence of the transition from a *sparse* to a *dense* canopy regime (Nepf, 2012); *ii)* the understanding of the role played by λ, h and ΔS in determining the character of the intra-canopy flow; *iii)* the identification of the relevant length scales in the velocity layers characterising the canopy flow; *iv)* the production

of a detailed description of the turbulent flow fields in and above the canopy under different regimes, via a triple decomposition technique.

Generally speaking, it is found that sparse and mildly dense configurations (i.e. $\lambda \lessapprox 0.26$) share several similarities with the canopies of the same solidity obtained by varying the height of the filament (Monti *et al.*, 2020). However, the overall intra-canopy flow experiences a slow down due to the decrease in the streamwise and spanwise permeability for increasing values of the stems number density. On the other hand, when comparing the densest cases of the current study and the one reported by Monti *et al.* (2020) (which shares the same magnitude of $\lambda = 0.56$), it turns out that the flow dynamics in the canopy region are of different nature. In the case of *tall* canopies considered in Monti *et al.* (2020), the canopy outer and inner layer momentum transfer takes place in the form of wall normal sweeps, driven by the external flow. When these *jet-like* structures approach the wall, they are deflected in the streamwise and spanwise directions re-energising the otherwise stagnant flow in the vicinity of the wall. In the densest case, obtained by clustering the filaments, the momentum redistribution in near wall region is partially inhibited by the decreased permeability in the directions parallel to the wall which is due to the increased filaments density. In this condition, the intensity of the wall-normal momentum directed towards the wall is weaker than the one observed by Monti *et al.* (2020). The deficit of transported, vertical momentum also prevents the formation of the *kink* in the mean velocity profile observed by Monti *et al.* (2020) in their densest (i.e. highest λ) case (see Figure 5.1).

For the canopy configurations considered in this work, it is known that the solidity value λ sets two separated, asymptotic regimes. The *sparse* regime happening for low values of the solidity is characterised by a friction dominated drag with the outer eddies able to penetrate fully the canopy. For large values of λ, *dense* regimes establish. These are characterised by high form drag and for shielding the external structures out of the inner canopy region. The transition from the sparse to dense regime is governed by the canopy aspect ratio (see Figure 5.6), which is defined as the ratio between the mean filament spacing and the filament height. In the transitional condition (i.e., $\Delta S/h = 1$), our simulations have proved that the mean location of the internal inflection point and

the virtual origin collapses onto a single point ($y/h \approx 0.5$). We have shown that this condition corresponds to $\lambda \approx 0.2$ (see Figure 5.9), which is very close to the commonly accepted value that separates sparse and dense regimes in the context of canopy flows (Nepf, 2012; Monti *et al.*, 2020) and of flows over rough surfaces (Schlichting, 1937; MacDonald *et al.*, 2016). At the onset of the dense condition, the parameter ΔS starts to play a determinant role controlling the size of the eddies that can cross the canopy interface at the tip of the filaments. By fixing the effective filter width for the external structures, the mean filament spacing essentially sets the location of the virtual origin seen by the outer flow (see Figure 5.7). It was also found that the drag exerted by the canopy on the outer flow (i.e., ΔU^+) starts to decrease when more densely packed canopies are considered. This behaviour can be attributed to the mutual sheltering effects of the downstream filaments that becomes important in the dense regime.

We have also identified the length scales that better characterise the flow layers that develop inside the canopy. Indeed, scaling the thickness of internal layers with the appropriate length scales allows to unravel universal features of the flow inside the canopy. In particular, we have established that the internal layer scales well with ΔS, suggesting that the nature of the inner flow is solely governed by the mean filament spacing, regardless of the way in which λ was varied (see Figure 5.4). In the limit of $\Delta S \to 0$, the internal layer thickness must collapse to zero since the wall normal sweeps are totally inhibited for very low stems spacing. Differently, when the solidity is increased by considering taller canopies, the inner layer thickness asymptotically becomes independent of h. Concerning the external canopy layer, it was found that the penetration depth of the outer flow is mainly set by the canopy height h, once again independently of the overall value assigned to λ (see Figure 5.5). However, the mean filament spacing ΔS controls the size of the eddies allowed to enter the canopy (i.e. the low-pass filter size). Indeed, the level of penetration goes to zero when $\Delta S \to 0$, satisfying the solid wall condition. Conversely, when the canopy height is increased towards the dense regime, the level of penetration saturates to ΔS.

To identify the coherent structures populating the canopy and the external regions, we have used a spectral analysis and the velocity autocorrelation functions. As already

highlighted by many other authors, also in our work we have found that the inflection point located at the tip of the canopy (arising as a result of the abrupt drag discontinuity) triggers an instability that generates localised *Kelvin-Helmholtz* like rollers (see Figure 5.26) enhancing the aforementioned wall-normal momentum transfer into the canopy. The occurrence of these spanwise coherent structures has been previously reported by many authors in the context of different shear flows over textured surfaces: in dense canopy flows (Monti *et al.*, 2020; Sharma & García-Mayoral, 2020*b*), above permeable substrates (Rosti *et al.*, 2018*a*; Gómez-de Segura & García-Mayoral, 2019), and ribletted surfaces (Garcia-Mayoral & Jimenez, 2011; Endrikat *et al.*, 2021). Apart from the vorticity rollers, the external flow is also populated by the canonical outer logarithmic structures (see Figure 5.28), which in turn generate strong sweeps and ejection events that permeate from and through the canopy layer. In particular, when the outer structures approach the canopy tip, they are discriminated by their size and their coherence is broken by the spikes of the canopy at the stems tips spaced ΔS. This interaction produces wall normal jets (i.e. sweeps) of a cross-sectional size in the order of the mean filament spacing. These jets carry momentum towards the canopy bed and also provide a redistribution of directional momentum by complying with the impermeability of the bed. This momentum redistribution produces coherent motions (see Figure 5.20) dominated by the velocity fluctuations along the stream and spanwise directions. Not all the momentum directed towards the wall is redistributed, a fraction of it is pushed away from the wall, giving rise to regions of high Reynolds stresses (i.e. $\langle u'v' \rangle$ peaks). The combination of these mechanisms, basically driven by the discharge of momentum towards the wall, essentially set the location of the internal inflection of the mean velocity profile. The above described mechanism comes into play at the onset of the transitional regime.

The outer structures embedded in the background of the outer logarithmic region, that are able to penetrate the canopy in the transitional and mildly dense regimes, leave their footprints within the canopy layer as well (see Figure 5.19). However, the memory of their presence diminishes as the solidity is increased, eventually vanishing in the fully dense regime. In this condition, the inner coherent motions are almost completely

isolated from the outer flow and a decoupling effect takes place producing a large scale separation between the inner and the outer layers in the canopy.

8.3 Effect of filament inclination in canopy flows

In the final stage of the thesis, we have undertaken a series of detailed numerical simulations of turbulent open channel flows bounded by a set of rigid, slender inclined filaments in different nominal regimes. The actual hydrodynamic regime of rigid canopy flows is primarily governed by three geometrical quantities: height h, spacing ΔS, and the angle θ° of the filament relative to the bottom impermeable wall. In this work, we have considered the variation of the filament orientation, θ°, which in turn modulates the frontal projected height of the canopy and implicitly modifies the value of λ. The latter can predict the resulting canopy regime *a priori* by simply considering the height and spacing of the filament. Thus, the most important outcomes of the research study have been: i.) the different regimes that emerge on the onset of various filament inclinations, ii.) a new length scale capable of capturing the level of penetration from the outer flow, iii.) a framework to predict the drag change for the external boundary layer, iv.) a detailed description of the interaction between the internal and external flows and their modulation by the filament inclination,, and v.) a detailed characterisation of the different regimes obtained via the analysis of the spectral decomposition of the turbulent flow field arising inside and outside the canopy.

The main physical mechanism responsible for the inception of various regimes and their different behaviours is the shielding effect of the inclining canopy, by which the penetration of the outer turbulent structures is obstructed by the geometrical constraint. As the external boundary does not perceive the full extent of the canopy, we have proposed a new length scale, termed as the geometrical penetration depth, which is capable of incorporating the constrained penetration of the outer flow eddies (see Figure 6.4). From a purely dimensional argument, this length scale can be interpreted as the $h_{gp}^{+} \sim \sqrt{\mathcal{K}}_{y}^{+}$, where $\sqrt{\mathcal{K}}_{y}^{+}$ is the non-dimensional square root of the wall-normal permeability (Gómez-de Segura & García-Mayoral, 2019). This stems from the fact that h_{gp} essentially determines the position of the virtual wall (or equivalently the level of

penetration) seen by the outer flow, which monotonically moves towards the tip of the canopy as the filaments are further inclined.

Coupled with the orientation of the filaments in the streamwise direction, the external flow experiences an alternating no slip (filament surface) and slip (in between filaments) condition along the spanwise direction at the virtual origin. Simultaneously, the drag offered by the overall canopy decreases, due to the decrease in the frontal projected area. Thus the canonical parameter ΔU^+, defined as the drag change (or resistance function equivalently, see Figure 6.6), enabled us to identify two regimes: a canopy regime, which corresponds to $\Delta U^+ >> 0$, comparable to a canonical canopy flow, and a roughness regime, in which overall drag offered by the canopy is comparable to a smooth wall flow (i.e., $\Delta U^+ \sim 0$). The canopy regime constitutes the low and mild angles of inclination. Based on the value of λ, these configurations nominally fall into the mildly dense regime. In this condition, the studied scenarios exhibited a behaviour very similar to the canopies that share the same magnitude of λ, computed by considering perpendicular filaments (see Figure 6.3 and 6.5). On the other hand, the extremely inclined configurations, associated with the roughness regime, present a significant departure from the canonical canopy flows. Instead, these inclined filaments asymptotically behave as roughness elements, with the angle of inclination controlling the depth of the virtual origin from the roughness crests (edge of the filament, see Figure 6.2). We have shown that the extremely inclined canopies can be interpreted as transitionally rough surfaces (Thakkar *et al.*, 2018), which are characterised by both viscous and pressure drag. In particular, the fully inclined configuration (i.e., $\theta^\circ = 90$) presented a total drag-reduction, that was comparable to the canonical ribletted surfaces (see Figure 6.9). Clearly, a transitional condition takes place between the two extremely inclined canopies (i.e., $\theta^\circ = 77.5, 90$), when the drag induced by the canopy is equivalent to the skin frictional drag of a smooth wall flow (i.e., $\Delta U^+ = 0$). The corresponding inclination angle was estimated to be $\theta^\circ \approx 84$, yielding a solidity of $\lambda \approx 0.1$, which is the accepted threshold for the sparse regime (Nepf, 2012).

The extremely inclined canopies can be envisaged as a surface composed of small textures, with the primary role of the latter being limited to displacing the quasi-near-

wall vortices. This was the fundamental principle used to describe the drag reduction mechanisms of riblets (Luchini *et al.*, 1991). The concept of protrusion height, postulated by the Luchini (1996), determines the drag change by considering the depth difference between the virtual walls seen by the mean flow and the near-wall flow. Building upon this idea, Ibrahim *et al.* (2021) proposed a virtual origin framework to predict the drag change and determine the turbulence abstract origin. When the wall-normal coordinates are shifted by the latter for the extremely inclined configurations, a smooth wall-like behaviour is recovered (see Figure 6.11). Yet, for the filament resolving simulations, we have shown that the drag computed by incorporating the difference between the mean flow origin and the turbulence origin underestimates the value of ΔU^+. Following a mass conservation argument in the region closer to the tip of the filament (see Figure 6.12), we have proposed an additional non-linear term called a transpiration virtual origin in the drag change law (see Equation 6.5). The resulting formulation accurately predicts ΔU^+, even for the canopy regime, although the latter violates the underlying assumptions that led to virtual origin framework (Ibrahim *et al.*, 2021).

The spectral analysis of the fluctuating velocity field allowed us to highlight several differences in the coherent motions that populate both the inner and outer regions. These remarkable differences arise primarily due to the filament inclination in the streamwise direction. The outer region is populated by the canonical logarithmic structures and the spanwise coherent motions, that are generated by the KH instability (see Figure 6.17). The latter is triggered by the abrupt drag discontinuity at the tip of the filament. We have established that the low and mildly inclined filaments behave similarly to a perpendicular canopy. However, at the onset of extreme filament inclination, we observed an absence of the spanwise coherent structures in the region outside the canopy, since the flow that develops over canopies, characterised by very high θ°, tend to behave as smooth-wall like flows (see Figure 6.13). The role of the filaments in these conditions is limited to the displacement of the near-wall vortices. The inner and outer layers are almost completely decoupled, with the only mode of communication limited to the wall-normal jets of size ΔS due to the high wall normal permeability of the canopy. The latter is generated by the breakup of the coherence of large structures, geometrically

induced by the mean filament spacing. These wall normal jets interact with the bottom impermeable wall to generate coherent motions of u' and w', which essentially sets the wall-normal location of the internal inflection point. In particular, when the canopy is inclined ($\theta^\circ > 0$), the wall-normal progression of these jets is geometrically constrained and the overall mechanism is weakened (see Figure 6.21). In this condition, the inclined filaments shelter the region by the bottom wall, by decreasing the overall transpiration through the canopy, thus inhibiting the momentum redistribution to structures living in that region, leading to a loss of coherence. However, for the $\theta^\circ = 77$ and $\theta^\circ = 90$ configurations, these complex wall-normal jets are eliminated by the extremely inclined filaments, leading to the absence of the internal inflection point.

Finally, the analysis presented thus far revealed that the solidity parameter λ is ineffective for determining the different regimes of canopy flows because canopies of the same solidity exhibit a radical behavioural change when they are simply inclined in the streamwise direction (Monti *et al.*, 2022). Nevertheless, λ enables us to identify sparse-dense asymptotic regimes (Nepf, 2012), by simply considering the geometrical parameters that are known *a priori*. Therefore, we propose an alternative geometrical ratio called the effective canopy aspect ratio, $\Lambda_{eff} = k_{eff}/\Delta S$, where k_{eff} is the portion of the canopy seen by the external flow. We have shown that the proposed parameter is robust in characterising both inclined and perpendicular canopies (see Figure 6.7).

8.4 Future Work

The main contribution of the present thesis lies in exploring the parameter space of turbulent shear flows that develop over canopies. As mentioned in the literature review (see Chapter 2), canopy flows are generally characterised by a large parametric space involving numerous geometrical scales, despite the fact that the current thesis concerns itself with a modest parametric study involving the mean filament spacing and the filament inclination. Nevertheless, the results from this thesis opens up new avenues of research in the field of canopy flows. The full understanding of the physics of the interaction between the turbulent flow and the filamentous surface and its subsequent exploitation will bring forth bio-inspired technological advances in various fields. For

example, the hydrological management of rivers, energy harvesting, and wings covered with filaments for flow control and drag-reduction purposes, etc. These examples highlight the potential applications of filamentous surfaces in the context of smart multi-functionary surfaces that leverage a complex fluid-structure interaction to achieve a number of tasks simultaneously.

The first major area that requires further research is the parameter space that characterises the global behaviour of canopy flows. In particular, the effect of the filament diameter d on the solidity λ in the context of perpendicular canopies should be investigated. The effect of the filament height was considered by Monti *et al.* (2020), while the present thesis incorporates the effects of the mean filament spacing ΔS. Indeed, a change in the diameter may yield a behaviour similar to the one observed when the filament spacing is modulated. However, increasing the filament diameter beyond a certain threshold may violate the slenderness condition ($d/h \ll 1$) of the filaments. In this scenario, varying the filament diameter is expected to lead to different behaviours as the intra-canopy region will be dominated by the wake created by the flow past larger filaments. The latter may also modify the mode of communication between the internal and external layers. Therefore, a parametric study similar to what we have seen in Chapter 5, possibly keeping the same values of solidity used in this work, should be undertaken as a continuation of this research.

In the present thesis and the majority of canopy flow, numerical investigations reported in archival journals have considered idealised canopies. The latter is modelled as a set of cylindrical or cuboidal elements with a finite cross-sectional area. The geometrical properties are uniform in the direction along the filament. However, the examples presented in Chapter 2 (i.e., plants and trees) exhibit a behaviour that is radically different from an idealised canopy. For instance, the presence of branches and leaves at various locations in a plant presents a geometrical anisotropy. This gives rise to a possible area of research, particularly relevant to the field of hydrology. Therefore, one could investigate the turbulent flow that develops over canopies composed of anisotropic filaments. The latter can be envisaged as filaments with non-uniform cross-sectional areas or filaments with blob volumes. This has the potential to modulate

the localised permeability, which in turn modifies the mechanisms associated with the fluid-structure interaction.

Concerning inclined canopies, the next obvious step is to explore negative angles of inclination (i.e., filaments that are inclined against the streamwise direction). This has been already explored by the authors of the current thesis, and the results have been published in the Journal of Fluid Mechanics. However, a possible scenario that needs further investigation could be based on inclining the filaments in the spanwise direction. Introducing a spanwise angle of inclination leads to different behaviours as they can induce different interactions with the external flow (i.e., quasi-streamwise vortices, velocity streaks, and KH structures) due to their orientation. In contrast to the streamwise inclination, the filaments inclined in the spanwise direction may enhance the spanwise flow. Hence, another parametric study similar to the one given in Chapter 6 should be considered. For this study, the same frontal projected heights of the canopy should be considered for a direct comparison.

Finally, once the effects of these extra parameters on rigid canopies are well understood, one could embark on an investigational campaign on canopies composed of flexible filaments. Apart from the general geometrical parameters, flexible filaments are also characterised by their structural properties, which will essentially enlarge the parametric study, thus opening more opportunities for engineering canopies that can deliver technological advantages. This parameter study would consider various regimes that emerge as a result of the adaptive reconfiguration of the canopy.

Bibliography

Abderrahaman-Elena, Nabil, Fairhall, Chris T & García-Mayoral, Ricardo 2019 Modulation of near-wall turbulence in the transitionally rough regime. *Journal of Fluid Mechanics* **865**, 1042–1071.

Abderrahaman-Elena, Nabil & García-Mayoral, Ricardo 2016 Geometry-induced fluctuations in the transitionally rough regime. In *Journal of Physics: Conference Series*, , vol. 708, p. 012009. IOP Publishing.

Ackerman, Josef Daniel 2000 Abiotic pollen and pollination: ecological, functional, and evolutionary perspectives. In *Pollen and pollination*, pp. 167–185. Springer.

Ankhelyi, Madeleine V, Wainwright, Dylan K & Lauder, George V 2018 Diversity of dermal denticle structure in sharks: Skin surface roughness and three-dimensional morphology. *Journal of morphology* **279** (8), 1132–1154.

Antonia, RA 1981 Conditional sampling in turbulence measurement. *Annual review of fluid mechanics* **13**, 131–156.

Bachmann, Thomas Willem 2010 Anatomical, morphometrical and biomechanical studies of barn owls' and pigeons' wings. PhD thesis, Aachen, Techn. Hochsch., Diss., 2010.

Bailey, Brian N & Stoll, Rob 2013 Turbulence in sparse, organized vegetative canopies: a large-eddy simulation study. *Boundary-layer meteorology* **147** (3), 369–400.

Bailey, Brian N & Stoll, R 2016 The creation and evolution of coherent structures in plant canopy flows and their role in turbulent transport. *Journal of Fluid Mechanics* **789**, 425–460.

Balachandar, S & Eaton, John K 2010 Turbulent dispersed multiphase flow. *Annual review of fluid mechanics* **42**, 111–133.

Balay, Satish, Abhyankar, Shrirang, Adams, Mark, Brown, Jed, Brune, Peter, Buschelman, Kris, Dalcin, LD, Eijkhout, Victor, Gropp, W, Kaushik, Dinesh & others 2017 Petsc users manual revision 3.8. *Tech. Rep.*. Argonne National Lab.(ANL), Argonne, IL (United States).

Baldocchi, Dennis, Falge, Eva, Gu, Lianhong, Olson, Richard, Hollinger, David, Running, Steve, Anthoni, Peter, Bernhofer, Ch, Davis, Kenneth, Evans, Robert & others 2001 Fluxnet: A new tool to study the temporal and spatial variability of ecosystem-scale carbon dioxide, water vapor, and energy flux densities. *Bulletin of the American Meteorological Society* **82** (11), 2415–2434.

Banyassady, Rayhaneh & Piomelli, Ugo 2015 Interaction of inner and outer layers in plane and radial wall jets. *Journal of Turbulence* **16** (5), 460–483.

Barlow, Janet & Coceal, Omduth 2008 A review of urban roughness sublayer turbulence .

Bechert, DW, Bruse, M & Hage, W 2000*a* Experiments with three-dimensional riblets as an idealized model of shark skin. *Experiments in fluids* **28** (5), 403–412.

Bechert, DW, Bruse, M, Hage, W & Meyer, R 2000*b* Fluid mechanics of biological surfaces and their technological application. *Naturwissenschaften* **87** (4), 157–171.

Bechert, DW, Bruse, M, Hage, W vd, Van der Hoeven, JG Th & Hoppe, G 1997 Experiments on drag-reducing surfaces and their optimization with an adjustable geometry. *Journal of fluid mechanics* **338**, 59–87.

Beem, Heather, Hildner, Matthew & Triantafyllou, Michael 2012 Calibration and validation of a harbor seal whisker-inspired flow sensor. *Smart Materials and Structures* **22** (1), 014012.

Bejan, A & Morega, Al M 1993 Optimal arrays of pin fins and plate fins in laminar forced convection .

Belcher, SE, Jerram, N & Hunt, JCR 2003 Adjustment of a turbulent boundary layer to a canopy of roughness elements. *Journal of Fluid Mechanics* **488**, 369–398.

Belcher, Stephen E, Harman, Ian N & Finnigan, John J 2012 The wind in the willows: flows in forest canopies in complex terrain. *Annual Review of Fluid Mechanics* **44** (1), 479–504.

Böhmer, K, Hemker, PW & Stetter, HJ 1984 The defect correction approach. In *Defect correction methods*, pp. 1–32. Springer.

Bottaro, Alessandro 2019 Flow over natural or engineered surfaces: an adjoint homogenization perspective. *Journal of Fluid Mechanics* **877**.

Bradshaw, P 2000 A note on "critical roughness height" and "transitional roughness". *Physics of Fluids* **12** (6), 1611–1614.

Brandt, Luca & Coletti, Filippo 2022 Particle-laden turbulence: progress and perspectives. *Annual Review of Fluid Mechanics* **54**, 159–189.

Breugem, WP, Boersma, BJ & Uittenbogaard, RE 2006 The influence of wall permeability on turbulent channel flow. *Journal of Fluid Mechanics* **562**, 35.

Brücker, Ch 2011 Interaction of flexible surface hairs with near-wall turbulence. *Journal of Physics: Condensed Matter* **23** (18), 184120.

Brücker, Christoph & Weidner, Christoph 2014 Influence of self-adaptive hairy flaps on the stall delay of an airfoil in ramp-up motion. *Journal of Fluids and Structures* **47**, 31–40.

Brunet, Yves 2020 Turbulent flow in plant canopies: historical perspective and overview. *Boundary-Layer Meteorology* **177** (2), 315–364.

Canuto, Claudio, Hussaini, M Yousuff, Quarteroni, Alfio, Thomas Jr, A & others 2012 *Spectral methods in fluid dynamics*. Springer Science & Business Media.

Chagot, Loïc, Moulin, Frédéric Y & Eiff, Olivier 2020 Towards converged statistics in three-dimensional canopy-dominated flows. *Experiments in Fluids* **61** (2), 1–18.

Chen, Su-Chin, Kuo, Yi-Ming & Li, Yu-Hsiu 2011 Flow characteristics within different configurations of submerged flexible vegetation. *Journal of Hydrology* **398** (1-2), 124–134.

Chorin, Alexandre Joel 1968 Numerical solution of the navier-stokes equations. *Mathematics of computation* **22** (104), 745–762.

Costanza, Robert, d'Arge, Ralph, De Groot, Rudolf, Farber, Stephen, Grasso, Monica, Hannon, Bruce, Limburg, Karin, Naeem, Shahid, O'neill, Robert V, Paruelo, Jose & others 1997 The value of the world's ecosystem services and natural capital. *nature* **387** (6630), 253–260.

Cui, Jie & Neary, Vincent S 2008 Les study of turbulent flows with submerged vegetation. *Journal of Hydraulic Research* **46** (3), 307–316.

Dalcin, Lisandro, Mortensen, Mikael & Keyes, David E 2019 Fast parallel multidimensional fft using advanced mpi. *Journal of Parallel and Distributed Computing* **128**, 137–150.

De Langre, Emmanuel 2008 Effects of wind on plants. *Annu. Rev. Fluid Mech.* **40**, 141–168.

De Langre, Emmanuel, Gutierrez, Alvaro & Cossé, Julia 2012 On the scaling of drag reduction by reconfiguration in plants. *Comptes Rendus Mécanique* **340** (1-2), 35–40.

Defina, Andrea & Bixio, Anna Chiara 2005 Mean flow and turbulence in vegetated open channel flow. *Water Resources Research* **41** (7).

Dehnhardt, Guido, Mauck, Bjorn, Hanke, Wolf & Bleckmann, Horst 2001 Hydrodynamic trail-following in harbor seals (phoca vitulina). *Science* **293** (5527), 102–104.

Dillon, Erin M, Norris, Richard D & Dea, Aaron O 2017 Dermal denticles as a tool to reconstruct shark communities. *Marine Ecology Progress Series* **566**, 117–134.

Dupont, Sylvain & Brunet, Yves 2008 Influence of foliar density profile on canopy flow: a large-eddy simulation study. *Agricultural and forest meteorology* **148** (6-7), 976–990.

Elahi, Hassan, Eugeni, Marco & Gaudenzi, Paolo 2018 A review on mechanisms for piezoelectric-based energy harvesters. *Energies* **11** (7), 1850.

Elshalakani, Mohamed, Muthuramalingam, Muthukumar & Bruecker, Christoph 2020 A deep-learning model for underwater position sensing of a wake's source using artificial seal whiskers. *Sensors* **20** (12), 3522.

Endrikat, S, Modesti, D, García-Mayoral, R, Hutchins, N & Chung, D 2021 Influence of riblet shapes on the occurrence of kelvin–helmholtz rollers. *Journal of Fluid Mechanics* **913**.

Fadlun, EA, Verzicco, Roberto, Orlandi, Paolo & Mohd-Yusof, J 2000 Combined immersed-boundary finite-difference methods for three-dimensional complex flow simulations. *Journal of computational physics* **161** (1), 35–60.

Favier, Julien, Revell, Alistair & Pinelli, Alfredo 2014 A lattice boltzmann–immersed boundary method to simulate the fluid interaction with moving and slender flexible objects. *Journal of Computational Physics* **261**, 145–161.

Ferziger, Joel H, Perić, Milovan & Street, Robert L 2002 *Computational methods for fluid dynamics*, , vol. 3. Springer.

Finnigan, John 2000 Turbulence in plant canopies. *Annual Review of Fluid Mechanics* **32** (1), 519–571.

Finnigan, John J & Shaw, Roger H 2008 Double-averaging methodology and its application to turbulent flow in and above vegetation canopies. *Acta Geophysica* **56** (3), 534–561.

Finnigan, John J, Shaw, Roger H & Patton, Edward G 2009 Turbulence structure above a vegetation canopy. *Journal of Fluid Mechanics* **637**, 387–424.

Flack, Karen A 2018 Moving beyond moody. *Journal of Fluid Mechanics* **842**, 1–4.

Flack, Karen A & Schultz, Michael P 2014 Roughness effects on wall-bounded turbulent flows. *Physics of Fluids* **26** (10), 101305.

Fliegauf, Manfred, Benzing, Thomas & Omran, Heymut 2007 When cilia go bad: cilia defects and ciliopathies. *Nature reviews Molecular cell biology* **8** (11), 880–893.

Garcia-Mayoral, Ricardo & Jimenez, Javier 2011 Hydrodynamic stability and breakdown of the viscous regime over riblets. *Journal of Fluid Mechanics* **678**, 317–347.

Garcia-Mayoral, Ricardo, Gómez-de Segura, Garazi & Fairhall, Chris T 2019 The control of near-wall turbulence through surface texturing. *Fluid Dynamics Research* **51** (1), 011410.

Germano, Massimo 1992 Turbulence: the filtering approach. *Journal of Fluid Mechanics* **238**, 325–336.

Germano, Massimo, Piomelli, Ugo, Moin, Parviz & Cabot, William H 1991 A dynamic subgrid-scale eddy viscosity model. *Physics of Fluids A: Fluid Dynamics* **3** (7), 1760–1765.

Ghisalberti, Marco & Nepf, HM 2004 The limited growth of vegetated shear layers. *Water Resources Research* **40** (7).

Ghisalberti, Marco & Nepf, Heidi 2009 Shallow flows over a permeable medium: the hydrodynamics of submerged aquatic canopies. *Transport in porous media* **78** (2), 309–326.

Ghisalberti, Marco & Nepf, Heidi M 2002 Mixing layers and coherent structures in vegetated aquatic flows. *Journal of Geophysical Research: Oceans* **107** (C2), 3–1.

Ghosal, Sandip, Lund, Thomas S, Moin, Parviz & Akselvoll, K 1995 A dynamic localization model for large-eddy simulation of turbulent flows. *J. Fluid Mech* **286**, 229–255.

Griffith, Boyce E & Patankar, Neelesh A 2020 Immersed methods for fluid–structure interaction. *Annual review of fluid mechanics* **52**, 421.

Guilmineau, Emmanuel & Queutey, P 2002 A numerical simulation of vortex shedding from an oscillating circular cylinder. *Journal of Fluids and Structures* **16** (6), 773–794.

Hama, Francis R 1954 Boundary layer characteristics for smooth and rough surfaces. *Trans. Soc. Nav. Arch. Marine Engrs.* **62**, 333–358.

Harman, Ian N & Finnigan, John J 2007 A simple unified theory for flow in the canopy and roughness sublayer. *Boundary-layer meteorology* **123** (2), 339–363.

Higham, Nicholas J 2009 Cholesky factorization. *Wiley interdisciplinary reviews: computational statistics* **1** (2), 251–254.

Hou, Shuling, Zou, Qisu, Chen, Shiyi, Doolen, Gary & Cogley, Allen C 1995 Simulation of cavity flow by the lattice boltzmann method. *Journal of computational physics* **118** (2), 329–347.

Hoyas, Sergio & Jiménez, Javier 2008 Reynolds number effects on the reynolds-stress budgets in turbulent channels. *Physics of Fluids* **20** (10), 101511.

Hurd, Catriona L 2000 Water motion, marine macroalgal physiology, and production. *Journal of Phycology* **36** (3), 453–472.

Ibrahim, Joseph I, Gómez-de Segura, Garazi, Chung, Daniel & García-Mayoral, Ricardo 2021 The smooth-wall-like behaviour of turbulence over drag-altering surfaces: a unifying virtual-origin framework. *Journal of Fluid Mechanics* **915**.

Itoh, Motoyuki, Tamano, Shinji, Iguchi, Ryo, Yokota, Kazuhiko, Akino, Norio, Hino, Ryutaro & Kubo, Shinji 2006 Turbulent drag reduction by the seal fur surface. *Physics of Fluids* **18** (6), 065102.

Jackson, PS 1981 On the displacement height in the logarithmic velocity profile. *Journal of fluid mechanics* **111**, 15–25.

Jiménez, Javier 1994 On the structure and control of near wall turbulence. *Physics of Fluids* **6** (2), 944–953.

Jiménez, Javier 2004 Turbulent flows over rough walls. *Annu. Rev. Fluid Mech.* **36**, 173–196.

Jiménez, Javier 2013 Near-wall turbulence. *Physics of Fluids* **25** (10), 101302.

Jiménez, Javier 2018 Coherent structures in wall-bounded turbulence. *Journal of Fluid Mechanics* **842**.

Jiménez, Javier & Pinelli, Alfredo 1999 The autonomous cycle of near-wall turbulence. *Journal of Fluid Mechanics* **389**, 335–359.

Jimenez, Javier, Uhlmann, Markus, Pinelli, Alfredo & Kawahara, Genta 2001 Turbulent shear flow over active and passive porous surfaces. *Journal of Fluid Mechanics* **442**, 89.

Khorasani, Seyed Morteza Habibi, Lācis, Uǧis, Pasche, Simon, Rosti, Marco Edoardo & Bagheri, Shervin 2022 Near-wall turbulence alteration with the transpiration-resistance model. *Journal of Fluid Mechanics* **942**.

Kim, John & Moin, Parviz 1985 Application of a fractional-step method to incompressible navier-stokes equations. *Journal of computational physics* **59** (2), 308–323.

Kim, John, Moin, Parviz & Moser, Robert 1987 Turbulence statistics in fully developed channel flow at low reynolds number. *Journal of fluid mechanics* **177**, 133–166.

Koch, Kerstin & Barthlott, Wilhelm 2009 Superhydrophobic and superhydrophilic plant surfaces: an inspiration for biomimetic materials. *Philosophical Transactions of the Royal Society A: Mathematical, Physical and Engineering Sciences* **367** (1893), 1487–1509.

Kovalev, Igor 2008 The functional role of the hollow region of the butterfly pyrameis atalanta (l.) scale. *Journal of Bionic Engineering* **5** (3), 224–230.

Kuwata, Y & Suga, K 2017 Direct numerical simulation of turbulence over anisotropic porous media. *Journal of Fluid Mechanics* **831**, 41.

Kwon, Yongseok & Jiménez, Javier 2021 An isolated logarithmic layer. *Journal of Fluid Mechanics* **916**.

Lācis, Uǧis, Sudhakar, Y, Pasche, Simon & Bagheri, Shervin 2020 Transfer of mass and momentum at rough and porous surfaces. *Journal of Fluid Mechanics* **884**.

Lee, Eon S, Ranasinghe, Dilhara R, Ahangar, Faraz Enayati, Amini, Seyedmorteza, Mara, Steven, Choi, Wonsik, Paulson, Suzanne & Zhu, Yifang 2018 Field evaluation of vegetation and noise barriers for mitigation of near-freeway air pollution under variable wind conditions. *Atmospheric Environment* **175**, 92–99.

Lee, Myoungkyu & Moser, Robert D 2015*a* Direct numerical simulation of turbulent channel flow up to. *Journal of fluid mechanics* **774**, 395–415.

Lee, Myoungkyu & Moser, Robert D. 2015*b* Direct numerical simulation of turbulent channel flow up to $Re_\tau \approx 5200$. *Journal of Fluid Mechanics* **774**, 395–415.

Leonard, Athony 1975 Energy cascade in large-eddy simulations of turbulent fluid flows. In *Advances in geophysics*, , vol. 18, pp. 237–248. Elsevier.

Leonardi, Stefano, Orlandi, Paolo & Antonia, Robert A 2007 Properties of d-and k-type roughness in a turbulent channel flow. *Physics of fluids* **19** (12), 125101.

Lightbody, Anne F & Nepf, Heidi M 2006 Prediction of velocity profiles and longitudinal dispersion in salt marsh vegetation. *Limnology and oceanography* **51** (1), 218–228.

Lilly, K 1966 The representation of small-scale turbulence in numerical simulation experiments .

Liu, D, Diplas, P, Fairbanks, JD & Hodges, CC 2008 An experimental study of flow through rigid vegetation. *Journal of Geophysical Research: Earth Surface* **113** (F4).

Liu, Wing Kam, Chen, Yijung, Uras, R Aziz & Chang, Chin Tang 1996 Generalized multiple scale reproducing kernel particle methods. *Computer Methods in Applied Mechanics and Engineering* **139** (1-4), 91–157.

Liu, Wing Kam, Jun, Sukky & Zhang, Yi Fei 1995 Reproducing kernel particle methods. *International journal for numerical methods in fluids* **20** (8-9), 1081–1106.

López, Fabián & García, Marcelo H 2001 Mean flow and turbulence structure of open-channel flow through non-emergent vegetation. *Journal of Hydraulic Engineering* **127** (5), 392–402.

Luchini, Paolo 1996 Reducing the turbulent skin friction. In *ECCOMAS conference on numerical methods in engineering*, pp. 465–470.

Luchini, Paolo, Manzo, Fernando & Pozzi, Amilcare 1991 Resistance of a grooved surface to parallel flow and cross-flow. *Journal of fluid mechanics* **228**, 87–109.

Luhar, Mitul & Nepf, Heidi M 2011 Flow-induced reconfiguration of buoyant and flexible aquatic vegetation. *Limnology and Oceanography* **56** (6), 2003–2017.

Luminari, Nicola, Airiau, Christophe & Bottaro, Alessandro 2016 Drag-model sensitivity of kelvin-helmholtz waves in canopy flows. *Physics of Fluids* **28** (12), 124103.

MacDonald, M, Chan, L, Chung, D, Hutchins, N & Ooi, A 2016 Turbulent flow over transitionally rough surfaces with varying roughness densities. *Journal of Fluid Mechanics* **804**, 130–161.

MacDonald, M, Ooi, A, García-Mayoral, R, Hutchins, N & Chung, D 2018 Direct numerical simulation of high aspect ratio spanwise-aligned bars. *Journal of Fluid Mechanics* **843**, 126–155.

Mars, Ross, Mathew, Kuruvilla & Ho, Goen 1999 The role of the submergent macrophyte triglochin huegelii in domestic greywater treatment. *Ecological Engineering* **12** (1-2), 57–66.

Mignot, Emmanuel, Barthélemy, Eric & Hurther, David 2009 Double-averaging analysis and local flow characterization of near-bed turbulence in gravel-bed channel flows. *Journal of Fluid Mechanics* **618**, 279–303.

Mittal, Rajat & Iaccarino, Gianluca 2005*a* Immersed boundary methods. *Annual Review of Fluid Mechanics* **37** (1), 239–261, arXiv: https://doi.org/10.1146/annurev.fluid.37.061903.175743.

Mittal, Rajat & Iaccarino, Gianluca 2005*b* Immersed boundary methods. *Annu. Rev. Fluid Mech.* **37**, 239–261.

Mizuno, Yoshinori & Jiménez, Javier 2013 Wall turbulence without walls. *Journal of Fluid Mechanics* **723**, 429–455.

Moin, Parviz & Mahesh, Krishnan 1998 Direct numerical simulation: a tool in turbulence research. *Annual review of fluid mechanics* **30** (1), 539–578.

Monti, A 2019 High-fidelity simulations of fully submerged, rigid canopy flows.

Monti, Alessandro, Nicholas, Shane, Omidyeganeh, Mohammad, Pinelli, Alfredo & Rosti, Marco E. 2022 On the solidity parameter in canopy flows. *Journal of Fluid Mechanics* **945**, A17.

Monti, Alessandro, Omidyeganeh, Mohammad, Eckhardt, Bruno & Pinelli, Alfredo 2020 On the genesis of different regimes in canopy flows: a numerical investigation. *Journal of Fluid Mechanics* **891**.

Monti, A, Omidyeganeh, M & Pinelli, A 2019 Large-eddy simulation of an open-channel flow bounded by a semi-dense rigid filamentous canopy: Scaling and flow structure. *Physics of Fluids* **31** (6), 065108.

Moser, Robert D, Haering, Sigfried W & Yalla, Gopal R 2021 Statistical properties of subgrid-scale turbulence models. *Annual Review of Fluid Mechanics* **53**, 255–286.

Moser, Robert D, Kim, John & Mansour, Nagi N 1999 Direct numerical simulation of turbulent channel flow up to re τ= 590. *Physics of fluids* **11** (4), 943–945.

Muzaferija, Samir 1994 Adaptive finite volume method for flow prediction using unstructured meshes and multigrid approach. PhD thesis, University of London London.

Nepf, Heidi M 1999 Drag, turbulence, and diffusion in flow through emergent vegetation. *Water resources research* **35** (2), 479–489.

Nepf, Heidi M 2012 Flow and transport in regions with aquatic vegetation. *Annual review of fluid mechanics* **44**, 123–142.

Nepf, Heidi M & Vivoni, ER 2000 Flow structure in depth-limited, vegetated flow. *Journal of Geophysical Research: Oceans* **105** (C12), 28547–28557.

Nezu, Iehisa & Sanjou, Michio 2008 Turburence structure and coherent motion in vegetated canopy open-channel flows. *Journal of hydro-environment research* **2** (2), 62–90.

Nikora, Vladimir, McEwan, Ian, McLean, Stephen, Coleman, Stephen, Pokrajac, Dubravka & Walters, Roy 2007*a* Double-averaging concept for rough-bed open-channel and overland flows: Theoretical background. *Journal of hydraulic Engineering* **133** (8), 873–883.

Nikora, Vladimir, McLean, Stephen, Coleman, Stephen, Pokrajac, Dubravka, McEwan, Ian, Campbell, Lorna, Aberle, Jochen, Clunie, Dougal & Koll, Katinka 2007*b* Double-averaging concept for rough-bed open-channel and overland flows: Applications. *Journal of hydraulic Engineering* **133** (8), 884–895.

Nikuradse, Johann 1933 Stromungsgesetze in rauhen rohren. *vdi-forschungsheft* **361**, 1.

Oeffner, Johannes & Lauder, George V 2012 The hydrodynamic function of shark skin and two biomimetic applications. *Journal of Experimental Biology* **215** (5), 785–795.

Okamoto, Taka-Aki & Nezu, Iehisa 2009 Turbulence structure and "monami" phenomena in flexible vegetated open-channel flows. *Journal of Hydraulic Research* **47** (6), 798–810.

Omidyeganeh, Mohammad & Piomelli, Ugo 2011 Large-eddy simulation of two-dimensional dunes in a steady, unidirectional flow. *Journal of Turbulence* (12), N42.

Omidyeganeh, Mohammad & Piomelli, Ugo 2013*a* Large-eddy simulation of three-dimensional dunes in a steady, unidirectional flow. part 1. turbulence statistics. *Journal of Fluid Mechanics* **721**, 454–483.

Omidyeganeh, Mohammad & Piomelli, Ugo 2013*b* Large-eddy simulation of three-dimensional dunes in a steady, unidirectional flow. part 2. flow structures. *Journal of Fluid Mechanics* **734**, 509–534.

Ong, Lawrence & Wallace, James M 1998 Joint probability density analysis of the structure and dynamics of the vorticity field of a turbulent boundary layer. *Journal of Fluid Mechanics* **367**, 291–328.

Orlandi, P & Leonardi, S 2008 Direct numerical simulation of three-dimensional turbulent rough channels: parameterization and flow physics. *Journal of Fluid Mechanics* **606**, 399–415.

Pan, Ying, Follett, Elizabeth, Chamecki, Marcelo & Nepf, Heidi 2014 Strong and weak, unsteady reconfiguration and its impact on turbulence structure within plant canopies. *Physics of Fluids* **26** (10), 2003–2017.

Park, H, Bae, K, Lee, B, Jeon, W-P & Choi, H 2010 Aerodynamic performance of a gliding swallowtail butterfly wing model. *Experimental Mechanics* **50** (9), 1313–1321.

Pedras, Marcos HJ & de Lemos, Marcelo JS 2000 On the definition of turbulent kinetic energy for flow in porous media. *International communications in heat and mass transfer* **27** (2), 211–220.

Perez Goodwyn, Pablo, Maezono, Yasunori, Hosoda, Naoe & Fujisaki, Kenji 2009 Waterproof and translucent wings at the same time: problems and solutions in butterflies. *Naturwissenschaften* **96** (7), 781–787.

Perry, Anthony Edward, Schofield, William H & Joubert, Peter N 1969 Rough wall turbulent boundary layers. *Journal of Fluid Mechanics* **37** (2), 383–413.

Peskin, Charles S 1972 Flow patterns around heart valves: a numerical method. *Journal of computational physics* **10** (2), 252–271.

Pinelli, Alfredo, Naqavi, IZ, Piomelli, Ugo & Favier, Julien 2010 Immersed-boundary methods for general finite-difference and finite-volume navier–stokes solvers. *Journal of Computational Physics* **229** (24), 9073–9091.

Pinelli, Alfredo, Omidyeganeh, Mohammad, Brücker, Christoph, Revell, Alistair, Sarkar, Abhishek & Alinovi, Edoardo 2017 The pelskin project: part iv—control of bluff body wakes using hairy filaments. *Meccanica* **52** (7), 1503–1514.

Piomelli, Ugo 1999 Large-eddy simulation: achievements and challenges. *Progress in aerospace sciences* **35** (4), 335–362.

Piomelli, Ugo, Cabot, William H, Moin, Parviz & Lee, Sangsan 1991 Subgrid-scale backscatter in turbulent and transitional flows. *Physics of Fluids A: Fluid Dynamics* **3** (7), 1766–1771.

Piomelli, Ugo, Moin, Parviz & Ferziger, Joel H 1988 Model consistency in large eddy simulation of turbulent channel flows. *The Physics of fluids* **31** (7), 1884–1891.

Piomelli, Ugo, Rouhi, Amirreza & Geurts, Bernard J 2015 A grid-independent length scale for large-eddy simulations. *Journal of fluid mechanics* **766**, 499.

Poggi, D, Katul, GG & Albertson, JD 2004*a* A note on the contribution of dispersive fluxes to momentum transfer within canopies. *Boundary-layer meteorology* **111** (3), 615–621.

Poggi, Davide & Katul, Gabriel G 2008 The effect of canopy roughness density on the constitutive components of the dispersive stresses. *Experiments in fluids* **45** (1), 111–121.

Poggi, Davide, Porporato, Amilcare, Ridolfi, Luca, Albertson, JD & Katul, GG 2004*b* The effect of vegetation density on canopy sub-layer turbulence. *Boundary-Layer Meteorology* **111** (3), 565–587.

Pope, Stephen B 2000 *Turbulent flows*. Cambridge university press.

Pope, Stephen B 2004 Ten questions concerning the large-eddy simulation of turbulent flows. *New journal of Physics* **6** (1), 35.

Prasad, Ajay K & Koseff, Jeffrey R 1989 Reynolds number and end-wall effects on a lid-driven cavity flow. *Physics of Fluids A: Fluid Dynamics* **1** (2), 208–218.

Raupach, M. R., Antonia, R. A. & Rajagopalan, S. 1991 Rough-Wall Turbulent Boundary Layers. *Applied Mechanics Reviews* **44** (1), 1–25.

Raupach, Michael R, Finnigan, John J & Brunet, Yves 1996 Coherent eddies and turbulence in vegetation canopies: the mixing-layer analogy. In *Boundary-layer meteorology 25th anniversary volume, 1970–1995*, pp. 351–382. Springer.

Raupach, M R & Thom, A S 1981 Turbulence in and above plant canopies. *Annual Review of Fluid Mechanics* **13** (1), 97–129.

Ree, William Oscar & Palmer, Vernon John 1949 *Flow of water in channels protected by vegetative linings*. US Department of Agriculture.

Reynolds, WC & Hussain, AKMF 1972 The mechanics of an organized wave in turbulent shear flow. part 3. theoretical models and comparisons with experiments. *Journal of Fluid Mechanics* **54** (2), 263–288.

Rhie, CM & Chow, W Li 1983 Numerical study of the turbulent flow past an airfoil with trailing edge separation. *AIAA journal* **21** (11), 1525–1532.

Rogers, Michael M & Moser, Robert D 1994 Direct simulation of a self-similar turbulent mixing layer. *Physics of Fluids* **6** (2), 903–923.

Roma, Alexandre M, Peskin, Charles S & Berger, Marsha J 1999 An adaptive version of the immersed boundary method. *Journal of computational physics* **153** (2), 509–534.

Rosen, Moe Wm & Cornford, Neri E 1971 Fluid friction of fish slimes. *Nature* **234** (5323), 49–51.

Rosti, Marco 2016 Direct numerical simulation of an aerofoil at high angle of attack and its control. PhD thesis, City, University of London.

Rosti, Marco E & Brandt, Luca 2017 Numerical simulation of turbulent channel flow over a viscous hyper-elastic wall. *Journal of Fluid Mechanics* **830**, 708–735.

Rosti, Marco E, Brandt, Luca & Pinelli, Alfredo 2018*a* Turbulent channel flow over an anisotropic porous wall–drag increase and reduction. *Journal of Fluid Mechanics* **842**, 381–394.

Rosti, Marco E, Cortelezzi, Luca & Quadrio, Maurizio 2015 Direct numerical simulation of turbulent channel flow over porous walls. *Journal of Fluid Mechanics* **784**, 396–442.

Rosti, Marco E, Omidyeganeh, Mohammad & Pinelli, Alfredo 2016 Direct numerical simulation of the flow around an aerofoil in ramp-up motion. *Physics of Fluids* **28** (2), 025106.

Rosti, Marco E, Omidyeganeh, Mohammad & Pinelli, Alfredo 2018*b* Numerical simulation of a passive control of the flow around an aerofoil using a flexible, self adaptive flaplet. *Flow, Turbulence and Combustion* **100** (4), 1111–1143.

Rothstein, Jonathan P 2010 Slip on superhydrophobic surfaces. *Annual review of fluid mechanics* **42**, 89–109.

Rouhi, Amirreza, Piomelli, Ugo & Geurts, Bernardus J 2016 Dynamic subfilter-scale stress model for large-eddy simulations. *Physical review fluids* **1** (4), 044401.

Schlichting, Hermann 1937 *Experimental investigation of the problem of surface roughness*. National Advisory Commitee for Aeronautics.

Scotti, Alberto 2006 Direct numerical simulation of turbulent channel flows with boundary roughened with virtual sandpaper. *Physics of Fluids* **18** (3), 031701.

Gómez-de Segura, Garazi & García-Mayoral, Ricardo 2019 Turbulent drag reduction by anisotropic permeable substrates–analysis and direct numerical simulations. *Journal of Fluid Mechanics* **875**, 124–172.

Gómez-de Segura, Garazi & García-Mayoral, Ricardo 2020 Imposing virtual origins on the velocity components in direct numerical simulations. *International Journal of Heat and Fluid Flow* **86**, 108675.

Sharma, Akshath & García-Mayoral, Ricardo 2020*a* Scaling and dynamics of turbulence over sparse canopies. *Journal of Fluid Mechanics* **888**.

Sharma, Akshath & García-Mayoral, Ricardo 2020*b* Turbulent flows over dense filament canopies. *Journal of Fluid Mechanics* **888**.

Shephard, Kerry L 1994 Functions for fish mucus. *Reviews in fish biology and fisheries* **4** (4), 401–429.

Shimizu, Yoshihiko, Tsujimoto, Tetsuro, Nakagawa, Hiroji & Kitamura, Tadanori 1991 Experimental study on flow over rigid vegetation simulated by cylinders with equi-spacing. *Doboku Gakkai Ronbunshu* **1991** (438), 31–40.

Sleijpen, Gerard LG, Van der Vorst, Henk A & Fokkema, Diederik R 1994 Bicgstab (l) and other hybrid bi-cg methods. *Numerical Algorithms* **7** (1), 75–109.

Smagorinsky, Joseph 1963 General circulation experiments with the primitive equations: I. the basic experiment. *Monthly weather review* **91** (3), 99–164.

Spalart, Philippe R & McLean, J Douglas 2011 Drag reduction: enticing turbulence, and then an industry. *Philosophical Transactions of the Royal Society A: Mathematical, Physical and Engineering Sciences* **369** (1940), 1556–1569.

Stoesser, Thorsten, Salvador, Guillermo Palau, Rodi, Wolfgang & Diplas, Panayiotis 2009 Large eddy simulation of turbulent flow through submerged vegetation. *Transport in porous media* **78** (3), 347–365.

Suardi, C. A. 2020 Separating flows around swept and unswept wings with laminar and turbulent free stream conditions.

Suga, Kazuhiko, Okazaki, Yuki, Ho, Unde & Kuwata, Yusuke 2018 Anisotropic wall permeability effects on turbulent channel flows. *Journal of Fluid Mechanics* **855**, 983–1016.

Sundin, Johan & Bagheri, Shervin 2019 Interaction between hairy surfaces and turbulence for different surface time scales. *Journal of Fluid Mechanics* **861**, 556–584.

Thakkar, M, Busse, A & Sandham, ND 2018 Direct numerical simulation of turbulent channel flow over a surrogate for nikuradse-type roughness. *Journal of Fluid Mechanics* **837**.

Townsend, AA 1976 The structure of turbulent shear flow (cambridge u. press) .

Triantafyllou, Michael S, Weymouth, Gabriel D & Miao, Jainmin 2016 Biomimetic survival hydrodynamics and flow sensing. *Annual Review of Fluid Mechanics* **48** (1).

Tschisgale, Silvio, Löhrer, Bastian, Meller, Richard & Fröhlich, Jochen 2021 Large eddy simulation of the fluid–structure interaction in an abstracted aquatic canopy consisting of flexible blades. *Journal of Fluid Mechanics* **916**.

Tuerke, Florian & Jiménez, Javier 2013 Simulations of turbulent channels with prescribed velocity profiles. *Journal of Fluid Mechanics* .

Vogel, Steven 1984 Drag and flexibility in sessile organisms. *American Zoologist* **24** (1), 37–44.

Wallace, James M 2016 Quadrant analysis in turbulence research: history and evolution. *Annual Review of Fluid Mechanics* **48**, 131–158.

Watanabe, Tsutomu 2004 Large-eddy simulation of coherent turbulence structures associated with scalar ramps over plant canopies. *Boundary-Layer Meteorology* **112** (2), 307–341.

Webb, RL, Eckert, ERG & Goldstein, RJf 1971 Heat transfer and friction in tubes with repeated-rib roughness. *International journal of heat and mass transfer* **14** (4), 601–617.

White, Brian L & Nepf, Heidi M 2007 Shear instability and coherent structures in shallow flow adjacent to a porous layer. *Journal of Fluid Mechanics* **593**, 1–32.

Williamson, CH 1996 K. vortex dynamics in the cylinder wake. *Annual Review of Fluid Mechanics* **28** (1), 477–539.

Yang, Ulrike Meier & others 2002 Boomeramg: a parallel algebraic multigrid solver and preconditioner. *Applied Numerical Mathematics* **41** (1), 155–177.

Yang, Xiang IA, Sadique, Jasim, Mittal, Rajat & Meneveau, Charles 2016 Exponential roughness layer and analytical model for turbulent boundary layer flow over rectangular-prism roughness elements. *Journal of Fluid Mechanics* **789**, 127.

Yoshizawa, Akira 1982 A statistically-derived subgrid model for the large-eddy simulation of turbulence. *The Physics of Fluids* **25** (9), 1532–1538.

Yuan, Junlin & Piomelli, Ugo 2014 Roughness effects on the reynolds stress budgets in near-wall turbulence. *Journal of Fluid Mechanics* **760**.

Zampogna, Giuseppe A & Bottaro, Alessandro 2016 Fluid flow over and through a regular bundle of rigid fibres. *Journal of Fluid Mechanics* **792**, 5.

Zampogna, Giuseppe A, Pluvinage, Franck, Kourta, Azeddine & Bottaro, Alessandro 2016 Instability of canopy flows. *Water Resources Research* **52** (7), 5421–5432.

Zhang, Lucy, Gerstenberger, Axel, Wang, Xiaodong & Liu, Wing Kam 2004 Immersed finite element method. *Computer Methods in Applied Mechanics and Engineering* **193** (21-22), 2051–2067.

Zhang, Wen, Zhu, Xiaowei, Yang, Xiang IA & Wan, Minping 2022 Evidence for raupach et al.'s mixing-layer analogy in deep homogeneous urban-canopy flows. *Journal of Fluid Mechanics* **944**.

Zheng, Yongmei, Gao, Xuefeng & Jiang, Lei 2007 Directional adhesion of superhydrophobic butterfly wings. *Soft Matter* **3** (2), 178–182.